DISSERTATION

INVESTIGATING THE ROLE OF CHEMICAL ADDITIVES IN THE STRUCTURE AND DYNAMICS OF ELECTROLYTE MIXTURES VIA 2D INFRARED SPECTROSCOPY AND MICROSCOPY

Submitted by

Clara Anne Tibbetts

Department of Chemistry

In partial fulfillment of the requirements

For the Degree of Doctor of Philosophy

Colorado State University

Fort Collins, Colorado

Fall 2022

Doctoral Committee:

Advisor: Amber T. Krummel

Nancy Levinger
Jesse Wilson
Anthony Rappe

ABSTRACT

INVESTIGATING THE ROLE OF CHEMICAL ADDITIVES IN THE STRUCTURE AND DYNAMICS OF ELECTROLYTE MIXTURES VIA 2D INFRARED SPECTROSCOPY AND MICROSCOPY

The research in this dissertation is focused on the impact that additives have on the chemical structure and dynamics of electrolyte solutions that can be used in electrochemical devices such as batteries or solar devices. Two-dimensional infrared spectroscopy (2D IR) has been used in conjunction with linear Fourier Transform infrared spectroscopy (FTIR), rheology, molecular dynamics, and density functional theory to study organic carbonate and ionic liquid mixtures. In addition, 2D IR microscopy is successfully implemented to study ionic liquid mixtures in different environments including a microdroplet and a copper electrochemical cell.

2D IR and molecular dynamics simulations of organic carbonate mixtures with varied amounts of a common additive, fluoroethylene carbonate (FEC), show that even in small quantities FEC can induce changes in the solvent structure. Experimental results demonstrated that at low concentrations FEC slows spectral diffusion. Cylindrical distribution functions calculated from molecular dynamics simulations in conjunction with experimental results suggest the slowing is due to significant changes in the behavior of one of the solution components, ethylene carbonate. Furthermore, a combination of experimental anisotropy and viscosity, and computational rotational correlation functions shows that local solvent rigidity increases with high amounts of FEC. Moreover, these results show that additional FEC increases macroscopic viscosity which is correlated to global solvent orientational relaxation. In functional batteries FEC is shown to dramatically impact how the solid electrolyte interphase forms, a layer that impacts battery metrics such as lifetime and safety.[1–3] Therefore, it is possible that the observed changes in the solvent structure upon addition of FEC has implications in how the solid electrolyte interphase forms.

The combination of linear and 2D IR spectroscopy with viscosity measurements is used to study the impact of small amounts of water (between ~1.32 and 21.6% mole fraction water) on the structure and dynamics of room-temperature ionic liquid mixtures. Specifically, the effects of water on a mixture of 1-butyl-3-methylimidazolium tetrafluoroborate ($BmimBF_4$) and 1-butyl-3-methylimidazolium dicyanamide (BmimDCA) room-temperature ionic liquid (RTIL) was investigated by tracking changes in the vibrational features of the dicyanamide anion (DCA). Shifts in the infrared peak frequencies of DCA indicated the formation of water-associated and non-water-associated DCA populations. Time-dependent 2D IR shows differences in the dynamic behavior of the water-associated and non-water-associated populations of DCA at low (below 2.5% χ_{Water}), mid (between 2.5% χ_{Water} and 9.6% χ_{Water}), and high (between 11.6% χ_{Water} and 21.6% χ_{Water}) water concentrations. The vibrational relaxation occurs more quickly with increasing water content for water-associated populations of DCA, indicating water introduces additional pathways for relaxation, possibly via new bath modes. On the other hand, spectral diffusion of water-associated populations slows significantly with more water, suggesting water induces the formation of distinct and non- or very slowly interchangeable local environments. It is possible that in a functional electrochemical device with a water and RTIL electrolyte the introduction of these diverse local solvent environments might impact device performance. If water could be introduced in a system in a way that increased ion-mobility but does not cause undesirable interfacial interactions near an electrode this could improve device efficiency. Therefore, determining if and how this local heterogeneity presents itself in an operational electrochemical cell is an important next step.

Ultrafast 2D IR microscopy is discussed as an emerging imaging platform that is a promising tool for investigating heterogeneous samples across multiple time scales and length scales, including electrochemical devices. However, there are numerous practical considerations in the implementation of 2D IR microscopy. Some of these considerations include mid-IR laser sources, repetition rates, mid-IR pulse shaping, noise reduction, microscope design, and detection limitations. In this work we show the implementation of improvements in spectral resolution and noise reduction and the consequent successful

imaging of a BmimDCA:BmimBF$_4$ electrolyte in two different scenarios—a droplet and a copper electrochemical cell. Imaging the BmimDCA:BmimBF$_4$ microdroplet shows how 2D IR imaging can be used to probe dynamics on a spatial scale. Results indicate the solvent dynamics in the microdroplet are spatially homogenous. Imaging experiments of the RTIL electrolyte in a copper cell, demonstrates a practical application of ultrafast 2D IR microscopy to study functional electrochemical devices. 2D IR spectra collected between the copper counter electrode and working electrode showed dramatic changes in peak positions and shapes suggesting the formation of DCA copper complexes. These results suggest 2D IR microscopy will allow chemical exchange dynamics of different species involved in the electrochemical reactions to be monitored as they evolve from the counter electrode to the working electrode. This work establishes 2D IR microscopy as a tool well equipped to connect molecular level condensed phase reaction dynamics to micro- and mesoscale spatial dependence in an electrochemical cell.

ACKNOWLEDGEMENTS

First, I want to thank Dr. Amber Krummel for being a truly excellent advisor and mentor for the last six years. Thank you for always pushing me to be a better scientist (and to have more confidence and speak louder). I always appreciate being able to stop by your office to discuss my endless science questions. In addition, I greatly appreciate your constant support of myself (and all the graduate students in our group) personally and academically, you always go above and beyond. Moreover, I am continually impressed by your advocacy behalf of all students. And thank you for supporting my own interests outside of the lab- policy and advocacy work are incredibly important to me and I know that I am lucky to have an advisor who supports that work.

I want to thank my committee Dr. Nancy Levinger, Dr. Jesse Wilson, and Dr. Tony Rappe for reading this dissertation and being a part of my PhD journey.

I also want to thank the excellent collaborators I have had the pleasure of working with over the years: Dr. Steve Corcelli, Dr. Shelby Brantly, Nathan Gimble, and Dr. Amy Prieto. You have each provided invaluable assistance in putting together a cool scientific puzzle (read on to Chapter 3 to find out more!).

Next, I want to thank everyone in the Krummel research group, past and present. Special thanks to Yusef for being the best lab counterpart I could ever ask for; you have been integral to my journey and an invaluable source of support. Thanks to; Brad for always pushing me to be a better (and more skeptical) scientist, supporting me when I needed it, and for all the coffee conversations; Luke for always providing excellent scientific insights and for commiserating over moody lasers and the state of the world; Autumn for being always bringing the enthusiasm and sticking through the long nights collecting data; Kat for being so welcoming and my original mentor in the group; Max and Kuhs for putting up with my endless questions; Tom for the KitchenAid – so much stress baking was made possible due to your kind donation.

In addition, I want to thank the other graduate students in the 2016 p-chem cohort– Yusef, Megan, Alireza, and David. Thank you for being moral and academic support during classes and excellent friends throughout.

Next, I want to thank the Willamette Chemistry department, in particular Professor Chuck Williamson. I would not have pursued chemistry, let alone physical chemistry if it wasn't for you. Moreover, your ability to make any topic accessible and exciting has inspired me throughout my graduate career to find fun ways to explain complex topics.

Next, I want to thank my ever-growing science advocacy, communication, and policy community. This PhD process has taught me a lot, including that one of my favorite parts of science is talking about it and thinking about big picture problems. I specifically want to thank Amanda and the other original Science in Action founders for creating a space at CSU for those of us interested in science policy. I want to thank Peter Backlund for being a science policy role model and always supporting the work of Science in Action. In addition, I want to thank Sam and Christina for being great mentors, collaborators, and integral parts of my job search.

Next, I want to thank friends that have kept me grounded during this journey. Just to name a few- the chemists always willing to have a brunch or movie night; the pre-pandemic Quantum Mechanics softball team for pep talks and providing an excellent mid-week outlet for my never-ending stress; Nathan for being a true friend since middle school, and always being up for a virtual chat or boardgame session; Rae for always being down for an adventure and welcoming us in BV; Cal for being an excellent roommate, enthusiastic editor, and just all-round lovely human; Lindsay for being a stellar friend, an excellent collaborator on advocacy projects, and always being willing to cook a delicious meal together.

Lastly, I want to thank my family. My parents for being supportive in all ways, whether by just talking on the phone, driving to Colorado for Christmas when I couldn't fly home, or sending endless amounts of coffee to feed my caffeine addiction. My delightful sister, Lucy, for fun adventures, always

introducing me to new catchphrases, constantly listening to my rants, and giving excellent pep talks. And finally Jewels for being my true other half for the last 9.5 years. Our time together and endless adventures have meant the world to me, and I am certain that we can make 3961 miles feel like nothing.

TABLE OF CONTENTS

LIST OF FIGURES

CHAPTER 1
Introduction

This initial chapter will briefly motivate the need for energy storage devices in the transition to clean energy. The following discussion will have an emphasis on batteries, including lithium-ion batteries, as a specific energy storage method. Next, spectroscopy and ultrafast spectroscopy will be introduced as a potential tool to research electrochemical devices such as batteries. Finally, the chapter will end with a short outline of the following chapters of this dissertation.

1.1 Reaching Decarbonization Goals

With the ever-impending need for climate change mitigation, implementing policy and technology to help reduce greenhouse gas emissions and decarbonize our economy are essential. Proposed paths to lowering economy-wide emissions include focusing on the power sector and substituting decarbonized electricity for fossil fuels as much as possible in transportation, industry, and buildings.[4] To meet this goal the ability to both generate and store clean energy is key.

1.2 What is Energy Storage and Why is it Important for Decarbonization?

Energy storage is the ability to capture energy at one time and then use it later. Different types of technologies save energy in different forms including chemical, kinetic, or thermal and then convert that energy into electricity when it is needed.[5] Similarly to how refrigerators let us store food for days or weeks, the ability to store energy and use it when most needed enables an electricity grid to operate flexibly. Effective energy storage plays an increasingly critical role as we transition to accommodating higher levels of renewable energy. Intermittent energy sources like wind and solar only generate power when the sun is shining, or the wind is blowing, making energy storage important to be able to supply communities with constant energy streams.[6,7]

Energy storage already plays a central role in the operation of our electricity system to store electricity during low demand and release it into the grid during high demand, typically over a daily cycle. The initial application of pumped hydroelectricity storage occurred in the late 19th century in Europe, and as of 2020, pumped hydro storage still accounts for approximately 99% of the total grid-scale electricity

storage capacity in the United States.[4] This storage technology works by pumping water back behind hydroelectric dams or to secondary storage sites and then generating electricity later when water is released to drive a turbine. One downside to pumped hydropower is geographical limitations, namely a difference in elevation, which is not available in all locations. Conversely, electrochemical storage, like batteries, is more suitable for maintaining an uninterrupted power supply.[8] These factors explain why lithium-ion batteries, like those used in personal devices like cell phones and laptops, are one of the fastest growing energy storage technologies. Lithium-ion batteries in the form of large battery banks are becoming more commonplace in homes, communities, and at the utility-scale.

1.2.1 Batteries: A Form of Energy Storage

Batteries store energy through an electrochemical process. This means that electricity is converted to chemical energy and then back to electrical energy when needed. Primary batteries, like alkaline ones, cannot be recharged because the chemical reactions that generate the power are not reversible. On the other hand, secondary batteries like lead-acid batteries and lithium ion batteries are rechargeable because the chemical reactions they use are reversible.[9] When a battery is discharged, the reaction proceeds in one direction and releases energy. Conversely, when the battery is charging, the reaction switches direction and the device absorbs energy. Batteries typically share common components including a positive electrode (called the cathode, connected to the batteries positive (+) terminal), a negative electrode (called the anode, connected to the negative (-) terminal) and an electrolyte solution that helps ions move between the electrodes. When a lithium-ion battery is charged, ions flow from the cathode to the anode. When the battery is discharged, the ions reverse course (Figure 1-1).[10]

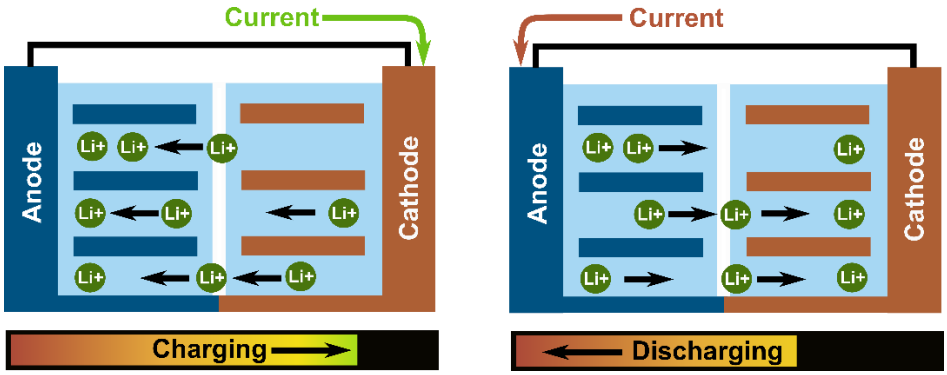

Figure 1-1 (Left) a cartoon of a charging lithium-ion battery with lithium ions flowing from the cathode to the anode. (Right) A cartoon discharging battery with lithium ions flowing from the anode to the cathode.

1.2.2 Battery Research and Development

As billions of people bear witness to rapid technological developments in the battery world - faster charging, electric vehicles with increased range, and longer battery lifetimes - it is important to understand the work behind the improvements. Ultimately, it is a story of tweaks: small improvements in manufacturing, slight alterations of materials, and some gains in performance. The breadth of research on energy storage technologies is incredibly expansive. Researchers are continually tackling questions of material safety, stability, efficiency, ethical sourcing, and cost.[8,9] The work in this dissertation focuses primarily on the electrolytes that can be used in lithium-ion batteries or other electrochemical applications.

1.2.2.1 Research on Electrolytes

Lithium-ion batteries eventually stop charging and die, and one reason for this is the breakdown of the molecules in the electrolyte. This breakdown forms a layer of degraded electrolyte components on the anode. This layer is called the solid electrolyte interphase (or interface) (SEI). This layer can act like a brick wall, forming an impenetrable barrier and stopping the flow of ions between the electrodes, causing the battery to die. One way to engineer this inevitable process in our favor is to make the layer more like a gated fence that only lithium has the key to. Therefore, lithium can move back and forth, giving the battery a longer life. The structure of this layer can be manipulated by changing the composition of the electrolyte solution, consequently altering the battery's lifetime.[10–12]

Many of the advances made in liquid electrolyte mixtures have been iterative and discovered using trial and error. For example, it has been found that certain chemicals added to the electrolyte mixture in small amounts can dramatically improve battery lifetimes.[3,13,14] Understanding why these specific chemical additives have such an impact is an ongoing field of research, and if we are to significantly improve current performance of lithium-ion batteries, as well as rapidly deploy new battery chemistries, we must implement effective tools to help understand fundamental nature of the electrolytes that are currently being used. This will enable the development of design rules that can guide future development of novel electrolytes.

1.3 Spectroscopy as a Tool to Study Batteries

1.3.1 Introduction to Spectroscopy

Spectroscopy is a tool frequently used to study chemical systems, including energy storage devices like lithium-ion batteries.[15–19] Spectroscopy is the study of how electromagnetic radiation – such as visible light, infrared light, or x-rays - interact with matter.[20] When a beam of electromagnetic radiation hits some form of matter, the light might be absorbed, reflected, or refracted. For example, we can consider seeing as a form of spectroscopy – we view the world by the interaction that visible light has with the receptors in our eyes. Light is emitted from some source like the sun or a lightbulb and then reflected by, absorbed by, or transmitted through everything around us. How much and what spectral regions are absorbed depends on the types of molecules in these objects. The light that is not absorbed reaches our eyes carrying information of the molecular structure of our surroundings with it. In our eyes color is then analyzed by photoreceptors. We essentially perform a spectroscopic experiment any time we look at something. Now, our eyes can only gather limited amounts of information about our surroundings because we only see visible wavelengths, but different instruments can detect different parts of the electromagnetic spectrum. Depending on the wavelength of light used, the light-matter interactions will provide different information about a system. For example, infrared light can be used to study the way that molecules vibrate (Figure 1-2).

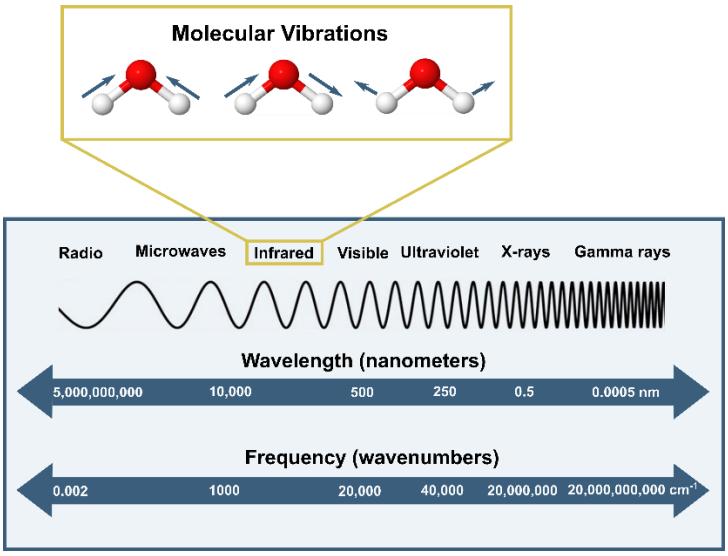

Figure 1-2 A cartoon scale representing the relative wavelengths and frequencies for different types of electromagnetic radiation. Boxed in yellow are three water molecules with arrows representing the direction of motion for a specific vibration. (Left water) Symmetric stretch. (Middle water) Asymmetric stretch. (Right) Bend.

Tracking how a molecule vibrates can tell us information about the chemical environment around the molecule.[21] A common type of spectroscopy that uses infrared light to track vibrations is called Fourier Transform Infrared Spectroscopy or FTIR. An apparatus for spectroscopic studies is called a spectrometer and a graph of a particular property of matter against wavelength or frequency is called a spectrum. An example of a spectrum of some water vibrations is shown in Figure 1-3. In this figure there are two different spectra, the dark purple is a spectrum of a sample with a small amount of water, and we see two peaks. These peaks correspond to two of the types of vibrations a water molecule can undergo, a symmetric stretch where the two oxygens move in the same direction at the same time, and an asymmetric stretch, when the two oxygens stretch in opposite directions. The lighter purple spectrum is from a sample with more water. Here we see a new peak at lower frequency corresponding to water interacting with other water molecules. Thus, these spectra helped identify the presence of water in each the sample, and new peaks told us something about how the water is interacting with its surroundings, and the peak heights tells us about the amount of water present. This ability to track peak locations, shifts, and intensities make infrared spectroscopy a powerful technique for studying chemical systems.

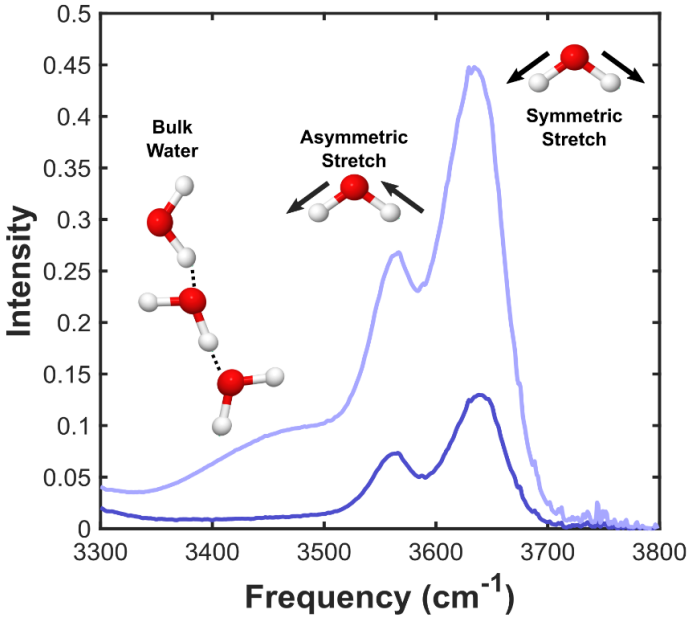

Figure 1-3 Linear FTIR. Dark purple curve is an ionic liquid mixture with 2.5 mole percent water. Light purple curve is an ionic liquid mixture with 17.8 mole percent water. Water molecules represent the different vibrational modes present.

Many researchers have implemented different types of spectroscopies to better understand battery electrolytes and the SEI in one way or another. Studies have been conducted to better understand the morphology of the SEI using a tools like electron microscopies[3,22] its chemical composition using tools like FTIR and x-ray spectroscopies[15] and the behavior of the SEI over time using all these methods while a battery operates.[1,23] However, despite the entire kitchen sink being thrown at fully understanding this issue, there remain a number of unanswered questions. Another, newer spectroscopic tool that can be used to study electrolytes and the SEI is ultrafast spectroscopy. What makes ultrafast methods a unique category of spectroscopy is the speed at which we can gather information, it essentially allowing researchers to make chemical movies. Collecting chemical movies will provide a better picture of the molecular motions occurring in the electrolyte and help researchers understand how each electrolyte component might be impacting how the SEI forms.

1.3.2 Ultrafast Spectroscopy: Making Chemical Movies of Batteries

Ultrafast measurements gather frames upon frames of data, much like a movie consists of frames of film. And much like how traditional filmmaking and photography have dramatically altered the way we can

interpret the world around us, so too can ultrafast spectroscopy alter how we understand chemistry. Take, for example, the invention of slow-motion photography. With it, we can capture the flap of a hummingbird's wings or the finish of a horse race, motions too fast for the human eye. (Figure 1-4).

Figure 1-4 Finish of a horse race captured with slow-motion photography.

In chemistry, we need an analogue to track fast chemical changes. In film, to capture rapid motions, we need cameras with shutter speeds fast enough to avoid the blurring of images that is caused by movement of the subject. When that subject changes from a horse to a molecule vibrating, we need something fast enough to capture 10,000,000,000,000 frames per second - femtoseconds. Ultrafast spectroscopic techniques can do this by using incredibly short pulses of light from powerful lasers (Figure 1-5).

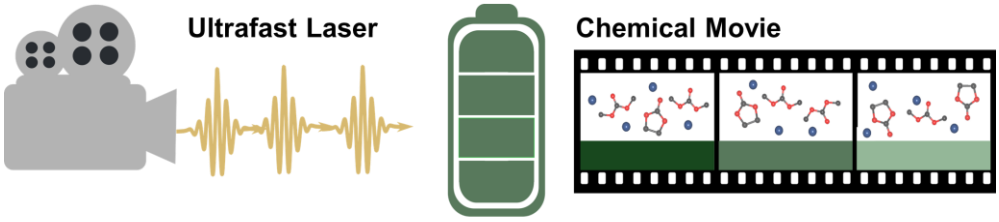

Figure 1-5 Cartoon of an ultrafast laser making a chemical movie of a battery.

Combining the images from these short pulses allows us to assemble "chemical movies," which can provide more information about how different materials in these electrochemical devices are impacting their surrounding environment and consequently how their dynamic behavior might impact overall device efficacy.[17,24] The work in this dissertation uses ultrafast spectroscopy including techniques called 2D infrared spectroscopy and 2D infrared microscopy to investigate different electrolyte mixtures.

1.4 Dissertation Outline

The work presented in the following chapters focuses on two specific types of electrolytes that can be used in electrochemical devices including those used for energy storage: organic carbonates and room temperature ionic liquids. A type of ultrafast spectroscopy, two-dimensional infrared spectroscopy (2D IR), is the main tool used to investigate the impact that different types of chemical additives have on the behavior of these electrolytes.

Chapter 2 includes a more in-depth introduction to the specific chemical systems, and details on sample preparation. In addition, the chapter further details the theory of linear and 2D infrared spectroscopy and provides examples of data analysis techniques to gain molecular level structure and dynamics from 2D IR. Chapter 3 is a manuscript in progress, addressing the role that a chemical additive, fluoroethylene carbonate, has on the structure and dynamics of organic carbonate electrolytes commonly used in lithium or sodium ion batteries. Chapter 4 is also a manuscript in progress, addressing the role that water as a contaminant or additive plays in ionic liquid mixtures which have been used as electrolytes in applications for solar energy generation[25,26] and battery electrolytes.[27,28] Chapter 5 is a published book chapter[29] outlining the state of 2D IR imaging and practical considerations when setting up a 2D IR microscopy experiment. Chapter 6 outlines some future directions for the ionic liquid systems discussed in both Chapter 4 and 5. Finally, Chapter 7 is a conclusion and summary of preceding work.

CHAPTER 2

Background Information

The goal of this work is to investigate the role chemical additives play in determining the structure and dynamics of electrolyte mixtures. The two types of electrolytes investigated in this work are (1) organic carbonate mixtures frequently used in devices like lithium or sodium ion batteries and (2) room-temperature ionic liquids often used in solar cells, batteries, and chemical extractions. This chapter introduces the spectroscopic techniques and methods used to study these electrolyte solutions. First a brief introduction to the organic carbonate and ionic liquid electrolyte sample systems is given. More details on these systems will be in Chapters 3 and 4 respectively. Next will be a short introduction to linear infrared spectroscopy followed by a very brief introduction to nonlinear optics, after which there will be a discussion of 2D infrared spectroscopy (2D IR) and the types of data that can be extracted from a spectrum or series of spectra. Last there will be a walk-through of our 100 kHz 2D IR spectrometer. Additional information on the practical elements of 2D IR and 2D IR microscopy will be included in Chapter 5.

2.1 Electrolytes

Electrolytes are a key area of research in the development of effective batteries or of other electrochemical applications including energy generation technologies such as dye-sensitized solar cells. Some properties that are important for an ideal battery electrolyte include those listed in Table 2-1.

Table 2-1 Some physical properties of electrolyte solutions relevant to batteries

Property	**Ideal for a Battery Electrolyte**
Electrochemical window	Stable over a wide range of voltages to allow cell reactions without electrolyte decomposition
Ionic Conductivity	High ionic conductivity (A few mS/cm is minimally required)
Viscosity	Low viscosity tends to track with higher ion mobility
Thermal stability	Liquid over a wide range of temperatures. Higher flash points are safer
Cost	Low monetary and environmental cost are preferred.
Compatibility	Noncorrosive and nonreactive components help ensure cell longevity.

2.1.1 Ion-Batteries and the Solid Electrolyte Interphase

Lithium-ion batteries (LIBs) and sodium-ion batteries (SIBs) play an important role in storing chemical energy for conversion to electrical energy. LIBs are currently used in an array of applications, including many portable devices, electric vehicles, satellites, and power grids.[30-31,32] Therefore, there is significant interest in furthering the development of SIBs and LIBs. Successful batteries must have high capacity, low cost, small size, safe functioning, and the ability to produce power over time. One factor impacting these battery characteristics is the degradation of the electrolyte to create the solid electrolyte interphase (or interface) (SEI). The SEI forms during the cycling of a full battery on the anode surface and can impact the capacity, lifetime, and safety of a battery. Thus, understanding the formation, composition, and structure of the SEI is crucial to improving battery technology.

The SEI forms when the reduction potential of the electrolyte solution in LIBs and SIBs is higher than the sodiation or lithiation potential at the working electrode. This can be seen by looking at the relative voltages of possible reduction events in a battery. As a note, for the present study all work is done on a half-cell battery set-up, so diagrams will be based on a half-cell battery. Figure 2-1 depicts a relative scale of reduction events occurring in a half-cell battery. In Figure 2-1, V_{OC} represents the open circuit potential of the cell before any current is passed. When the discharge process begins, the voltage is decreased towards the relative zero which is based on the reduction of sodium metal. The electrolyte reduction, and consequent SEI formation, begins at a higher potential than the sodiation event at the cathode material, in this example, antimony. If the electrolyte reduction occurred at a potential lower than sodiation, the SEI would not form.[30,33] Often electrolyte solutions with a wider electrochemical window, such that SEI formation does not occur, are either unsafe or expensive. Thus, most research is focused on improving the SEIs that do form.

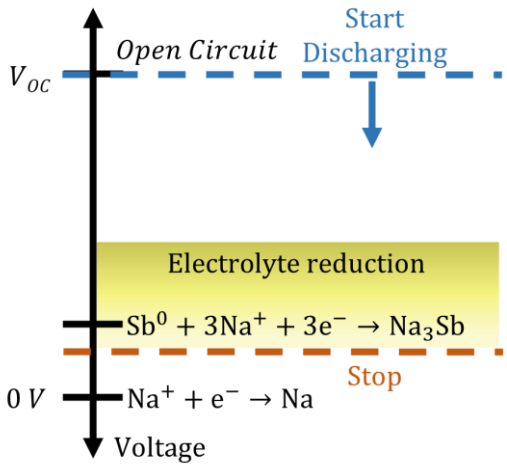

Figure 2-1 Relative scale of reduction events in a sodium half-cell battery during discharge, starting at the open circuit potential.

The chemical reactions occurring during the formation of the electrolyte are dependent on an array of variables including the temperature, electrode material, electrode surface condition, electrolyte components and concentrations, the reductive potential applied, and the reduction activation energy for a reaction.[31] The remaining work in this dissertation will focus on the electrolyte components.

2.1.2 Organic Electrolytes

Organic electrolytes are the most well-known form of electrolytes. A typical organic electrolyte involves a metal salt and some weakly coordinating anion dissolved in an organic mixture. Organic carbonates like ethylene carbonate, dimethyl carbonate and others are often the base electrolytes used in LIBs. The impact of the electrolyte components on the SEI formation is shown in Figure 2-2. Two additives, fluoroethylene carbonate (FEC) and vinylene carbonate (VC), were added to a base electrolyte to improve the lifetime of the battery by changing the way the SEI formed. In Figure 2-3 the base electrolyte has a capacity that decreases to zero by the 100th cycle, unlike the VC-doped or FEC-doped solutions.[34] These results together suggest that the electrolyte components have a large impact on the SEI formation, and consequently the battery lifetime. Therefore, investigating the nature of each component and the behavior of the electrolyte solution under an applied potential is important for further understanding the role of the SEI. Though there are many possible reactions electrolyte solutions can undergo during reduction, reactions are often categorized as one of three types. These potential reactions include one-electron reduction, two-electron

reduction, or secondary reactions with some impurity or a product of one of the other reaction categories[31]. Since the components and the rate of SEI formation can have drastic impacts on battery lifetime and capacity, researching the components and the formation of the SEI is crucial to furthering SIB and LIB technology. Chapter 3 will discuss how fluoroethylene additives impact the structure and dynamics of organic carbonate mixtures.

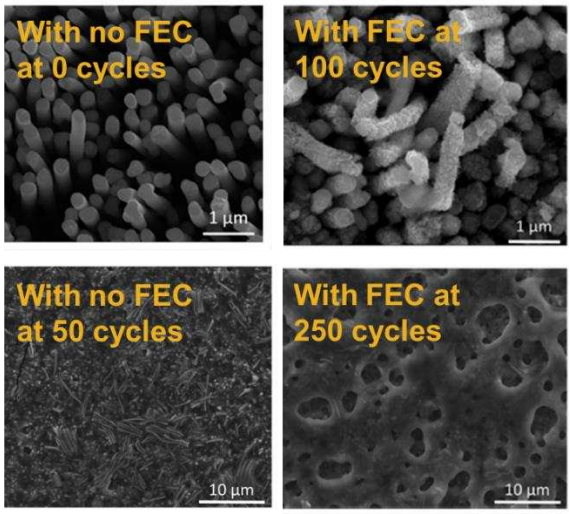

Figure 2-2 Transmission electron microscopy images show what an electrode looks like after different numbers of charge cycles before and after the addition of FEC. Modified from reference 3.

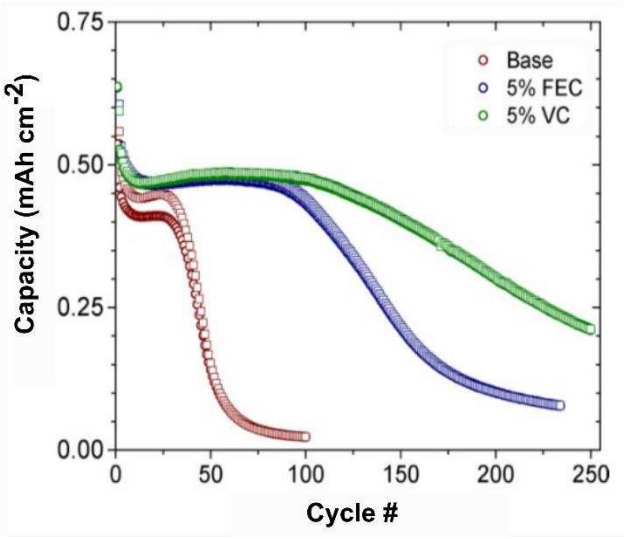

Figure 2-3 Battery capacity over battery cycle for SEIs formed from three distinct electrolyte solutions. Red circles are the base electrolyte of ethylene and diethylene carbonate. Green circles are a base electrolyte with 5 wt % of vinylene carbonate. The blue circles represent the base electrolyte with 5 wt % fluoroethylene carbonate. Modified from reference 3.

2.1.3 Room Temperature Ionic Liquids

Ionic liquids (ILs) are another category of electrolyte – though less commonly used in current battery technologies than organic electrolytes.[35] Ionic liquids are fluids composed entirely of ionic species, and unlike molten salts, like NaCl that melt at ~ 800°C, ILs often are liquid at or near room temperature (RTILs). This class of liquids is appealing for a wide array of applications including catalysis[36,37], renewable energy generation[25,26,38,39] and storage[27,28,40,41], fuels[42,43], and biomass dissolution.[44] In terms of their applications in electrochemical devices as an electrolyte, RTILS have some pros and cons. Their frequently large electrochemical window, high thermal stability, and low flammability of ILs are all positive attributes for electrolytes (Table 1). However, due to the high viscosity and relatively low lithium mobility displayed by most of the IL-based electrolytes,[35,45,46] the performance of IL-based LIBs are still not fully comparable with that of devices containing conventional electrolytes. Additionally, the cost of ILs is relatively high with respect to the conventional electrolytes. Different routes for improving ILs as an electrolyte include rational design of new ionic pairs[47,48] and the use of ILs in mixtures with other electrolytes including organic solvents.[46,49] Chapter 4 will discuss how water as an additive in IL mixtures changes the structure and dynamics of the solution. The following sections will discuss introduce spectroscopy as a tool to study complex chemical systems like organic carbonate mixtures and ionic liquids.

2.2 Introduction to Linear Infrared Spectroscopy

Molecular vibrations provide a powerful tool for probing the chemical structure and dynamics of complex condensed phase systems, including electrolyte mixtures. Vibrational modes of a molecule are determined by the way the atoms move in relation to each other and are consequently sensitive to chemical structure and solvent environment. In a room-temperature condensed phase system the chemical environment is dynamic; with molecules moving, vibrating, and rotating. Consequently, the net electric field of the environment is also constantly in flux, and consequently a vibrational oscillator's interaction with a surrounding solvent environment is constantly changing. This can be thought about using a Morse potential to describe a chemical bond. In a solvent the energy surface will be compressed or stretched as the solvent is pushing and pulling on the chemical bond of interest (Figure 2-4).[50] This will lead to changes in the

vibrational energy levels. Thus, when looking at an entire sample, there will be a distribution of vibrational frequencies for each mode based on the system heterogeneity.

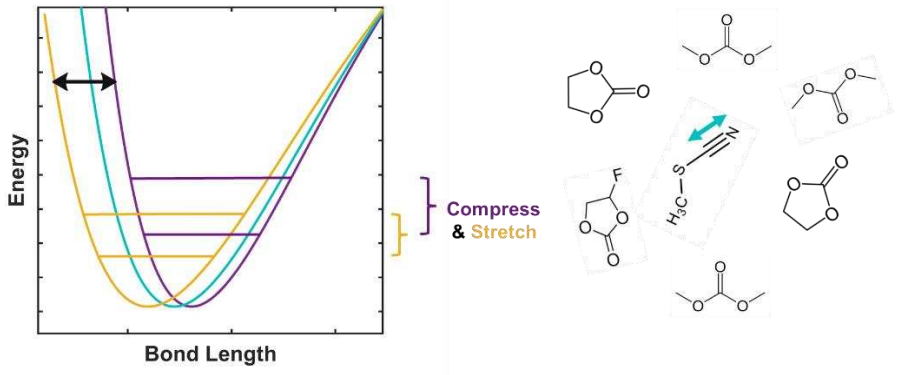

Figure 2-4 (Left) Representative morse potentials for three hypothetical oscillators shown in gold, teal, and purple. The horizontal lines indicate vibrational energy levels on the gold and purple potential wells for comparison of the impact compression and stretching have on the relative energies. (Right) Example solvent environment for a cyanate oscillator, teal arrow.

One approach to measuring these vibrational modes is infrared spectroscopy because the frequencies at which molecules vibrate correlate with infrared radiation. In a linear infrared absorption experiment when a resonant infrared light source is incident on a molecule, the light wave drives a vibrational excitation. The vibration changes the molecule's dipole moment, which then generates a new wave of the same frequency. The wave destructively interferes with the original incident wave, resulting in depletion of the incident light source. This leads to the "absorption" spectrum of the molecule. Analysis of an absorption spectrum can provide valuable information about the chemical sample. Linear Fourier Transform spectroscopy (FTIR) for example can measure the frequency, peak width, and intensity of the absorption of IR light by a particular bond (Figure 2-5). Peak frequency is dictated by the type of bond and solvent interactions. The linewidth reports on the distribution of solvent environments in the chemical system (rainbow peaks in Figure 2-5).[50] This distribution is called inhomogenous broadening.

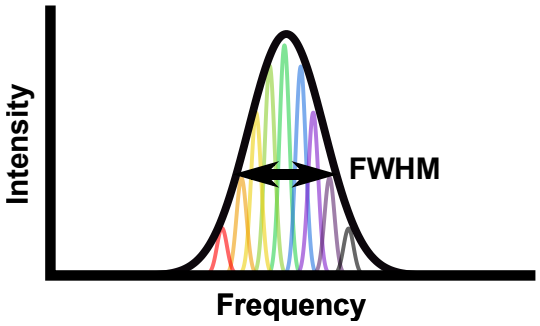

Figure 2-5 Cartoon linear FTIR spectrum. Black gaussian representing the total peak, with rainbow gaussians representing inhomogenous broadening. FWHM stands for full width half maximum.

An example linear FTIR spectrum is shown in Figure 2-6. This region of the spectrum shows three peaks unique to carbon nitrogen (CN) stretches of a dicyanamide anion in an ionic liquid mixture.

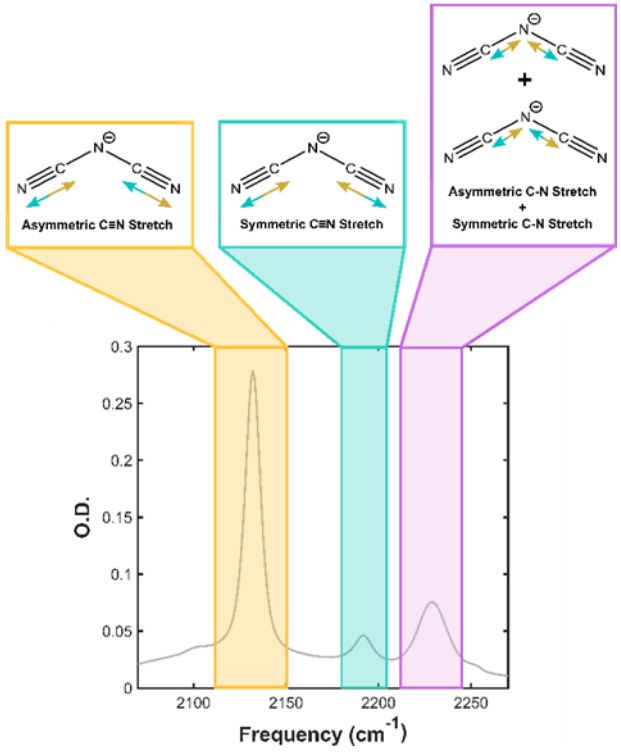

Figure 2-6 Linear FTIR spectrum of three DCA vibrational modes. Highlighted in yellow at 2132 cm^{-1} is the asymmetric C≡N stretch. Highlighted in blue at 2192 cm^{-1} is the symmetric C≡N stretch. Highlighted in purple at 2225 cm^{-1} is a combination mode corresponding to a C-N symmetric and asymmetric stretches.

The peak centered at 2134 cm^{-1} corresponds to the asymmetric C≡N stretch and the peak 2190 cm^{-1} at is the symmetric C≡N stretch. The peak at 2225 cm^{-1} corresponds to a combination band between the C-N symmetric and asymmetric stretches. This peak is in Fermi resonance with the asymmetric C≡N stretch[51]

and is consequently higher in frequency and intensity than expected for a combination band. Figure 2-7 illustrates an energy level diagram showing the split caused by the Fermi resonance between the asymmetric C≡N stretch and the combination mode. Fermi resonance most often occurs between a fundamental mode and then an overtone or combination mode of lower frequency modes.[50]

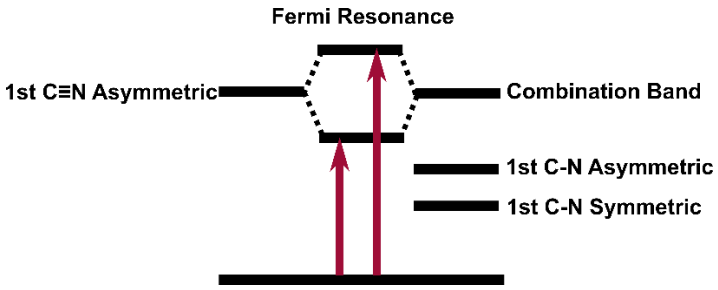

Figure 2-7 Cartoon representing the relative energy level diagrams for the Fermi Resonance in DCA.

Changes in peak location and shape between samples with the same oscillator can provide information about solvent interactions. For example, when water is introduced to the ionic liquid mixture, we see each DCA peak shift and broaden (Figure 2-8). This is likely due to the introduction of more possible hydrogen bonding interactions of the DCA anion with water molecules.[52–54] Further discussion of mode assignments and peak shifting in these systems will discussed in Chapter 4.

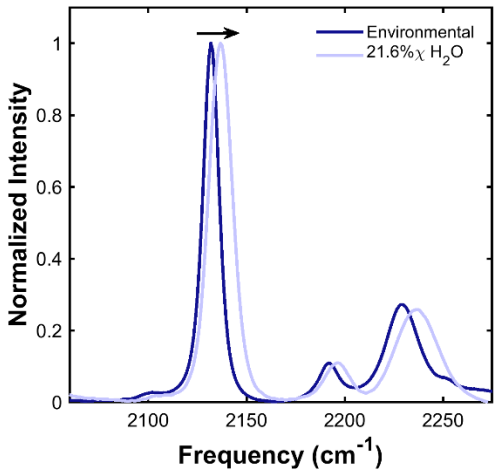

Figure 2-8 Self-normalized linear FTIR spectra for an BmimDCA in BmimBF4 with an environmental concentration of water (1.32 mole percent)(dark) and 21.6 mole percent water (light).

2.3 Nonlinear Spectroscopy

Consider a sample of some dielectric medium with some n dipoles each one with an inherent dipole moment $\overrightarrow{\mu_i}$. Then the resulting macroscopic polarization of the material is the average sum of the dipole moments (Equation 2-1).

$$\vec{P} = \langle \sum_{i=1}^{n} \vec{\mu}_i \rangle \qquad 2\text{-}1$$

In an isotropic dielectric material and in the absence of some external radiation this sum would be zero. However, when a fluctuating electric field hits the sample it induces a displacement of the electron density of the molecule, changing the molecular dipole (Equation 2-2).

$$\vec{m}_i = \vec{\mu}_i + \vec{\mu}_{induced} \qquad 2\text{-}2$$

Thus, the resultant macroscopic polarization is no longer zero and has directionality based on the incident field (Equation 2-3). This directionality will be important for a discussion on anisotropy in Section 2.6.2.

$$\vec{P} = \langle \sum_{i=1}^{n} \vec{m}_i \rangle \qquad 2\text{-}3$$

The change in dipole is related to the molecular polarizability α_i. Polarizability essentially expresses the ability of atoms and molecules of a dielectric material to be polarized. The molecular polarizability is closely related to the structure and bonding properties of the molecule.

The bulk polarization can also be described with the following equation where the polarization induced in a material is related to the input electric field through the susceptibility. Macroscopic susceptibilities, representing a collection of dipoles, are related to corresponding molecular susceptibilities. In Equation 2-4, $\vec{P}$ represents the real macroscopic, polarization, $\vec{\mathrm{E}}(\mathrm{t})$ the real, time dependent electric field, and $\chi^{(\mathrm{n})}$ the n$^{\mathrm{th}}$ order susceptibility.[20]

$$\vec{P} = \epsilon_0 \chi^{(1)} \vec{E}(t) + \epsilon_0 \chi^{(2)} \overrightarrow{E^2}(t) + \epsilon_0 \chi^{(3)} \overrightarrow{E^3}(t) + \ldots \epsilon_0 \chi^{(n)} \overrightarrow{E^n}(t) \qquad 2\text{-}4$$

Equation 2-5 defines the electric field, dependent on wavevector direction, *k*, frequency, ω, phase, φ, time, *t*, and direction, *z*.

$$\vec{E} = \frac{1}{2}E_0 e^{i(kz-wt+\varphi)} + \frac{1}{2}E_0 e^{-i(kz-wt+\varphi)} \qquad 2\text{-}5$$

Linear spectroscopy, such as linear FTIR or UV-Vis, encompasses scenarios in which a single weak electric field interacts with a system. In these cases, the macroscopic polarization (Equation 2-4) behaves linearly and only the first term is important. In a quantum view, this scenario can be thought of as one photon in and one photon out. Nonlinear spectroscopy refers to situations that do not conform to this picture, including the case where the system is exposed to multiple fields or the situation where the system response behaves outside what can be described as linear, for example when a sample is hit with very intense light. This results in needing more terms in the macroscopic polarization to describe the behavior of the system.

2.3.1 2D IR: A Third-Order Nonlinear Process

2D IR will be described more thoroughly in the following sections, but here it is used as an example of a third order nonlinear spectroscopic technique. In the case of 2D IR the macroscopic polarizability is a function of three input electric fields (Equation 2-6). The typical pulse sequence used for 2D experiments is shown in Figure 2-9a. In Equation 2-6, E_1, E_2, and E_3 are the electric fields of the three incident laser pulses. $R^{(3)}$ is the third order response function of the chemical system, and t_1, t_2, and t_3 are time intervals during which each pulse interacts with the system.

$$P^{(3)} \propto \int_0^\infty dt_3 \int_0^\infty dt_2 \int_0^\infty dt_1 \, E_3(t-t_3)E_2(t-t_3-t_2)\cdot E_1(t-t_3-t_2-t_1)\cdot R^{(3)}(t_3,t_2,t_1) \qquad 2\text{-}6$$

The complete derivation of both first and third-order response functions can be found elsewhere and will not be included in this dissertation.[50] Ultimately, the third-order response function can be thought of as a quantum correlation function involving a time dependent dipole operator, $\vec{\mu}(t)$, and a density matrix, $\rho(t)$, to describe the system. In brief, a density matrix is used to track the quantum states of an ensemble of objects, like a wavefunction which describes the evolution of a single quantum mechanical object. Equation 2-7 shows a third order response function.

$$R^{(3)}(t_3,t_2,t_1) = \left(\frac{2\pi i}{h}\right)^3 \langle\Big[\big[[\mu(t_1+t_2+t_3),\mu(t_1+t_2)],\mu(t_1)\big],\mu(0)\Big]\rho(\infty)\rangle \qquad 2\text{-}7$$

The density matrix describes a collection of anharmonic, quantum oscillators and the dipole operators which move the system between population and coherence states. This movement can be represented using Feynman diagrams which provide a way to visualize the time-ordered processes in a 2D IR experiment resulting in the total response function in Equation 2-7. The following section will further describe how to read a Feynman diagram and show Feynman pathways that contribute peaks in a conventional 2D spectrum of a system with two coupled vibrational modes. Moreover, during each time interval the system can undergo different processes.[50] Section 2.6 will explain about the different dynamic processes that can be tracked using 2D IR.

2.4 Introduction to 2D Infrared Spectroscopy

As stated above, 2D IR is a nonlinear optical technique dependent on the interaction of three electric fields in time and space to generate a fourth signal field. Figure 2-9 shows the possible interactions of the pulse sequence with a single anharmonic vibrational mode, and the resulting 2D spectrum. The first pump pulse generates a coherence state (or linear superposition between the ground state and the first excited state) (red dashed arrows). The second pump pulse (solid red arrows) generates a population state, either in the ground or first excited state. The third pulse (grey dashed arrows), the probe, generates another coherence state between the ground and first or first and second excited state. The emitted field (solid yellow and blue arrows) is then detected. The blue circle represents signals from ground state bleach (GSB), $v = |0\rangle \rightarrow |1\rangle$ and stimulated emission (SE), $v = |1\rangle \rightarrow |0\rangle$. The yellow circle represents excited state absorption (ESA) signal from $v = |1\rangle \rightarrow |2\rangle$. Like linear FTIR spectroscopy, 2D IR spectra give information about the frequency, lifetime, and intensity of vibrational modes present in a sample. However, because 2D IR is an ultrafast time-resolved spectroscopy that acts as a frequency-frequency correlation plot, additional information about a sample's chemical structure and dynamics can be gleaned.

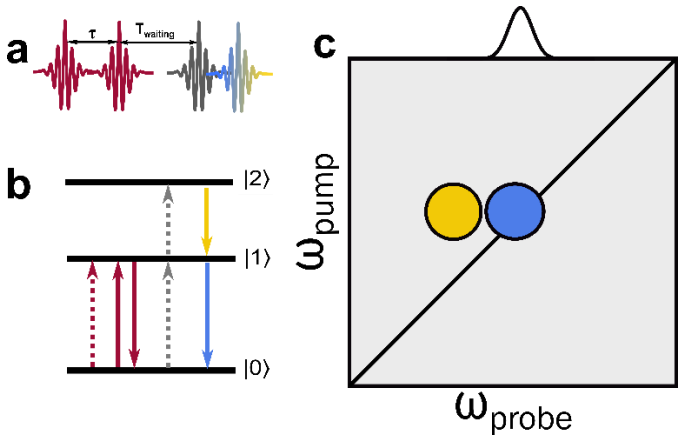

Figure 2-9 (a) Typical 2D IR pulse sequence. Red being the two pump pulses. Grey being the probe pulse and the blue/gold pulse being the signal. (b) Representative energy level diagram for an anharmonic oscillator and the possible interactions with each pulse of light. (c) Cartoon of the resulting 2D IR spectrum from the interactions in (b) with the blue circle representing the contributions from the ground state bleach and the stimulated emission and the gold circle representing the excited state absorption. The black gaussian is representative of the linear spectrum for a corresponding oscillator.

Specifically, valuable information about vibrational anharmonicity, spectral diffusion, vibrational coupling, energy transfer, and chemical exchange can be determined. Since the first 2D IR in 1998 by Hamm and Lim,[55] measuring protein dynamics 2D IR has been used to investigate the structure and dynamics of many different systems including biological systems,[56–59] electrolytes,[24,60–64] and interfacial regions.[65,66] The following sections 2.5 through 2.6 will outline some features in 2D IR experiments that can provide a molecular level picture of a chemical sample. First, information gained from static 2D IR spectra will be discussed. Second, time-dependent 2D IR experiments will be addressed.

2.5 Conventional 2D IR Cross Peaks Coupled Oscillators

In the case of multiple vibrational modes being excited, it is important to consider the additional peaks possible in a 2D spectrum. In a system where there is vibrational coupling between excited modes, cross-peaks are often expected.[50] Figure 2-9a shows an energy level diagram representative of transitions possible in a two-state system. As an example, we consider a system with symmetric and asymmetric stretches, mode s and mode a, respectively. Figure 2-9b shows the possible peaks corresponding to the energy level diagram. Figure 2-9c shows the specific pathways that contribute to each peak using Feynman diagrams.

2.5.1.1 Aside on Feynman Diagrams

One way to visualize the interactions that lead to each peak in a 2D spectrum is to use Feynman diagrams. Each Feyman pathway is a graphic representation of the interactions that go into building the response function in Equation 2-7. Figure 2-10 shows an example diagram that we will walk through explicitly. The states shown between the vertical bars are the vibrational states occupied with time progressing vertically from bottom to top. Arrows indicate the interaction of the electric field with an arrow pointing inwards representing absorption and an arrow pointing away indicating stimulated emission. In other words, arrows indicate field interactions on the ket (left) and bra (right) and an arrow pointing in toward the system represents an increase in the eigenstate of the bra or ket, and an arrow point out represents a decrease. The form $|n\ n|$ represents a population state and $|n\ m|$ represents a coherence between vibrational state n and m.

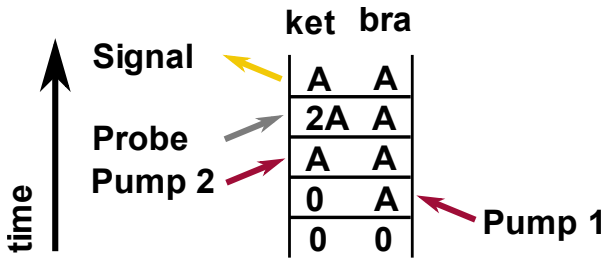

Figure 2-10 A walk through of a representative Feynman diagram for an excited state absorption peak.

(1) Pump 1, is the first interaction in time of the and generates a coherence between the ground state and first vibrational excited state for some mode A.

(2) Pump 2, is the second interaction in time and generates a population in the first excited state of mode A.

(3) Probe, generates a coherence between the first and second vibrational excited states of mode A.

(4) Signal is emitted from the second to the first vibrational excited state, resulting in a population state in the first excited state of mode A.

Next, Figure 2-11 shows Feynman pathways contributing to the conventional peaks expected in a 2D IR spectrum. As a note there are two versions of the Feynman diagram: the diagram on the left is called a rephasing path and the one on the right is non-rephasing. To explain rephasing versus non-rephasing we can use an analogy. Consider a race of runners (or a collection of oscillating dipoles with slightly different transition frequencies). They all start running at one time (pump 1) but as the race progresses some runners go faster and some slower (oscillators preces at different speeds), and they are no longer the same distance

from the starting line (oscillators dephasing). However, at some predetermined time during the race (probe) the runners are told to run backwards (rephasing pathway). As they do this, the runners eventually all end up at the start (back in phase). Conversely, if at the predetermined time (probe) they continue running in the same direction (non-rephasing pathway), they will become further away from each other and the starting line (more dephased). In the Feynman diagrams the difference between rephasing and non-rephasing is determined by the relative direction of the pump 1 arrow and the probe arrow. Feynman diagram arrows in the same direction represent a non-rephasing pathway. 2D spectra can be collected[50] or analyzed[67] to independently assess the rephasing and non-rephasing spectra. However, the 2D spectra presented in this work are all purely absorptive and thus are the result of adding both the rephasing and non-rephasing pathways contributions.

Section 2.6 will discuss additional dynamic processes that can add to the cross-peaks seen in a 2D spectrum. In addition, Chapter 4 will include how we can use polarization dependence of cross-peaks to learn about the relative angle between two dipoles.

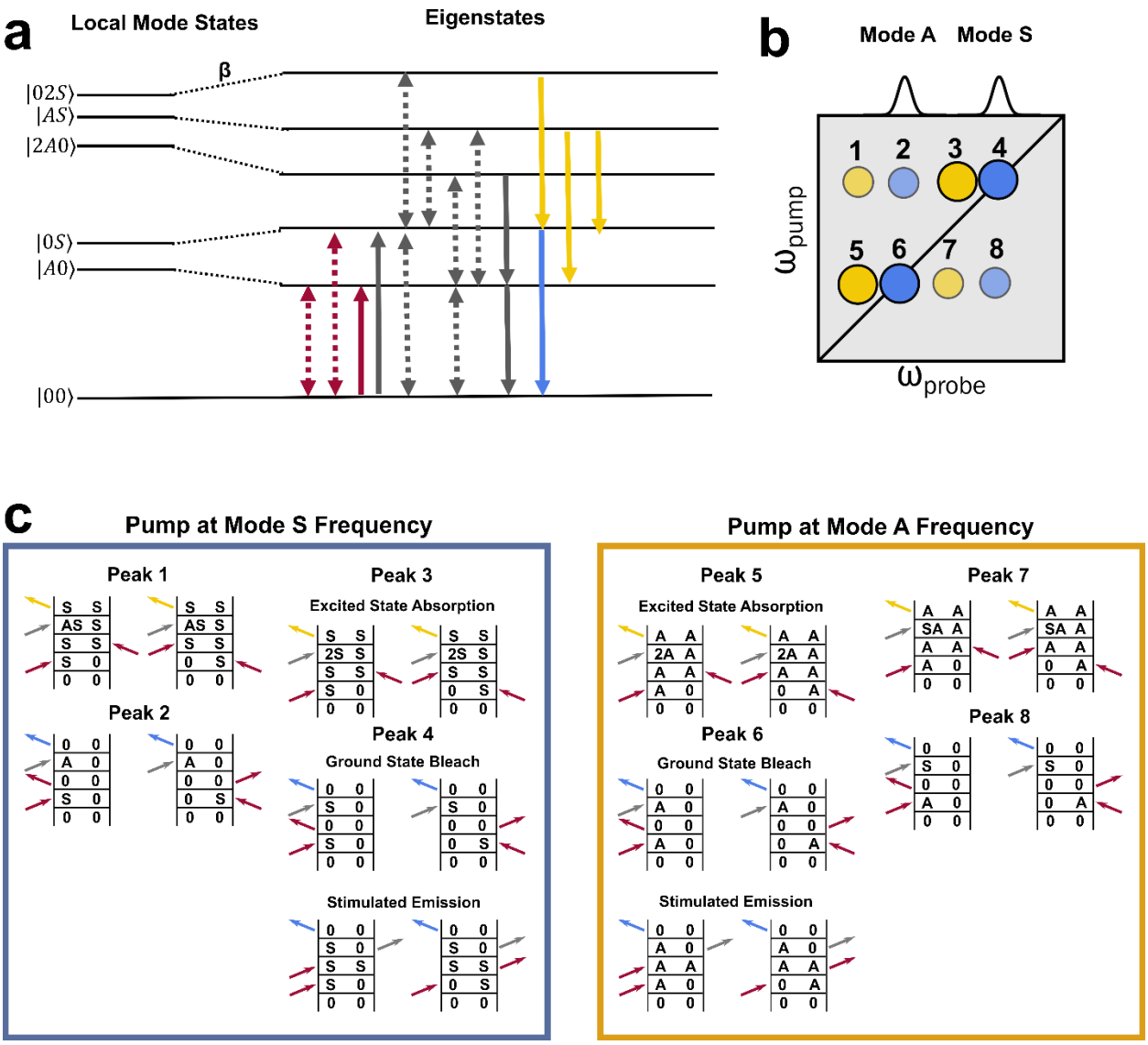

Figure 2-11 (a) Possible energy interactions with two coupled anharmonic oscillators. Red arrows indicate interactions with the pump pulses. Grey arrows indicate interactions with the probe pulse. Yellow and blue indicate the signal pathways. (b) is a 2D spectrum representative of transitions shown in (a). (c) Feynman pathways corresponding to the numbered peaks in (b).

2.6 Time-Dependent 2D IR to Extract Dynamics

By modulating the time in between the final pump and probe pulse ($T_{Waiting}$), the timescales for different dynamic processes in a sample can be extracted. This section will walk through a few types of waiting time experiments that can provide valuable information about a system and how to analyze a series of 2D spectra to get quantitative information. The types of processes that will be discussed include spectral diffusion, orientational relaxation, quantum beating, and population transfer.

Additional dynamic processes such as chemical exchange and coherence transfer are important to consider in analyzing 2D spectra, however they will not be discussed in depth here. Briefly, chemical exchange occurs when a probe is in multiple distinct configurations, for example bound to an ion, and then switches configuration over time. This process generates 2D IR cross peaks that grow with time. Work by Hamm and Zanni[50] can provide a more in depth introduction to chemical exchange. Chemical exchange will be briefly discussed in Chapter 5. Coherence transfer is a process where energy is transferred between modes while the system is in a coherence state. Coherence transfer is particularly important to consider when tracking population transfer because there is possible overlap in the peaks originating from each process.[68] Papers by Khalil *et al*.[69] Marroux *et al*.[68], Baiz *et al*.[70], and Eckert *et al*.[71] are valuable resources for learning more about coherence transfer.

2.6.1 Spectral Diffusion from 2D IR

Like in linear FTIR when a vibrational oscillator is pumped in a 2D IR experiment it is in a particular environment and absorbs at a particular frequency resulting in an inhomogeneously broadened absorption spectrum,(Figure 2-12a. Figure 2-12b illustrates a 2D IR spectrum at $T_{Waiting}$ =0. In this spectrum the peak is elongated along the diagonal with the diagonal width representing the inhomogeneous broadening of the system. As the solvent structure and resulting interactions change, the probe samples other frequencies that correspond to different structural configurations. The time dependence of this sampling process is called spectral diffusion and can be described by the frequency-frequency correlation function (FFCF). The time and frequency resolution of 2D IR allows the FFCF to be approximated. Being able to estimate this function is valuable because the FFCF essentially represents a weighted average of all the possible motions of the solvent environment contributing to spectral diffusion. This can include molecular motions like librations, hydrogen-bond making and breaking, ion-cage rearrangement, or solvent exchange.[56,59,64,72]

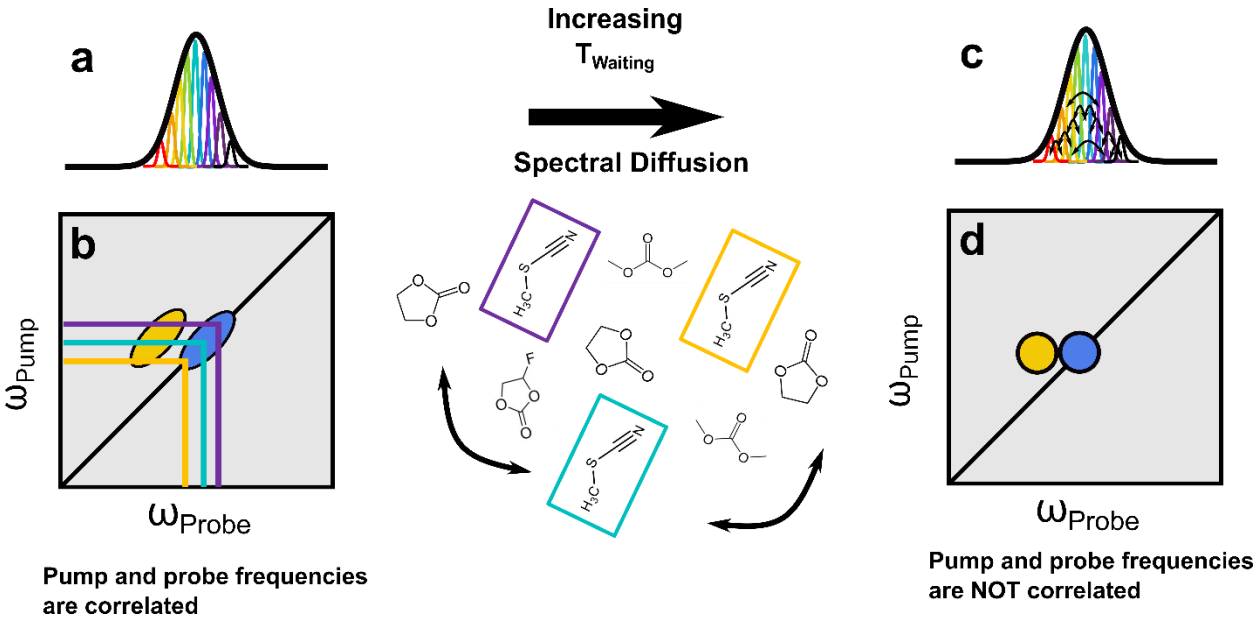

Figure 2-12 (a) Cartoon linear IR peak at $T_{Waiting}$ = 0 (b) cartoon 2D IR spectrum at $T_{Waiting}$ = 0 (c) 2D IR spectrum at an increased $T_{Waiting}$ d) Linear IR peak at an increased $T_{Waiting}$ e) $T_{Waiting}$ approaching infinity, the inverse center line slope is approaching zero

At $T_{Waiting}$ =0 diagonal elongation of a 2D IR peak indicates that each molecule in a certain environment is pumped and probed at the same frequency (Figure 2-12b). This correlation between the pump and probe frequencies occurs because the solvent has not had time to rearrange around the probe molecule. However, as $T_{Waiting}$ increases, the molecules can rearrange and sample other environments. In a linear spectrum this process is imperceptible (Figure 2-12c), however in 2D IR the loss of correlation can be tracked as the peaks become spherical (Figure 2-12d). There are multiple techniques to quantify this change in peak shapes, including center line slope analysis (CLS), nodal line slope analysis (NLS) or tracking peak ellipticity.[50,73,74] In this work inverse CLS has been used. In practice to extract the inverse CLS it is necessary to pull out the center of the on-diagonal transition of interest at each pump frequency. There are a few approaches to doing this which are outlined in Table 2-2. For the work included here Method 1 has been used.

Table 2-2 Methods for CLS extraction and their corresponding benefits and downsides.

	CLS Extraction Method	Benefits	Downsides
Method 1	Take a series of 5-8 (depends on peak width) pump cuts of the 0-1 transition across the peak and find the minima.	Very easy to implement. Not dependent on the fit quality.	Impacted by frequency dependent behavior (i.e. multiple modes overlapped)
Method 2	Take a series of 5-8 (depends on peak width) pump cuts of the 0-1 transition across the peak and fit the cut to two gaussians and then extract the amplitude of the negative going gaussian.	Relatively easy to implement.	More time consuming. Relies on having good and consistent fits.
Method 3	Fit your peaks to 2D-Gaussians. If you have two modes subtract one peak from the raw data then perform CLS using either method above or perform CLS on the gaussian fits. [62,75]	Can help deconvolute multiple modes. Good for example if you have an ion-associated peak, say like with lithium and a carbonate.	Time consuming. Very challenging to implement if there is substantial peak overlap.

An example of CLS extraction at a single $T_{Waiting}$ is shown in Figure 2-13. Here each dot represents the minimum found on the corresponding pump cut, and the dashed line represents the fit to the minima. The inverse of this slope of this fit is the resulting CLS at that time point. This process is repeated at each $T_{Waiting}$ step to gather a CLS decay versus time and consequently approximate the FFCF (Figure 2-14).

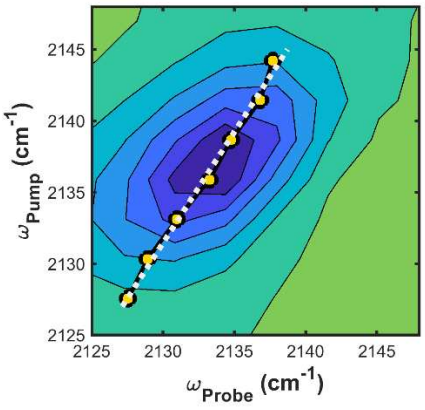

Figure 2-13 Example 2D IR spectrum taken at $T_{Waiting}$ equal to 0.6 ps with the corresponding CLS overlaid. The yellow dots outlined in black represent the found minimum at each pump cut. The white line represents the linear fit to the minima. The slope of the white line is the CLS at that point in time.

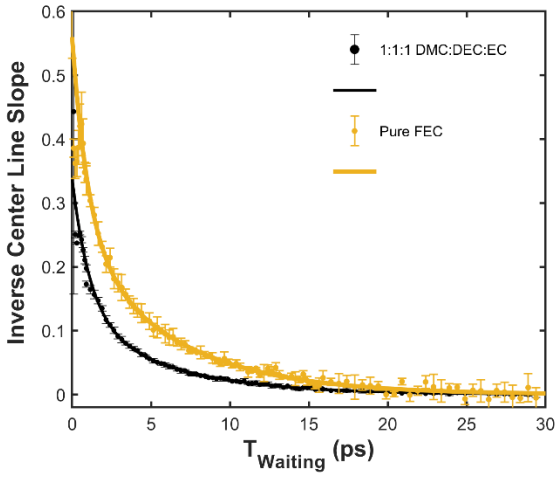

Figure 2-14 Two example inverse CLS decays for two organic carbonate mixtures. The gold curve corresponds to a solution of fluoroethylene carbonate and the black curve to a 1:1:1 by mass mixture of dimethyl carbonate (DMC), diethyl carbonate (DEC), and ethylene carbonate (EC)

CLS decays are fit with some number of exponential decays. Equation 2-8 is an example of using a bi-exponential fitting equation to approximate the FFCF. In Equation 2, δω(0) represents the frequency fluctuations at $T_{Waiting}$=0. The other terms $\Delta\omega_1$, $\Delta\omega_2$ are amplitudes and τ_1, and τ_2 time constants.[50]

$$\langle \delta\omega(T_{waiting})\delta\omega(0)\rangle \approx \Delta\omega_1^2 e^{\frac{T_{waiting}}{\tau_1}} + \Delta\omega_2^2 e^{\frac{T_{waiting}}{\tau_2}} \qquad 2\text{-}8$$

Figure 2-14 shows two examples of CLS decays for two different organic carbonate solutions. The gold curve corresponds to a solution of fluoroethylene carbonate that decays more slowly than the mixture of dimethyl carbonate, diethyl carbonate, and ethylene carbonate. Chapter 3 will further describe the molecular reasoning for this change in CLS by using molecular dynamics simulations to aid in interpretation. In addition, Chapter 4 will include further discussions on CLS as applied to ionic liquid – water mixtures.

Another way to visualize this data is to look at the found minima on the probe axis of each pump cut over time. Figure 2-15 shows an example of the tracked minima of the on-diagonal peak for seven pump cuts over time.

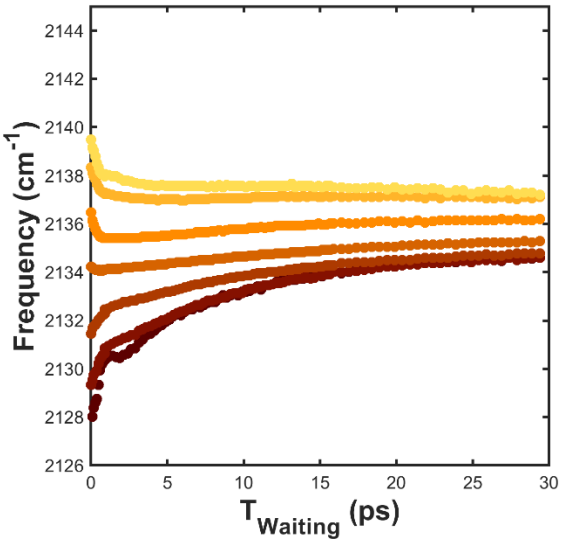

Figure 2-15 Example of a plot showing the probe frequency at the minima found at each pump cut plotted versus $T_{Waiting}$.

2.6.2 Anisotropy Measurements

As the time, $T_{Waiting}$, between the second pump pulse and the probe pulse is increased, the unit vector of a vibrational transition dipole will have time to reorient as the molecule rotates and undergoes conformational changes. These orientational dynamics can be measured with polarization dependent 2D IR measurements. Section 2.7.2 will describe how the polarization of the pump and probe pulses are controlled optically. The two polarization schemes used to track orientational dynamics are parallel and perpendicular. Parallel, also referred to as co-polarized or XXXX, means that both pump pulses, the probe pulse and the signal, are all the same polarization. Perpendicular, also referred to as cross-polarized or XXYY means that the pump pulses and the probe pulse, are perpendicular polarizations. In each polarization the 2D signal intensity is extracted from the on-diagonal 2D IR peak for a given vibrational mode. This can be done by tracking the peak minima for each pump cut or by integrating a box over the FWHM of the peak along the pump and probe axis. These two methods should give the same result (+/- some noise) except in the scenario where you have frequency dependent behavior as a result of distinct populations. An example of frequency dependent behavior is discussed in Chapter 4.[76]

Equation 2-9 is then used to calculate the anisotropy from polarization dependent intensities as a function of waiting time. The anisotropy is a dimensionless quantity that is independent of the total intensity

of the sample. This is because the difference (I ‖ – I⊥) is normalized by the total intensity, which is equal to I‖ + 2I⊥ .[77]

$$r(T_W) = \frac{I_{\parallel}(T_W) - I_{\perp}(T_W)}{I_{\parallel}(T_W) + 2I_{\perp}(T_W)} \qquad 2\text{-}9$$

Figure 2-16 shows three scenarios to explain the relative signal intensities that we see for different polarization configurations at different waiting times. In each black box there are different oscillators, each with a dipole in a unique direction.

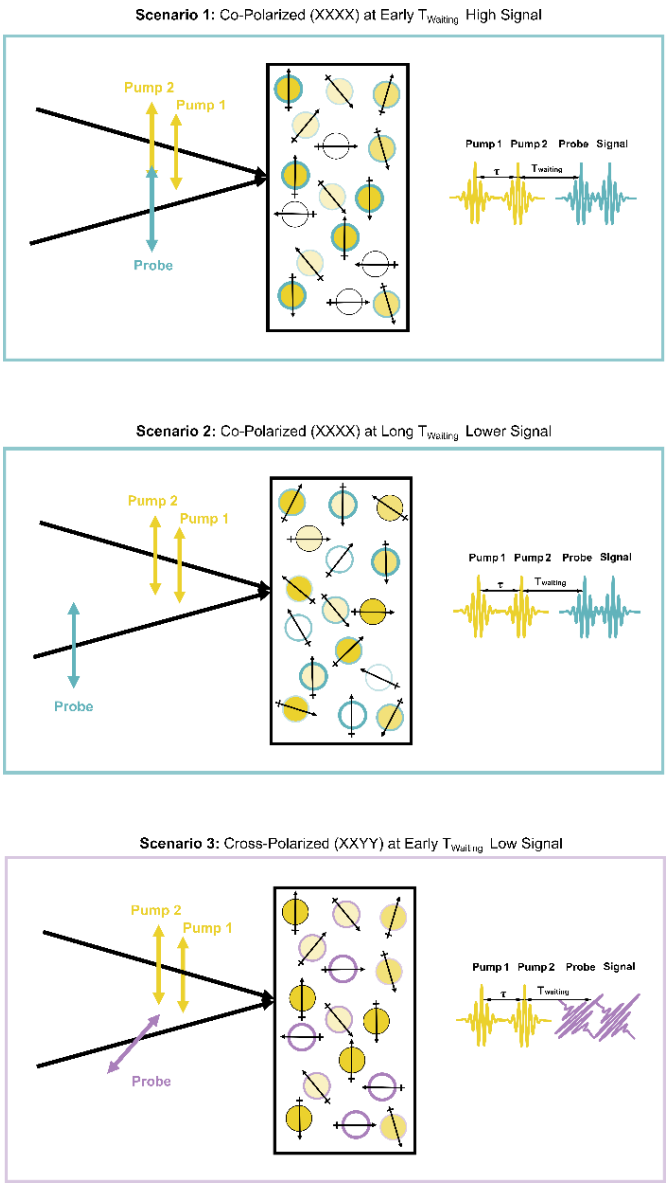

Figure 2-16 Cartoons representing three scenarios during polarization dependent 2D IR experiments.

In scenario 1 the oscillators highlighted in the darkest gold represent those with the strongest response to the pump pulses because their polarizations are aligned. Specifically, the probability of the absorption is proportional to the cosine square of the angle between the exciting light and the transition dipole (Equation 2-10 and Figure 2-17).[77,78] The reasoning for this relationship can be seen by looking at a single oscillator with a transition dipole some angle θ from z (Figure 2-17). In this case the probability for a molecule with the transition dipole $\vec{\mu}$ to absorb a photon with the electric vector $\hat{\varepsilon}$ polarized along z is $|\vec{\mu} \cdot \hat{\varepsilon}|^2 = \vec{\mu}_z^2$, which can be expanded in Equations 2-10 and 2-11 to give an initial distribution W in Equation 2-12.

$$\vec{\mu}_z^2 = \frac{\|\vec{\mu}\|(\cos\theta)^2}{volume\ of\ a\ sphere} \qquad 2\text{-}10$$

$$\vec{\mu}_z^2 = \frac{\|\vec{\mu}\|(\cos\theta)^2}{\frac{4}{3}\pi r^3} \qquad 2\text{-}11$$

$$W(\theta_0, \phi_0) = \left({}^{3}/_{4\pi}\right)(\cos\theta)^2 \qquad 2\text{-}12$$

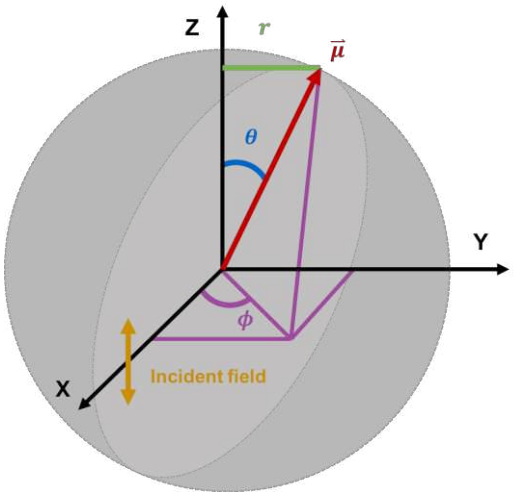

Figure 2-17 Experimental geometry, with the sample is placed at the origin; μ is a transition dipole. The incident light travels along x, polarized parallel to z.

In the cartoon representations in Figure 2-16 each oscillator with progressively lighter yellow shading represents those oscillators that are less in line with the pump pulses and consequently less likely to be excited. Similarly, the color and weight of the oscillator outline represents how in line they are with the incoming probe pulse. In scenario 1 we see the darkest yellow and darkest teal oscillators are the same, this is because the probe and pump are parallel and there was no time in between the final pump and the probe for the oscillators to rotate. Conversely, in scenario 2 we see that with increased time between the final

pump pulse and the probe pulse the oscillators have been given enough time that they have changed orientation. Thus, the oscillators probed are different than those that were pumped, resulting in a lower signal intensity than scenario 1. Therefore, as a function of time we expect the co-polarized signal intensity to decay (Figure 2-18). Scenario 3 represents a situation where the probe is perpendicular to the pump at early $T_{Waiting}$. Here we see that the number of excited oscillators that the probe will see is small. With increasing time between the pump and probe it is possible that the cross-polarized signal will increase as excited oscillators rotate to become more in line with the probe (seen in Figure 2-18a). Taking these scenarios together it is then expected that the most anisotropic signal (biggest difference between co and cross-polarized signals) will be at early times and then decay with increasing waiting time. An example of this anisotropy decay can be seen in Figure 2-18b. To understand more fully why the anisotropy for these experiments is anticipated to be between 0 and 0.4 one must derive the time dependent probability evolution function $W(\theta,\varphi,t)$. This can be done using spherical harmonics and a useful derivation is found in work on fluorescence anisotropy by Tao *et al.*[78]

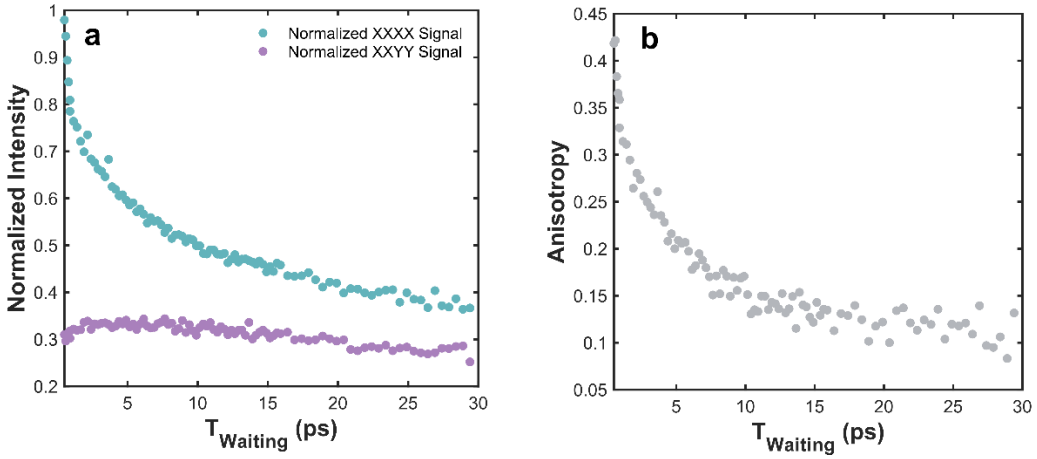

Figure 2-18 (a) Example signal decays for two polarization conditions. In teal dots the co-polarized signal and in purple the cross-polarized signal. (b) Resulting anisotropy decay from the signal intensities shown in (a) using Equation 2-9.

Once collected and extracted, experimental anisotropy data can often be modelled to get a better molecular level interpretation of the results. For example, if the data is best fit with a biexponential decay a chemical explanation for the short and long decays is needed. Many models have been developed to explain restricted rotational diffusion.[79] One commonly used route of interpretation is via the wobble-in-a-cone model.[80–83]

This model breaks the orientational correlation function into a slow and fast component. Assuming the two motions in the biexponential are independent, the total correlation function is given by the product of the fast and slow components (Equation 2-13).

$$C_{Total}(T_W) = C_{slow}(T_W) * C_{fast}(T_W) \qquad 2\text{-}13$$

Within this model, the short time decay can be described as the local reorientation of the probe within a restricted cone (Equation 2-14) and the long-time decay by the global reorientation of the probe (Equation 2-14). Figure 2-19 shows a visual representation of this model.

$$C_{fast}(T_W) = (1 - S^2)e^{-T_W/\tau_{Cone}} + S^2 \qquad 2\text{-}14$$

In Equation 2-14 S^2 represents an order parameter with values in a range of 0 to 1 with $|S|$ equal to 0 representing an isotropic motion and $|S|$ equal to 1 representing a completely restricted motion.

$$C_{slow}(T_W) = e^{-T_W/\tau_{slow}} \qquad 2\text{-}15$$

Multiplication of Equations 2-14 and 2-15 results in the total correlation function, Equation 2-16 with τ_{fast} related to τ_{slow} and τ_{cone} by Equation 2-17.

$$C_{Total}(T_W) = (1 - S^2)e^{-T_W/\tau_{fast}} + S^2\left(e^{-T_W/\tau_{slow}}\right) \qquad 2\text{-}16$$

$$\frac{1}{\tau_{fast}} = \frac{1}{\tau_{slow}} + \frac{1}{\tau_{cone}} \qquad 2\text{-}17$$

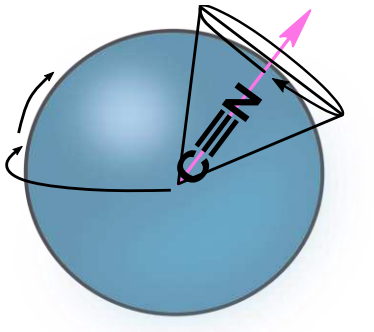

Figure 2-19 Cartoon representation of the cone restricted wobble-in-a-cone motion and the global reorientation motion for a cyanate stretch

$$\theta = cos^{-1}\left\{\left(1/2\right)\left[\sqrt{1 + 8|S|} - 1\right]\right\} \quad 2\text{-}18$$

From order parameter S the angle of restriction can be calculated (Equation 2-18). This angle is the cone semi-angle. In addition, the wobbling-in-a-cone diffusion constant D_c can be calculated using S, τ_{cone}, and the cone semi angle (Equation 2-19).

$$D_c = \frac{x_c^2(1+x_c)^2\left\{ln\left[{}^{(1+x_c)}/_2\right]+{}^{(1-x_c)}/_2\right\}}{\tau_c(1-S^2)[2(x_c-1)]} + \frac{(1-x_c)(6+8x_c-x_c^2-12x_c^3-7x_c^4)}{24\tau_c(1-S^2)} \qquad 2\text{-}19$$

The long-time component contributing to the orientational relaxation can then be attributed to the global reorientation of the probe. The inverse global diffusion time D_g^{-1} can be calculated with Equation 2-20.

$$D_g = \frac{1}{6\tau_{slow}} \qquad 2\text{-}20$$

In Chapter 3 this model is applied to anisotropy decays from different mixture of organic carbonates to explain differences in rotational behavior seen upon the addition of the chemical additive fluoroethylene carbonate.

2.6.3 Quantum Beating

Quantum beats (QB) (or interstate coherences) arise from the coherent superposition of excited states. Figure 2-20 shows possible Feynman pathways that lead to QB.

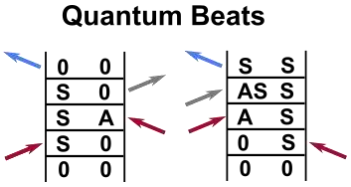

Figure 2-20 Feynman diagrams for quantum beating pathways in a system with an asymmetric (A) and symmetric (S) stretch.

QB will cause oscillations in the 2D signal.[68] There are two ways to confirm the presence of QBs. First, the oscillations can be extracted from the 2D signal in some manner and then Fourier transformed. In Figure 2-21 this is done by first fitting the signal intensity to the anticipated growth and decay functions, and then taking the residuals that are now just the oscillatory component. The residuals can then be Fourier transformed. The FT peak should show up at the difference in frequency between the two modes that are involved in the quantum beating (shown purple in Figure 2-21). In this case we are looking at the signal

intensity of a cross peak between the C≡N asymmetric and symmetric stretches of DCA. The frequency difference between these two modes is 60 cm^{-1}, which matches well with the peak in Figure 2-21.

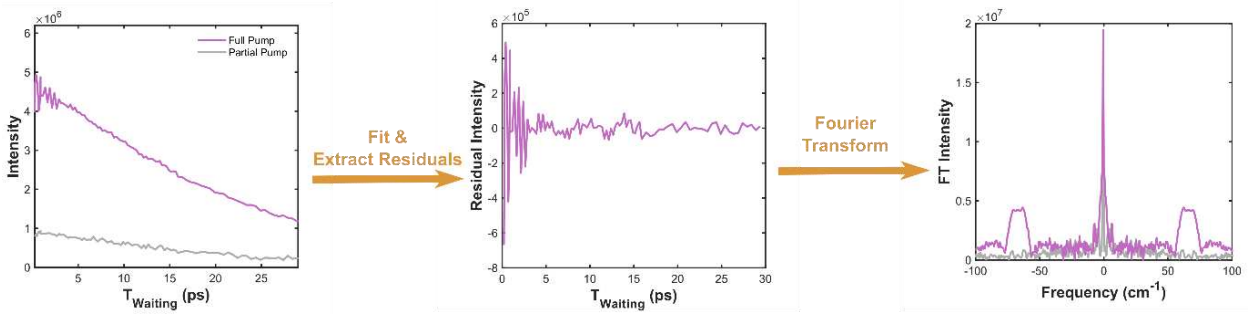

Figure 2-21 Steps for extracting quantum beating. (Left) Cross peak signal intensity between an asymmetric and symmetric stretch versus TWaiting for DCA pumping all vibrational modes of interest (purple) and pumping just the symmetric stretch (grey). (Middle) The signal intensities (left) were fit with a growth and decay. The residuals were then extracted. (Right) The residuals were then Fourier Transformed.

The second approach to confirm the presence of QBs is to do pump-selective experiments.[68] In this case for the DCA, three separate experiments were performed for each vibrational mode of interest. Figure 2-22 shows on the left a 2D spectrum taken with the full pump bandwidth, on the right a spectrum after only pumping the C≡N symmetric stretch (boxed in pink). Signal intensity decays for the pump-selective experiment are overlaid in Figure 2-21 and are missing the oscillations characteristic of quantum beating. In addition, the FT of the fit residuals to the pump-selective decay shows no peak at ~ 60 cm^{-1}. Quantum beating can be impacted by the solvent environment. This is the case for DCA and will be discussed further in Chapter 4.

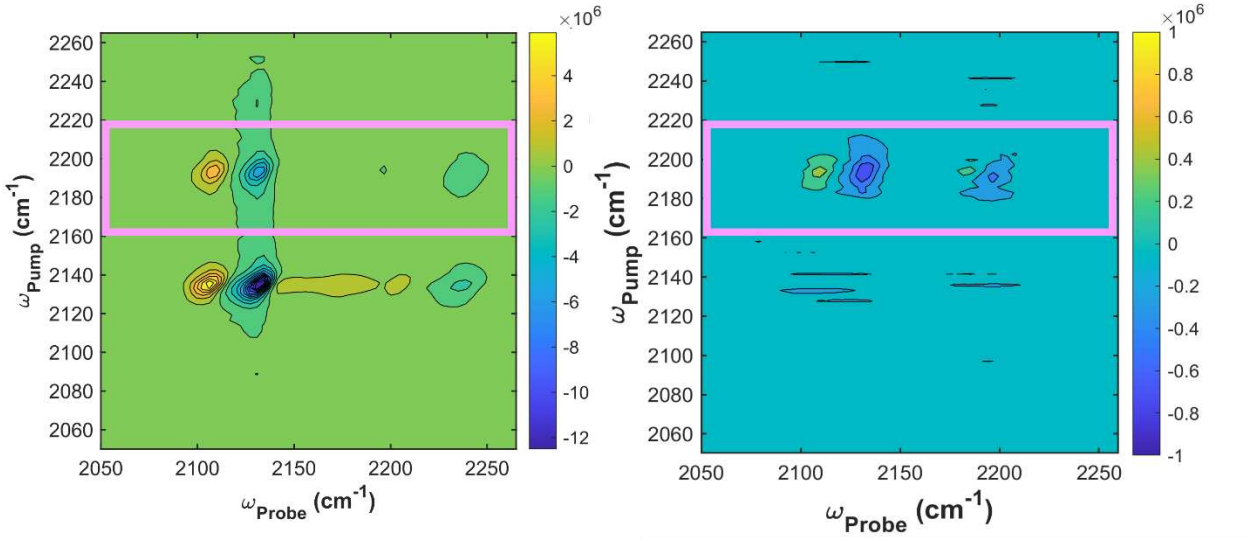

Figure 2-22 Two 2D IR spectra (left) fully pumped DCA (right) only symmetric stretch pumped DCA. Pink boxes are highlighting the symmetric stretch region.

2.6.4 Population Transfer

In addition to the conventionally anticipated cross peaks discussed in Section 2.5, it is possible during pulse interactions for energy transfer between states to occur. One mechanism of energy transfer is population transfer (PT) between states. Significant population transfer leads to the formation of new peaks, in addition to new contributions to existing peaks. These additions to a 2D spectrum are represented with a cartoon and corresponding Feynman pathways in Figure 2-23. Here the same 2D spectrum as in Figure 2-11 is shown with labels PT indicating where contributions to the signal from population transfer occur.[68]

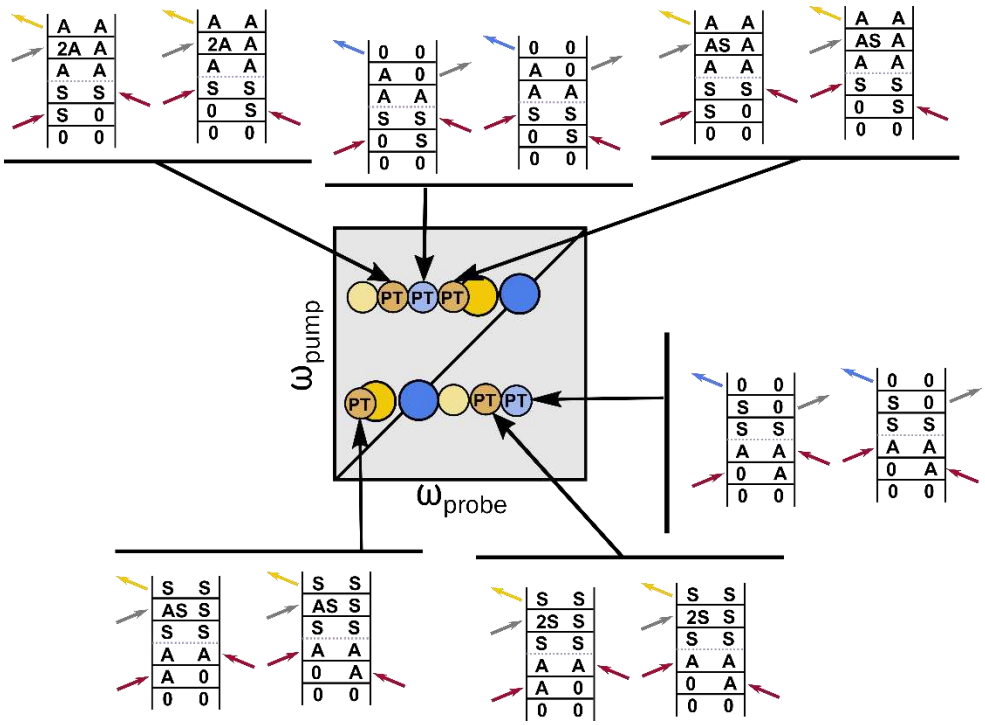

Figure 2-23 Cartoon 2D IR spectrum with the PT representing where population transfer pathways will contribute to the signal. Surrounding the spectrum are Feynman pathways for each conventional population transfer pathway.

Chapter 4 will deal with a special case of population transfer for DCA where energy transfer occurs to a dark state and additional new peaks arise.

2.7 100 kHz 2D IR Spectrometer

This section details the system used to experimentally collect 2D IR spectra. All pump-probe 2D IR measurements in this work were made using the system depicted in Figure 2-24.[84] Chapter 5 will discuss the addition of an optical path used for 2D IR microscopy on the same instrument.

Light generation originates at the ytterbium fiber oscillator, labelled as the Y-Fi Oscillator on the top-left side of the diagram in Figure 2-24. The first initial six boxes are all steps to reach the generation of the 4.65 µm, mid-IR light, shown in the orange beam path. The pump and probe pulses used in all 2D IR measurements are centered at 4.65 µm. The endpoint of the optical pathway is the mercury cadmium telluride (MCT) detector, where 2D IR spectra are collected. Next a more in-depth discussion of the nonlinear processes, optics, and techniques used to make these experiments possible is given.

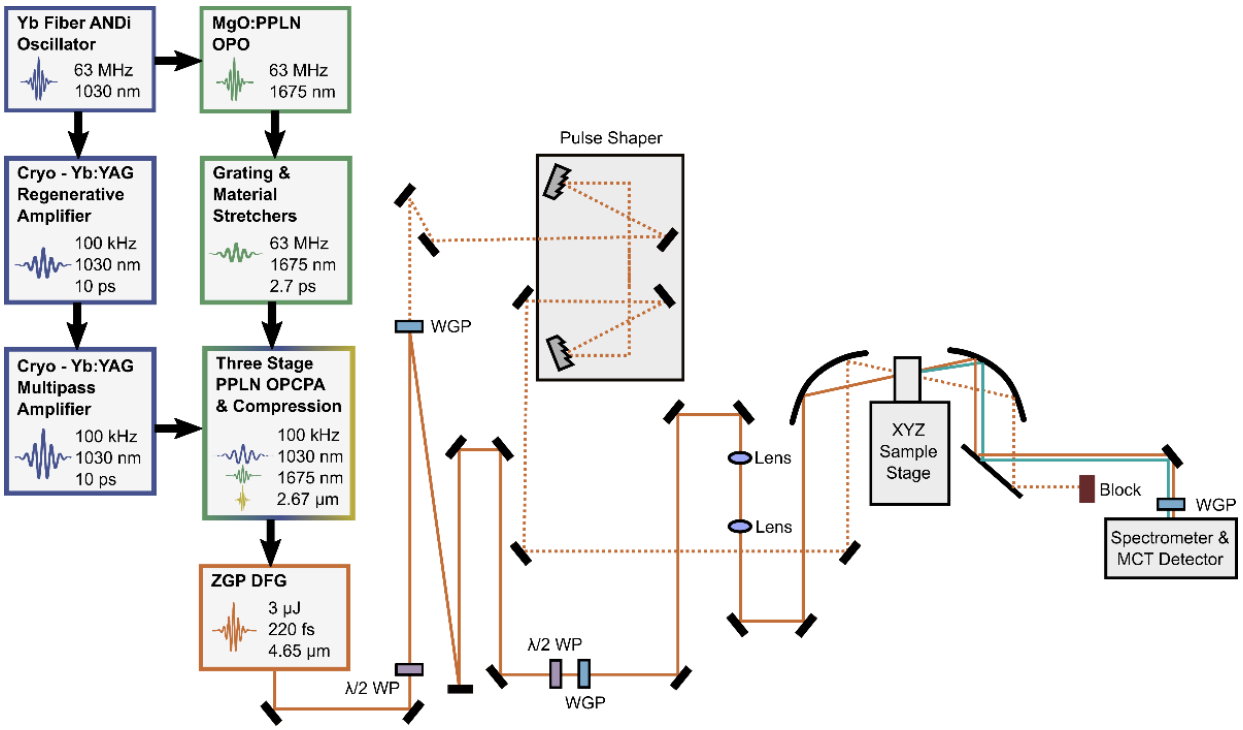

Figure 2-24 Current 100 kHz 2D IR laser system. Yb-Fiber meaning ytterbium fiber. ANDi meaning all normal dispersion. Cryo Yb:YAG meaning cryogenically cooled yttrium aluminum garnet doped gain medium. PPLN meaning periodically poled lithium niobite. OPO defined as optical parametric oscillator. OPCPA defined as optical parametrically chirped pulse amplification. ZPG meaning zinc germanium diphosphide. DFG defined as difference frequency generation. WP short for waveplate and WGP for wire grid polarizer. MCT stands for mercury cadmium telluride.

To generate ultrashort pulses in the mid IR region this laser system relies on a sequence of five second order nonlinear processes. These processes include optical parametric oscillator (OPO), three stages of optical parametric chirped pulse amplification (OPCPA), and a fourth difference frequency generation (DFG) process.

The KM lab, All Normal Dispersion Ytterbium-Fiber mode-locked oscillator (ANDi Y-Fi) generates the pump pulses for the three OPCPA stages. The Y-Fi output, 1030 nm, is sent through a cryogenically cooled Yb:YAG regenerative amplifier (regen). The Y-Fi output is stretched due to gain-narrowing in the Yb:YAG crystal to around 10 ps in the regen. The regen output is then sent through a cryogenically cooled multipass Yb:YAG amplifier.

The remaining Y-Fi output is compressed and sent to the OPO to generate 170 fs pulses centered at 1675 nm. These pulses are then stretched with a grating a material stretcher and used to seed the three

OPCPA stages. OPO and the other nonlinear processes used in this system will be briefly explained in the following section.

2.7.1 Nonlinear Processes used in the System

Second order nonlinear processes are $\chi^{(2)}$ processes (Equation 2-4). They are reliant on the mixing of three electromagnetic waves in a nonlinear medium. One possible process is second harmonic generation (SHG), where two input photons with equal wavelengths are combined to make a third photon at one half the input wavelength. Another process is difference frequency generation, where two input photons are combined such that the frequency of the output photon, called the idler, is the difference between the two input frequencies.

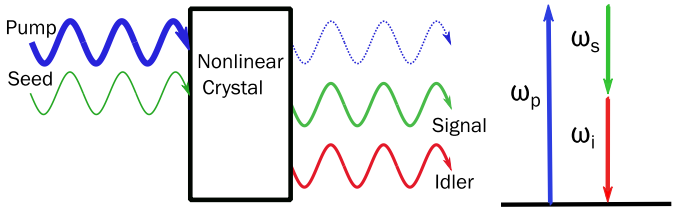

Figure 2-25 Optical parametric amplification that occurs in each PPLN crystal.

Optical parametric amplification (OPA) is essentially DFG with the caveat that the signal frequency is also amplified and therefore it deserves a whole new name. The relationship between the frequencies involved in DFG is shown in Equation 2-21 and Figure 2-25.[85]

$$\hbar\omega_{pump} = \hbar\omega_{signal} + \hbar\omega_{idler} \qquad 2\text{-}21$$

In the current laser system, there are three OPCPA stages. These stages use magnesium doped periodically poled lithium niobite (PPLN) crystals. The process of OPCPA involves the optical parametric amplification of chirped pulses. A chirped pulse means that each different frequency of light is separated in time, causing a longer pulse duration. In this case the 1675 nm pulses are chirped when passing through the grating stretcher.

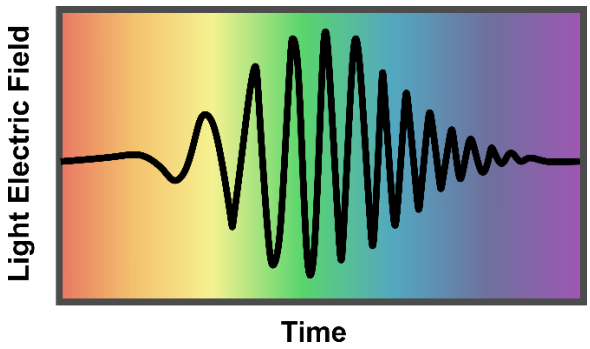

Figure 2-26 A depiction of a chirped pulse, with the blue frequencies earlier in time. Remade from reference 86.

This can be seen in Figure 2-26, where the blue frequencies of light travel first in time.[86] In each of the three PPLN crystals OPA occurs. In the case of the three OPCPA stages, the pump is the 1030 nm light, the seed is 1675 nm light, and the idler is 2.67 µm. Figure 2-25 illustrates the relationship between the frequencies of the three pulses. Three stages, instead of one, are used for maintaining the large bandwidth of the input pulses. A large frequency bandwidth results in short pulses in time which is needed for the time resolution of the 2D IR experiments. While travelling through a PPLN crystal with no phase matching, the generated light and input light will deconstructively interfere such that the output of generated photons is weak. Conversely, if a crystal is quasi-phase matched for a specific wavelength, the outer frequencies of the pulse will still deconstructively interfere with the generated light. However, this interference is to a lesser extent and only significant after a longer crystal distance. In this system, 3 mm long crystals were used to optimize the amplification of the signal frequency, and generation of the idler frequency, while minimizing bandwidth narrowing.[84,87]

After the three PPLN stages, another DFG process using the 2.67 µm idler and the 1.68 µm signal occurs in zinc germanium diphosphide (ZGP) to generate approximately 2-4 µJ of 4.65 µm mid-IR light, with a 220fs pulse length. The 4.65 µm light that is generated is used for all 2D IR measurements. The bandwidth of the 4.65 µm pulses is ~265 nm. The bandwidth dictates the vibrational frequencies that can be probed using this current 2D IR system.

2.7.2 After the generation of the Mid-IR light

2.7.2.1 Polarization Control

A half waveplate (λ/2) and wire grid polarizer (WGP) on the optical path of the 4.65 μm output are used to divide the light into separate pump and probe lines. After the polarizer the pump light is P-polarized. For reference Figure 2-27 shows the difference between S and P polarized light hitting a polarizing cube.

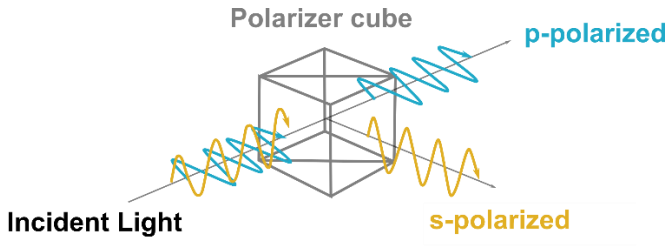

Figure 2-27 Showing the difference in s- and p-polarized light incident on a polarizing cube. S-polarized is in yellow and p-polarized is in blue.

2.7.2.2 Pulse Shaping

The pump light is then sent to a mid-IR (PhaseTech Spectroscopy) pulse shaper. The pulse shaper uses a Germanium acousto-optic modulator (AOM) to generate pump pulse pairs at 100 kHz with a varied delay and phase between the pulses.

The pulse shaper works by using a piezoelectric transducer to convert an electrical signal to an acoustic wave. The acoustic wave modulates the refractive index of the crystal. This variation in refractive index is called a mask and acts like a programmable grating (Figure 2-28). This allows control over the output waveform.[88] Figure 2-28 shows a cartoon representation of this shaping process with df representing the resolution in frequency based on the separation across the AOM, dT represents the separation between the two generated pump pulses in time. More details on pulse shaping will be given in Chapter 5.

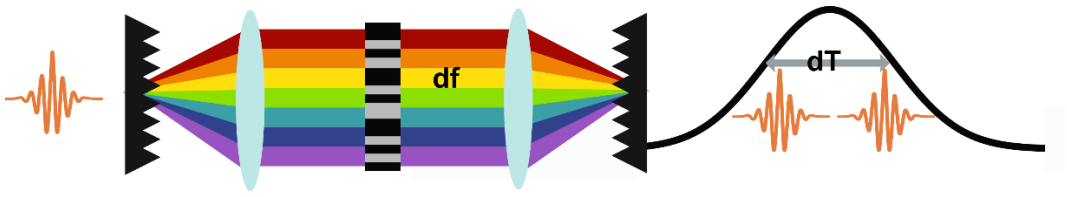

Figure 2-28 Cartoon representation of a pulse shaper. In orange, a single pulse hits a grating and is dispersed in frequency then collimated onto the AOM. The resulting shaped light is recombined and is now essentially two pulses in time.

2.7.2.3 Probe Line

The rest of the 4.65 μm light, now S-polarized after the λ/2 and WGP, is the probe line. The probe light travels through another waveplate and polarizer to allow for cross polarization schemes.

2.7.2.4 Data Collection

The probe and the pump pulse are centered on a CaF_2 sample cell off a parabolic mirror. After the sample cell, probe light is focused onto the 1 x 64 element MCT array detector. A 100 lines/ mm grating is used for experiments in this work. Entering the detector, the slit width used is 0.15 mm. Any of the remaining pump light making it to the detector is blocked with an index card. For background and scatter removal a 1900 cm^{-1} partial rotating frame and a four-frame phase cycling procedure are used. Both rotating frame and phase cycling are described next.

2.7.2.5 Phase Cycling

When collecting 2D IR, signal scatter and other undesired signals, such as transient absorption, are part of the signal. Thus, having a way to remove these additions to the signal is important for collecting a clear 2D IR spectrum, and the method used here is phase cycling. Equation 2-5 shows the phase dependence of each electric field. In both rotating frame and phase cycling, the pulse shaper is used to control the phase of the pulses.

Phase cycling is dependent on the fact that the third order 2D IR signal is a function of the difference in phase between the two pump pulses, whereas unwanted signals such as transient absorption or scatter are not. For example, with a two-frame phase cycling scheme, the signal is collected at $\Delta\varphi_{12}$ equals 0 and $\Delta\varphi_{12}$ equals π. The difference between these two signals is taken, resulting in the third order 2D IR signal doubling and the unwanted signals not dependent on $\Delta\varphi_{12}$ cancelling. Thus, the signal to noise ratio in the collected data is increased. This can be improved even further with four frame phase cycling; Table 2 includes the relative phase added to each pump pulse in a four-frame phase cycling scheme. In a 4-frame scheme the signal plotted is then Signal(A-B) + Signal(C-D), which then quadruples the signal to noise ratio (Table 2-3).[72] While 4-frame phase cycling is sufficient in a pump probe geometry, in a completely collinear geometry it is necessary to increase the phase cycles or use cross polarized pump and probe beams.

If the pump beams can be sufficiently eliminated with crossed polarizers, four phase cycles can be used. If however the pump beam reduction is not sufficient it is necessary to add a chopper and use 8-frame phase cycling in which the probe beam is chopped as shown in Table 2-4.[89] In Chapter 5 collinear geometries will be further discussed as a necessity for 2D IR microscopy.

Table 2-3 Phase added to each pump pulse in a four-frame phase cycling scheme, with A-D being the four frames.

	Φ_1	Φ_2
A	0	0
B	0	π
C	π	π
D	π	0

Table 2-4 8-frame phase cycling scheme implemented by Baiz et al.[89] A dash refers to the probe field being chopped. The 0 and π represent the phase of carrier field.

	Phase						
	Input Fields			**Detected**			
Frame	**Φ_1**	**Φ_2**	**Φ_3**	**E_1E_2**	**E_1E_3**	**E_2E_3**	**S_{2DIR}**
A	0	0	0	0	0	0	0
B	0	π	0	0	π	π	π**
C	π	0	0	π	π	0	π**
D	π	π	0	π	0	π	0
E	0	0	-	0	-	-	-
F	0	π	-	π	-	-	-
G	π	0	-	π	-	-	-
H	π	π	-	0	-	-	-
Signal I: (B+C) - (A+D) = $4S_{2DIR}$ +$4E_1E_2$ **Signal II:** (F+G) - (E+H) = $4E_1E_2$ **Signal I - Signal II = $4S_{2DIR}$** ** phase being ± π depending on the response functions							

2.7.2.6 Rotating Frame

A rotating frame works by shifting the phase between the two pump pulses while τ is changed to decrease the period of the emitted signal field (Equation 2-22). In Equation 2-22, ω_i is a constant, the frequency by which the fundamental frequency is shifted.[72] In all experiments in this work ω_i was set to 1900 cm^{-1}.

$$\Delta\varphi_{12} = -\omega_i\tau \qquad 2\text{-}22$$

The result of rotating the frame is illustrated in Figure 2-29. This allows a method of sampling the output signal less frequently without violating the Nyquist criterion. An analogy to explain rotating frame is the

observation of a carousel (Figure 2-30). If we stand next to a running carousel, it is so fast that it is blurry because our eyes cannot sample fast enough and is akin to collecting signal with no rotating frame. If we however hop on the carousel as it moves, the objects on it will become static and is akin to using a full rotating frame to remove oscillations from our signal. The third scenario is that we jog alongside the carousel and get a better picture of the objects on the carousel because our relative speed to the ride is faster than standing watching it.

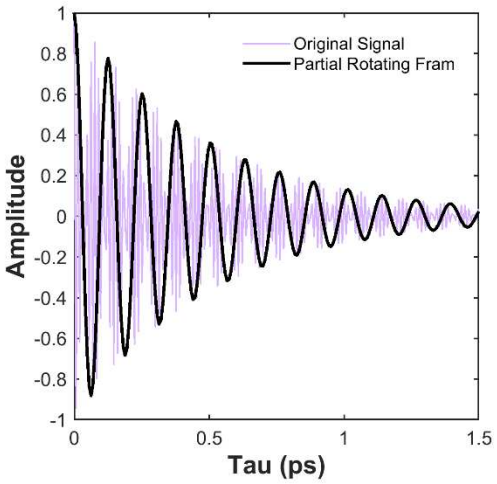

Figure 2-29 Model free induction decays. In purple the original signal. In black the same signal but with rotating frame applied.

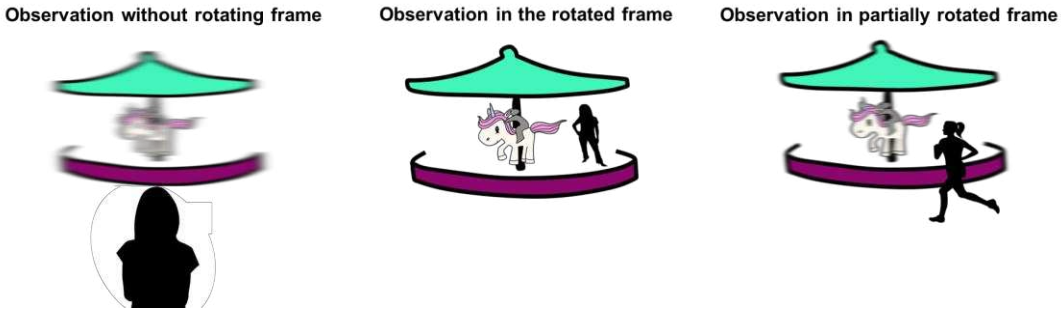

Figure 2-30 Analogy of observing a carousel to explain rotating frame.

CHAPTER 3

Fluoroethylene Carbonate Additive Drives Structuring in Organic Carbonate Electrolytes[1]

There is increasing demand to extend new energy storage technologies toward emerging applications such as grid storage for renewably generated energy. Most of these storage devices rely on materials that can reversibly store alkali ions, operate over large voltage windows, and achieve high energy densities through storing a reasonable number of ions per unit volume and mass. Lithium ion batteries (LIBs) in particular are currently the most widely used technology across a range of markets [10,90,91]. There is no one perfect battery for every application, however, so there is significant interest in furthering the diversification of LIB chemistry, as well as moving beyond lithium to developing more sustainable alternatives, such as sodium ion batteries (SIBs).

One of the significant challenges in energy storage is developing rational methods to control degradation, to extend cycle life. The electrolytes used in batteries are a significant component in the overall performance of a battery, and optimization of the mixtures of components in liquid electrolytes is a primary way to improve battery cycle life. This is because the degradation of electrolytes on electrode surfaces forms a solid electrolyte interphase (or interface) (SEI). The SEI forms from the degradation of the electrolyte on the anode surface due to reduction potentials experienced during charging. The structure and composition of the electrolyte and subsequently the SEI, as well as how it changes upon repeated cycling, is key to battery performance [10–12]. Much of the advances made in liquid electrolyte mixtures have been iterative and discovered using trial and error. If we are to make a disruptive improvement to current LIB performance, as well as rapidly deploy new battery chemistries, we must develop better tools to understand the structure and dynamics of the electrolytes that are currently used, across several time and length scales, not just at the SEI but in the bulk of the liquid electrolyte between the active electrodes.

[1] This chapter is a manuscript in progress. Molecular dynamics simulations were performed by Dr. Shelby Brantley in Dr. Steve Corcelli's Research group. X-ray photoelectron spectroscopy and battery cycling was done by Nathan Gimble in Dr. Amy Prieto's research group. Editing of the introduction was done by Dr. Amy Prieto. Guidance on analysis and interpretation was given from Amber Krummel and Steve Corcelli.

As the SEI is derived from the electrolyte, thorough characterization and understanding of the electrolyte dynamics is critical for improving important battery metrics like rate lifetime and safety. One of the most popular and commonly used electrolyte solutions for lithium and sodium ion battery electrolytes are a lithium or sodium supporting electrolyte salt dissolved in a mixtures of organic carbonates.[11] There is often a mix of cyclic carbonates (Figure 3-1a) like ethylene carbonate (EC) with linear carbonates such as dimethyl carbonate (DMC), or diethyl carbonate (DEC). Certain additive molecules like fluoroethylene carbonate (FEC) or vinylene carbonate (VC) are frequently added in small concentrations to improve battery lifetimes and efficiencies due to the impact they have on the degradation of the electrolyte solution and the formation of the solid electrolyte interphase [12,14,92]. These mixtures of compounds have been optimized through trial and error, a process that was time intensive and expensive and we do not have the luxury of further iteration. Rather, a complete understanding of the current system particularly the role of additives will reveal which properties are important for battery performance.

Changes in solvent structure driven by additives could impact how electrolyte degradation, and consequently SEI formation proceeds. In this work, linear infrared (IR) and two-dimensional infrared (2D IR) spectroscopies in combination with molecular dynamics simulations and rheology measurements were used to investigate the impact of FEC on the bulk structure and dynamics of a base electrolyte solution. 2D IR is a technique that can resolve ultrafast structure and dynamics of the electrolyte solution. Previous 2D IR studies on organic carbonate electrolytes have been focused on the solvation structure of carbonates around lithium ions or the mobility of Li-ions in the carbonates [17,24,93,94]. However, more complex base electrolyte solutions with more than two base carbonate components, or the addition of an additive molecule, like fluoroethylene carbonate have yet to be investigated using 2D IR spectroscopy. It is clear from the literature that there are dramatic changes in solvation structures of the electrolyte solutions as the regimes from dilute electrolyte to highly concentrated electrolytes are traversed. In the highly concentrated electrolyte regime, contact ion pairs and ion aggregates dominate the system. However, for commercial electrolytes—1 M concentration of supporting electrolyte—the vast majority of the molecular interactions

are among the carbonate solvent system rather than the solvated ions. Therefore, attention must be paid to the reorganization of the carbonate solutions in the absence of ions as well. Here we show that additives such as FEC, one of the most widely used for LIBs, drive structural changes in the electrolyte even before the addition of any lithium salts. This suggests that the composition of neutral solvent molecules and additives is a key driver in the structure and dynamics of the solution and must be understood as a baseline before the addition of supporting electrolytes to understand the degradation of these mixtures at electrode surfaces.

A limiting factor in using vibrational spectroscopy to study these carbonate electrolyte mixtures is the spectral congestion from overlapping modes in the carbonyl region (Figure A1). One route to circumvent this issue is the introduction of a vibrational probe. Neutral cyanates are a category of vibrational probes that have been shown to be effective at reporting on bulk structure and dynamics and include molecules like methyl thiocyanate (MeSCN) (Figure 3-1b). MeSCN has been shown to accurately report on solvent dynamics in systems like water [62,95]. Moreover, we show that MeSCN has a minimal influence on cycling or SEI formation when added to a sodium ion battery (Figure A5), suggesting it is not substantially altering the electrolyte solution. Therefore, it is a viable route for probing the structure and dynamics of organic carbonate electrolyte mixtures. We investigate mixtures with 5%, 25%, 50% and 100%

FEC in the 1:1:1 DMC:EC: DEC mixture using the cyanate stretch of MeSCN as a vibrational probe. The linear IR spectrum of MeSCN in each mixture are shown in Figure 3-1. Slight broadening and shifting of the main cyanate peak is observed with increasing FEC concentration. Additional FTIR spectra, fitting

results, and estimated relative numbers of molecules for each component can be found in Table A1, and Figure A3.

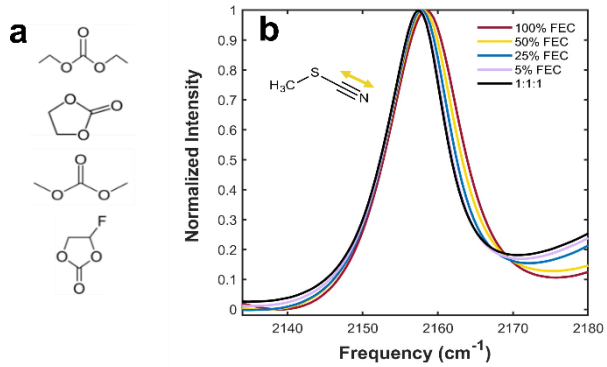

Figure 3-1 (a) The four organic carbonates used in this work. Diethyl carbonate, ethylene carbonate, dimethyl carbonate, and fluoroethylene carbonate. (b) Chemical structure of methyl thiocyanate with the cyanate stretch indicated by a yellow double-sided arrow. Five FTIR spectra zoomed in on the methyl thiocyanate cyanate stretch for each solution studied, 100 % FEC (red), 50% FEC (yellow), 25% FEC (blue), 5% FEC (purple) and 0% FEC (black).

Ultrafast spectroscopy allows the direct observation of chemical dynamics on timescales closely matching those of molecular motions. 2D IR is the result of mixing three electric fields in time and space to generate a fourth signal field. Figure 3-2a shows a typical pulse sequence and the possible interactions of the pulse sequence with an anharmonic vibrational mode (Figure 3-2b). Figure 3-2c and d provide representative 2D spectra, showing the cyanate stretch of MeSCN in fluoroethylene carbonate. The on-diagonal blue contours represent signals from a ground state bleach (GSB), $v = |0\rangle \rightarrow |1\rangle$ and stimulated emission (SE) $v = |1\rangle \rightarrow |0\rangle$. The off-diagonal yellow contours represent excited state absorption (ESA) signals from $v = |1\rangle \rightarrow |2\rangle$. The ESA signal is shifted to lower frequency due to vibrational anharmonicity of the cyanate stretch. More details on the 2D IR experiments performed can be found in SI Section 5.

Since 2D IR acts as a frequency-frequency correlation map between the excitation (pump) and detection (probe) frequencies, time-resolved information about the interactions of molecules with their solvent environment can elucidated by tracking peak shapes over time [50]. Specifically, we perform inverse center line slope (CLS) analysis to track the peak slope over time. Fits to CLS decays are then used to approximate the frequency-fluctuation correlation function (FFCF), thus measuring spectral diffusion and reporting on condensed phase dynamics in each carbonate mixture. Equation 3-1 is the FFCF approximated by a biexponential as a function of waiting time (T_W) which is used to fit CLS decays (Figure 3-2e).

$$C(T_W) = \langle \delta\omega(T_W), \delta\omega(0) \rangle \approx a_1 e^{T_W/\tau_{short}} + a_2 e^{T_W/\tau_{long}} \qquad 3\text{-}1$$

In Equation 1, C represents the FFCF, as a function of T_W, $\delta\omega$ represents the instantaneous frequency, and the short and long-time constant are τ_{short} and τ_{long} with amplitudes a_1 and a_2 respectively. Fitting details can be found in SI Section 6.

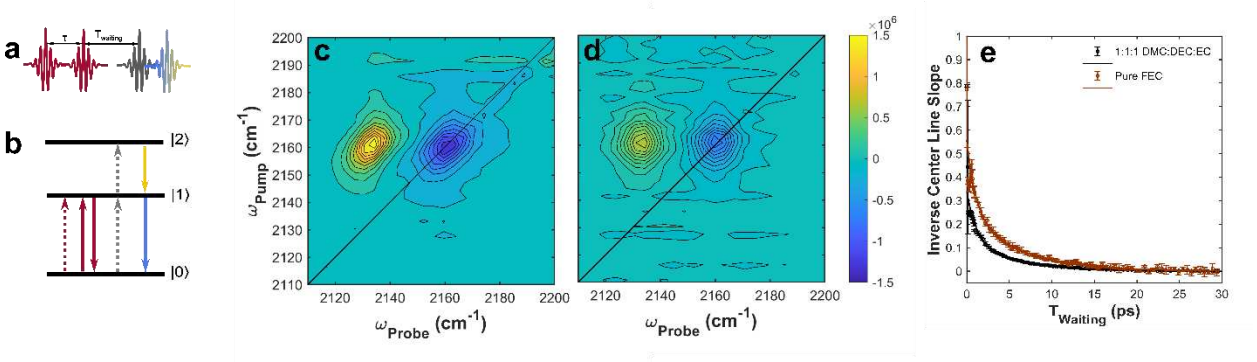

Figure 3-2 (a) Representative 2D IR pulse sequence with pump pulses in red, the probe in grey, and the signal in gold/blue. (b) Cartoon representation of the vibrational energy levels accessed by the pulse sequence in (a). (c) XXXX 2D IR spectrum of MeSCN at $T_{Waiting}$ equal to 400 fs (d) XXXX 2D IR spectrum at 20.4 ps. (e) Two example CLS decays for the 1:1:1 DEC:DMC:EC mixture and the purely FEC mixture.

Interestingly, the time scales from the CLS fits to the approximate FFCF for the mixture show a nonmonotonic dependence on the concentration of FEC. As FEC is added to the carbonate mixture, the fast time component, τ_{Fast}, of the FFCF decelerates until 25% FEC by volume. Whereas, the slow time component, τ_{Slow}, become significantly slower with the addition of FEC up to 5% before decreasing again (Figure 3-3). Slowing of spectral diffusion suggests that the solvent environment is changing in a way that makes it more difficult for the solvent environment to rearrange around the probe.

To gain a better molecular level picture of the changes in solvation structure after adding fluoroethylene carbonate, molecular dynamics (MD) simulations were performed on MeSCN in pure FEC, a 1:1:1 by mass solution of DMC, DEC, and EC, and a solution of 5% FEC in the 1:1:1 mixture. These simulations were done using the TINKER modeling package and the AMOEBA force field. The systems are built using Packmol with each system containing four MeSCN molecules whose CN stretches serve as vibrational probes. SI Section 7 contains additional parameters and Table A2 contains the amount of each

electrolyte component used. The electric field correlation functions from MD for MeSCN in each solution provide a metric to compare with experimental CLS results (Figure A7).

There are qualitative similarities between the simulated electric field correlation functions and the experimental results. However, we note a dramatic difference in relative timescales between the computational and experimental results (Figure A7). We attribute this discrepancy to the ability of the model to capture the system polarizability. To quantify the systematic difference in time constants between MD results and experiment, the electric field correlation functions and the CLS results were integrated to generate a single weighted time constant and the ratios between each weighted time constant for the three comparable mixtures were taken (Figure A9). Another general concern when working with probe molecules is to ensure aggregation of a specific component is not occurring near the probe. Quantifying aggregation can be done by determining the percentage of the trajectory each component is the closest to MeSCN and comparing to the statistically expected value based on the number of molecules present. Based on the calculated percentages, the solutions have an appropriate distribution of nearest molecules, and no aggregation is evident (Table A3). Given these checks we moved to use the structural results from the MD to help interpret the CLS results.

Structural changes can be assessed using cylindrical distribution functions (CDF) generated from the MD simulations. The CDFs can provide a look at the different solvation shells for the individual solvent molecules, which provide information about where the molecule is interacting with the probe. We use CDFs calculated such that the nitrogen of MeSCN is the reference atom and the carbonyl carbon is the used for the density of DMC, DEC, and EC. The fluorinated carbon is used for the density of FEC. Resulting CDFs can be seen for 1:1:1 DMC:DEC:EC and 1:1:1 DMC:DEC:EC with 5% FEC by volume in Figures S12 and S13 respectively. Surprisingly, EC has a much different CDF in 1:1:1 DMC:DEC:EC than when FEC is added to the solution (Figure 3-3). DMC and DEC remain essentially unaffected by the addition of FEC.

This means when FEC is added to the electrolyte solution EC disrupted in the solvation shell surrounding the probe and thus, the carbonate solution has altered structural properties.

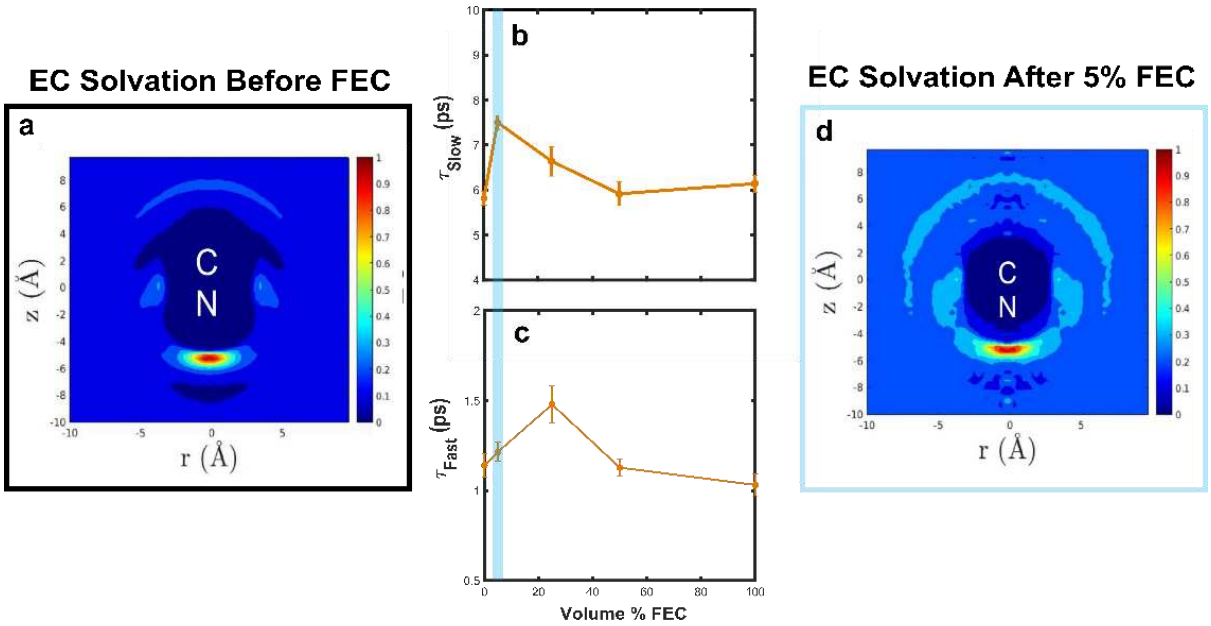

Figure 3-3 (a) The CDF corresponding to the solvation of EC around MeSCN in the 1:1:1 mixture. (b) The long time component of the CLS biexponential fit. Highlighted in blue is the time constant corresponding to the solution with 5% FEC. (c) Short-time component of the CLS biexponential fit. (d) CDF corresponding to the solvation of EC around MeSCN in the 5% FEC mixture.

Together, the increased decay times in the experimental CLS and solvent shell reorganization seen in simulated CDF results point to FEC driving significant structuring and reorganization in an organic carbonate mixture at low concentrations before the addition of any sodium or lithium salt (Figure 3-3). Specifically, the EC is most perturbed by the FEC addition. These changes suggest that the composition of the neutral solvent molecules plays an important role in the overall solution structure. Given the common use of 5% FEC in industrial organic carbonate electrolyte solutions in LIBs having a clear picture of the additive role in these mixtures is essential.

To gain an even more complete picture of the system anisotropy measurements are used to investigate orientational dynamics, which can be impacted by system properties like viscosity or the strength of solvent-solute interactions [96]. Using polarization dependent measurements time-dependent anisotropy can be calculated from 2D IR spectra [50]. Specifically, two series of measurements are made, one in which the pump and probe pulses are the same polarization and one where the pump and probe pulses

are perpendicular (Figure 3-4a). Then as the time between the second pump pulse and the probe pulse is increased the unit vector of a vibrational transition dipole will have time to reorient as the molecule itself rotates and undergoes conformational changes. We calculated the anisotropy ($r(T_W)$) via Equation 3-2 using the normalized integrated signal intensity as a function of T_W for parallel, $I_{\parallel}$, and perpendicular $I_{\perp}$ polarization schemes [29]. Additional details on signal normalization and integration can be found in Section 10 of the SI.

$$r(T_W) = \frac{I_{\parallel}(T_W) - I_{\perp}(T_W)}{I_{\parallel}(T_W) + 2I_{\perp}(T_W)} \qquad 3\text{-}2$$

In addition, experimental results were compared with calculated rotational correlation functions from the MD simulations. Experimental anisotropy data and MeSCN rotational correlation functions show the same qualitative trend in terms of time constants, seen in Table A4. Though, like the electric field correlation functions and the CLS measurements, there is a discrepancy in the timescales between the rotational correlation functions and the experimental anisotropy.

The simulated rotational correlation functions can provide information about which components have altered dynamics caused by the addition of FEC. The rotational correlation functions for the carbonyl bond of each electrolyte component are shown in Figure A17. The only component with a significant dynamic change is FEC. Pure FEC solution shows much slower rotational dynamics than the FEC molecules in the 1:1:1 DMC:DEC:EC with 5% FEC, revealing that when FEC is used an additive with electrolyte solutions, it is able to reorient more quickly. This suggests that the interactions between FEC and DMC, DEC, and EC are weaker than FEC-FEC interactions.

To gain additional molecular details the experimental anisotropy data are explored using a physical model. Experimental data were best fit with biexponential decays. To explain this biexponential behavior of the anisotropy we turn to prior models that have been developed to explain rotational diffusion.[79] One route of interpretation is via the wobble-in-a-cone model [80,81] (Figure 3-3b). This model breaks the orientational correlation function into a slow and fast component. In this model, the short time decay is described as the local reorientation of the probe, in this case the cyanate-stretch of MeSCN, within a

restricted cone. The long-time decay is then attributed to the full, global reorientation of the probe (Table A4). Assuming the two motions in the biexponential are independent, the total correlation function is given by the product of the fast and slow component, Equation 3-3 and 3-4 respectively.

$$C_{fast}(T_W) = (1 - S^2)e^{-T_W/\tau_{Cone}} + S^2 \qquad 3\text{-}3$$

In Equation 3-3, S^2 represents an order parameter with values in a range of 0 to 1 with |S| equal to 0 representing an isotropic motion and |S| equal to 1 representing a completely restricted motion.

$$C_{slow}(T_W) = e^{-T_W/\tau_{slow}} \qquad 3\text{-}4$$

Multiplication of Equation 3-3 and 3-4 results in the total correlation function in Equation 3-5. This total correlation function is used to fit our anisotropy decays.

$$0.4 * C_{Total}(T_W) = (1 - S^2)e^{-T_W/\tau_{fast}} + S^2\left(e^{-T_W/\tau_{slow}}\right) + offset \qquad 3\text{-}5$$

From these fit results a cone angle, cone diffusion time and global diffusion time can be calculated. Details on these calculations and fitting results can be found in SI Section 10 and Table A4. The inverse global diffusion time for MeSCN generally slows with increasing amounts of FEC (Table A4). In the absence of strong solute-solvent interactions it has been shown that reorientation times can be attributed to solvent viscosity.[97,98] Thus, rheology measurements were made on each solution to test whether there was a correlation between global reorientation times and bulk viscosity. Full experimental details and results for the viscosity measurements over a range of shear rates are given in SI Section 11. Figure 3-4d shows there is a correlation between the macroscopic viscosity and the global reorientation. Thus, we suggest that the slowing of the global diffusion time with additional FEC is tied to changes in macroscopic viscosity.

Trends in the cone semi-angle and the inverse cone diffusion time for each carbonate mixture are displayed in Figure 3-4c. As the cone angle decreases, the inverse cone diffusion time increases slightly, with a peak at 50% FEC. This relationship suggests an increasing rigidity of the surrounding solvent, restricting the probe's ability to reorient quickly as the cone shrinks. Similar connections between solvent rigidity and cone angle have been made in work by Tan *et al*. studying reverse micelles.[82]

Ultimately, these changes in the rotational dynamics, like CLS and CDF results, support the idea that additive molecules can induce a pre-structuring in electrolyte mixtures prior to the addition of salts. However, unlike with the CLS and CDF, we see more dramatic changes in the structure and orientational dynamics at concentrations above 5% FEC. This is an interesting difference to note since 5% by volume FEC is a commonly used additive concentration.

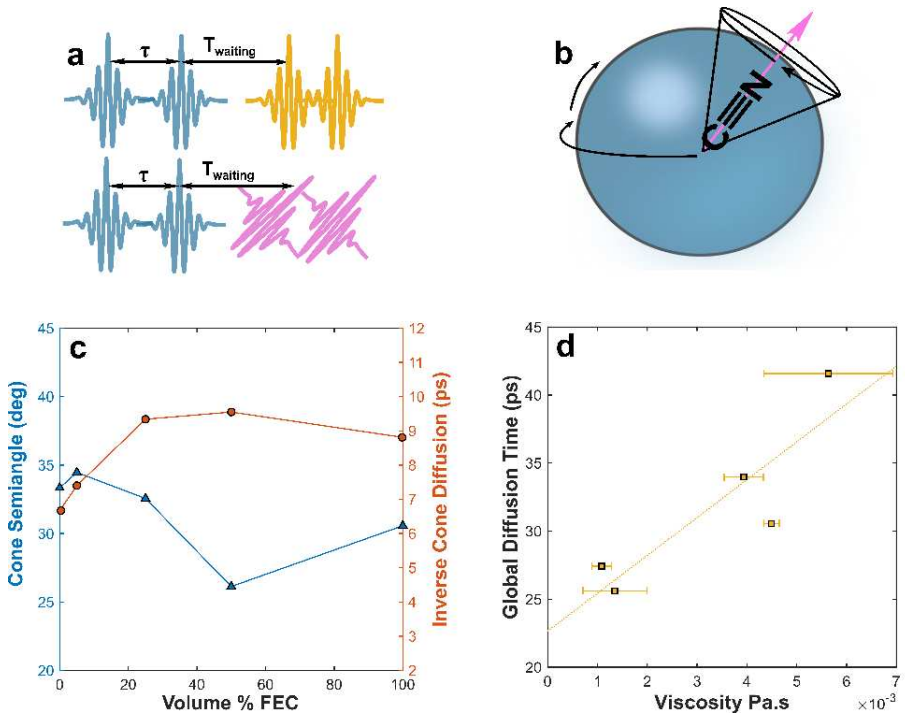

Figure 3-4 (a) Cartoon pulse sequence for a co-polarized 2D IR experiment (top) and cross-polarized (bottom). (b) Cartoon representation of the reorientation of a cyanate with the wobbling-in-a-cone and global reorientation represented with black arrows. (c) Anisotropy fit results. In blue (left axis) there is the cone semi-angle. In orange (right axis) is the inverse cone diffusion time. (d) Correlation plot between the viscosity (at a shear rate of 25 Hz) and the global diffusion time (ps).

3.1 Outlook

Overall, the additive FEC is shown to induce structural changes in a base electrolyte mixture of organic carbonates, even before the addition of any salts. Experimental CLS demonstrated that at low concentrations the introduction of FEC slows spectral diffusion, suggesting a change in solvent environment. Computational CDF results in conjunction with these CLS results indicated solvent reorganization upon the addition of FEC significantly impacts EC solvation. Future work, directly probing the coupling and energy transfer between EC and the other carbonates is underway and may provide additional insight into role EC plays in mixtures with additives. Furthermore, using a combination of

experimental anisotropy, rheology, and computational rotational correlation functions we found (1) an increasing solvent rigidity at higher amounts of FEC (2) additional FEC increases macroscopic viscosity (3) global solvent reorientation is correlated to macroscopic viscosity and (4) the interactions between FEC and DMC, DEC, and EC are weaker than FEC-FEC interactions.

The observed pre-structuring of the solvent environment upon addition of FEC could have implications in driving certain routes for SEI formation, consequently having an impact on important battery metrics like rate lifetime and safety. The pre-structuring of the solvent environment could also dictate potential solvation pathways for high ionic strength species and suggests the carbonate mixture is not a passive environment. Future studies investigating other additives like VC would determine if electrolyte pre-structuring is unique to FEC or more broadly induced by common additives.[92]

CHAPTER 4

Dicyanamide Anion Reports on Water Induced Local Structural and Dynamic Heterogeneity in Ionic Liquid Mixtures[2]

4.1 Summary

The effects of limited amounts (under 21.6% χ_{Water}) of water on 1-butyl-3-methylimidazolium tetrafluoroborate ($BmimBF_4$) and 1-butyl-3-methylimidazolium dicyanamide (BmimDCA) room-temperature ionic liquid (RTIL) mixtures were characterized by tracking changes in the linear and two-dimensional infrared (2D IR) vibrational features of the dicyanamide anion (DCA). Peak shifts with increasing water suggest the formation of water associated and "dry" DCA populations. Further results showed clear differences in the dynamic behavior of these different populations of DCA at low (defined here as below 2.5% χ_{Water}), mid (defined here as between 2.5% χ_{Water} and 9.6% χ_{Water}), and high (defined here as between 11.6% χ_{Water} and 21.6% χ_{Water}) range water concentrations. Vibrational relaxation is accelerated with increasing water content for water-associated populations of DCA, indicating water facilitates population relaxation, possibly through the provision of additional bath modes. Conversely, spectral diffusion of water-associated populations slowed dramatically with increasing water, suggesting water drives the formation of distinct and non- or very slowly interchangeable local solvent environments.

4.2 Introduction

Ionic liquids (ILs) are fluids composed entirely of ionic species and unlike molten salts, such as NaCl which melts at ~ 800°C, ILs often are liquid at or near room temperature (i.e. RTILs). This class of fluids is appealing for a wide array of applications including catalysis[36,37], renewable energy generation[25,26,38,39] and storage[27,28,40,41], fuels[42,43], and biomass dissolution.[44] With the growing use of ILs in many fields there has been extensive work into understanding how additives and contaminants impact the properties of RTIL mixtures. For example, given the hygroscopic characteristics of many ILs[99–101], water is commonly found in ILs. Thus, researchers have investigated methods for removing water from ILs[102] and quantifying water

[2] This chapter is a manuscript in progress. Autumn Wyatt prepared all samples studied here and helped with linear and 2D IR experiments and the viscosity measurements. Autumn wrote the section on rheology. Anthony Rappe performed the density functional calculations. Bradley Luther and Amber Krummel provided invaluable guidance on data interpretation and provided suggestions for analysis routes.

in IL samples.[103] In addition, there have been many studies into how sorption of water into IL mixtures can give rise to changes in properties including the electrochemical window, viscosity, density, and reactivity.[41,44,101] Ultimately, these changes can be beneficial or detrimental depending on the application. In some cases, like electrochemical devices such as dye-sensitized solar cells (DSSCs), there is a fine line between benefit and detriment. For example, simulations by Jeon *et al*. suggest some water can improve ion mobility in DSSC electrolytes consequently increasing rates of electron transfer and decreasing time for possible electron hole recombination, thereby improving DSSC performance. However, this benefit needs to be balanced with potential negative water-dye interactions at the DSSC electrode.[25,26] Therefore, researchers are left with a time and resource consuming "Goldilocks" problem trying to find just the right amount of water for every scenario. Thus, painting a clear molecular picture of the fundamental role water plays in ILs across a range of concentrations and types of RTILs is key for crafting the appropriate solvent mixtures.

One route for painting a clear picture of molecular dynamics and structure is via ultrafast spectroscopy. Two dimensional IR spectroscopy (2D IR) in particular has been used to reveal the ultrafast dynamics of water in multiple environments including biological systems,[56–59] inorganic aqueous electrolytes,[60–62] and at surfaces.[65] In addition, 2D IR has been used to investigate different ionic liquid mixtures[64,104–109], including water-IL mixtures.[76,110,111] The first 2D IR study of water and ILs was by Ren *et al*.[110] who compared a wet and dry RTIL sample using thiocyanate as a vibrational probe. They found that water-saturated ILs show two distinct types of dynamics and attributed this to probes in a water associated and non-water-associated sub ensemble. Another study by Wei *et al.*[111] investigated the RTIL, 1-butyl-3-methylimidazolium tetrafluoroborate (BmimBF$_4$), mixed with water and compared results to prior studies of mixtures of NaBF$_4$ in an aqueous system. They found that exchange between D_2O associated with BF$_4$ and associated with bulk water was 3X slower in the IL mixture. This suggested that the solvent dynamics are mediated by the steric effect of the cationic group in the ILs. Both these studies showed drastic impacts of water on the structure and dynamics of IL-water mixtures. These prior 2D IR studies have

focused primarily on systems with large amounts of water (15 mole percent water or higher). However, possible benefits of water to electrolyte mixtures have been posited at lower concentrations.[26] Thus, we investigate a series of concentrations between 1.3and 21.6% $\chi_{Water.}$ Specifically, we use a combination of linear and 2D IR spectroscopy and rheology to investigate the impact that water as an additive has on the structure and dynamics of 1-butyl-3-methylimidazolium dicyanamide (BmimDCA) (Figure 4-1). We find substantial changes in the dynamics experienced by DCA beginning at 2.5% $\chi_{Water.}$ These changes in dynamics point to distinct solvent environments induced by the presence of water in small amounts.

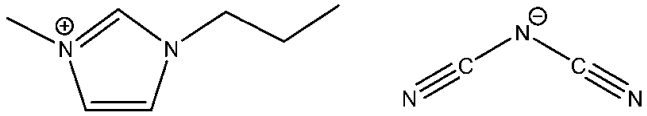

Figure 4-1 Molecular structure of the cation 1-butyl-3-methylimidazolium (Bmim) and the anion dicyanamide (DCA)

4.3 Methods

4.3.1 Sample Preparation

RTIL solutions used in the 2D IR, Fourier Transform infrared spectroscopy (FTIR), and viscosity measurements are comprised of 1-butyl-3-methylimidazolium tetrafluoroborate ($BmimBF_4$), 1-butyl-3-methylimidazolium dicyanamide (BmimDCA), and deionized water. $BmimBF_4$ (99% purity) and BmimDCA (>98% purity) are purchased from IoLiTec. BmimDCA was doped into $BmimBF_4$ at a ratio of 5:2000 by volume corresponding to a mole percent dicyanamide of 0.121. Water is doped into this bulk RTIL solution at concentrations of 0.5, 1, 2, 2.5, 4, and 5% H_2O by volume corresponding to mole percentages of 2.5, 4.99, 9.6, 11.8, 17.86, and 26.1, respectively. Another RTIL solution is a mixture of $BmimBF_4$ and 1-butyl-3-methylimidazolium bis(trifluoromethylsulfonyl)imide (BmimTFSI, IoLiTec, 99% purity). The BmimDCA is doped into the BmimTFSI at a ratio of 5:3000 by volume corresponding to a mole percent dicyanamide of 0.125. All samples are sonicated 10 minutes before use.

4.3.2 Linear FTIR Measurements and Fitting

Linear FTIR spectroscopy measurements are performed on a Bruker Optics Vertex 70. The spectral resolution is 2 cm^{-1} and 32 scans were averaged. The solutions are sandwiched between two 1mm calcium

fluoride (CaF_2) plates (Crystan) with a diameter of 25.4mm and the path length was set to 15μm with a Teflon spacer (Harrick).

FTIR fitting is done in the MATLAB curve fitting toolbox. Between 2050 cm^{-1} and 2260 cm^{-1} a background subtraction is done by fitting a single Gaussian to the broad feature (from BF_4 and water) under the DCA peaks of interest. Next, three Gaussians are simultaneously fit to the DCA peaks. The asymmetric and symmetric water peaks were simultaneously fit to two Gaussians. A third Gaussian in the water region was introduced at higher water concentrations (starting at 11.8 mole % water) to account for the bulk water.

4.3.3 **2D IR Measurements**

The 2D IR spectra are collected using a 2D IR spectrometer described previously.[112] Briefly, the generation of 220 fs mid-IR pulses centered at 4650 nm is achieved with optical parametric chirped-pulse amplification (OPCPA) and difference frequency generation (DFG) in magnesium doped periodically poled lithium niobate (MgO:PPLN) and zinc germanium diphosphide (ZGP), respectively. All measurements herein use a pump-probe optical geometry. The power measured before the sample focus for the probe line is ~ 5 mW, giving a pulse energy of 50 nJ at the 100 kHz repetition rate of our laser.

A series of 601 pump pulse pairs from 0 to 6 ps are taken in 10 fs steps. Data along the pump axis is then zero-padded to 1202. The power of the pump is ~ 17 mW resulting in a pulse energy of ~75 nJ per pulse. Spectra are acquired using four-frame phase cycling scheme with a rotating frame of 1900 cm^{-1}.[113] Each 2D IR spectrum is averaged 500x and repeated in triplicate. A two-pixel noise reduction scheme described in previous work and based on work by Feng *et al*. and Robben *et al*. is used in the data acquisition.[29,95,114] A half wave plate followed by a wire grid polarizer (WGP) along the probe line are used to rotate the polarization prior to the sample 45° relative to the pump. A second WGP prior to detection selects signal parallel (XXXX) or perpendicular (XXYY). The waiting time between the second pump and probe ($T_{Waiting}$) are scanned from 0 to 30 ps and spectra are collected in XXYY and XXXX polarization schemes for the seven IL mixtures. For the first 0.9 ps of the scan, 100 fs step sizes are taken, 0.25 ps steps are taken for the next 15 ps, and 2 ps steps are taken for the final 14 ps.

4.3.4 **Rheology Measurements**

Viscosity measurements are performed on a TA Instruments Discovery HR-2 with a 40mm diameter flat parallel aluminum Peltier plate. An equilibration time of 60s is applied before each measurement and the temperature is held constant at 25°C. The shear rate varies on a logarithmic sweep from 2-25s^{-1} over ~12min with 10 points per decade and a geometry gap of 500 µm to observe the shear stress and viscosity. Each sample is measured in triplicate and averaged. The measurements are performed on a hybrid rheometer using two round, flat plates. The bottom plate remains stationary while the top plate rotates at a specific velocity range to set the applied shear rate (Equation 4-1).

$$Shear\ Rate\ (S^{-1}) = Plate\ Velocity\ (m/S)/Geometry\ Gap\ (m) \qquad (4\text{-}1)$$

As the shear rate changes, the shear stress value is obtained by measuring the force applied to the sample by the top plate and dividing it by the area of the plate. The viscosity is equal to the ratio of the shear stress to the shear rate.

4.3.5 **Quantum Calculations**

Quantum mechanical calculations were performed on a single DCA anion to gain insight into low-frequency modes that may contribute to the dark state observed in the 2D IR spectra. All optimization and anharmonic frequency calculations were done using density functional theory with a B3LYP functional and a 6-311+G(2d,2p) basis set. Table 4-1 shows the resulting nine fundamental vibrations of the DCA anion.

Table 4-1 Vibrational modes, motion descriptions, and fundamental frequencies from DFT calculations on DCA.

	Frequency (cm^{-1})	**Description**
Mode 1	169.6	Scissor full
Mode 2	537.8	Rocking
Mode 3	560.0	Twist
Mode 4	572.3	Twist
Mode 5	683.9	Scissor C-N
Mode 6	931.6	Symmetric C-N Stretch
Mode 7	1370.0	Asymmetric C-N Stretch
Mode 8	2259.5	Asymmetric C≡N Stretch
Mode 9	2294.7	Symmetric C≡N Stretch

4.4 Results and Discussion

4.4.1 Vibrational Peak Assignments

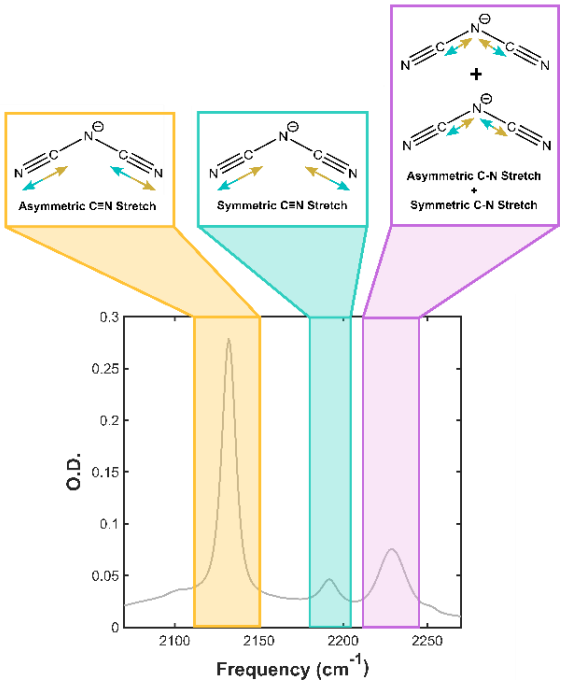

Figure 4-2 Linear FTIR spectrum of three DCA vibrational modes. Highlighted in yellow at 2132 cm^{-1} is the asymmetric C≡N stretch. Highlighted in blue at 2192 cm^{-1} is the symmetric C≡N stretch. Highlighted in purple at 2225 cm^{-1} is a combination mode corresponding to a C-N symmetric and asymmetric stretches.

Figure 4-2 shows the three peaks unique to CN stretches of dicyanamide that are tracked in this study. The peak centered at 2132 cm^{-1} corresponds to the asymmetric C≡N stretch and the peak 2192 cm^{-1} at is the symmetric C≡N stretch. The peak at 2230 cm^{-1} corresponds to a combination band between the C-N symmetric and asymmetric stretches. This peak is likely in Fermi resonance with the asymmetric C≡N stretch[51] and is consequently higher in frequency and intensity than expected for this combination band. Past researchers have debated the assignment of these three peaks, with uncertainty about which was the symmetric stretch and which the combination band.[42,51,115] 2D IR brings further evidence that the peak at 2192 cm^{-1} is indeed the symmetric stretch. The intensity of cross-peaks relative to diagonal peaks in a purely absorptive 2D IR spectrum can give information about the angle between coupled transition dipoles (Equation 4-2).[50]

$$\frac{S_{XXXX}}{3S_{XXYY}} = \frac{4P_2+5}{10-P_2} \qquad (4\text{-}2)$$

In Equation 4-2, S_{XXXX} and S_{XXYY} are the 2D signal in the parallel and perpendicular polarization conditions, respectively. P_2 is the second order Legendre polynomial in terms of the angle between the two modes, $\theta_{\alpha\beta}$ (Equation 4-3).

$$P_2 = \frac{1}{2}\left(cos^2\,\theta_{\alpha\beta} - 1\right) \qquad (4\text{-}3)$$

Implementing Equation 4-2, it is found that the DCA mode at 2134 cm^{-1} and 2230 cm^{-1} are closer to parallel than the peak at 2132 cm^{-1} and 2192 cm^{-1}, which suggests that the 2192 cm^{-1} peak is the symmetric C≡N stretch (Figure 4-3).

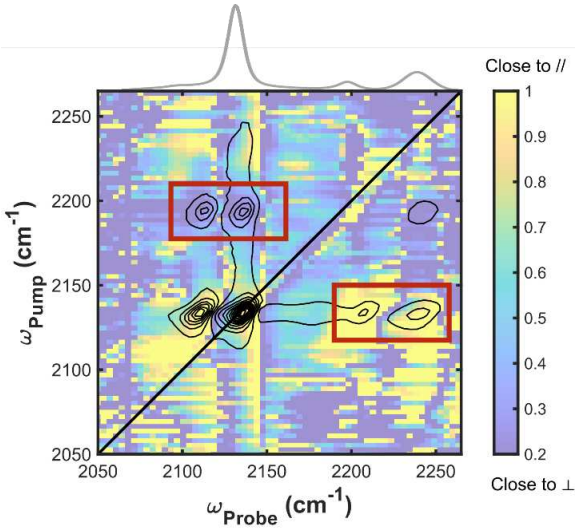

Figure 4-3 The ratio given in Equation 4-2 for an example 2D IR spectrum of an environmental BmimDCA in $BmimBF_4$ sample at 900 fs. The grey spectrum is the corresponding linear FTIR. The black contours show the locations of observed peaks. The red boxes show two example regions of interest. The top left box shows a cross peak between the symmetric and asymmetric stretch. The ratio here is close to 0.2 and consequently these modes are close to perpendicular. The lower right box is a cross peak between the combination band and the asymmetric stretch. The ratio in this region is predominantly close to 1, meaning these modes are close to parallel.

4.4.2 **Assigning 2D IR Features**

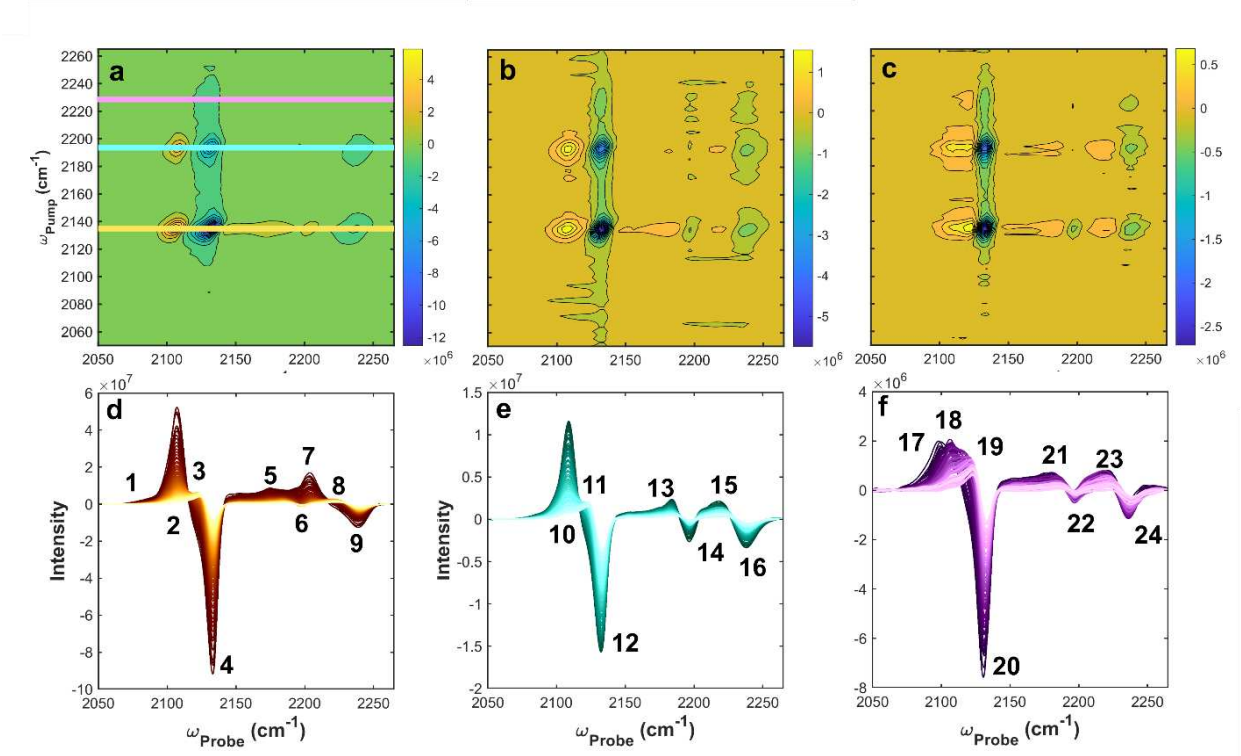

Figure 4-4 (a) Isotropic 2D IR spectrum for the environmental BmimDCA in BmimBF$_4$ sample taken at 900 fs. The purple line corresponds to a cut through the center of the combination mode. The turquoise line represents a cut through the symmetric mode and the orange line represents a cut through the asymmetric mode. (b) Isotropic 2D IR spectrum for the environmental BmimDCA in BmimBF$_4$ sample taken at 8.15 ps (c) Isotropic 2D IR spectrum for the environmental BmimDCA in BmimBF$_4$ sample taken at 20.4 ps. (d) Cut corresponding to the orange line in (a) the shading dark to light represents cuts taken at each time point between 200 fs and 30 ps. The numbers correspond to the peaks that are identified in the main text. (e) same as (d) but for the symmetric mode (f) same as (d) but for the combination mode.

Figure 4-4a shows an isotropic 2D IR spectrum. This spectrum includes the asymmetric C≡N stretch, the symmetric C≡N stretch, and the combination band between the C-N symmetric and asymmetric stretches of DCA at $T_{Waiting}$ equals 900 fs. However, in this system the relative intensity differences between the asymmetric stretch versus the other two modes makes those peaks difficult to see. Figure B5 shows a zoomed in version of the spectrum focused on the higher frequency modes. Figure 4-4b and c show spectra from 8.15 ps and 20.4 ps, respectively. The on-diagonal blue contours represent signals from a ground state bleach (GSB), $v = |0\rangle \rightarrow |1\rangle$ and stimulated emission (SE) $v = |1\rangle \rightarrow |0\rangle$, peaks 4, 14, and 24 in Figure 4-4d, e, and f respectively for each vibrational mode. The corresponding off-diagonal gold contours

represent excited state absorption (ESA) signals from $v = |1\rangle \rightarrow |2\rangle$, peaks 2, 13, and 23. The ESA signal is shifted to lower frequency due to vibrational anharmonicity of each mode.

Since the cross-peaks and off-diagonal peaks are numerous and somewhat complicated, we will walk through their assignments here. The expected cross peaks between coupled modes in conventional 2D IR are peaks 5, 6, 7, 9, 10, 12, 15, 16, 17, 20, 21, and 22.[50] Beyond these cross-peaks we see multiple peaks arise from different forms of energy transfer. First, as a function of time, we see the growth of peak 3. Prior transient absorption experiments of dicyanamide by Hunger *et al.*[115] show a similar feature, and this peak was attributed to an intermediate excited state.[115] Other researchers investigating different molecular probes have seen the same double-peak off-diagonal structure and attributed it to transfer of energy to a dark state.[52,116,117] The dark state is likely a combination of low-frequency modes of the dicyanamide anion (Table 4-1). A combination of DCA modes 2-5 would result in a frequency close to the energy of the asymmetric stretch. Figure 4-3a shows an energy level diagram explaining this picture and Figure 4-5b shows a corresponding Feynman diagram.

In addition to the presence of the dark state feature, there are additional peaks attributed to population transfer between the asymmetric stretch and the combination mode.[68,118] These peaks are 1, 8 and 18 in Figure 4-4d and f. The presence of these peaks is explained by an example of a contributing Feynman pathway in Figure 4-5c.

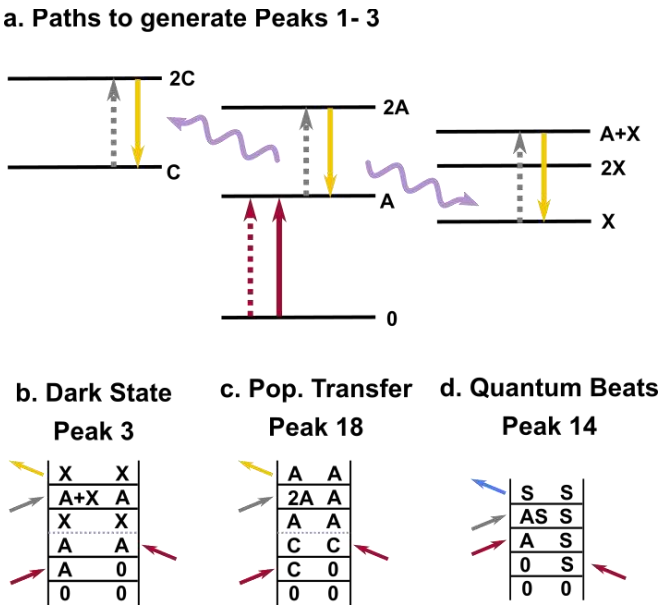

Figure 4-5 (a) Energy pathways to generate peaks 1-3 in Figure 4-4. A refers to asymmetric, C refers to combination mode, and X refers to the dark state. The red lines correspond to the initially pumped state, with the dotted arrow being the initial pump generating a coherence and the solid red arrow being the second pump generating a population. The grey arrows represent the probe. The purple squiggly arrows represent energy or population transfer to the combination mode (left) and dark states (right). (b) Example Feynman diagram for generation of the dark state peak 3. (c) Example Feynman diagram for population transfer between the combination mode and asymmetric stretch. (d) Example Feynman diagram for quantum beating in signal decays between the symmetric and asymmetric stretch.

4.4.3 **Solvent Dependent Quantum Beating**

In addition to a multitude of spectral features, there are apparent oscillations in signal decays. We attribute these to quantum beating between the asymmetric and symmetric mode. To confirm this, the signal of Peak 12 in Figure 4-4 was fit to a growth and decay curve. The residuals, which were primarily the oscillations, were then Fourier Transformed. The result showed a peak close to 60 cm^{-1} which corresponds well to the separation between the two modes (Figure B4). To further test this we performed pump-selective experiments similar to work by Marroux *et al.*[68] Figure 4-6 shows the signal decay for the absolute value of peak 12 for three different experiments. In teal is the signal decay for the environmental BmimDCA in $BmimBF_4$ sample. In purple is the decay for the same sample pumping exclusively the symmetric mode. In this decay the beating is non-existent because the asymmetric stretch was not pumped. This lack of quantum beating in the pump-selective experiment can be explained by the Feynman diagram in Figure 4-5d. In addition, to determine how quantum beating was facilitated in the system we additionally looked at BmimDCA in BmimTFSI. Interestingly, in this system there were no clear oscillations (Figure 4-6). This

suggests that the bulk anion in the mixture is playing a significant role in driving quantum beating between DCA modes.

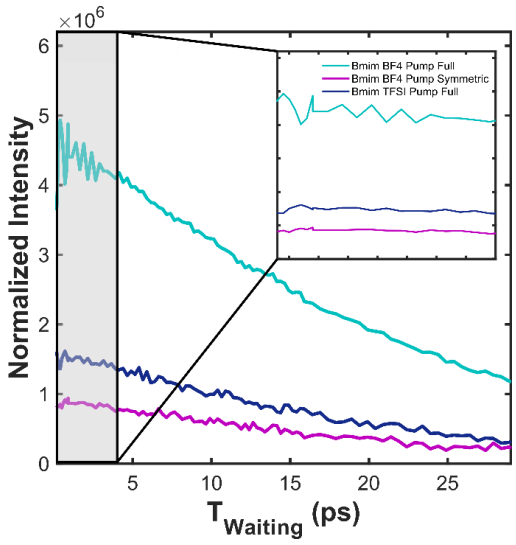

Figure 4-6 Signal intensity of Peak 12 for DCA in BmimBF4 (teal), DCA in BmimBF4 pumped exclusively at symmetric stretch frequency (purple), and DCA in BmimTFSI (navy).

4.4.4 **Water-Dependent Measurements**

To test the effect of water we compared a series of water RTIL mixtures. The lowest water content measured was from the environmental amount of water present in a sample left exposed to the lab conditions. Based the amplitude of both the asymmetric and symmetric OH stretches (Figure 4-7) this was extrapolated to be 1.32% χ_{Water}. As a function of increasing water concentration, we see a broadening and shift to higher frequencies in the linear FTIR spectra (Figure 4-8). Additional fitting parameters can be found in Table B1. This is likely due to the introduction of additional hydrogen bonding interactions of the DCA anion with water molecules. Work on nitriles such as methyl thiocyanate, with water has been shown to lead to blue-shifted and broadened peaks. This has been suggested to be due to the growth of a population of hydrogen-bonded nitriles, making the peak a weighted average of the two populations.[53,54] Thus, we suggest that the shifting and broadening in the DCA peaks of interest is caused by an increase in the number of DCA anions associated with water. This is supported by the work of Kabanda *et al.*[119] who performed DFT on 1-ethyl-3-methylimidazolium dicyanamide (EmimDCA) and water. They determined three likely configurations of

water bound to DCA and in two of the three configurations saw an increase in the frequency of the fundamental asymmetric C≡N stretch.[119]

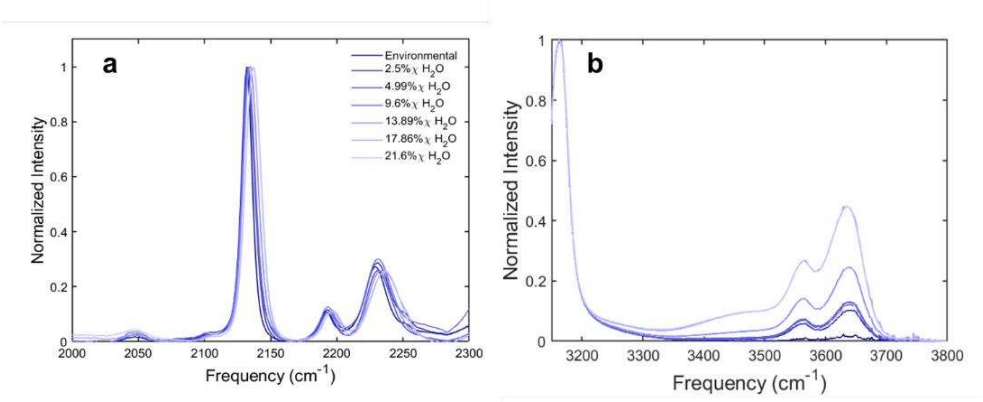

Figure 4-7 Linear FTIR corresponding to each concentration of water tested. Colors dark to light represent increasing water. (a) focused on the three DCA modes of interest, normalized to the asymmetric stretch. (b) The water region of the spectrum showing the bulk water peak, the symmetric and asymmetric peaks.

Based on the lack of a substantial peak between 3400 cm^{-1} and 3500 cm^{-1} in the water region of the FTIR it is likely that for the environmental sample and those with water doped between 2.5% χ_{Water} and 9.6% χ_{Water} there are minimal water-water interactions (Figure B2). However, at concentrations between 11.8% χ_{Water} and 21.6% χ_{Water} we see a clear increase in the bulk water peak suggesting that there are more water-water interactions.

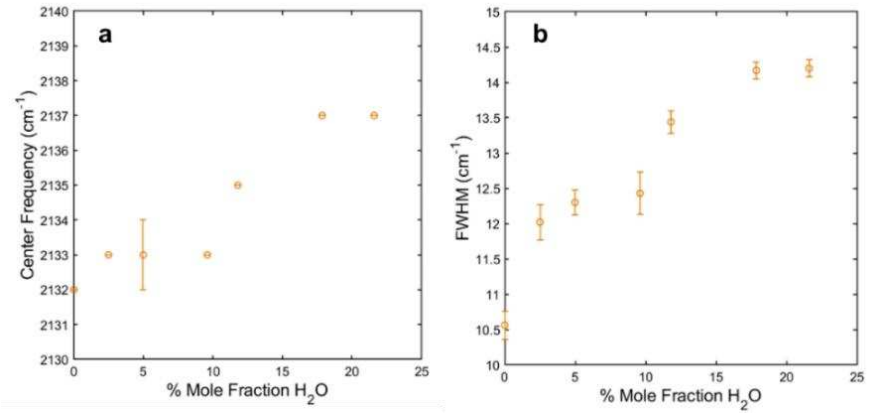

Figure 4-8 Linear FTIR fitting parameters as a function of water for the asymmetric stretch (a) The center frequency of the asymmetric peak. (b) The full width half max (FWHM) of the asymmetric stretch.

4.4.5 **Viscosity**

By increasing the concentration of water, the viscosity of the RTIL mixtures decrease (Figure 4-9). This macroscopic trend may be explained by changes on the molecular level. With the addition of water the strength of association between RTIL cations and anions decreases as water is incorporated into the structure.[120] The viscosity values are similar to those reported on $BmimBF_4$ water mixtures by Liu *et al*.[120] We note that the trends at the shear rates less than $6s^{-1}$ suggest that the viscosities are shear rate dependent. Focusing on the higher rates, the relationship between viscosity and shear rate is linear which, by definition, suggests Newtonian behavior. This is supported by the increasing linear relationship between the shear rate and shear stress, shown in Figure B4.

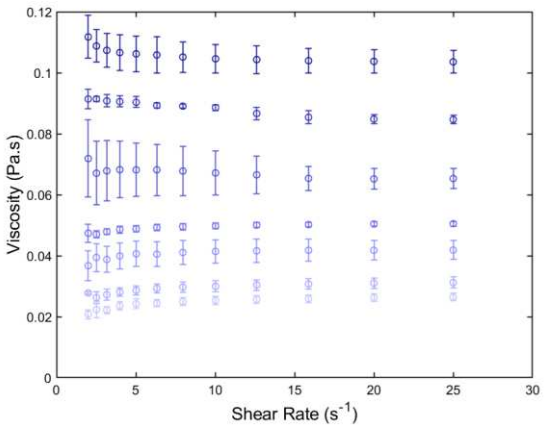

Figure 4-9 Viscosity as a function of shear rate for each water sample, with dark to light being increasing amounts of water.

4.4.6 **Vibrational Relaxation**

The vibrational relaxation time is the decay time for an excited state population relaxing to the ground state. Relaxation timescales are representative of local environments and depend on coupling between the mode of interest and available intramolecular or bath modes. The frequency dependent population relaxation, P(t), is determined from the isotropic signal, which is free from the effects of rotation (Equation 4-4).[76]

$$P(T_W) = \left(S_{\parallel}(T_W) + 2S_{\perp}(T_W)\right)/3 \tag{4-4}$$

Isotropic population decay data for each slice perpendicular to the pump axis were fit using a biexponential equation. All the fitting parameters can be found in Tables S2-S9. As a function of increasing water there

is a decrease in the long time constant, τ_2. In addition, with increasing frequency this decrease is more dramatic, suggesting that population relaxation occurs faster for DCA anions associated with more water (Figure 4-10). It is possible that the presence of more bulk-like water altered the RTIL ionic region by providing additional bath modes of appropriate energy for the DCA to relax into and consequently decreasing the time for relaxation. For the short time decay, τ_1, we again see frequency dependent behavior with water-dependent changes being more significant at higher frequencies, and more consistent decay times for the mid-water range. Figure A7 shows three representative cuts from Figure 4-10 with error bars to demonstrate the significance of the observed changes.

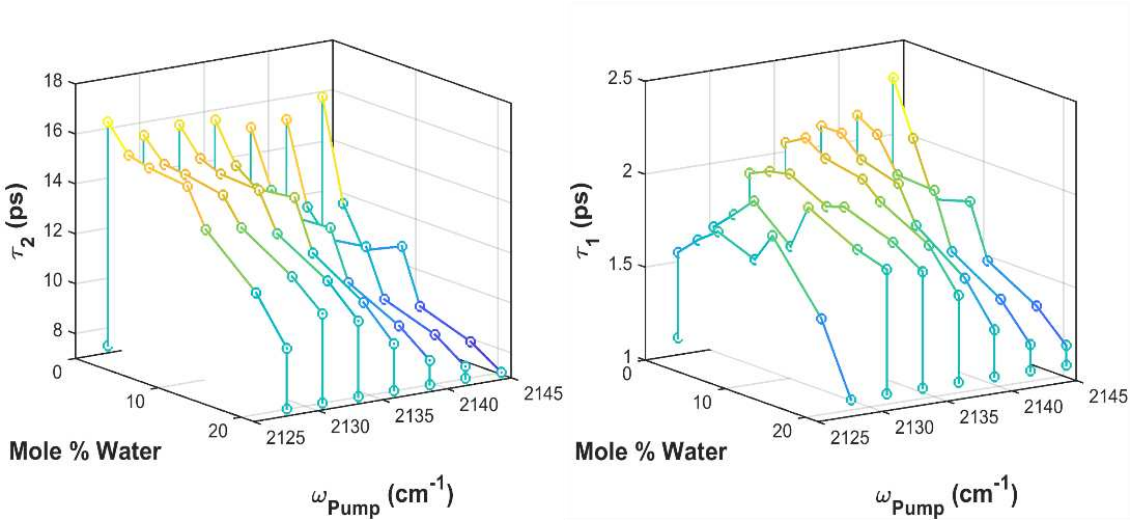

Figure 4-10 Long- and short-time constants from fitting a biexponential to the isotropic signal decay of each pump cut through the asymmetric on-diagonal peak, as a function of water.

4.4.7 **Orientational Dynamics**

To examine the rotational dynamics of the DCA probe polarization dependent 2D IR measurements were performed. Anisotropy is calculated using signal intensities from the XXXX and XXYY polarization schemes (Equation 4-5). Raw anisotropy data showed a systematic offset, with all the data beginning at ~0.5 (above the anticipated maximum of 0.4). Thus, to account for any error in shifts between XXXX and XXYY, data collection schemes prior to averaging and fitting the signal intensities for the XXXX decay were self-normalized. The XXYY signal intensities were then self-normalized to 1/3. Therefore, in this

analysis we do not address any fast orientational motions that may in practice have led to the initial value beginning below 0.4 and instead focus on discussing slower contributions to the decay. Given the likelihood of multiple DCA populations it is important to consider how they may reorient with different rates and have distinct orientational correlation functions contributing to the overall anisotropy decay.[76] Thus, at each frequency across the peak (in this case we focused on the asymmetric stretch) the rotational decay of each population will contribute based on the amount of that population present, and weighted by their respective vibrational relaxation decay as well.

$$r(T_W) = \frac{I_{\parallel}(T_W) - I_{\perp}(T_W)}{I_{\parallel}(T_W) + 2I_{\perp}(T_W)} \tag{4-5}$$

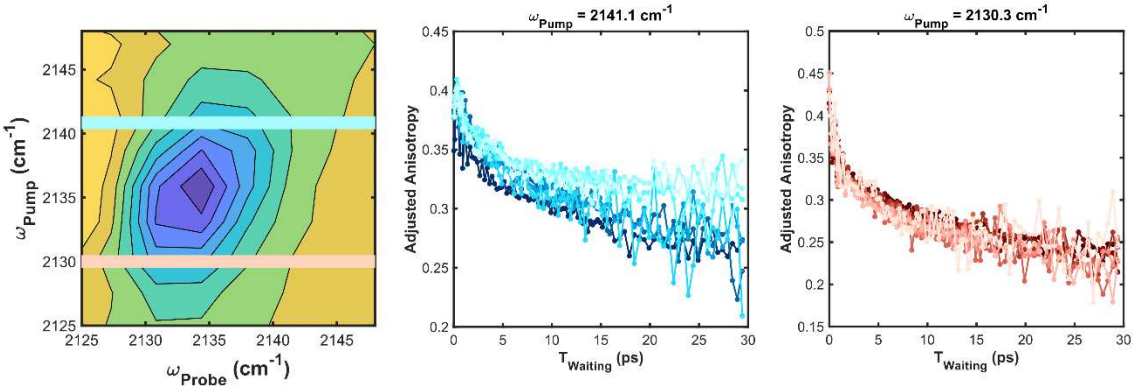

Figure 4-11 Representative cuts perpendicular to the pump axis at 2141.1 cm^{-1} and 2130.3 cm^{-1}. Anisotropy decays from dark to light correspond to increasing amounts of water.

To compare the frequency dependence of the orientational dynamics each pump cut was analyzed independently. Figure 4-11 shows two representative cuts and the anisotropy decay at that frequency as a function of water (dark to light data). For the cut at 2130.3 cm^{-1} we see similar decay behavior across water concentrations, except for the highest water concentration (21.6% χ_{Water}) which plateaus a bit, causing the long time constant to increase (darkest color in Figure 4-12). Conversely for the higher frequency cut at 2141.1 cm^{-1} we see more variation in the anisotropy decays and the respective fits (lightest color in Figure 4-12). The long-time constant increases from 131 ps for the environmental sample to 339 ps for the 17.9% χ_{Water} and 1000 ps for the 21.6% χ_{Water}. The water-dependency at higher frequencies again point to the high frequency DCA populations being water associated and the low frequency populations being dry.

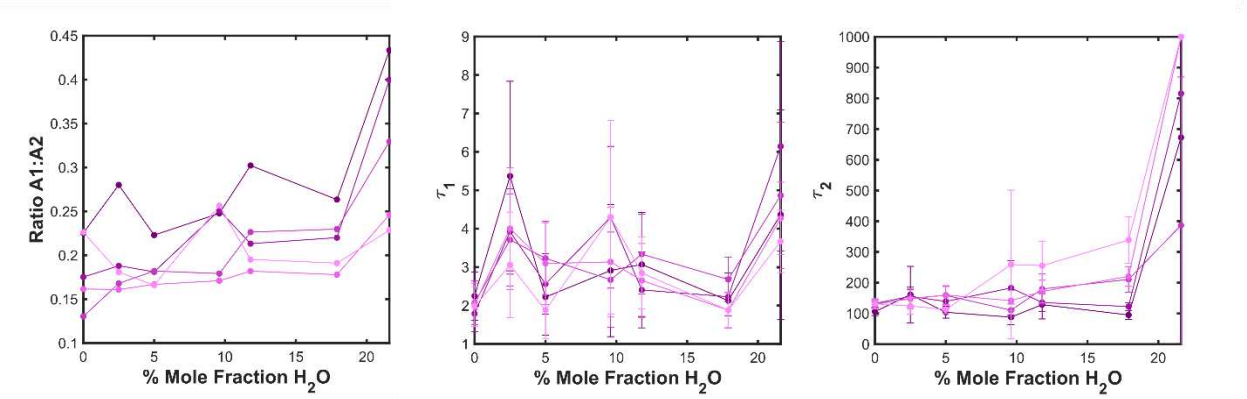

Figure 4-12 Fit results from anisotropy decays. Dark to light represents increasing frequency between 2130 cm^{-1} and 2141 cm^{-1}.

4.4.8 **Spectral Diffusion Dynamics**

When each DCA vibrational mode is pumped, it is in a particular environment, and absorbs at a particular frequency resulting in an inhomogeneously broadened absorption spectrum. As the solvent structure and resulting interactions with DCA change, the probe samples other frequencies that correspond to different structural configurations. The time dependence of this sampling process is called spectral diffusion. To track spectral diffusion, we used center line slope analysis (CLS) which can approximate the frequency-frequency correlation function (FFCF). CLS values can potentially range from 1, for a peak fully correlated along the diagonal, to zero, for an uncorrelated, round peak. Specifically, we analyzed the diagonal peak for the asymmetric C≡N stretch. In this system dramatic asymmetry in the CLS behavior is observed (Figure 4-13), with distinct behaviors at low versus high frequencies across the peak. Asymmetry of CLS has been previously associated with multiple underlying modes.[109] Here it is possible there are multiple populations of DCA; some that are hydrogen-bonded and some that are not. However, these populations are not separated enough that they lead to asymmetry or multiple peaks in the 2nd derivative of the linear IR spectra (Figure 4-13 and Figure B1).[29] Given this substantial overlap, it was not possible to fit the spectra to two 2D gaussians as done previously by Yuan *et al*.[62] However, to more qualitatively assess differences in the high and low frequency portions of the peak, we separated the peak into seven pump cuts and performed CLS of the top and bottom three cuts independently (Figure 4-14). Interestingly, the nature of this

asymmetry changes based on water content, and the most substantial changes are in the behavior of the DCA populations at high frequencies.

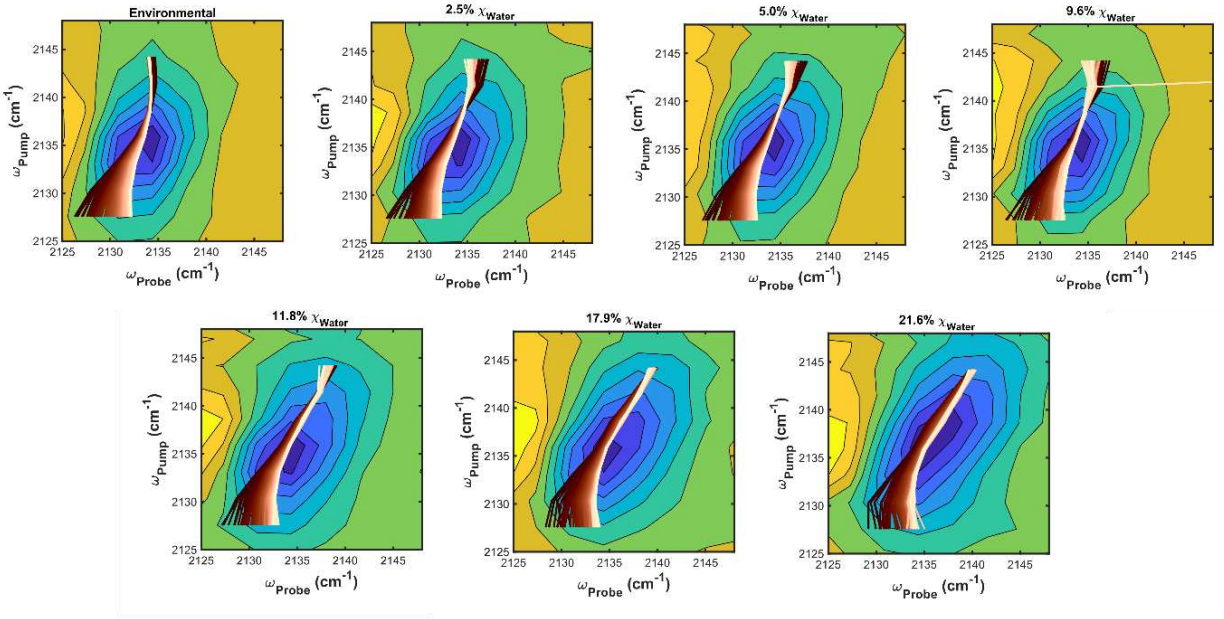

Figure 4-13 Center line slope decays for each water sample, from short time (dark red) to long time (light red) overlaid on a XXXX 2D IR spectrum taken at $T_{Waiting}$ equal to 20.4ps.

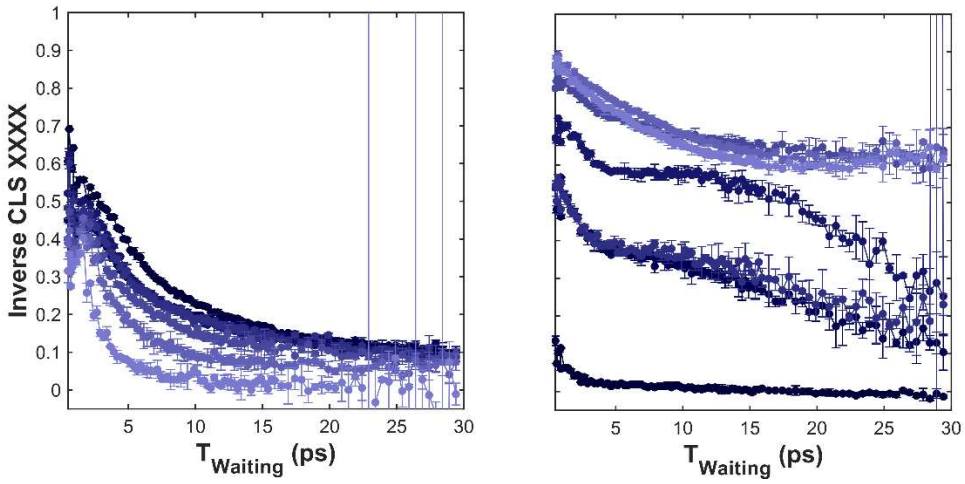

Figure 4-14 (left) CLS for the top three frequency cuts 2138 to 2144 cm-1 versus (right) CLS for the lower three cuts of 2127 to 2133 cm-1. Dark to light represents increasing amounts of water. Error bars are from the standard deviation of triplicate measurements

At low (defined here as 1.3 χ_{Water}) concentrations of water we see the high-frequency region of the CLS almost at zero. This possibly suggests very fast spectral diffusion of the higher frequency modes.

Conversely at low frequencies we see a much longer decay to zero. The frequency dependent asymmetry of the CLS is lessened at samples in the mid-range water samples (defined here as between 2.5% χ_{Water} and 9.6% χ_{Water}). At high frequencies we see some initial fast spectral diffusion followed by a slower decay. At low frequencies the behavior is more like that of the environmental sample. At higher concentrations of water (defined here as between 11.6% χ_{Water} and 21.6% χ_{Water}) we see a different form of asymmetry. In these samples we see a very short and minimal initial drop in the CLS. However, after that initial drop, over the course of the time window of the experiment almost no change in CLS slope is seen.

To try and interpret these interesting trends it is important to consider that the FFCF timescales represent all the possible motions of the solvent environment contributing to spectral diffusion. Thus, we must hypothesize the possible types of environments available to the DCA molecules and how solvent motions around and interactions with DCA may be changing as the amount of water in the system is increased.

First, we consider the bulk structure of our environmental sample. It has been shown by numerous researchers that long alkyl chain ionic liquids have segregated polar and non-polar domains. However $BmimBF_4$, having a relatively short alkyl chain, has been shown to have some apolar aggregation but not large extended or continuous apolar regions.[76,104,121] Since the bulk of this sample is $BmimBF_4$ it is likely there is some minimal phase separation in the environmental sample.

In the environmental sample DCA is likely in a somewhat more polar region. Prior researchers have used cyanate-based anions to probe local dynamics of ionic liquid mixtures including thiocyanate (SCN) and dicyanamide (DCA). Results of these studies suggested that the anionic probes are reporting on local dynamics and are located in primarily cationic regions.[111,115] Within this more polar region DCA could be “free”, hydrogen-bonded to Bmim in some conformation, or interacting with an isolated water molecule. The DCA probes could then be experiencing quick librational or orientational motions of the surrounding solvent and undergoing hydrogen-bond making and breaking.[59] In addition, recent work by Kabanda *et al*.[119] demonstrated that two likely configurations of Emim bound to DCA show up at distinct frequencies.

The difference between the two configurations is a slight twist of the cation. The less stable of the two conformations is found to be at a higher frequency.[119] It is possible that fast orientational motion of the cation led to fast spectral diffusion between the possible configurations of DCA.

For the mid-range water mixtures, we could perhaps find DCA isolated, hydrogen-bonded to Bmim, hydrogen-bonded to a single or a couple waters (at the center or end nitrogen or both), or bonded to a water bridged to a Bmim. With this increase in possible solvent configurations to sample, it is possible that the slight slowing of the high-frequency spectral diffusion is due to the increase of solvent exchange between water and cations.[59] Solvent exchange is a slower process than the quick orientational or librational motions so the more solvent exchange occurring the slower the overall CLS will be. Given the likelihood that both the Bmim and water are interacting with DCA molecules and the increase in available water there most likely a resulting increase in solvent exchange events contributing to spectral diffusion.

For high-range water mixtures there are substantial water-water interactions, and it is likely that there may be clustering of waters near the DCA anions. Work by Jagoda-Cwiklik *et al.*[122] used DFT to show that it is more energetically favorable for water to clump on one side of a DCA anion rather than bind at different nitrogen atoms. Work by Jeon *et al.*[26] also suggests that water may act as a bridge between cations and anions in RTIL mixtures. This idea is also supported by research by Moreno *et al.*[123] who used molecular dynamics (MD) simulations of $BmimBF_4$ and water mixtures to show that with increasing water the ionic network is swollen in a nonspecific way by the appearance of water clusters.[123] Thus, in the high-water range DCA is likely experiencing a wide array of interactions with different shapes and sizes of clusters. The dramatic slowing of long-time timescales of the high-frequency CLS in these high-water samples may be due to long-lived lifetimes of rigid, water-induced local cage structures around the anion. This local cage picture is based on work by Brinzer *et al.*[64] who attributed the slow timescale of CO_2 spectral diffusion in an RTIL mixture to structural relaxation of the solvent due to the breakup of local ion shells. They note that prior to the cage breaking up, the vibrational probe is stuck in a relatively well-ordered local environment, though the immediate solvent shell can undergo librational and other fast motions. These

fast motions only sample a tight range of instantaneous frequencies, but variation in instantaneous frequency between different local environments can give rise to a large inhomogeneous linewidth.[64] Thus, we suggest that the higher frequency populations of DCA (likely those associated with an array of water clusters) experience slow spectral diffusion because the solvent cages created near water pockets become more difficult to break out of. Conversely those DCA at lower frequencies (likely not associated with water) can more quickly undergo local solvent exchange, hydrogen-bond making, and quick orientational and librational motion, leading to faster spectral diffusion.

Figure 4-15 is a scheme representing solvent interactions and motions that may be contributing to spectral diffusion in these three water content regions, low, mid, and high. In the low-content scenario we indicate the presence of orientational and librational motions in addition to hydrogen making and breaking. In the mid-water content scenario, we indicate interactions between DCA and water, and the additional process of solvent exchange between cations and water. In the high-water content scenario, we introduce larger groupings of water molecules near or interacting with DCA which introduces additional slower local cage dynamics, and consequently results in very slow exchange between distinct DCA populations.

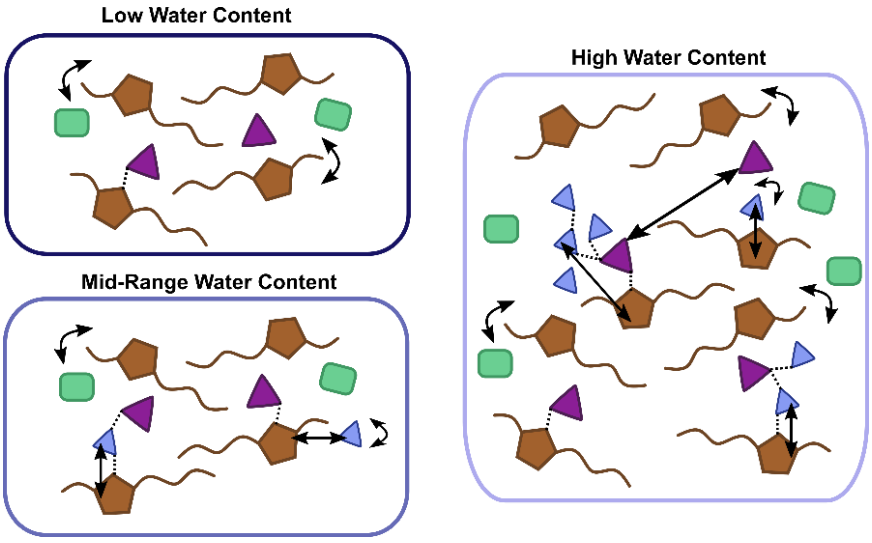

Figure 4-15 Schemes representing possible examples of molecular level interactions and motions in low, mid, and high water content samples. The brown pentagon shapes represent Bmim. The green rectangles represent BF_4. The purple triangles represent DCA and the blue triangles water. Bent arrows represent select examples of where fast orientational, or librational motions may impact DCA spectral diffusion. Dashed lines represent select examples of where hydrogen-bond making or breaking might impact DCA spectral diffusion. Straight arrows represent examples of possible solvent exchange that may impact DCA spectral diffusion.

4.5 Conclusion and Outlook

The impact of small amounts of water (between ~1.32 [environmental] and 21.6% mole fraction water) on the structure and dynamics of BmimBF4 with BmimDCA mixtures have been characterized using a combination of primarily linear and 2D IR spectroscopy with additional information gained from viscosity measurements and DFT calculations.

The wide diversity of local solvent environments was reported on by tracking three vibrational modes of the dicyanamide anion. Frequency dependent CLS analysis showed clear differences in the dynamics of different populations of DCA at low, mid, and high-range water concentrations. Higher amounts of water led to the formation of rigid local cage behavior that dramatically slowed spectral diffusion for water-associated DCA. Analysis of isotropic signal decay showed vibrational relaxation is accelerated with increasing water content for water-associated populations of DCA, indicating water facilities energy relaxation, possibly through the provision of additional bath modes. Macroscopic drops in viscosity suggest that overall molecular interactions are weakening overall, and as water disrupts interactions between the cations and anions of the RTIL mixture.

Ultimately, this work has provided further insight into the dramatic role water can play in altering the behavior of RTIL mixtures. Small amounts of water add to the heterogeneity of RTIL solutions by creating local environments with distinct structures and consequently unique dynamics. Future extended $T_{Waiting}$ experiments could provide more clarity on how static these caged DCA molecules are and provide better estimates of long time orientational dynamics which extend substantially beyond the timescales studied here. In addition, molecular dynamics simulations of this system would provide confirmation of the proposed molecular level picture. Work using 2D IR Microscopy to investigate how water RTIL mixtures behave under an applied potential and at an electrode interface is underway to help further connect how these diverse local environments might be exploited to provide benefits in applications like electrochemical cells. Initial findings can be found in previously published work.[29]

CHAPTER 5

Practical Aspects of 2D Infrared Microscopy[3]

5.1 Summary

The desire to investigate the chemical and structural dynamics of spatially heterogenous samples spurred the development of coherent multidimensional microscopy techniques. The effective implementation of these techniques requires tackling an array of technical obstacles. Herein we discuss the implications of 2D IR microscopy and approaches to overcome obstacles in collecting 2D IR images. Practical elements we address include repetition rate, pulse shaping, noise reduction methods, microscope design considerations, and detection limitations. Furthermore, we demonstrate avenues of analysis in 2D IR microscopy by showcasing images of two different room temperature ionic liquid samples. First, we show analysis of an ionic liquid microdroplet. Second, we show the impact of copper electrodes and an applied potential on an ionic liquid electrolyte. The analysis techniques we use include spatially tracking center line slopes, signal intensities, and cross-peaks ratios.

5.2 Introduction

Measurement scientists continuously push to develop instrumentation to directly probe and visualize chemical structures and dynamics across multiple length scales and time scales with an eye toward marrying molecular level details to micro- or mesoscale processes. Coherent multidimensional spectroscopy techniques including two-dimensional electronic spectroscopy (2D ES), two-dimensional infrared (2D IR) spectroscopy, and the emerging two-dimensional vibrational electronic (2D VE) spectroscopy technique have been shown to be powerful tools for directly measuring dynamic processes occurring on molecular

[3] Reprinted with permission from {Tibbetts, C. A.; Wyatt, A. B.; Luther, B. M.; Krummel, A. T. Practical Aspects of 2D IR Microscopy. In *Emerging Trends in Chemical Applications of Lasers*; ACS Books; American Chemical Society, 2021} Copyright {2021} American Chemical Society. In addition, the authors are grateful for the generous funding that has supported the instrument development efforts from the U.S. Department of Energy, Office of Science, Basic Energy Sciences, Chemical Sciences, Geosciences and Biosciences under the DOE Early Career, Award No. DE-SC0016137. In addition, the authors are grateful for the generous funding from the Monfort Excellence Fund at CSU and the Air Force Office of Scientific Research, Molecular Dynamics and Theoretical Chemistry Program to support investigations of RTIL dynamics near interfaces, Award No. FA9550-20-1-0401.

time scales. For example, molecular vibrations occur on the order of tens of femtoseconds and thus can be considered a molecular time scale. Furthermore, molecular vibrations can be report molecular structure and can be sensitive to their local environments. Similarly, electronic and vibronic transitions in a molecular system can report molecular level structures and time scales for energy transfer processes, charge transport, and structural rearrangements. Hence, coherent multidimensional spectroscopy measurements noted above are used to quantitatively tease apart contributions to spectral signatures from large structural rearrangements, reorganization of local solvent structures, and energy transfer events taking place throughout many different types of relaxation processes. However, we exist in a world of systems that are a larger network of interactions and as such, it is important to produce an understanding of how quantitative molecular level details drive micro- to mesoscale outcomes. Moving to imaging modalities based on spatially resolving spectral signatures observed in coherent multidimensional spectroscopy measurements is one avenue that holds the promise of connecting molecular level details to micro- and mesoscale processes in a quantitative manner.

Recently, investigators have imaged biological and materials systems with spatially resolved 2D ES,[124,125] 2D white light spectroscopy,[126] and 2D IR spectroscopy.[127–129] Although, there have been relatively few investigations utilizing these new imaging techniques, it is already clear that these approaches are particularly useful for observing the length scales over which heterogeneity in the system of interest may drive micro- to mesoscopic outcomes. For example, in work by Ogilvie and coworkers, using spatially resolved fluorescence detected 2D ES, they were able to uncover changes in exciton structure of photosynthetic bacteria which were dependent upon the growth conditions presented to a mixture of photosynthetic bacteria.[124] Recent work by Zanni and coworkers demonstrated the utility of spatially resolved 2D white light spectroscopy to link variation in sample morphology of an organic semiconductor, TIPS-pentacene, to observed changes in energy transfer pathways in the system.[126] In the work presented herein, we will focus on the practical aspects associated with utilizing 2D IR imaging to investigate chemistry across multiple length scales.

2D IR spectroscopy provides access to investigating vibrational dynamics quantitatively across timescales ranging from femtoseconds to nanoseconds.[130] The femtosecond time resolution is achieved using ultrashort mid-IR pulses and access to vibrational dynamics on the nanosecond timescale depends on the vibrational lifetime of the oscillator. In addition, 2D IR experiments can be used to discern the homogeneous contributions from the inhomogeneous contributions to observed linewidths in 2D IR spectra. Taken together the vibrational dynamics probed during a 2D IR spectroscopy experiment provide quantitative details of chemical dynamics in condensed phase systems including the evolution of chemical structures, the reorganization of solvent structures, and the dynamic exchange which may occur between chemical species in a mixture. The quantitative details observed in 2D IR experiments have generated important advancements made in understanding the role of hydrogen bonding in proton transfer events,[131] the dynamics involved with crossing over from liquid to glassy regimes in molecular glasses,[130,132] and the role of multipole interactions in ionic liquids to name a few.[133–135] The ability to better understand the dynamics of chemical systems is a key strength of 2D IR spectroscopy. The wealth of information available in a 2D IR spectrum or a time-dependent 2D IR dataset makes the potential quite high for 2D IR microscopy approaches to connect molecular level details to mesoscale processes and thus provide new avenues for discovery. Systems that may be susceptible to long range interactions or may be heterogeneous over multiple length scales will be important targets for imaging modalities such as 2D IR microscopy. For example, systems like polymeric mixtures or mixtures of ionic liquids that undergo phase segregations, phase separations, or phase transitions, including the transition to glass-like regimes, will be important to interrogate using 2D IR microscopy because it is highly likely that molecular level details will play an important role in driving the phase behaviors of these systems at micro- to mesoscopic length scales. In this chapter we will focus on describing several dynamic observables available from 2D IR microscopy measurements of an ionic liquid electrolyte in two different geometries—a microdroplet and a copper electrochemical cell.

Room temperature ionic liquids (RTILs) have received much attention due to the vast number of applications they can be used in such as catalysis, green solvents, extraction agents, lubrication, and as

electrolyte solutions in fuel cell technology.[136–140] They are low melting salts with unique properties such as having a wide electrochemical window, an extremely low vapor pressure, and structural microheterogeneity.[141–143] These properties make RTILs strong candidates for a wide variety of applications from biotechnology[144] to energy technology,[145–147] including as reaction media.[148,149] Many different approaches to investigating structure-function relationships in ILs have been utilized including many different types of spectroscopy techniques, imaging techniques, along with a host of theoretical techniques including electronic structure and molecular dynamics simulations.[133,150–153,153–157] On the one hand, these experimental and computational investigations have certainly produced a vast literature and deep understanding of ILs. On the other hand, interesting phenomena have been observed which reveal the oddities of ILs, especially with regards to the IL behavior in the presence of an interface.

Although RTILs can be tailored to specific purposes due to the ease of interchanging the counter ions involved, this is done in large part using empirical evidence, rather than having the ability to predict the behavior of RTILs. Therefore, it is crucial to gain insights into the fundamental aspects of interactions within RTILs including structural dynamics, solute-solvent interactions, and solvation dynamics. Recently, investigators have turned to nonlinear optical spectroscopy techniques including sum frequency generation spectroscopy[158] and two-dimensional infrared (2D IR) spectroscopy[150,151,159–162] to characterize RTILs at interfaces and measure the dynamics that occur in bulk RTIL environments, respectively. In order to advance the utility of RTILs in microdroplet chemistry and electrochemistry, the length scales over which various dynamical behaviors exist are important.[160,163–167] Recently we have begun to interrogate RTIL electrolytes near fluid interfaces such as silicon oil and near electrode surfaces including platinum, gold, and copper electrodes using 2D IR microscopy. In our efforts to push the utility of 2D IR microscopy forward, we have overcome technical challenges which might otherwise prevent the adoption of 2D IR microscopy by a broader community of researchers. In this chapter we present the implementation of solutions to technical challenges faced in 2D IR microscopy experiments and further showcase the utility of using 2D IR microscopy to observe dynamics behaviors in RTIL electrolytes across multiple length scales.

5.3 Technical Aspects of 2D IR Microscopy

5.3.1 Molecular Information Acquired from 2D IR Spectroscopy

2D IR is a four wave mixing process dependent on the interaction of three electric fields in time and space to generate a fourth signal field.[21] Figure 5-1 shows the possible interactions of the pulse sequence with an anharmonic vibrational mode, and the resulting 2D spectrum. Similar to linear IR spectroscopy, 2D IR spectra give information about the frequency, lifetime, and intensity of vibrational modes present in a sample. However, because 2D IR is an ultrafast time-resolved spectroscopy that acts as a frequency-

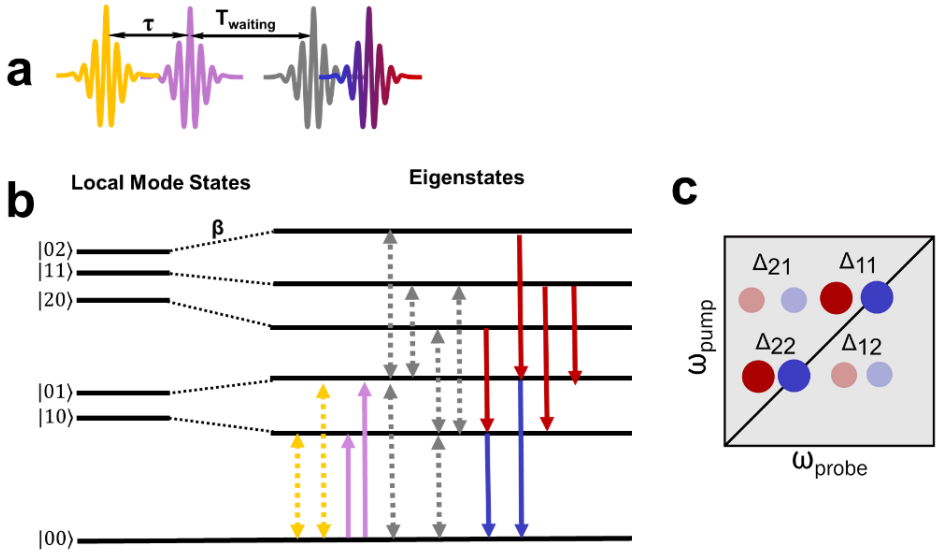

frequency correlation plot, additional information about a sample's chemical dynamics can be elucidated. Specifically, valuable information about spectral diffusion, vibrational coupling, and chemical exchange can be gained.

Figure 5-1 a) Pulse sequence for a 2D experiment with two pump pulses separated by time τ followed by the probe after $T_{Waiting}$, followed by emission of the 2D signal. b) Simplified energy diagram relevant to 2D IR of two coupled oscillators. The gold dashed line as the result of the first pump pulse creating a coherence between the ground and first excited eigenstates. The two solid purple lines resulting from the second pump pulse driving population states, the six gray dashed arrows representing a coherence between |00⟩ and both the |01⟩ and |01⟩ , the |10⟩ and |20⟩ or |11⟩ , and the |01⟩ and |02⟩ or |11⟩ states generated by the probe, and the solid red and blue lines as emission of the 2D signal. c) Representative purely absorptive 2D IR spectrum with on-diagonal red peaks corresponding to excited state absorption, and blue to ground state bleach and stimulated emission. The off-diagonal peaks are cross-peaks from the coupled states.

The power of being able to track each of these observables is amplified in spatially heterogenous systems. Thus, with advent of 2D IR microscopy investigators have a new suite of experimental handles to resolve spatial differences in an array of samples. Below, we outline the practical considerations involved in fast

collection of 2D IR spectroscopy and microscopy. We will then demonstrate 100 kHz 2D IR microscopy on a two RTIL samples to showcase the potential avenues of data analysis.

5.3.2 2D IR Experimental Details

The typical pulse sequence used for 2D experiments is shown in Figure 5-1a. Three ultrafast pulses are incident on the sample. The first two pulses are used to pump the system with a delay τ between them and the third pulse probes at a waiting time delay T_W. In a pump-probe optical geometry the probe beam is sent to a spectrometer where the signal and colinear probe are collected in a self-heterodyning manner. Scanning the delay τ between pump pulses for a specific T_W generates effective pump amplitudes that oscillate with τ for each frequency present in the pump pulse allowing a pump axis to be generated by Fourier transform along the τ axis.

Interactions between the three pulses can generate signals other than the desired 2D signal. These interactions can be removed along with transient absorption and scattering with the use of phase cycling.[168] Phase cycling involves rotating the relative carrier envelope phase of the pump pulses. Phase cycling can be done with 2, 4, or 8 phase cycles preformed for each pump delay. While 2 and 4 phase cycles are useful for eliminating transient absorption and some scattering, 8-frame phase cycling, which involves chopping the probe beam, leads to dramatic reduction of scattering and removal of interactions between the scanned pump and stationary probe pulses.[127,169] For all 2D experiments the stability of the laser system is crucial as small changes in the signal are being detected. It is particularly important that the stability of the laser is high over the collection time of a single free induction decay.

5.3.3 Implementation of 100 kHz Data Collection

The generation of the pump axis by Fourier transform of pump delays necessitates many pump delays to be generated. For example, a 6 ps collection time is necessary for generating a 2.78 cm^{-1} resolution pump axis (assuming 1 to 1 zero padding). With a 10 fs step size that is 600 time delays, with total shots equal to the number of time delays times the number of phase cycles. For 4 and 8-frame phase cycle data this

results in 2400 and 4800 shots respectively for an individual 2D IR spectrum. When averaging and collection of multiple spatial locations is considered, the laser repetition rate becomes important for collecting an image in a reasonable time, and the transition from 1kHz systems to 100 kHz systems becomes relevant.

Non-linear spectroscopy at 100 kHz has gained significant attention not only due to decreased collection time but also because of increased signal to noise. In 2014 Kanal *et al.* demonstrated improved signal to noise transient absorption spectroscopy at 100 kHz.[170] Similar results were seen for 2D IR spectroscopy in 2016 by the Krummel group at Colorado State University followed in 2017 by the Donaldson group at Rutherford Appleton Laboratory, and in 2D electronic spectroscopy by the Zanni group at the University of Wisconsin, Madison in 2017.[171–173] While some speculated that 100 kHz 2D spectroscopy would suffer from loss in signal and thermal effects recent demonstrations show just the opposite. Work done by the Krummel group showed that pulse energies necessary for 100 kHz 2D IR could be reduced to 40 nJ and that a single 2D IR spectrum could be collected in ~7 ms without using any undersampling methods or utilizing a rotating frame to lower the number of time delays required in the experiments.[171] This has allowed the Krummel group to collect data sets in multiple locations in microfluidic samples and to preform 2D IR microscopy on ionic liquids.[174] Work done by the Donaldson group demonstrated increased signal to noise allowing 2D IR spectra to be collected on weak samples including ~50 μM Amide I groups as well as showing that thermal effects resulted in less than a one degree change in sample temperature.[172] Work done by the Zanni group, using continuum generation, showed that 100 kHz data collection actually decreased the collection time by a factor of 200, instead of the predicted 100, due the increase in signal to noise in their experiment.[173] These results are due to the improved data collection rate and to the longer pulse energy correlation time in Yb systems compared to Ti:sapphire. These advantages shown in the above papers depend on collecting each laser shot at 100 kHz and being able to phase cycle (shape pulse pairs) on a shot-to-shot basis. We will discuss these next.

5.3.4 100 kHz Pulse Shaping and Detection

Shaping in the mid-IR has been demonstrated at 100 kHz using Ge based acousto-optic modulators (AOMs).[171,172] With a speed of sound of over 5400 m/s in Ge, a commercially available ~ 60 mm aperture can be used at 100 kHz (transit time ~ 10 μs). Increasing the repetition rate necessitates shorter Ge crystals and comes at a cost of reduced bandwidth for the pulses and decreased pump resolution due to loss of frequency resolution in the pulse shaper shown below. A general layout for a pulse shaper is shown in Figure 5-2a.[175] The shaper has a 4f geometry where the first grating sits one focal length (f) away from the focusing optic and the mask sits one focal length after the focusing optic. This places the acousto-optic mask (AOM) in the Fourier plane where the spectral features are separated and can be manipulated in phase and amplitude. A second lens and grating recombine the spectral features generating the pulse pairs with the desired delay. The pump axis of the 2D spectrum is generated by Fourier transforming multiple pump delay spectra. Important features of the pulse shaper resolution are shown in Figure 5-2b, which include the smallest spectral feature attainable, δf, that is inversely related to the maximum temporal window T. The maximum temporal window is gaussian in shape and determines the maximum delay between pump pulses achievable as the delayed pulse amplitude will decay as the delay increases. The temporal window therefore defines the pump delays available and the maximum pump delay in turn determines the frequency resolution of the 2D spectrum's pump dimension (with the frequency axis resolution equal to the reciprocal of the maximum time delay). To summarize, the frequency resolution of the shaper will depend on the grating dispersion and the size of the AOM used, i.e. increasing dispersion will increase frequency resolution but at the cost of increased AOM size. Filling of the AOM aperture is necessary for maximum resolution. It should be noted that the frequency resolution in the Fourier plane also depends on the number of grating lines illuminated and therefore improves as the size of the input beam increases.

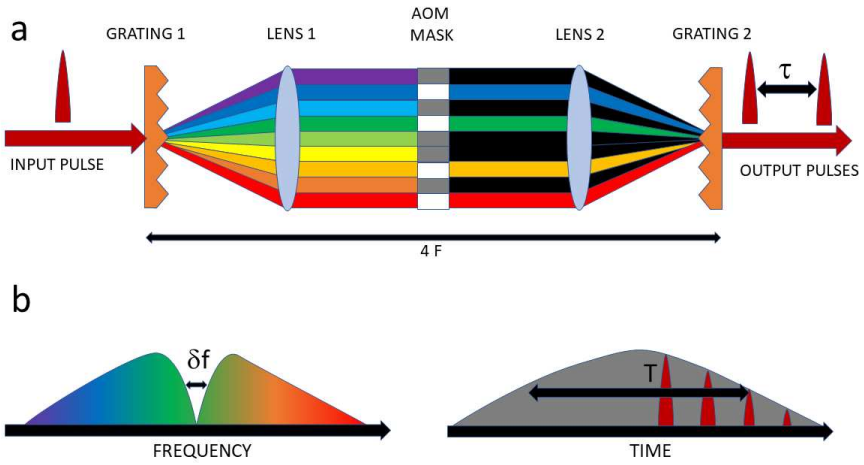

Figure 5-2 a) General pulse shaper layout consisting of two grating separated by 4f, two lenses separated by 2f, and a mask in the Fourier plane. b) On the left the smallest spectral feature δf is shown which is related to the maximum temporal window T shown on the right. As δf decreases, T increases allowing for higher resolution on the 2D pump axis.

The effects of shaper resolution are shown for our shaper (Phasetech Quickshape) with 150 ln/mm and 300 ln/mm gratings in Figure 3.

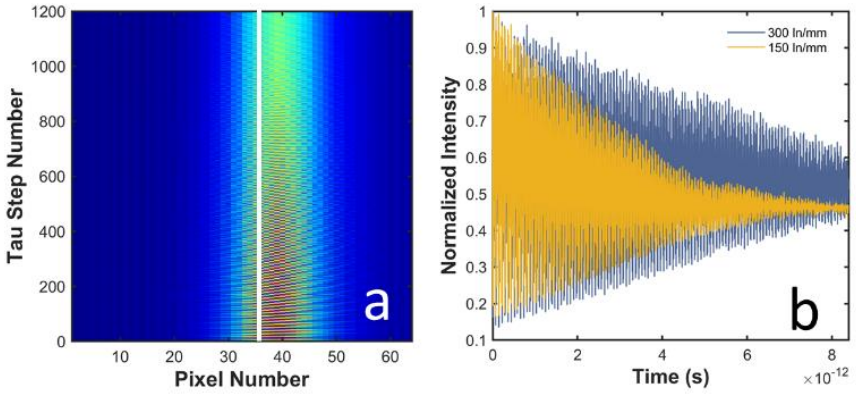

Figure 5-3 a) Example spectra collected as a function of pump delay τ for pulse pairs generated from our pulse shaper on a 64 channel MCT. b) Line out of pixel 35 showing the decay of the pump pulse pair intensity with delay τ. Increasing the grating ln/mm form 150 ln/mm (yellow) to 300 ln/mm decreases δf by a factor of two and increases T by a factor of two. Increasing T allows more pump delays to be collected, increasing the pump axis resolution of the 2D IR spectrum.

Figure 5-3a shows the pump pulse pair spectra with increasing pump delay τ on the Y axis and the MCT pixel on the X axis. A line out at pixel 35 (white line in Figure 5-3a) is shown in Figure 5-3b for the pulse shaper with 150 ln/mm and 300 ln/mm gratings. Changing from 150 ln/mm to 300 ln/mm gratings in the

shaper results in a doubling of the dispersion and halving of δf in the Fourier plane of the shaper. This can be seen in the amplitudes as a function of delay for the pump pulse pairs shown in Figure 5-3b. The half-width half-max HWHM decay time for the delayed pulse changes from 1.7 ps to 3.4 ps going from the 150 ln/mm grating to the 300 ln/mm grating. The doubling of T for the shaper allows us to increase the maximum pump delay from 3 ps to 6 ps and since the delta frequency of the pump axis goes as the reciprocal of the maximum pump delay, the delta frequency is halved (from 5.55 cm^{-1} to 2.78 cm^{-1}). Pump resolution is important for resolving features and increasing the number of pump slices available for center line slope analysis. It is also important since the pump pulse pair envelope will be convolved into the line shape of the 2D spectrum. This is shown in Figure 5-4b where the pump pulse pairs have been Fourier transformed for both 150 ln/mm, τ_{max} = 3 ps collections and 300 ln/mm τ_{max} = 6 ps setups shown in Figure 4a. The resulting Fourier transform will be convolved with the 2D line shape (Figure 5-4c), which for gaussians goes as the square root of the sum of the squares (Equation 1). The resulting 2D linewidths are shown in Figure 5-4d.

It is important to remember that even though the frequency axis resolution generated from the maximum pump delay can be on the order of 2 cm^{-1} or better, the convolving factor is likely larger. Figure 5-5 shows results from modelling pump energy decays based on our experimental 1.7 ps (yellow curve) and 3.4 ps (blue curve) HWHM decays; as well as a square wave (no decay of the second pump pulse, blue curve) that would be generated if a delay line was used instead of a pulse shaper. It can be seen that even with the square wave going out 10 ps the convolving factor is on the order of 4 cm^{-1}. The orange and black stars show the experimental FWHM's of the convolving factors for the 1.7 ps and 3.4 ps HWHM decays shown in Figure 5-4a, for 3 and 6 ps collection windows. This results in instrument resolutions of 13.9 and 7.0 cm-1 for the 3 and 6 ps windows respectively. Going to a collection window of 10 ps would allow us to achieve 5.5 cm-1 resolution at the potential cost of decreased signal to noise and increased collection time (Figure 5-5).

The convolving factors are similar to those in a double resonance 2D IR experiments where an etalon generating the pump leads to the convolution of the Lorentzian decay with the third order signal causing broadening along the pump axis or to applying apodization functions to free induction decays).[73,176,177] Though it has been shown by Kwak *et al.* and Guo *et al.* that apodization has a minimal impact on CLS analysis, it does impact other methods of approximating the frequency-frequency correlation function such as ellipticity.[177] Moreover, the loss of resolution could cause issues when there are two oscillators with different dynamics that are not resolved.[178]

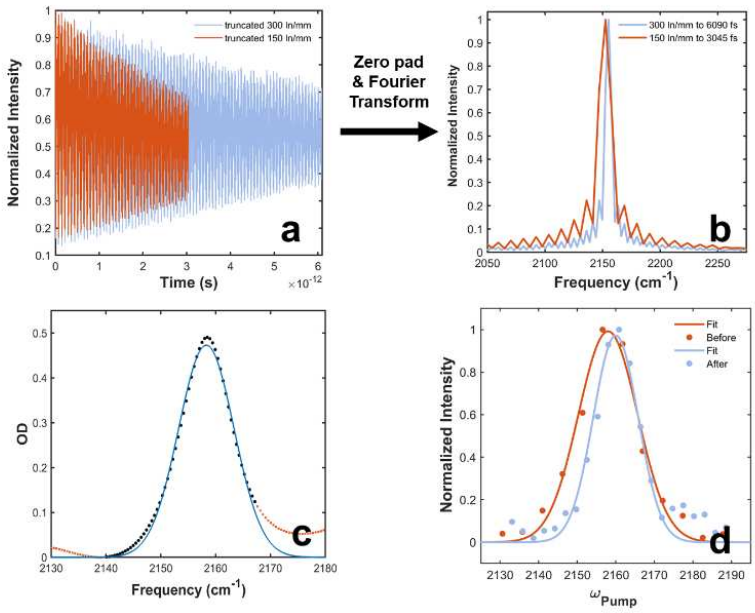

Figure 5-4 a) Line out of pixel 35 showing the decay of the pump pulse pair intensity with delay τ for a 3 ps (150 ln/mm, red curve) and 6 ps (300 ln/mm, blue curve). b) Zero padded Fourier transforms of a). c) In blue, a gaussian fit to the linear FTIR, black dots, of the C≡N stretch of methyl thiocyanate in fluoroethylene carbonate. d) 2D IR linewidths resulting from the 3 ps delay (red) and 6 ps delay (blue) collections of the same chemical sample as in c.

$$FWHM_{measured} = \sqrt{(FWHM_{pump\ envelope})^2 + (FWHM_{2D\ signal})^2} \qquad 5\text{-}1$$

In conclusion, the practical aspects of pulse shaping are determined by the characteristics of the shaper (grating dispersion and AOM aperture) and the bandwidth of the pump laser. Increasing the AOM aperture will allow longer pulse delays, both increasing pump resolution and decreasing convolution broadening but at the expense of the shaper repetition rate. Increasing grating dispersion has the same advantages but is

limited by the laser bandwidth and AOM aperture size. While 100 kHz shaping has been achieved, moving forward to higher repetition rates will require new advancements in shaper technology or reduction in available bandwidths.

Collection of the 2D IR signal is done with mercury-cadmium- telluride (MCT) linear arrays. Use of a 100 ln/mm grating and a standard 64 elements MCT array results in 3.2 cm^{-1} resolution along the probe axis centered at 4.65 µm. While this is better than the pump resolution (with 6 ps delay window = 2.78 cm^{-1} FFT resolution and 7 cm^{-1} instrument resolution) it can be further improved with a 300 ln/mm grating to 1.6 cm^{-1}. Commercially available detectors at 100 kHz can be equipped with 128-pixel arrays allowing for larger bandwidths or greater resolution. While these systems are commercially available it should be noted that photoconductive MCT response times are approximately 10 µs limiting collection rates to 100 kHz. Collection rates can be improved by adjusting the bandwidth of the MCT array, but this is a critical limitation on the current commercially available detection systems. The future will depend on the development of commercialized high speed photovoltaic MCT arrays that will allow collection rates to more than double.

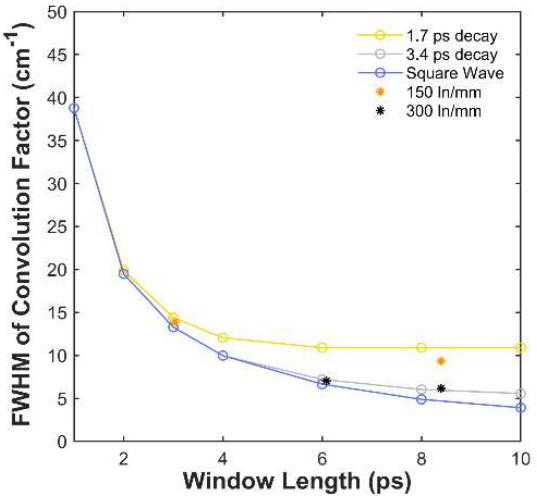

Figure 5-5 Window length refers to the final tau delay between two pump pulses. FWHM of the convolution factor is the FWHM of the FFT of a specific pump intensity decay. Open circles refer to modelled data. 1.7 and 3.4 ps decays refer to the HWHM of the modelled pump decay being Fourier transformed. Orange stars correspond to the FWHM of the FFT of the pump decay for the 150 ln/mm grating at two different window lengths. Black stars correspond to the FWHM of the FFT of the pump decay for the 300 ln/mm grating at two different window lengths.

5.3.5 Noise Reduction and Signal Normalization

While faster collection rates are important for 2D IR microscopy, collection times can also be reduced by improving signal to noise. It was already mentioned above that the use of 100 kHz Yb systems over 1 kHz Ti:sapphire systems resulted in improved signal to noise due to the longer pulse energy correlation time in Yb systems compared to Ti:sapphire. Noise reduction techniques have been developed that use the difference methods inherent in 2D and other nonlinear spectroscopies to reduce noise contributions.[179,180] These techniques work using a reference detector and determining the correlation of shot-to-shot differences between pixels on the reference detector and the signal detector. Recently these techniques have been demonstrated using edge pixels, which don't contain signal, to monitor fluctuations in the shot-to-shot data.[181] We have implemented noise reduction based on the covariance of pixels which do not carry 2D signal to reduce the effects of shot-to-shot laser fluctuations. This allows the noise reduction to be done in real time as the data is collected and improves the quality of the 2D data. Figure 5-6 shows a pump slice from a 2D spectrum collected on methyl thiocyanate in dimethyl carbonate, ethylene carbonate, and diethylene carbonate. The noise reduction was done using the probe pixel at 2087 cm^{-1}. There is a dramatic improvement which decreases as you move farther away from the reference pixel. When collecting data, we choose a reference pixel on either side of the 2D features to improve the noise reduction across the pump slice. Noise reduction has improved the signal to noise so that we may now watch a "live" 2D signal that updates in real time allowing us to tweak beam overlaps to maximize the 2D signal. While this leads to improvements in data collection, care must be taken to make sure there is no signal in the reference channels

and the improvement is largest near the reference channels. The use of an external reference detector would lead to even higher signal to noise improvements and decrease in collection times.

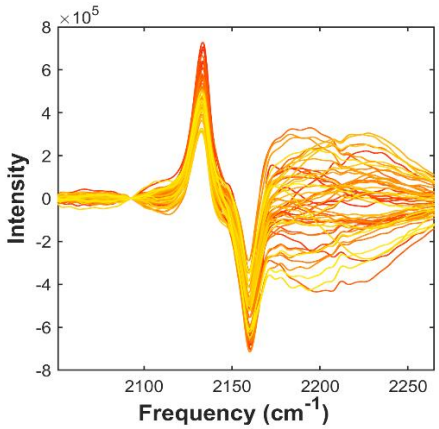

Figure 5-6 2D IR pump line out for methyl thiocyanate in dimethyl carbonate, ethylene carbonate and diethylene carbonate with noise reduction applied at 2087 cm^{-1}. Noise reduction improves the low frequency side near the reference pixel dramatically, but the benefit decreases as one moves away from the reference pixel.

It should also be noted that for colinear 2D geometries, 8-frame phase cycling can be important for removing scatter and improving signal to noise. This comes at the expense of doubling the number of pulses needed for a single 2D spectrum and at 100 kHz requires a chopper running at 50 kHz. With commercial choppers runnning only up to ~10 kHz this can be difficult to achieve and is best accomplished with a pulse shaper on the probe line as well. This has the added advantage of being able to compensate for any group velocity dispersion that the probe pulse may aquire before the sample.

Finally, the 2D signal is sensitive to changes in the long-term laser power. The magnitude of the 2D signal when self-heterodyned with the probe pulse will be linearly proportional to both the pump and probe laser intensity. When pump and probe intensities are equal the magnitude of the 2D signal will go as the laser power squared. This can be seen in Figure 5-7a where the blue dots show a long time decrease in the laser power monitored by the probe pulse on pixel 36 of the MCT array. The 2D intensity drops as well (blue dots) and the drop in the 2D signal intensity is matched by the drop in the probe power squared (orange dots). Normalizing the 2D data with the probe power squared results in a stable 2D intensity shown by the grey dots in Figure 5-7a. In Figure 5-7b the blue dots again show the probe power measured at pixel 36, over

the course of a $T_{Waiting}$ experiment, and the square of the probe power represented by the orange dots. The resulting 2D signal intensity is shown before (blue dots) and after normalization (grey dots).

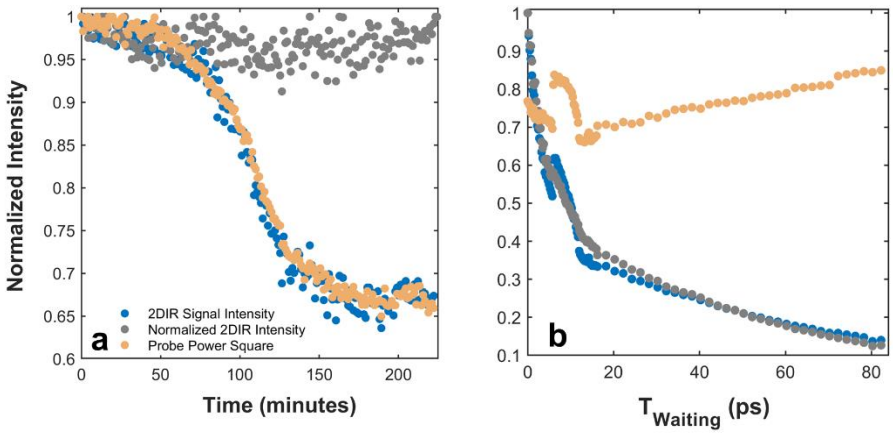

Figure 5-7 Normalization of 2D IR intensity is shown for long term drift in laser power. a) Orange dots show drift in probe intensity squared monitored at pixel 36 of the MCT array, while blue dots show the drift in the 2D IR signal intensity. Normalization of the 2D signal with the probe intensity squared yields the grey dots. All data collected at T_w equal to 0 ps. b) Blue dots show drift in probe intensity squared monitored at pixel 36 of the MCT array during a T_w collection. Orange dots show the probe intensity squared which is used to normalize the 2D intensities (blue dots) to give the grey dots.

5.3.6 Microscope Design

2D IR microscopes have been implemented in two forms shown in Figure 5-8. The first is a scanning microscope in which the microscope image is created by stepping the sample and colleting 2D spectra at each spatial location shown in Figure 5-8a and the second is wide-field microscopy where a large area is illuminated and imaged onto a MCT array, collecting multiple spatial locations simultaneously, shown in Figure 5-8b.[127,128] In both cases the use of short working distance objectives prevents spatial separation of the pump and probe lines and necessitates the use of a colinear and cross polarized geometry. Wire grid polarizers are used to combine the pump and probe lines and then separate them after the sample. Objectives are available in transmission and reflection geometries that provide diffraction limited performance. Reflective objectives preserve the temporal profile of the pulse but come with lower beam throughput. Transmission objectives offer greater throughput and ease of use but come with dispersion, which depending on pulse length may be important. For instance, a Si-Ge achromat with 3mm center thicknesses for each material will have a negligible effect on a 200 fs transform limited pulse at 5 µm but will double the length of a 50 fs pulse. Aspheric lenses made from ZnSe have low dispersion but suffer

from larger aberrations. Scanning microscopes report resolution on the order of 12 µm while a widefield microscope has been reported with a resolution of 3.5 µm.[127,128]

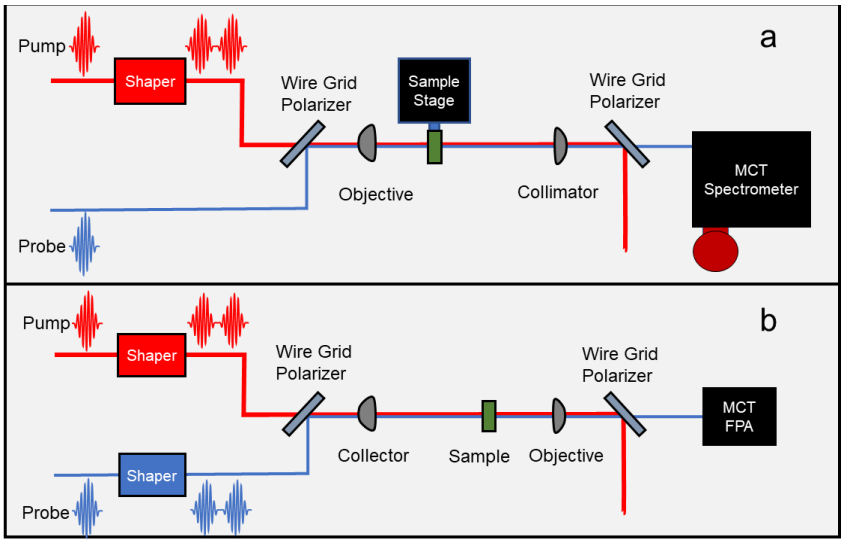

Figure 5-8: a) Setup for a scanning 2D IR microscope. A single pulse shaper is used to generate pulse pairs for the pump line and a spectrometer is used to collect the probe spectra. The sample is scanned using a stage and the image is generated point by point. b) Widefield 2D IR microscope utilizing 2 pulse shapers to generate pulse pairs in both the pump and probe beam lines. A larger area of the sample is illuminated and imaged onto a FPA allowing multiple spatial locations to be collected simultaneously.

Scanning microscopy has the advantage of utilizing a traditional spectrometer to collect the entire probe spectrum on a shot-to-shot basis, while wide field microscopy collects the probe spectrum in the time domain by the addition of a time delayed local oscillator (LO) to the probe line. The need for a LO necessitates the addition of a pulse shaper to the probe line while eliminating the need for a spectrometer. Wide field experiments are currently limited to 1 kHz by the readout time of the focal point arrays (FPA). FPA's with 128 x 128 pixels are available allowing 16,384 spatial locations to be collected simultaneously. While wide field microscopes collect 16,384 points simultaneously, it comes at the expense of 100 times reduction in collection rate and the need to collect a full set of probe delays. The number of probe delays will depend on the desired probe resolution and if one wants to compare to a 64-element linear array spectrometer then 32 delays will be needed to create 64 steps in the frequency axis after zero padding. So, while the wide field microscope will collect 16,384 spatial points simultaneously it will do it at a repetition rate that is 3200 times slower. This will still result in a 5 times faster collection for the 16,384 points. The

five times faster collection does not take into account signal to noise or the convolving factor for the instrument resolution. Scanning microscope probe resolution can be increased by going to 128-pixel MCT array at no cost in terms of collection time, with better than 2 cm^{-1} resolution. Matching that performance in the wide field convolving factor would require a 20 ps square wave delay from the probe pulse shaper, which might not be accessible with standard shaper resolutions (see discussion on δf and T above). The number of points needed in collecting those delays would increase and while rotating frame can be used to decrease the Nyquist frequency, reasonable steps or increased averaging would be necessary to maintain signal to noise. Scanning microscopes are hindered by the added time needed to move the sample, which can be quite significant depending on the stage, while widefield microscopes suffer from coherence effects and poor signal to noise from 1kHz data collection, which can be as great as 200 times worse.[173,182] As FPA's increase in size or speed the advantages of wide field microscopy rapidly increase. For samples that have smaller regions of interest or require high spectral resolution, scanning microscopes have an advantage.

5.4 Scanning 100kHz 2D IR Microscopy of Ionic Liquids

To showcase the different observables offered by 2D IR microscopy we present spatially resolved 2D IR data collected on two RTIL samples. First, we show 2D IR dynamics data collected on a microdroplet. Then we show the impact of introducing copper electrodes and an applied potential to a RTIL sample.

All 2D IR spectra are collected with a 100 kHz, mid-IR source. Briefly, a Yb fiber, all normal dispersion (ANDi) oscillator output is split and used to seed a cryogenically cooled Yb (cryo-Yb) amplifier as well as pump a 1675 nm optical parametric oscillator (OPO). The 1675 nm OPO output is then used as the seed for a magnesium doped, periodically poled, lithium niobate (PPLN) based optical parametric chirped-pulse amplifier (OPCPA) pumped by the cryo-Yb amplifiers at 1030 nm. The 1675 nm seed and 2670 nm idler are used for difference frequency generation (DFG) in zinc germanium phosphide (ZGP) at 4650 nm. More details on the system are found in previous work.[171] Figure 5-9 is a schematic outlining the 2D IR microscope. The microscope combines the pump and probe lines colinearly using a wire grid polarizer with the pump beam p-polarized and the probe s-polarized. Both beams are focused onto the

sample with a silicon-germanium achromatic lens. The samples are mounted in one- or two-inch lens mounts and magnetically attached to a 2-axis translation stage (Figure 5-9).

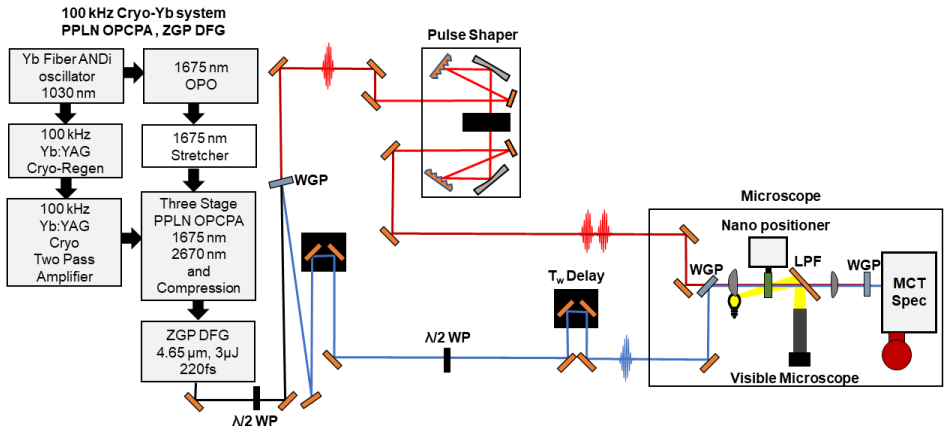

Figure 5-9 100 kHz 2D-IR microscope. The front end starts with a Yb- fiber ANDi oscillator which is split to seed a 100 kHz two stage cryo-Yb amplifier as well as pump a 1675 nm OPO. The OPO output seeds a PPLN OPCPA which is pumped by the 1030 nm output of the Yb amplifiers. DFG using ZGP results in 3 µJ at 4650 nm. The DFG output is split using a half wave plate (λ/2 WP) and wire grid polarizer (WGP). The pump line is sent to a pulse shaper to generate pulse pairs and the probe goes to a delay line. Pump and probe pulses are recombined with half wave plates and wire grid polarizers. A SiGe objective focuses the colinear beams to the sample which is controlled by a three-axis nano positioner. A long pass filter is used to divert light to a visible microscope while letting the mid-IR pass. The pump beam is removed with a WGP and the probe and signal beams are sent to a 100 kHz spectrometer with a MCT array.

During imaging, the stage is moved in X and Y with a nano positioner and two micro positioners (Nano-3D200 and MMP, Mad City Labs Inc.) For collection of all 2D spectra a series of 601 pulse pairs delayed from 0 to 6 ps in 10 fs steps were used. Hence, the spectral resolution along the pump axis, after zero-padding to 2N, is 2.78 cm^{-1}. In addition, spectra were collected using 4-frame phase cycling and a 1900 cm^{-1} rotating frame, and pulse energies of 30 nJ/pulse were used.

5.4.1 2D IR Microscopy of a RTIL Microdroplet

5.4.1.1 Sample Preparation

The samples used in the 2D IR and linear FTIR experiments were room temperature ionic liquid microdroplets surrounded by silicone oil. The drops were made from a solution of 1-butyl-3-methylimidazolium dicyanamide [Bmim DCA] in 1-butyl-3-methylimidazolium tetrafluoroborate [Bmim BF_4]. The asymmetric cyanate stretch of the [Bmim DCA] is used as the primary vibrational probe. The

[Bmim DCA] is doped at a ratio of 1:500 by volume into the [Bmim BF_4]. Corresponding to a mole percent of 0.09685. The dimethyl silicone oil was obtained from Thomas Scientific, SF96/50 and the [Bmim BF_4] and [Bmim DCA] from IoLiTec. The samples were placed between two 1 mm thick calcium fluoride (CaF_2) plates (Crystran) that were 25.4 mm in diameter. The sample path lengths were set to 15 µm using a Teflon spacer (Harrick).

5.4.1.2 Linear FTIR Microscopy

All FTIR measurements were made on a Bruker Optics Hyperion 3000. The spectral resolution was 2 cm^{-1} and 32 scans were averaged. The FTIR microscope utilizes a 64 x 64 element MCT FPA detector with 2.7 µm pixels and 0.4 numerical aperture (NA).

In Figure 5-10 we show the infrared spectrum, and the corresponding second derivative spectrum of the microdroplet in the region between 2050 – 2300 cm^{-1}. This spectrum highlights three distinct peaks due to the $[DCA]^-$ probe molecule monitored in this work. The most intense band is centered at 2133 cm^{-1} and corresponds to the asymmetric C≡N stretching mode. The two weaker modes at 2195 and 2235 cm^{-1} correspond to the symmetric C≡N stretch and the combination band of the C-N asymmetric and C-N symmetric stretch, respectively.[43,183] Figure 5-11 shows the imaged RTIL microdroplet with the intensity between 2122 and 2140 cm^{-1} integrated and plotted as an intensity map.

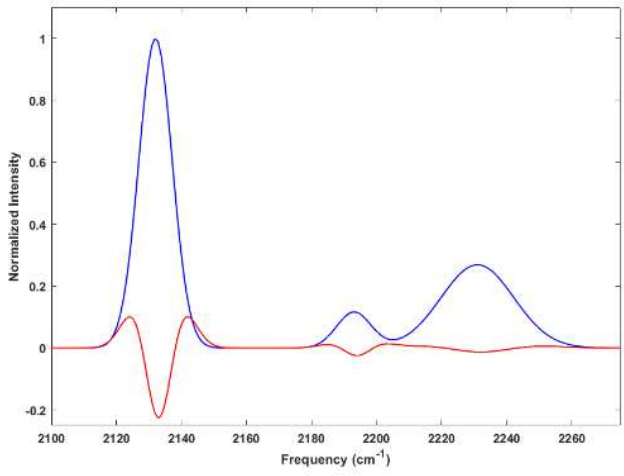

Figure 5-10 a) FTIR of bulk [Bmim DCA: Bmim BF_4](1:500 by volume) shown in blue, with background correction. The red line shows the corresponding second derivative spectrum.

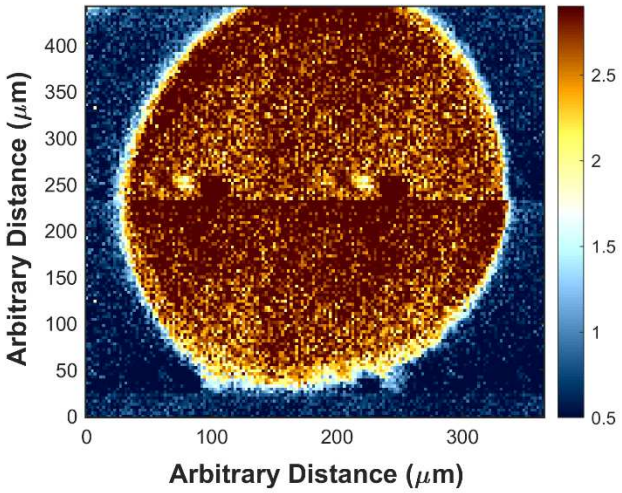

Figure 5-11 Chemical map of [Bmim DCA] in a [Bmim BF_4] droplet generated by integrating the intensity of the asymmetric C≡N stretch spectral feature observed in the FTIR spectra collected across the [Bmim DCA:Bmim BF_4] droplet.

5.4.1.3 2D IR Results

Dynamics data from in both the 2DIR microscope (collinear geometry) and the pump-probe geometry were collected for comparison and proof of replicability. In the collinear geometry the XXYY polarization scheme was used. In the pump-probe geometry both XXYY and XXXX polarization schemes were used. These bulk measurements of Bmim DCA in Bmim BF_4 are shown in Figure 5-12. The results show the expected overlap between the XXYY polarization scheme in both the collinear and pump-probe geometry. Center line slope curves were fit with biexponential decays to approximate the frequency-frequency correlation function (Equation 5-2), with the resulting time constants shown in Table 5-1.

$$\langle \delta\omega(T_{waiting})\delta\omega(0)\rangle \approx a_1 e^{\frac{T_{waiting}}{\tau_1}} + a_2 e^{\frac{T_{waiting}}{\tau_2}} \qquad 5\text{-}2$$

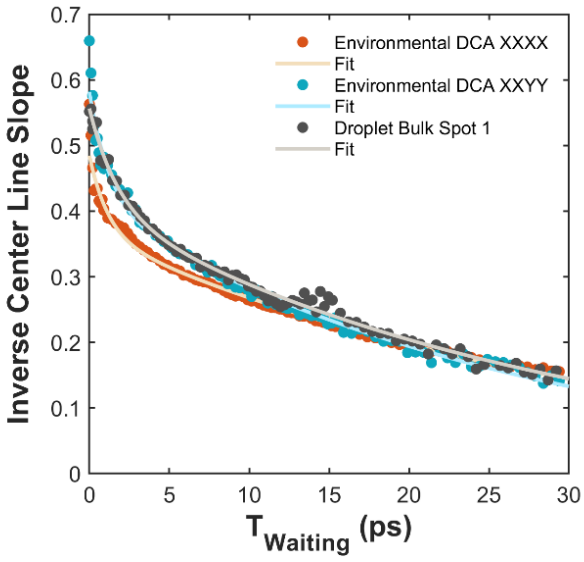

Figure 5-12 Comparison of CLS curves generated from measurements made on bulk Bmim DCA: Bmim BF4 samples in a cross polarized pump-probe geometry and the colinear geometry. Overlap of the blue and grey curves confirms the match between the data acquired in both experimental geometries.

Table 5-1 Time constants and amplitudes from biexponential fits to curves shown in Figure 12. Error bars correspond to 95% confidence interval of the fit for each variable.

	a_1	τ_1 (ps)	a_2	τ_2 (ps)
Pump Probe XXYY	0.17 ± 0.01	1.3 ± 0.87	0.41 ± 0.01	26.5 ± 1.2
Bulk Droplet XXYY	0.15 ± 0.01	1.8 ± 0.32	0.41 ± 0.01	29.8 ± 1.4
Pump Probe XXXX	0.12 ± 0.01	1.2 ± 0.21	0.37 ± 0.01	32.3 ± 1.1

The full 2D IR image of the [Bmim DCA:Bmim BF_4] droplet is shown in Figure 5-13 and is comprised of data fully averaged 300 times. The integrated intensity of the diagonal peak corresponding to the $\nu = 0 \rightarrow 1$ transition of the asymmetric C≡N stretch of the $[DCA]^-$ is shown overlaid as points on the brightfield image of the microdroplet in Figure 5-13b. To collect the image 25 µm steps were taken in X and Y. To explore chemical dynamics near the interface of the microdroplet a column was chosen as a region of interest (ROI), shown by the gold box in Figure 5-13b, in this region steps were then taken in 5 µm steps across the interface, with the corresponding integrated intensity of the same diagonal peak being shown in Figure

5-13c. For ten spots in the ROI, 2D IR spectra were collected as a function of waiting time ($T_{waiting}$). Data were collected in 100 fs steps for steps 0 – 500 fs, 250 fs for steps 500 – 15 ps and in 500 fs steps to 28 ps.

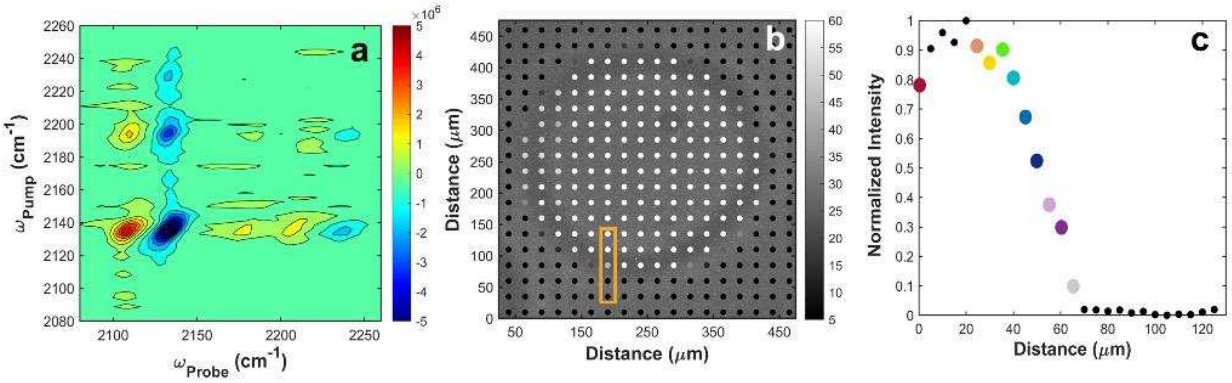

Figure 5-13 a) Representative 2D IR spectrum taken from the center of the RTIL microdroplet at $T_{Waiting}$ equal to zero. b) Shows the RTIL microdroplet brightfield image with the scaled integrated intensity of the 0-1 transition for the asymmetric C≡N stretch of the [DCA]$^-$ overlaid at points where the spectra were collected. The gold box corresponds to the area where data in (c) is collected across the interface. c) Colored dots correspond to spatial locations across the interface where full $T_{Waiting}$ experiments were performed to $T_{Waiting}$ =30 ps. The y-axis shows the self-normalized integrated intensity of the 0-1 transition for the asymmetric C≡N stretch of the [DCA]$^-$.

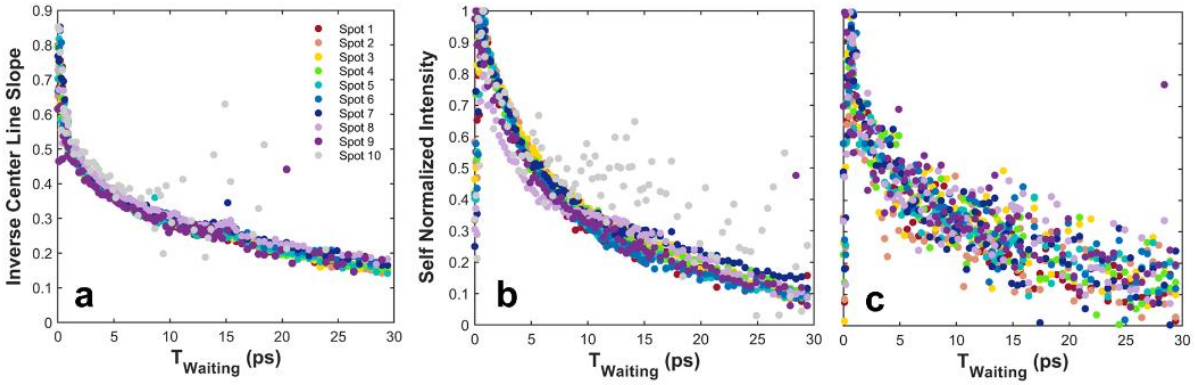

Figure 5-14 a) Center line slope analysis done on the 0-1 transition of the asymmetric C≡N stretch of the [DCA]$^-$ corresponding to the spots shown in Figure 13c. b) Shows the self-normalized integrated intensity of the 0-1 transition of the asymmetric C≡N as a function of space and $T_{Waiting}$. C) Shows the self-normalized integrated intensity of the negative cross peak between the asymmetric C≡N and the combination mode of the of the C-N asymmetric and C-N symmetric stretch. Integration was done for the cross peak centered at 2130 cm^{-1} on the pump axis, and 2220 cm^{-1} on the probe axis of the 2D IR spectrum shown in Figure 13a.

Figure 5-14a shows the resulting center line slope analysis for each of the ten spots from the bulk ionic liquid across the droplet interface. Negligible differences are observed spatially. Similar spatial homogeneity is shown in the results in Figure 5-14b and 14c where the intensity of the 0-1 peak for the asymmetric C≡N stretch of the [DCA]$^-$ and the negative cross peak between the asymmetric C≡N and the combination mode of the of the C-N asymmetric and C-N symmetric stretch, respectively. Despite the

homogenous nature of the RTIL microdroplet shown here, these observables can provide valuable insight in more spatially heterogeneous systems of interest.

5.4.2 2D IR Microscopy Monitoring the Oxidation of Copper Electrodes in [Bmim DCA:Bmim BF_4]

As illustrated with the image of a RTIL microdroplet there a multitude of avenues to extract valuable chemical structure and dynamics from 2D IR microscope images. Here we demonstrate a more spatially complex system of interest, an RTIL mixture as an electrolyte in a copper electrochemical cell. We observe the introduction of new chemical species as a function of space from an electrode and the resulting 2D IR spectral changes that are seen. Future work will expand on the dynamics and time dependent chemistry of this system.

5.4.2.1 Sample Preparation

The electrolyte used in the 2D IR and linear FTIR experiments are made from a solution of 1-butyl-3-methylimidazolium tetrafluoroborate [Bmim BF_4] and 1-butyl-3-methylimidazolium dicyanamide [Bmim DCA]. The [Bmim DCA] is doped at a ratio of 3:1250 by volume into the [Bmim BF_4]. The samples were placed between two 3 mm thick CaF_2 plates that are 50.8 mm diameter; the path length of the cell was set to ~35 μm by the copper electrodes used in this electrochemical cell. One third of the top CaF_2 plate was cut off using a diamond saw to expose the electrode for ease of connection to the potentiostat. The electrodes are copper tape. Figure 5-15 shows the electrochemical cell used; the cell is symmetric, with a floating reference on the counter electrode (CE). The sample holder used is a modified LMR2 optics holder (Thorlabs). For 2D IR and FTIR experiments run in conjunction with chronoamperometry a Gamry Instruments Interface 1010 E Potentiostat was used to hold a constant potential and measure the resulting current. A potential of -2.5V with respect to the CE electrode was held constant through the course of the measurements.

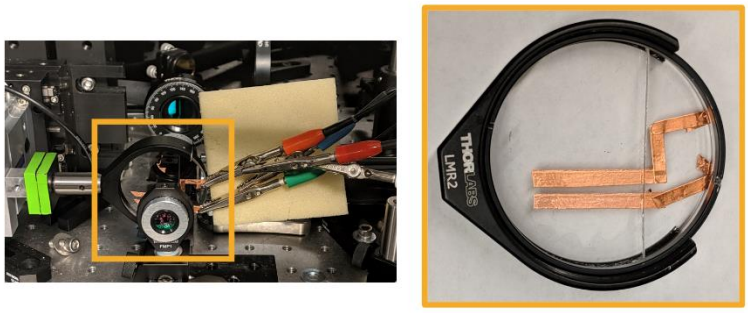

Figure 5-15 Image of 2D IR microscope setup, with inset showing the symmetric copper cell used for electrochemical experiments.

5.4.2.2 2D IR and FTIR Results

The presence of copper electrodes produced notable changes to the linear IR and 2D IR spectra of [Bmim DCA] in [Bmim BF_4]. A peak at 2156 cm^{-1} is prominent in Figure 5-16b and d and a peak at 2176 cm^{-1} is clearly present in Figure 5-18d. These new peaks exhibited in Figure 5-16d are observed at all spatial locations distributed between the electrodes.

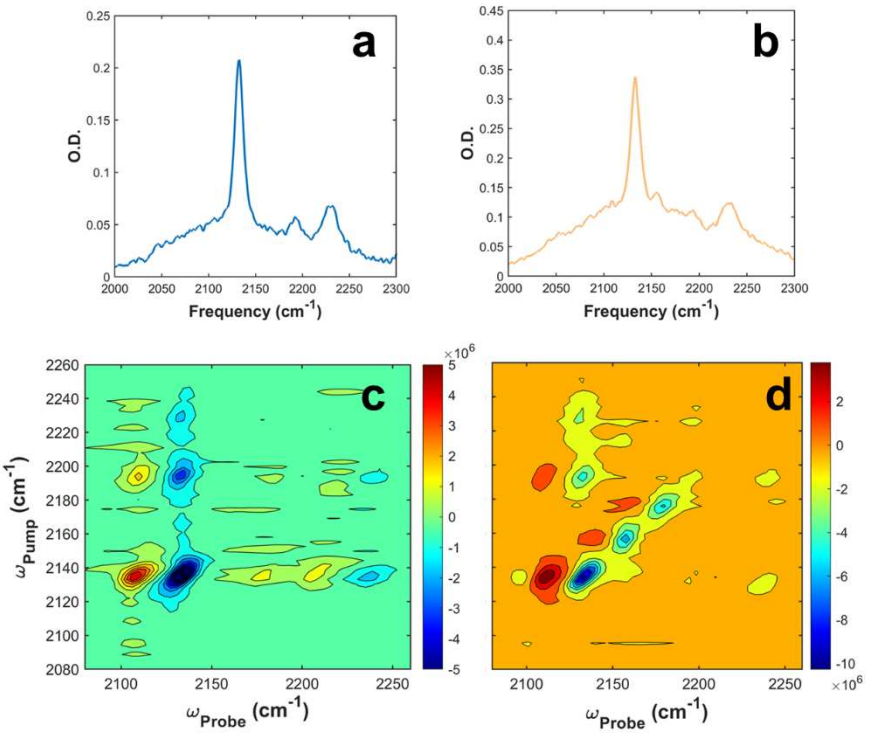

Figure 5-16 a) FTIR of bulk Bmim DCA in Bmim BF_4 b) FTIR of Bmim DCA in Bmim BF_4 between two copper electrodes with no applied potential present. c) 2D IR corresponding to the sample shown in (a). d) 2D IR spectrum corresponding to sample in (b).

To independently test the impact of copper introduced to the [Bmim DCA: Bmim BF_4] electrolyte, CuCl and $Cu(OAc)_2$ were independently added. With the addition of a Cu(I) salt into the bulk [Bmim DCA: Bmim BF_4] electrolyte new peaks appeared (Figure 5-17b), which correlate to those observed in the 2D IR spectrum of the [Bmim DCA: Bmim BF_4] electrolyte between two copper electrodes (Figure 5-16b and Figure 5-16d).

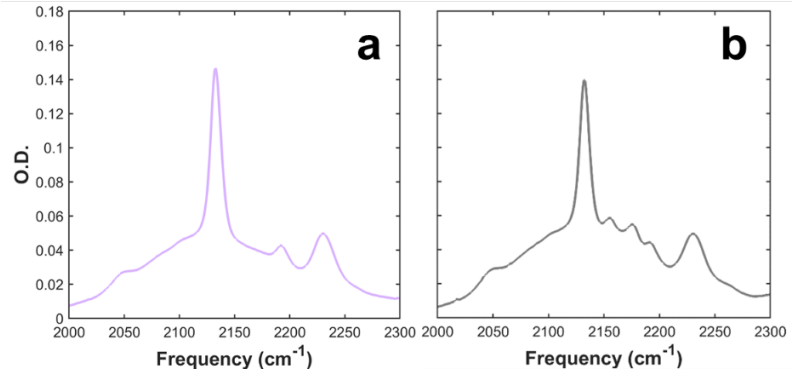

Figure 5-17 a) FTIR of bulk Bmim DCA in Bmim BF4 with Cu(OAc)2. b) FTIR of bulk Bmim DCA in BF4 with CuCl.

With the introduction of an applied potential to the electrochemical cell further changes in the 2D IR spectra are observed. In regions close to the working electrode (WE) spectra, as seen at 640 µm in Figure 5-18, the features correspond to those present with no applied potential (Figure 5-16b and d) which also correlate to those seen with $[DCA]^-$ in the presence of CuCl (Figure 17b). Near the counter electrode (CE), seen at 20 µm in Figure 5-18, the main $[DCA]^-$ peak at 2133 cm^{-1} is not present, instead the most intense signal is seen at 2230 cm^{-1}. In between the two electrodes, for example at 470 µm from the CE shown in Figure 5-18, the dominant intensity is spread across a broad region centered at 2220 cm^{-1}.

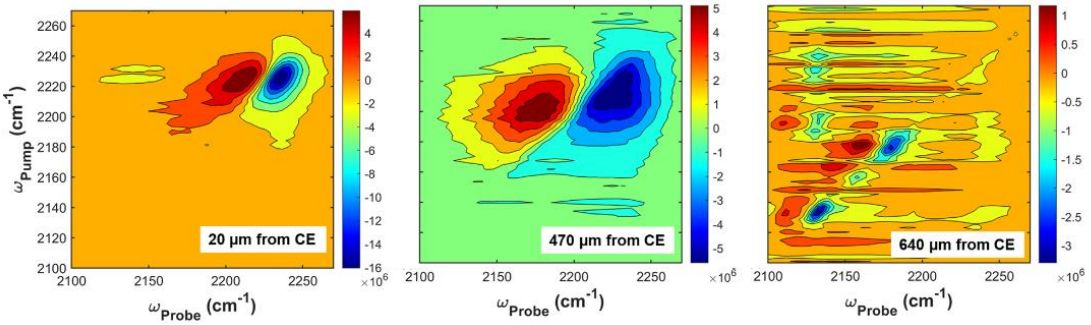

Figure 5-18 Three representative 2D IR spectra from different spatial regions between the counter and working electrodes. Distance from the CE is shown in white inset boxes and corresponds to the location on Figure 19.

To further visualize these spectral changes as a function of space between electrodes, Figure 5-19 shows the scaled and normalized integration of 2D IR signal centered at 2230 cm^{-1}, 2176 cm^{-1}, 2156 cm^{-1}, and 2130 cm^{-1}, with a 20 µm horizontal offset.

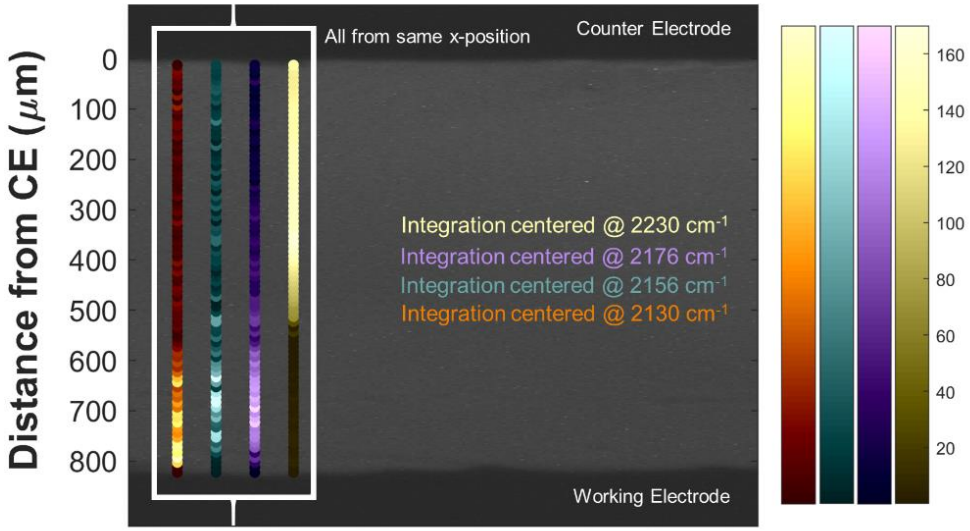

Figure 5-19 Black and white brightfield taken of a small section of the copper electrodes in Figure 15. Overlaid in gold, purple, blue, and orange dots are the scaled and integrated intensity for the ν=0→1 transitions of the modes centered at 2230, 2176, 2156, and 2130 cm^{-1} respectively. The x-positions are arbitrarily offset, all the data is from the same dataset.[184]

At the CE oxidation of the copper electrode could lead to the introduction of more copper ions in solution. Thus, there is the possibility for the formation of copper [DCA] complexes. The existence of multiple species of copper complexes could explain the dramatic spectral changes near the CE due to shifts or even the disappearance of the C≡N and C-N stretches of $[DCA]^-$ when complexed with copper. Figure 5-20b shows cuts at 2200 cm^{-1} (illustrated in Figure 5-20a) as a function of distance from the CE. Closer to the CE the ν=0→1 peak exhibits a shape indicative of an underlying cross peak, and in Figure 5-20c the ratio between the intensity at 2217 cm^{-1} and 2235 cm^{-1} is plotted versus distance from the CE. The change in ratio between these peaks suggests a variation in chemical exchange occurring on a spatial scale. The ratio plateaus to slightly above 1 at close to 500 µm from the CE, where the influence of copper complexes decay and the unbound asymmetric C≡N stretch of $[DCA]^-$ returns to dominating the 2D IR spectra. A deeper analysis of these features is required in order to fully appreciate the wealth of information contained within this data and is currently an active area of research for us. Notably, this data points to the possibility of

spatially resolving ultrafast chemical exchange dynamics across microscopic length scales and much longer time scales as the coordinated copper complexes are transported from the CE to the WE.

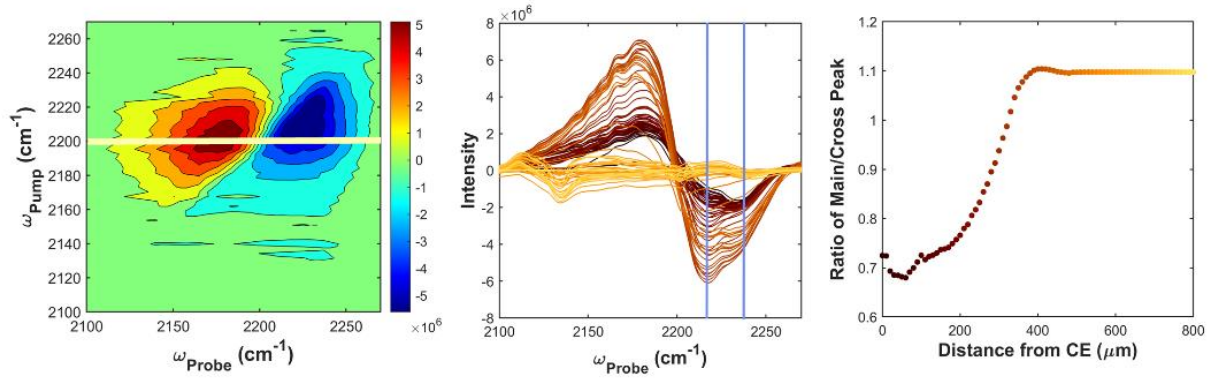

Figure 5-20 a) Spectrum taken 470 μm from the CE, the yellow line parallel to the probe axis corresponds to the line out at 2200 cm^{-1}. b) from dark brown to gold shows data corresponding to the line out in (a) as a function of distance from the CE in 10 um steps. Blue vertical lines correspond to slices where peaks were extracted to compare the intensities of the diagonal peak and cross peak. (c) Shows a ratio between the peak taken at the left blue line in (b) divided by the intensity at the right blue line in (b) as a function of distance from the CE.

5.5 Conclusions and Outlook

In summary, the work presented in this chapter provides details of necessary elements required for the application of ultrafast 2D IR microscopy to heterogeneous chemical systems in practice. We provide a discussion of technical challenges associated with mid-IR laser source repetition rate, mid-IR pulse shaping, noise reduction methods, microscope design considerations, and detection limitations. Within the discussion of these aspects of ultrafast 2D IR microscopy the approaches we have placed into practice are presented in order to allow more widespread access to this emerging imaging modality of ultrafast 2D IR microscopy.

The combination of efforts to incorporate improvements in spectral resolution and noise reduction methods into our 2D IR microscope produces a path to the practical application of ultrafast 2D IR microscopy to a [BmimDCA:BmimBF$_4$] RTIL electrolyte in two different spatial geometries—a droplet and a copper electrochemical cell. The [BmimDCA:BmimBF$_4$] droplet is cast in silicon oil and thus has a fluid interface which poses the possibility of the molecular interface perturbing the dynamics of the RTIL across the droplet. We demonstrate how 2D IR imaging can be used to probe spatial dependence of ultrafast

dynamics in the [BmimDCA:$BmimBF_4$] droplet by monitoring spectral diffusion in a ROI spanning the interface and bulk regions of the droplet. In the [BmimDCA:$BmimBF_4$] RTIL droplet, spatial variation of the 2D IR spectral diffusion is not detected. However, as one moves to investigations of RTILs containing ions with greater complexity including diversity in functional groups, hydrogen-bonding characteristics, and polarity, having the capability to monitor the spatial variation of 2D IR spectral diffusion will be useful. The 2D IR imaging experiments of the [BmimDCA:$BmimBF_4$] electrolyte in the copper electrochemical cell, demonstrates a practical application of ultrafast 2D IR microscopy to study functional devices. Functional devices represent an application in which a systems science approach is required to gain potential paradigm shifting insights. 2D IR imaging of the [BmimDCA:$BmimBF_4$] electrolyte from the copper counter electrode to the copper working electrode showcases the potential of 2D IR microscopy for connecting molecular level condensed phase reaction dynamics to micro- and mesoscale spatial dependence relative to the electrodes in an electrochemical cell. More specifically, our results demonstrate the possibility of monitoring chemical exchange dynamics as the species contributing to the electrochemical reactions evolve from the counter electrode to the working electrode in this copper electrochemical cell.

Ultrafast 2D IR microscopy is clearly an emerging imaging platform that is a promising tool for investigating heterogeneous samples across multiple time scales and length scales, thus contributing a systems level view of the sample of interest. Given the commercial availability and relatively low cost of Yb-fiber based, high-repetition rate mid-IR laser sources, it is expected that a broader range of investigators will begin to consider the utility and potential of ultrafast 2D IR microscopy along with other emerging imaging platforms based on coherent multidimensional spectroscopy techniques.

CHAPTER 6
Future Work[4]

The ultrafast 2D IR experiments previously discussed in this work have provided valuable information about the way that certain additives drive structuring in liquid electrolytes. Tracking vibrational and rotational motions on ultrafast timescales helped resolve molecular level information about local solvent environments. Chapter 3 showed that FEC drives solvent structuring in a mixture of organic carbonates, prior to the addition of salt or the application of an external potential. Chapter 4 results showed water induces local heterogeneity in ionic liquid mixtures that varies dramatically with water concentration. These experiments provide foundational knowledge of the bulk structure and dynamics of common electrolyte solutions and serve as an excellent jumping off point to investigate how these systems may behave in more complex environments. In practice, an electrochemical device has more components to the system than just the electrolyte. These additional components include the supporting electrolyte, the electrode, and an external voltage potential. Therefore, it is important to build a picture of the contributions of each component independently and then bring the system together. Thus, next steps in this work involve continuing to add complexity to the system and ultimately using microscopy to image electrochemical cells *in operando*. In this chapter some preliminary methods and results are shared. Preliminary experiments discussed here focused on RTIL mixtures; and can be extended to the organic carbonate electrolytes for future studies.

6.1 Works towards Designing Controlled *In Situ* Electrochemical Experiments

6.1.1 Incorporating an Electrochemical Reference

Chapter 5 showed preliminary work investigating the interaction of dicyanamide with oxidized copper in a symmetrical copper electrochemical cell using linear FTIR and 2D IR. This work left many unanswered questions including what copper dicyanamide complexes are forming. One important control that can help

[4] This chapter is unpublished preliminary work. Kelly Nieto performed the gold vapor deposition for the electrochemical cells, Thinh Tran cut the CaF_2 plates and Dr. Bradly Luther cut the LMR2.

in answering this question is the inclusion of an electrochemical reference into the cell. A reference is important so that accurate and precise data on the potentials of different redox processes can be determined. In addition, it will allow for confidence that a constant applied potential is applied during chronoamperometry experiments. In the copper system previously discussed, given the ongoing nature of the copper oxidation over the course of the experiment, it is unlikely that a constant voltage was applied over the course of the experiment. Thus, introducing an additional reference will be important to assure a constant applied voltage throughout the experiment.

There are multiple possible directions for references in ionic liquid systems. Most researchers working with ionic liquid mixtures have used internal standards including quasi-reference systems with a metal organic standards like ferrocene.[185–188] Different pseudo reference electrode materials have been used, commonly silver[189–192] and platinum[193] are used; less frequently, materials like aluminum wire[194] or magnesium.[187] Others researchers have worked on developing more reliable references and have investigated using metal couples such as Ag|Ag+.[195]

Here, we have just begun to investigate how an internal ferrocene reference might be incorporated into our current set-up. The first question asked was whether just the incorporation of ferrocene would impact the chemical structure and dynamics of the ionic liquid mixtures. Thus, the first control completed was investigating the addition of ferrocene with no applied potential in the RTIL mixture.

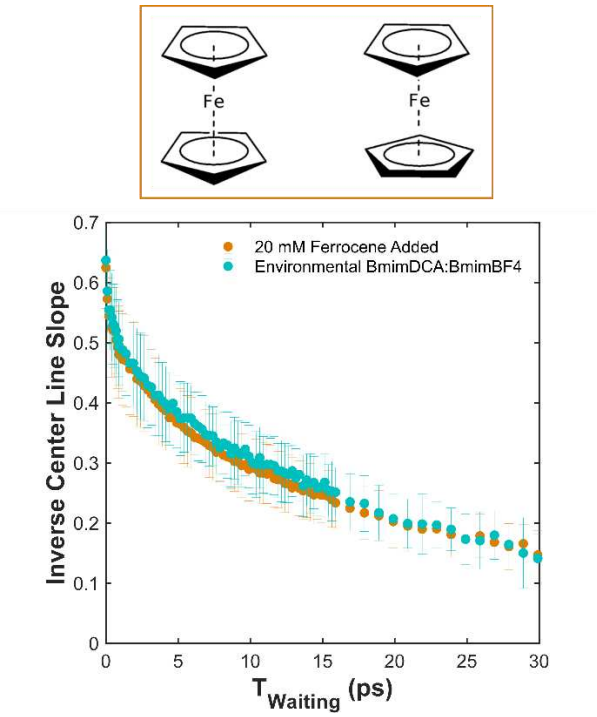

Figure 6-1 Inverse center line slope results from XXXX 2D IR experiments. In orange the results of the environmental BmimBF4:BmimDCA sample with 20 mM ferrocene. In teal the environmental BmimBF4:BmimDCA sample.

6.1.1.1 Sample Preparation

RTIL solutions used in the 2D IR are comprised of 1-butyl-3-methylimidazolium tetrafluoroborate ($BmimBF_4$), 1-butyl-3-methylimidazolium dicyanamide (BmimDCA), and deionized water. $BmimBF_4$ (99% purity) and BmimDCA (>98% purity) are purchased from IoLiTec. BmimDCA was doped into $BmimBF_4$ at a ratio of 5:2000 by volume corresponding to a mole percent dicyanamide of 0.121. 20 mM of ferrocene (of unknown origin) was added to solution. All samples were sonicated for 1hour before use to incorporate the ferrocene as fully as possible, however longer sonication may be necessary.

All 2D IR spectra collected were done in the same manner as described in Chapter 4.

6.1.1.2 Results and Future Directions

To determine if neutral ferrocene was significantly impacting the RTIL dynamics center line slope analysis (CLS) is used. Specifically, CLS of the asymmetric C≡N stretch of DCA is performed using seven pump cuts from 2127.6 to 2144.2 cm^{-1}. Error bars in Figure 6-1 represent the 95% confidence interval of the linear fit to seven minima across the peak. The relatively large spread of the error bars is indicative of the

anticipated asymmetry in the CLS across the peak (as discussed in Chapter 4). Figure 6-1 shows no substantial changes with or without the addition of neutral ferrocene. This lack of change is anticipated given the bulky neutral nature of ferrocene; strong interactions with the dicyanamide anions are not anticipated.

Next control experiments would include incorporating the ferrocene IL mixture into an electrochemical cell with an applied potential to see the impact that the redox of ferrocene has on the chemical structure and dynamics of the mixture. If the dynamics are unperturbed or perturbed in a way that is easily accounted for then the incorporation of electrode materials that introduce interesting chemistry, such as the copper oxidation process is possible. In addition, work on developing a cell compatible with 2D IR that can incorporate different electrode materials more easily would be beneficial.

6.1.2 Role of an Applied Potential on the Structure and Dynamics of RTIL mixtures

The goal of this work was to investigate the impact of an applied potential on the system prior to introducing complex electrochemistry. However, the chosen gold electrodes were found to be more reactive than anticipated and therefore the goal of studying solely the impact of a field was not met. However, the following section outlines the cell preparation and some experimental results.

6.1.2.1 Au Symmetric Electrochemical Cell Setup

Gold electrodes were made by covering a 50.8 mm diameter, 4 mm thick CaF_2 plate (Crystran) with Kapton tape excluding the desired pattern for two symmetric electrodes (Figure 6-2). In the middle of the plate the distance between the electrodes is kept between 1-3 mm. Near the edges of the CaF_2 plate more distance was added in order to prevent contact between the alligator clips hooked up to the electrodes could be easily avoided. Gold electrodes are grown using a physical vapor deposition process. A layer of chromium was first deposited to aid with the binding to CaF_2. The strip of gold was grown to a thickness of approximately 200 nm. To house the cell a modified Thorlabs LMR2 is used. This sample cell is chosen because it is a common holder for optics and is easily integrated into our existing 2D IR Microscopy set-up. The LMR2 is cut as shown in Figure 6-2 to allow clamps to be attached without contacting the metal LMR2. Approximately one third of the top CaF_2 (without the electrodes) is removed via cutting with a diamond

saw. This is again to allow easy attachment of the alligator clips. Copper tape is used to protect the ends of the electrodes when alligator clamps are used to hook up the potentiostat. The gold is easily damaged so keeping it covered will prolong the lifetime of the cell. However, the copper should not extend to the point of having contact with the electrolyte solution. A 15 μm Teflon spacer (Harricks) is used to set the pathlength and contain the electrolyte solution.

For chronoamperometry experiments a Gamry Instruments Interface 1010 E Potentiostat was used to apply a constant voltage to the cell. Experiments were done between -1V and -5V with respect to the reference, which was attached to the counter electrode.

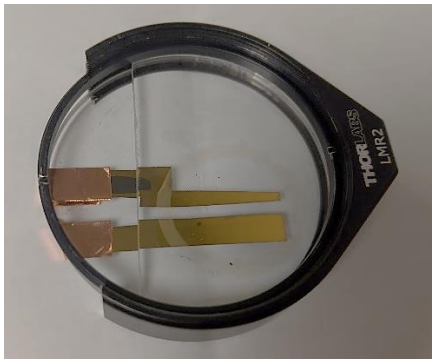

Figure 6-2 Symmetric gold electrochemical cell.

6.1.2.2 Linear FTIR Microscopy

Linear IR microscopy and spectroscopy measurements were done using the Bruker Optics Hyperion 3000 microscope with a mid-IR source. The detector used in conjunction with the Hyperion 3000 microscope is a focal plane array detector (FPA) of 64 x 64 elements. The objective used is 15x. The spectral range of the microscope is 600 to 7500 cm^{-1}. The spectral resolution of the measurements was set at 2 cm^{-1}. All linear IR microscopy images were collected in transmission mode. A series of spectra were taken at points between each electrode. The spectra were extracted, background subtracted, using OPUS software. Extracted spectra were then plotted in MATLAB.

6.1.2.3 Results from High- Applied Potential Au Experiments

Initial linear FTIR experiments tested the impact of applied voltages between -1 V and -5V, on the environmental BmimDCA in BmimBF4 (described above and in Chapter 4). No substantial change in the

linear FTIR spectrum was seen until -5V. Figure 6-3 shows the result of applying a -5V potential between the Au electrodes. At -5V visible changes to the gold electrode became apparent and substantial changes in the linear FTIR were seen. Figure 6-3a shows the Au electrochemical cell backlit to highlight the stripping that occurred on the counter electrode. Figure 6-3b shows a linear FTIR taken at points in the highlighted box in Figure 6-3a. These spectra are focused on the asymmetric C≡N stretch, the symmetric C≡N stretch, and the C-N asymmetric and C-N symmetric combination mode of DCA. Closer to the counter electrode there (Steps 1-3) there is a dramatic reduction and shift of the asymmetric C≡N stretch and the combination mode. Closest to the counter electrode the symmetric stretch has essentially disappeared. These trends are likely due to the introduction of gold ions into solution as a result of the counter electrode being stripped. It is likely that the peak which shifted to higher frequency likely is the DCA associated with the gold. Stripping of gold in ionic liquids at high enough potentials has been shown to occur in the presence of water.[103] Interestingly in the linear FTIR of the water asymmetric and symmetric stretches there is a slight drop in intensity and a slight growth of the bulk water peak near the counter electrode. Overall, the linear FTIR data suggest that the electrolyte's proximity to the counter/reference electrode alters the local structure of the DCA, most likely due to the introduction of gold ions into solution. These initial observations are interesting, and more experiments are required to unravel the nature of the RTIL electrolyte system in the presence of reactive electrodes and an external applied field.

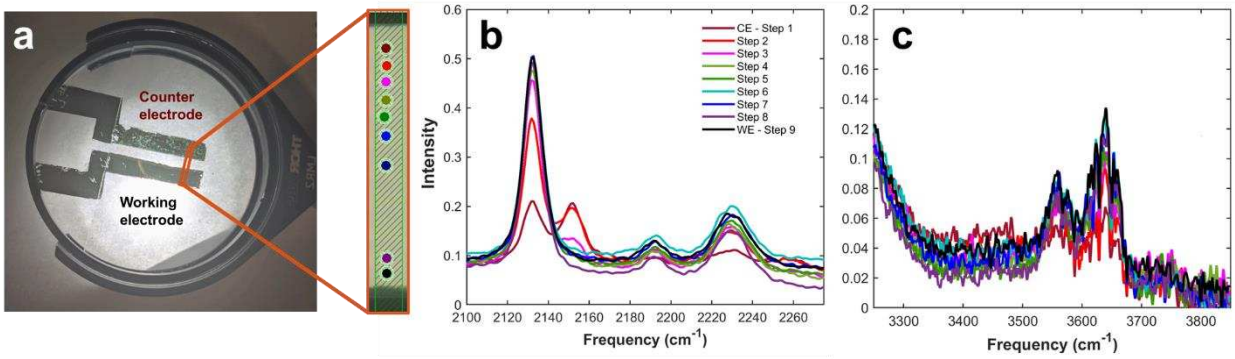

Figure 6-3 (a) Gold electrochemical cell after an experiment with -5V applied potential. Counter electrode is the top electrode. The bottom electrode is the working electrode. The orange box highlights where linear IR microscopy was performed. The image to the right is taken with a visible microscope and the points highlighted show where IR spectra were collected. (b) IR spectra taken at the colored dots in (a) showing changes in DCA absorptions from the counter to working electrode. (c) IR spectra also corresponding to the dots in (a) showing the water stretch region.

6.1.2.4 Results from Low- Applied Potential Au Experiments

2D IR experiments of a symmetric gold cell with a -2V potential were performed. This voltage was chosen because based on the linear FTIR experiments the gold electrode seemed unreactive at this potential. To determine if the applied potential was significantly impacting the RTIL dynamics CLS of the asymmetric C≡N stretch of DCA is performed using seven pump cuts from 2127.6 to 2144.2 cm^{-1}. Error bars in Figure 6-4 represent the standard deviation of triplicate measurements. Results showed a slight offset between the no potential solution and the applied potential solution (Figure 6-4). However, after the experiment the potential was turned off and the potentiostat disconnected, the system was left to rest for ~ 45 minutes and then the 2D measurements repeated. In this case the offset remains. This might suggest a more permanent change to the system perhaps indicating even at this potential the electrode is undergoing a chemical change and introducing long-lived structural changes to the system. This trend needs to be further confirmed by additional experiments.

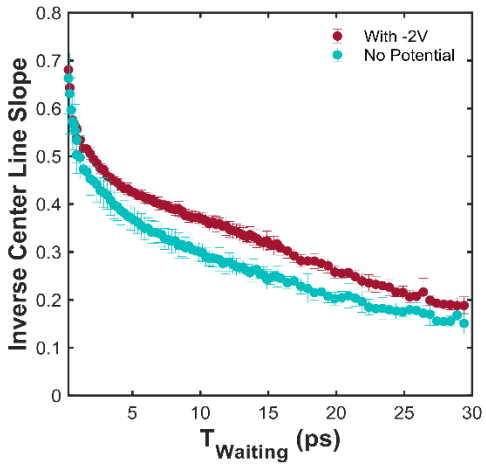

Figure 6-4 Inverse center line slope results from XXXX 2D IR experiments. In red the results of the environmental BmimBF4:BmimDCA sample with an applied -2V potential. In teal the environmental BmimBF4:BmimDCA sample.

6.1.2.5 Next steps

To determine the nature of the offset in the CLS introduced when a -2V potential was applied future work should include the introduction of a reference and cyclic voltammetry to determine at what voltage redox events occur. Moreover, a series of 2D IR measurements with smaller changes in voltage and longer waiting periods after the applied potential experiment should be undertaken to determine if the offset is replicable, long-lived, and voltage dependent. In addition, future experiments could integrate less reactive electrodes, such as platinum, to eliminate the chemical effects introduced by the stripping of the gold electrodes. An experimental system using platinum could truly investigate the role of the applied voltage potential without undesirable side reactions.

CHAPTER 7
Conclusion

The research described in this dissertation helped to uncover the impact that chemical additives have on the chemical structure and dynamics of electrolyte solutions that can be used in electrochemical applications such as batteries or solar devices. To this end 2D IR is used in conjunction with techniques including linear FTIR, rheology, molecular dynamics, and density functional theory to help answer questions about chemical structure and solvent dynamics of organic carbonate and ionic liquid mixtures. In addition, 2D IR microscopy as a relatively new tool to study functional electrochemical cells is introduced and implemented.

The 2D IR and molecular dynamics simulations of organic carbonate mixtures with varied amounts of the additive fluoroethylene carbonate (FEC) showed that even in small quantities FEC can induce structuring in the solvent environment. Center line slope (CLS) analysis of 2D IR spectra show that spectral diffusion slows with the addition of small amounts of FEC, suggesting a change in solvent environment. Computational cylindrical distribution functions in conjunction with CLS results suggested that the slowing is due to solvent reorganization, specifically significant changes in ethylene carbonate (EC) solvation. Furthermore, a combination of experimental anisotropy, rheology, and computational rotational correlation functions shows (1) increasing local solvent rigidity occurs high amounts of FEC (2) additional FEC increases macroscopic viscosity (3) a correlation exists between global solvent reorientation and macroscopic viscosity and (4) the interactions between FEC and the other carbonates are weaker than FEC-FEC interactions. Overall, these results suggest pre-structuring of the solvent environment upon addition of FEC. This pre-structuring could have implications in driving certain routes the formation of the solid electrolyte interphase, consequently having an impact on important battery lifetimes and safety.

Results of the investigation into the impact of small amounts of water (between ~1.32 and 21.6% mole fraction water) on the structure and dynamics of BmimBF4 with BmimDCA showed a wide diversity of local solvent environments of the dicyanamide anion. Blue-shifts in both linear and 2D IR spectra with

increasing water suggest the formation of water-associated and non-water-associated DCA populations. Time-dependent 2D IR results indicate substantially different dynamic behavior of these different populations of DCA at low (below 2.5% χ_{Water}), mid (between 2.5% χ_{Water} and 9.6% χ_{Water}), and high (between 11.6% χ_{Water} and 21.6% χ_{Water}) water concentrations. Asymmetry in the CLS analysis showed clear differences in the spectral diffusion timescales for the non-water and water-associated populations of DCA at low, mid, and high-range water concentrations. Higher amounts of water led to the formation of rigid local cages that hinder spectral diffusion for water-associated DCA. Vibrational relaxation timescales decrease with increasing water for the water-associated populations of DCA and remain more constant for the non-water-associated populations. These trends point to water facilitating population relaxation, potentially through the addition of more bath modes. In addition, rheology measurements show that the macroscopic viscosity decreases with increasing water suggest that on a bulk scale molecular interactions are weakening, suggesting that water is shields interactions between the cations and anions of the RTIL mixture. Ultimately, this work has provided further insight into the dramatic role water can play in altering the dynamic behavior of RTIL mixtures. Small amounts of water add to the heterogeneity of RTIL solutions by creating local environments with distinct structures and consequently unique dynamics. It is possible that in a functional electrochemical device with a water and RTIL electrolyte that the introduction of these diverse local solvent environments might be exploited to provide benefits. If water could be introduced in a system in a way that increased ion-mobility yet avoided inducing negative interfacial interactions at an electrode this could improve device performance. Determining if and how this clustering presents itself in an operational electrochemical cell would be a beneficial next step.

Future investigations of these electrolyte solutions should be done in more complex situations given that in an electrochemical device there are more components than just the electrolyte. Thus, next steps in this work involve continuing to add complexity to the system and ultimately using microscopy to image electrochemical cells *in operando*. Ultrafast 2D IR microscopy is an emerging imaging platform that is a promising tool for investigating heterogeneous samples across various time and length scales. However,

when implementing 2D IR microscopy there are several important practical considerations that need to be taken into account. Some of these technical challenges are associated with mid-IR laser source repetition rate, pulse shaping, noise reduction, microscope design, and detection schemes. Implementation of improvements in spectral resolution and noise reduction methods into our 100 kHz 2D IR microscope allowed for the successful imaging of a BmimDCA:$BmimBF_4$ electrolyte in two different scenarios—a droplet and a symmetric copper electrochemical cell. Imaging the BmimDCA:$BmimBF_4$ microdroplet demonstrated how 2D IR imaging can be used to probe dynamics on a spatial scale. The BmimDCA:$BmimBF_4$ microdroplet was found to be spatially homogenous. The 2D IR imaging experiments of the BmimDCA:$BmimBF_4$ electrolyte in a copper electrochemical cell, demonstrates a practical application of ultrafast 2D IR microscopy to study functional devices. 2D IR imaging of the BmimDCA:$BmimBF_4$ electrolyte from the copper counter electrode to the copper working electrode showed dramatic changes in peak positions and shapes suggesting the formation of DCA copper complexes. The drastic changes as a function of space introduce the possibility of monitoring chemical exchange dynamics as the species contributing to the electrochemical reactions evolve from the counter electrode to the working electrode. These initial experiments suggest 2D IR microscopy is a technique well equipped to connect molecular level condensed phase reaction dynamics to micro- and mesoscale spatial dependence in an heterogenous environments like an electrochemical device.

The chemical information about the role additives play in determining electrolyte structure and dynamics gained in this work in conjunction with the implementation of 2D IR microscopy pave a path for future researchers to gain a better understanding of how mixed electrolyte solutions behave in an operational environment. A clear and fundamental picture of bulk and interfacial dynamics can help inform the design of next generation electrochemical devices.

References

(1) An, S. J.; Li, J.; Daniel, C.; Mohanty, D.; Nagpure, S.; Wood, D. L. The State of Understanding of the Lithium-Ion-Battery Graphite Solid Electrolyte Interphase (SEI) and Its Relationship to Formation Cycling. *Carbon* **2016**, *105*, 52–76. https://doi.org/10.1016/j.carbon.2016.04.008.

(2) Gimble, N. J.; Kraynak, L. A.; Schneider, J. D.; Schulze, M. C.; Prieto, A. L. X-Ray Photoelectron Spectroscopy as a Probe for Understanding the Potential-Dependent Impact of Fluoroethylene Carbonate on the Solid Electrolyte Interface Formation in Na/Cu2Sb Batteries. *Journal of Power Sources* **2021**, *489*, 229171. https://doi.org/10.1016/j.jpowsour.2020.229171.

(3) Jackson, E. D.; Prieto, A. L. Copper Antimonide Nanowire Array Lithium Ion Anodes Stabilized by Electrolyte Additives. *ACS Applied Materials and Interfaces* **2016**, *8* (44), 30379–30386. https://doi.org/10.1021/acsami.6b08033.

(4) *The Future of Energy Storage: An Interdisciplinary MIT Study*; MIT Energy Initiative; Massachusetts Institute of Technology, 2022.

(5) Tan, K. M.; Babu, T. S.; Ramachandaramurthy, V. K.; Kasinathan, P.; Solanki, S. G.; Raveendran, S. K. Empowering Smart Grid: A Comprehensive Review of Energy Storage Technology and Application with Renewable Energy Integration. *Journal of Energy Storage* **2021**, *39*, 102591. https://doi.org/10.1016/j.est.2021.102591.

(6) Olabi, A. G.; Onumaegbu, C.; Wilberforce, T.; Ramadan, M.; Abdelkareem, M. A.; Al – Alami, A. H. Critical Review of Energy Storage Systems. *Energy* **2021**, *214*, 118987. https://doi.org/10.1016/j.energy.2020.118987.

(7) *Energy Storage: How It Works and Its Role in and Equitable Clean Energy Future*; Explainer; Union of Concerned Scientists, 2015.

(8) Borah, R.; Hughson, F. R.; Johnston, J.; Nann, T. On Battery Materials and Methods. *Materials Today Advances* **2020**, *6*, 100046. https://doi.org/10.1016/j.mtadv.2019.100046.

(9) Goodenough, J. B.; Kim, Y. Challenges for Rechargeable Li Batteries. *Chemistry of Materials* **2010**, *22* (3), 587–603. https://doi.org/10.1021/cm901452z.

(10) Goodenough, J. B. Energy Storage Materials: A Perspective. *Energy Storage Materials* **2015**, *1*, 158–161. https://doi.org/10.1016/j.ensm.2015.07.001.

(11) Xu, K. Electrolytes and Interphases in Li-Ion Batteries and Beyond - Chemical Reviews (ACS Publications). *Chemical Reviews* **2014**, *114*.

(12) Palacín, M. R.; de Guibert, A. Why Do Batteries Fail? *Science* **2016**, *351* (6273), 1253292. https://doi.org/10.1126/science.1253292.

(13) Horowitz, Y.; Steinrück, H. G.; Han, H. L.; Cao, C.; Abate, I. I.; Tsao, Y.; Toney, M. F.; Somorjai, G. A. Fluoroethylene Carbonate Induces Ordered Electrolyte Interface on Silicon and Sapphire Surfaces as Revealed by Sum Frequency Generation Vibrational Spectroscopy and X-Ray Reflectivity. *Nano Letters* **2018**, *18* (3), 2105–2111. https://doi.org/10.1021/acs.nanolett.8b00298.

(14) Shkrob, I. A.; Wishart, J. F.; Abraham, D. P. What Makes Fluoroethylene Carbonate Different? *J. Phys. Chem. C* **2015**, *119* (27), 14954–14964. https://doi.org/10.1021/acs.jpcc.5b03591.

(15) Marino, C.; Boulaoued, A.; Fullenwarth, J.; Maurin, D.; Louvain, N.; Bantignies, J. L.; Stievano, L.; Monconduit, L. Solvation and Dynamics of Lithium Ions in Carbonate-Based Electrolytes during Cycling Followed by Operando Infrared Spectroscopy: The Example of NiSb2, a Typical Negative Conversion-Type Electrode Material for Lithium Batteries. *Journal of Physical Chemistry C* **2017**, *121* (48), 26598–26606. https://doi.org/10.1021/acs.jpcc.7b06685.

(16) Loaiza, L. C.; Louvain, N.; Fraisse, B.; Boulaoued, A.; Iadecola, A.; Johansson, P.; Stievano, L.; Seznec, V.; Monconduit, L. Electrochemical Lithiation of Ge: New Insights by Operando Spectroscopy and Diffraction. *Journal of Physical Chemistry C* **2018**, *122* (7), 3709–3718. https://doi.org/10.1021/acs.jpcc.7b11249.

(17) Lee, K.-K.; Park, K.; Lee, H.; Noh, Y.; Kossowska, D.; Kwak, K.; Cho, M. Ultrafast Fluxional Exchange Dynamics in Electrolyte Solvation Sheath of Lithium Ion Battery. *Nature Communications* **2017**, *8* (1). https://doi.org/10.1038/ncomms14658.

(18) Fulfer, K. D.; Kuroda, D. G. Solvation Structure and Dynamics of the Lithium Ion in Organic Carbonate-Based Electrolytes: A Time-Dependent Infrared Spectroscopy Study. *J. Phys. Chem. C* **2016**, *120* (42), 24011–24022. https://doi.org/10.1021/acs.jpcc.6b08607.

(19) Peled, E.; Menkin, S. Review—SEI: Past, Present and Future. *Journal of The Electrochemical Society* **2017**, *164* (7), A1703–A1719. https://doi.org/10.1149/2.1441707jes.

(20) McHale, J. L. *Molecular Spectroscopy*, 0 ed.; CRC Press, 2017. https://doi.org/10.1201/9781315115214.

(21) Hamm, Peter Zanni, M. *Concepts and Methods of 2D Infrared Spectroscopy*; Cambridge University Press, 2011.

(22) Zeng, Z.; Liang, W. I.; Liao, H. G.; Xin, H. L.; Chu, Y. H.; Zheng, H. Visualization of Electrode-Electrolyte Interfaces in LiPF 6/EC/DEC Electrolyte for Lithium Ion Batteries via in Situ TEM. *Nano Letters* **2014**, *14* (4), 1745–1750. https://doi.org/10.1021/nl403922u.

(23) Shi, F.; Ross, P. N.; Somorjai, G. A.; Komvopoulos, K. The Chemistry of Electrolyte Reduction on Silicon Electrodes Revealed by *in Situ* ATR-FTIR Spectroscopy. *The Journal of Physical Chemistry C* **2017**, *121* (27), 14476–14483. https://doi.org/10.1021/acs.jpcc.7b04132.

(24) Fulfer, K. D.; Kuroda, D. G. Solvation Structure and Dynamics of the Lithium Ion in Organic Carbonate-Based Electrolytes: A Time-Dependent Infrared Spectroscopy Study. *J. Phys. Chem. C* **2016**, *120* (42), 24011–24022. https://doi.org/10.1021/acs.jpcc.6b08607.

(25) Bella, F.; Gerbaldi, C.; Barolo, C.; Grätzel, M. Aqueous Dye-Sensitized Solar Cells. *Chem. Soc. Rev.* **2015**, *44* (11), 3431–3473. https://doi.org/10.1039/C4CS00456F.

(26) Jeon, J.; Kim, H.; Goddard, W. A.; Pascal, T. A.; Lee, G.-I.; Kang, J. K. The Role of Confined Water in Ionic Liquid Electrolytes for Dye-Sensitized Solar Cells. *J. Phys. Chem. Lett.* **2012**, *3* (4), 556–559. https://doi.org/10.1021/jz3000036.

(27) Elia, G. A.; Ulissi, U.; Jeong, S.; Passerini, S.; Hassoun, J. Exceptional Long-Life Performance of Lithium-Ion Batteries Using Ionic Liquid-Based Electrolytes. *Energy Environ. Sci.* **2016**, *9* (10), 3210–3220. https://doi.org/10.1039/C6EE01295G.

(28) Bi, S.; Wang, R.; Liu, S.; Yan, J.; Mao, B.; Kornyshev, A. A.; Feng, G. Minimizing the Electrosorption of Water from Humid Ionic Liquids on Electrodes. *Nat Commun* **2018**, *9* (1), 5222. https://doi.org/10.1038/s41467-018-07674-0.

(29) Tibbetts, C. A.; Wyatt, A. B.; Luther, B. M.; Krummel, A. T. Practical Aspects of 2D IR Microscopy. In *Emerging Trends in Chemical Applications of Lasers*; ACS Books; American Chemical Society, 2021.

(30) Goodenough, J. B.; Kim, Y. Challenges for Rechargeable Li Batteries. *Chemistry of Materials* **2010**, *22* (3), 587–603. https://doi.org/10.1021/cm901452z.

(31) An, S. J.; Li, J.; Daniel, C.; Mohanty, D.; Nagpure, S.; Wood, D. L. The State of Understanding of the Lithium-Ion-Battery Graphite Solid Electrolyte Interphase (SEI) and Its Relationship to Formation Cycling. *Carbon* **2016**, *105*, 52–76. https://doi.org/10.1016/j.carbon.2016.04.008.

(32) Roy, P.; Srivastava, S. K. Nanostructured Anode Materials for Lithium Ion Batteries. *J. Mater. Chem. A* **2015**, *3* (6), 2454–2484. https://doi.org/10.1039/C4TA04980B.

(33) Liu, C.; Neale, Z. G.; Cao, G. Understanding Electrochemical Potentials of Cathode Materials in Rechargeable Batteries. *Materials Today* **2016**, *19* (2), 109–123. https://doi.org/10.1016/j.mattod.2015.10.009.

(34) Jackson, E. D.; Prieto, A. L. Copper Antimonide Nanowire Array Lithium Ion Anodes Stabilized by Electrolyte Additives. *ACS Applied Materials and Interfaces* **2016**, *8* (44), 30379–30386. https://doi.org/10.1021/acsami.6b08033.

(35) Balducci, A. Ionic Liquids in Lithium-Ion Batteries. *Top Curr Chem (Z)* **2017**, *375* (2), 20. https://doi.org/10.1007/s41061-017-0109-8.

(36) Welton, T. Room-Temperature Ionic Liquids. Solvents for Synthesis and Catalysis. *Chem. Rev.* **1999**, *99* (8), 2071–2084. https://doi.org/10.1021/cr980032t.

(37) Wang, Y.-L.; Li, B.; Sarman, S.; Mocci, F.; Lu, Z.-Y.; Yuan, J.; Laaksonen, A.; Fayer, M. D. Microstructural and Dynamical Heterogeneities in Ionic Liquids. *Chem. Rev.* **2020**, *120* (13), 5798–5877. https://doi.org/10.1021/acs.chemrev.9b00693.

(38) Bai, Y.; Zhang, J.; Wang, Y.; Zhang, M.; Wang, P. Lithium-Modulated Conduction Band Edge Shifts and Charge-Transfer Dynamics in Dye-Sensitized Solar Cells Based on a Dicyanamide Ionic Liquid. *Langmuir* **2011**, *27* (8), 4749–4755. https://doi.org/10.1021/la200156m.

(39) Fedorov, M. V.; Kornyshev, A. A. Ionic Liquids at Electrified Interfaces. *Chem. Rev.* **2014**, *114* (5), 2978–3036. https://doi.org/10.1021/cr400374x.

(40) Becker, M.; Rentsch, D.; Reber, D.; Aribia, A.; Battaglia, C.; Kühnel, R. The Hydrotropic Effect of Ionic Liquids in Water-in-Salt Electrolytes**. *Angew. Chem. Int. Ed.* **2021**, *60* (25), 14100–14108. https://doi.org/10.1002/anie.202103375.

(41) Forsyth, M.; Hilder, M.; Zhang, Y.; Chen, F.; Carre, L.; Rakov, D. A.; Armand, M.; Macfarlane, D. R.; Pozo-Gonzalo, C.; Howlett, P. C. Tuning Sodium Interfacial Chemistry with Mixed-Anion Ionic Liquid Electrolytes. *ACS Appl. Mater. Interfaces* **2019**, *11* (46), 43093–43106. https://doi.org/10.1021/acsami.9b12913.

(42) Lucas, M.; Brotton, S. J.; Shukla, S. K.; Yu, J.; Anderson, S. L.; Kaiser, R. I. Oxidation of a Levitated Droplet of 1-Allyl-3-Methylimidazolium Dicyanamide by Nitrogen Dioxide. *J. Phys. Chem. A* **2019**, *123* (2), 400–416. https://doi.org/10.1021/acs.jpca.8b08395.

(43) Brotton, S. J.; Lucas, M.; Jensen, T. N.; Anderson, S. L.; Kaiser, R. I. Spectroscopic Study on the Intermediates and Reaction Rates in the Oxidation of Levitated Droplets of Energetic Ionic Liquids by Nitrogen Dioxide. *J. Phys. Chem. A* **2018**, *122* (37), 7351–7377. https://doi.org/10.1021/acs.jpca.8b05244.

(44) Chen, Y.; Cao, Y.; Zhang, Y.; Mu, T. Hydrogen Bonding between Acetate-Based Ionic Liquids and Water: Three Types of IR Absorption Peaks and NMR Chemical Shifts Change upon Dilution. *Journal of Molecular Structure* **2014**, *1058*, 244–251. https://doi.org/10.1016/j.molstruc.2013.11.010.

(45) Wilken, S.; Xiong, S.; Scheers, J.; Jacobsson, P.; Johansson, P. Ionic Liquids in Lithium Battery Electrolytes: Composition versus Safety and Physical Properties. *Journal of Power Sources* **2015**, *275*, 935–942. https://doi.org/10.1016/j.jpowsour.2014.11.071.

(46) Kühnel, R.-S.; Böckenfeld, N.; Passerini, S.; Winter, M.; Balducci, A. Mixtures of Ionic Liquid and Organic Carbonate as Electrolyte with Improved Safety and Performance for Rechargeable Lithium Batteries. *Electrochimica Acta* **2011**, *56* (11), 4092–4099. https://doi.org/10.1016/j.electacta.2011.01.116.

(47) Dohm, S.; Spohr, E.; Korth, M. Developing Adaptive QM/MM Computer Simulations for Electrochemistry. *J. Comput. Chem.* **2017**, *38* (1), 51–58. https://doi.org/10.1002/jcc.24513.

(48) Husch, T.; Yilmazer, N. D.; Balducci, A.; Korth, M. Large-Scale Virtual High-Throughput Screening for the Identification of New Battery Electrolyte Solvents: Computing Infrastructure and Collective Properties. *Phys. Chem. Chem. Phys.* **2015**, *17* (5), 3394–3401. https://doi.org/10.1039/C4CP04338C.

(49) Armand, M.; Endres, F.; MacFarlane, D. R.; Ohno, H.; Scrosati, B. Ionic-Liquid Materials for the Electrochemical Challenges of the Future. In *Materials for Sustainable Energy*; Co-Published with Macmillan Publishers Ltd, UK, 2010; pp 129–137. https://doi.org/10.1142/9789814317665_0020.

(50) Hamm, Peter Zanni, M. *Concepts and Methods of 2D Infrared Spectroscopy*; Cambridge University Press, 2011.

(51) Kiefer, J.; Noack, K.; Penna, T. C.; Ribeiro, M. C. C.; Weber, H.; Kirchner, B. Vibrational Signatures of Anionic Cyano Groups in Imidazolium Ionic Liquids. *Vibrational Spectroscopy* **2017**, *91*, 141–146. https://doi.org/10.1016/j.vibspec.2016.05.004.

(52) Zhang, W.; Markiewicz, B. N.; Doerksen, R. S.; Smith, III, A. B.; Gai, F. CN Stretching Vibration of 5-Cyanotryptophan as an Infrared Probe of Protein Local Environment: What Determines Its Frequency? *Phys. Chem. Chem. Phys.* **2016**, *18* (10), 7027–7034. https://doi.org/10.1039/C5CP04413H.

(53) Deb, P.; Haldar, T.; Kashid, S. M.; Banerjee, S.; Chakrabarty, S.; Bagchi, S. Correlating Nitrile IR Frequencies to Local Electrostatics Quantifies Noncovalent Interactions of Peptides and Proteins. *J. Phys. Chem. B* **2016**, *120* (17), 4034–4046. https://doi.org/10.1021/acs.jpcb.6b02732.

(54) Maj, M.; Ahn, C.; Błasiak, B.; Kwak, K.; Han, H.; Cho, M. Isonitrile as an Ultrasensitive Infrared Reporter of Hydrogen-Bonding Structure and Dynamics. *J. Phys. Chem. B* **2016**, *120* (39), 10167–10180. https://doi.org/10.1021/acs.jpcb.6b04319.

(55) Hamm, P.; Lim, M.; Hochstrasser, R. M. Structure of the Amide I Band of Peptides Measured by Femtosecond Nonlinear-Infrared Spectroscopy. *J. Phys. Chem. B* **1998**, *102* (31), 6123–6138. https://doi.org/10.1021/jp9813286.

(56) Elsaesser, T.; Szyc, Ł.; Yang, M. Ultrafast Structural and Vibrational Dynamics of the Hydration Shell around DNA. *EPJ Web of Conferences* **2013**, *41*, 06004. https://doi.org/10.1051/epjconf/20134106004.

(57) Yang, M.; Szyc, Ł.; Elsaesser, T. Vibrational Dynamics of the Water Shell of DNA Studied by Femtosecond Two-Dimensional Infrared Spectroscopy. *Journal of Photochemistry and Photobiology A: Chemistry* **2012**, *234*, 49–56. https://doi.org/10.1016/j.jphotochem.2011.11.014.

(58) Kim, Y. S.; Hochstrasser, R. M. Applications of 2D IR Spectroscopy to Peptides, Proteins, and Hydrogen-Bond Dynamics. *J. Phys. Chem. B* **2009**, *113* (24), 8231–8251. https://doi.org/10.1021/jp8113978.

(59) Dunbar, J. A.; Arthur, E. J.; White, A. M.; Kubarych, K. J. Ultrafast 2D-IR and Simulation Investigations of Preferential Solvation and Cosolvent Exchange Dynamics. *J. Phys. Chem. B* **2015**, *119* (20), 6271–6279. https://doi.org/10.1021/acs.jpcb.5b01952.

(60) Fournier, J. A.; Carpenter, W.; De Marco, L.; Tokmakoff, A. Interplay of Ion–Water and Water–Water Interactions within the Hydration Shells of Nitrate and Carbonate Directly Probed with 2D IR Spectroscopy. *J. Am. Chem. Soc.* **2016**, *138* (30), 9634–9645. https://doi.org/10.1021/jacs.6b05122.

(61) Fournier, J. A.; Carpenter, W. B.; Lewis, N. H. C.; Tokmakoff, A. Broadband 2D IR Spectroscopy Reveals Dominant Asymmetric H5O2+ Proton Hydration Structures in Acid Solutions. *Nature Chem* **2018**, *10* (9), 932–937. https://doi.org/10.1038/s41557-018-0091-y.

(62) Yuan, R.; Yan, C.; Fayer, M. Ion–Molecule Complex Dissociation and Formation Dynamics in LiCl Aqueous Solutions from 2D IR Spectroscopy. *The Journal of Physical Chemistry B* **2018**, *122* (46), 10582–10592. https://doi.org/10.1021/acs.jpcb.8b08743.

(63) Lee, K. K.; Park, K.; Lee, H.; Noh, Y.; Kossowska, D.; Kwak, K.; Cho, M. Ultrafast Fluxional Exchange Dynamics in Electrolyte Solvation Sheath of Lithium Ion Battery. *Nature Communications* **2017**, *8*, 1–9. https://doi.org/10.1038/ncomms14658.

(64) Brinzer, T.; Berquist, E. J.; Dutta, S.; Johnson, C. A.; Krisher, C. S.; Lambrecht, D. S.; Garrett-Roe, S. Ultrafast Vibrational Spectroscopy (2D-IR) of CO_2 in Ionic Liquids: Carbon Capture from Carbon Dioxide's Point of View. *The Journal of Chemical Physics* **2015**, *142* (21), 212425. https://doi.org/10.1063/1.4917467.

(65) Stirnemann, G.; Rossky, P. J.; Hynes, J. T.; Laage, D. Water Reorientation, Hydrogen-Bond Dynamics and 2D-IR Spectroscopy next to an Extended Hydrophobic Surface. *Faraday Discuss.* **2010**, *146*, 263. https://doi.org/10.1039/b925673c.

(66) Nishida, J.; Breen, J. P.; Wu, B.; Fayer, M. D. Extraordinary Slowing of Structural Dynamics in Thin Films of a Room Temperature Ionic Liquid. *ACS Cent. Sci.* **2018**, *4* (8), 1065–1073. https://doi.org/10.1021/acscentsci.8b00353.

(67) Zhang, Z.; Wells, K. L.; Hyland, E. W. J.; Tan, H.-S. Phase-Cycling Schemes for Pump–Probe Beam Geometry Two-Dimensional Electronic Spectroscopy. *Chemical Physics Letters* **2012**, *550*, 156–161. https://doi.org/10.1016/j.cplett.2012.08.037.

(68) Marroux, H. J. B.; Orr-Ewing, A. J. Distinguishing Population and Coherence Transfer Pathways in a Metal Dicarbonyl Complex Using Pulse-Shaped Two-Dimensional Infrared Spectroscopy. *J. Phys. Chem. B* **2016**, *120* (17), 4125–4130. https://doi.org/10.1021/acs.jpcb.6b02979.

(69) Khalil, M.; Demirdöven, N.; Tokmakoff, A. Vibrational Coherence Transfer Characterized with Fourier-Transform 2D IR Spectroscopy. *J. Chem. Phys.* **2004**, *121* (1), 362. https://doi.org/10.1063/1.1756870.

(70) Baiz, C. R.; Kubarych, K. J.; Geva, E. Molecular Theory and Simulation of Coherence Transfer in Metal Carbonyls and Its Signature on Multidimensional Infrared Spectra. *J. Phys. Chem. B* **2011**, *115* (18), 5322–5339. https://doi.org/10.1021/jp109357d.

(71) Eckert, P. A.; Kubarych, K. J. Vibrational Coherence Transfer Illuminates Dark Modes in Models of the FeFe Hydrogenase Active Site. *J. Chem. Phys.* **2019**, *151* (5), 054307. https://doi.org/10.1063/1.5111016.

(72) Hamm, Peter Zanni, M. *Concepts and Methods of 2D Infrared Spectroscopy*; Cambridge University Press, 2011.

(73) Guo, Q.; Pagano, P.; Li, Y.-L.; Kohen, A.; Cheatum, C. M. Line Shape Analysis of Two-Dimensional Infrared Spectra. *The Journal of Chemical Physics* **2015**, *142* (21), 212427. https://doi.org/10.1063/1.4918350.

(74) Roberts, S. T.; Loparo, J. J.; Tokmakoff, A. Characterization of Spectral Diffusion from Two-Dimensional Line Shapes. *The Journal of Chemical Physics* **2006**, *125* (8), 084502. https://doi.org/10.1063/1.2232271.

(75) Fenn, E. E.; Fayer, M. D. Extracting 2D IR Frequency-Frequency Correlation Functions from Two Component Systems. *The Journal of Chemical Physics* **2011**, *135* (7), 074502. https://doi.org/10.1063/1.3625278.

(76) Giammanco, C. H.; Kramer, P. L.; Wong, D. B.; Fayer, M. D. Water Dynamics in 1-Alkyl-3-Methylimidazolium Tetrafluoroborate Ionic Liquids. *J. Phys. Chem. B* **2016**, *120* (44), 11523–11538. https://doi.org/10.1021/acs.jpcb.6b08410.

(77) Lakowicz, J. R. *Principles of Fluorescence Spectroscopy*, 3rd ed.; Springer: New York, 2006.

(78) Tao, T. Time-Dependent Fluorescence Depolarization and Brownian Rotational Diffusion Coefficients of Macromolecules. *Biopolymers* **1969**, *8* (5), 609–632. https://doi.org/10.1002/bip.1969.360080505.

(79) Lipari, G.; Szabo, A. Model-Free Approach to the Interpretation of Nuclear Magnetic Resonance Relaxation in Macromolecules. 1. Theory and Range of Validity. *J. Am. Chem. Soc.* **1982**, *104* (17), 4546–4559. https://doi.org/10.1021/ja00381a009.

(80) Lipari, G.; Szabo, A. Effect of Librational Motion on Fluorescence Depolarization and Nuclear Magnetic Resonance Relaxation in Macromolecules and Membranes. *Biophysical Journal* **1980**, *30* (3), 489–506. https://doi.org/10.1016/S0006-3495(80)85109-5.

(81) Quitevis, E. L.; Marcus, A. H.; Fayer, M. D. Dynamics of Ionic Lipophilic Probes in Micelles: Picosecond Fluorescence Depolarization Measurements. *J. Phys. Chem.* **1993**, *97* (21), 5762–5769. https://doi.org/10.1021/j100123a049.

(82) Tan, H.-S.; Piletic, I. R.; Fayer, M. D. Orientational Dynamics of Water Confined on a Nanometer Length Scale in Reverse Micelles. *The Journal of Chemical Physics* **2005**, *122* (17), 174501. https://doi.org/10.1063/1.1883605.

(83) Tamimi, A.; Fayer, M. D. Ionic Liquid Dynamics Measured with 2D IR and IR Pump–Probe Experiments on a Linear Anion and the Influence of Potassium Cations. *J. Phys. Chem. B* **2016**, *120* (26), 5842–5854. https://doi.org/10.1021/acs.jpcb.6b00409.

(84) Luther, B. M.; Tracy, K. M.; Gerrity, M.; Brown, S.; Krummel, A. T. 2D IR Spectroscopy at 100 KHz Utilizing a Mid- IR OPCPA Laser Source. *Optics Express* **2016**, *24* (4), 10095–10100. https://doi.org/10.1364/OE.24.004117.

(85) Powers, P. E. *Fundamentals of Nonlinear Optics*; CRC Press: Boca Raton, 2015.

(86) Trebino, R. *Frequency-Resolved Optical Gating: The Measurement of Ultrashort Laser Pulses*; Springer Science + Business Media: New York, 2000.

(87) Thorlabs. Periodically Poled Lithium Niobate (PPLN) - Tutorial. *Catalog* **2014**, 686–690.

(88) Weiner, A. M. Ultrafast Optical Pulse Shaping: A Tutorial Review. *Optics Communications* **2011**, *284* (15), 3669–3692. https://doi.org/10.1016/j.optcom.2011.03.084.

(89) Baiz, C. R.; Schach, D.; Tokmakoff, A. Ultrafast 2D IR Microscopy. *Optics Express* **2014**, *22* (15), 875–885. https://doi.org/10.1364/OE.22.018724.

(90) An, S. J.; Li, J.; Daniel, C.; Mohanty, D.; Nagpure, S.; Wood, D. L. The State of Understanding of the Lithium-Ion-Battery Graphite Solid Electrolyte Interphase (SEI) and Its Relationship to Formation Cycling. *Carbon* **2016**, *105*, 52–76. https://doi.org/10.1016/j.carbon.2016.04.008.

(91) Roy, P.; Srivastava, S. K. Nanostructured Anode Materials for Lithium Ion Batteries. *J. Mater. Chem. A* **2015**, *3* (6), 2454–2484. https://doi.org/10.1039/C4TA04980B.

(92) Jackson, E. D.; Prieto, A. L. Copper Antimonide Nanowire Array Lithium Ion Anodes Stabilized by Electrolyte Additives. *ACS Applied Materials & Interfaces* **2016**, *8* (44), 30379–30386. https://doi.org/10.1021/acsami.6b08033.

(93) Lim, J.; Lee, K.-K.; Liang, C.; Park, K.-H.; Kim, M.; Kwak, K.; Cho, M. Two-Dimensional Infrared Spectroscopy and Molecular Dynamics Simulation Studies of Nonaqueous Lithium Ion Battery Electrolytes. *J. Phys. Chem. B* **2019**, *123* (31), 6651–6663. https://doi.org/10.1021/acs.jpcb.9b02026.

(94) Fulfer, K. D.; Kuroda, D. G. Ion Speciation of Lithium Hexafluorophosphate in Dimethyl Carbonate Solutions: An Infrared Spectroscopy Study. *Phys. Chem. Chem. Phys.* **2018**, *20* (35), 22710–22718. https://doi.org/10.1039/C8CP03315C.

(95) Robben, K. C.; Cheatum, C. M. Edge-Pixel Referencing Suppresses Correlated Baseline Noise in Heterodyned Spectroscopies. *J. Chem. Phys.* **2020**, *152* (9), 094201. https://doi.org/10.1063/1.5134987.

(96) Lavalette, D.; Tétreau, C.; Tourbez, M.; Blouquit, Y. Microscopic Viscosity and Rotational Diffusion of Proteins in a Macromolecular Environment. *Biophysical Journal* **1999**, *76* (5), 2744–2751. https://doi.org/10.1016/S0006-3495(99)77427-8.

(97) Alms, G. R.; Bauer, D. R.; Brauman, J. I.; Pecora, R. Depolarized Rayleigh Scattering and Orientational Relaxation of Molecules in Solution. I. Benzene, Toluene, and *Para* -xylene. *The Journal of Chemical Physics* **1973**, *58* (12), 5570–5578. https://doi.org/10.1063/1.1679181.

(98) Bauer, D. R.; Brauman, J. I.; Pecora, R. Molecular Reorientation in Liquids. Experimental Test of Hydrodynamic Models. *J. Am. Chem. Soc.* **1974**, *96* (22), 6840–6843. https://doi.org/10.1021/ja00829a004.

(99) Maiti, A.; Kumar, A.; Rogers, R. D. Water-Clustering in Hygroscopic Ionic Liquids—an Implicit Solvent Analysis. *Phys. Chem. Chem. Phys.* **2012**, *14* (15), 5139. https://doi.org/10.1039/c2cp00010e.

(100) Chen, Y.; Cao, Y.; Lu, X.; Zhao, C.; Yan, C.; Mu, T. Water Sorption in Protic Ionic Liquids: Correlation between Hygroscopicity and Polarity. *New J. Chem.* **2013**, *37* (7), 1959. https://doi.org/10.1039/c3nj00213f.

(101) Anaredy, R. S.; Lucio, A. J.; Shaw, S. K. Adventitious Water Sorption in a Hydrophilic and a Hydrophobic Ionic Liquid: Analysis and Implications. *ACS Omega* **2016**, *1* (3), 407–416. https://doi.org/10.1021/acsomega.6b00104.

(102) Ren, S.; Hou, Y.; Wu, W.; Liu, W. Purification of Ionic Liquids: Sweeping Solvents by Nitrogen. *J. Chem. Eng. Data* **2010**, *55* (11), 5074–5077. https://doi.org/10.1021/je100641a.

(103) Zhao, C.; Bond, A. M.; Lu, X. Determination of Water in Room Temperature Ionic Liquids by Cathodic Stripping Voltammetry at a Gold Electrode. *Anal. Chem.* **2012**, *84* (6), 2784–2791. https://doi.org/10.1021/ac2031173.

(104) Dutta, S.; Ren, Z.; Brinzer, T.; Garrett-Roe, S. Two-Dimensional Ultrafast Vibrational Spectroscopy of Azides in Ionic Liquids Reveals Solute-Specific Solvation. *Phys. Chem. Chem. Phys.* **2015**, *17* (40), 26575–26579. https://doi.org/10.1039/C5CP02119G.

(105) Kramer, P. L.; Giammanco, C. H.; Fayer, M. D. Dynamics of Water, Methanol, and Ethanol in a Room Temperature Ionic Liquid. *Journal of Chemical Physics* **2015**, *142* (21), 212408–212408. https://doi.org/10.1063/1.4914156.

(106) Tamimi, A.; Fayer, M. D. Ionic Liquid Dynamics Measured with 2D IR and IR Pump–Probe Experiments on a Linear Anion and the Influence of Potassium Cations. *J. Phys. Chem. B* **2016**, *120* (26), 5842–5854. https://doi.org/10.1021/acs.jpcb.6b00409.

(107) Guchhait, B.; Tibbetts, C. A.; Tracy, K. M.; Luther, B. M.; Krummel, A. T. Ultrafast Vibrational Dynamics of a Trigonal Planar Anionic Probe in Ionic Liquids (ILs): A Two-Dimensional Infrared (2DIR) Spectroscopic Investigation. *J. Chem. Phys.* **2020**, *152* (16), 164501. https://doi.org/10.1063/1.5141751.

(108) Yamada, S. A.; Bailey, H. E.; Tamimi, A.; Li, C.; Fayer, M. D. Dynamics in a Room-Temperature Ionic Liquid from the Cation Perspective: 2D IR Vibrational Echo Spectroscopy. *J. Am. Chem. Soc.* **2017**, *139* (6), 2408–2420. https://doi.org/10.1021/jacs.6b12011.

(109) Johnson, C. A.; Parker, A. W.; Donaldson, P. M.; Garrett-Roe, S. An Ultrafast Vibrational Study of Dynamical Heterogeneity in the Protic Ionic Liquid Ethyl-Ammonium Nitrate. I. Room Temperature Dynamics. *J. Chem. Phys.* **2021**, *154* (13), 134502. https://doi.org/10.1063/5.0044822.

(110) Ren, Z.; Brinzer, T.; Dutta, S.; Garrett-Roe, S. Thiocyanate as a Local Probe of Ultrafast Structure and Dynamics in Imidazolium-Based Ionic Liquids: Water-Induced Heterogeneity and Cation-Induced Ion Pairing. *J. Phys. Chem. B* **2015**, *119* (13), 4699–4712. https://doi.org/10.1021/jp512851v.

(111) Wei, Q.; Zhang, M.; Zhou, D.; Li, X.; Bian, H.; Fang, Y. Ultrafast Hydrogen Bond Exchanging between Water and Anions in Concentrated Ionic Liquid Aqueous Solutions. *J. Phys. Chem. B* **2019**, *123* (22), 4766–4775. https://doi.org/10.1021/acs.jpcb.9b03504.

(112) Luther, B. M.; Tracy, K. M.; Gerrity, M.; Brown, S.; Krummel, A. T. 2D IR Spectroscopy at 100 KHz Utilizing a Mid- IR OPCPA Laser Source. *Optics Express* **2016**, *24* (4), 10095–10100. https://doi.org/10.1364/OE.24.004117.

(113) Baiz, C. R.; Schach, D.; Tokmakoff, A. Ultrafast 2D IR Microscopy. *Optics Express* **2014**, *22* (15), 875–885. https://doi.org/10.1364/OE.22.018724.

(114) Feng, Y.; Vinogradov, I.; Ge, N.-H. General Noise Suppression Scheme with Reference Detection in Heterodyne Nonlinear Spectroscopy. *Opt. Express* **2017**, *25* (21), 26262. https://doi.org/10.1364/OE.25.026262.

(115) Hunger, J.; Roy, S.; Grechko, M.; Bonn, M. Dynamics of Dicyanamide in Ionic Liquids Is Dominated by Local Interactions. *J. Phys. Chem. B* **2019**, *123* (8), 1831–1839. https://doi.org/10.1021/acs.jpcb.8b10849.

(116) Lee, K.-K.; Park, K.-H.; Choi, J.-H.; Ha, J.-H.; Jeon, S.-J.; Cho, M. Ultrafast Vibrational Spectroscopy of Cyanophenols. *J. Phys. Chem. A* **2010**, *114* (8), 2757–2767. https://doi.org/10.1021/jp908696k.

(117) Vinogradov, I.; Feng, Y.; Kumar, S. K. K.; Guo, C.; Udagawa, N. S.; Ge, N.-H. Ultrafast Vibrational Dynamics of the Tyrosine Ring Mode and Its Application to Enkephalin Insertion into Phospholipid Membranes as Probed by Two-Dimensional Infrared Spectroscopy. *J. Chem. Phys.* **2021**, *155* (3), 035102. https://doi.org/10.1063/5.0054428.

(118) Khalil, M.; Demird??ven, N.; Tokmakoff, A. Coherent 2D IR Spectroscopy: Molecular Structure and Dynamics in Solution. *Journal of Physical Chemistry A* **2003**, *107* (27), 5258–5279. https://doi.org/10.1021/jp0219247.

(119) Kabanda, M. M.; Bahadur, I. Hydrogen Bonding between 1-Ethyl-3-Methyl-Imidazolium Dicyanamide Ionic Liquid and Selected Co-Solvents with Varying Polarity: A DFT Study. *Journal of Molecular Liquids* **2022**, 119418. https://doi.org/10.1016/j.molliq.2022.119418.

(120) Liu, W.; Zhao, T.; Zhang, Y.; Wang, H.; Yu, M. The Physical Properties of Aqueous Solutions of the Ionic Liquid [BMIM][BF4]. *J Solution Chem* **2006**, *35* (10), 1337–1346. https://doi.org/10.1007/s10953-006-9064-7.

(121) Triolo, A.; Russina, O.; Bleif, H.-J.; Di Cola, E. Nanoscale Segregation in Room Temperature Ionic Liquids. *J. Phys. Chem. B* **2007**, *111* (18), 4641–4644. https://doi.org/10.1021/jp067705t.

(122) Jagoda-Cwiklik, B.; Wang, X.-B.; Woo, H.-K.; Yang, J.; Wang, G.-J.; Zhou, M.; Jungwirth, P.; Wang, L.-S. Microsolvation of the Dicyanamide Anion: $[N(CN)_2^-](H_2O)_n$ ($n = 0-12$). *J. Phys. Chem. A* **2007**, *111* (32), 7719–7725. https://doi.org/10.1021/jp071832n.

(123) Moreno, M.; Castiglione, F.; Mele, A.; Pasqui, C.; Raos, G. Interaction of Water with the Model Ionic Liquid [Bmim][BF_4]: Molecular Dynamics Simulations and Comparison with NMR Data. *J. Phys. Chem. B* **2008**, *112* (26), 7826–7836. https://doi.org/10.1021/jp800383g.

(124) Tiwari, V.; Matutes, Y. A.; Gardiner, A. T.; Jansen, T. L. C.; Cogdell, R. J.; Ogilvie, J. P. Spatially-Resolved Fluorescence-Detected Two-Dimensional Electronic Spectroscopy Probes Varying Excitonic Structure in Photosynthetic Bacteria. *Nat Commun* **2018**, *9* (1), 4219. https://doi.org/10.1038/s41467-018-06619-x.

(125) Goetz, S.; Li, D.; Kolb, V.; Pflaum, J.; Brixner, T. Coherent Two-Dimensional Fluorescence Micro-Spectroscopy. *Opt. Express, OE* **2018**, *26* (4), 3915–3925. https://doi.org/10.1364/OE.26.003915.

(126) Jones, A. C.; Kearns, N. M.; Bohlmann Kunz, M.; Flach, J. T.; Zanni, M. T. Multidimensional Spectroscopy on the Microscale: Development of a Multimodal Imaging System Incorporating 2D White-Light Spectroscopy, Broadband Transient Absorption, and Atomic Force Microscopy. *J. Phys. Chem. A* **2019**, *123* (50), 10824–10836. https://doi.org/10.1021/acs.jpca.9b09099.

(127) Baiz, C. R.; Schach, D.; Tokmakoff, A. Ultrafast 2D IR Microscopy. *Opt. Express* **2014**, *22* (15), 18724. https://doi.org/10.1364/OE.22.018724.

(128) Ostrander, J. S.; Serrano, A. L.; Ghosh, A.; Zanni, M. T. Spatially Resolved Two-Dimensional Infrared Spectroscopy via Wide- Field Microscopy. *ACS Photonics* **2016**, *3*, 1315–1323. https://doi.org/10.1021/acsphotonics.6b00297.

(129) Tracy, K. M.; Guchhait, B.; Tibbetts, C.; Luther, B. M.; Krummel, A. Visualizing Chemical Dynamics in an Ionic Liquid Microdroplet Using Ultrafast 2D IR Microscopy. **2019**. https://doi.org/10.26434/chemrxiv.9936464.v1.

(130) Hoffman, D. J.; Sokolowsky, K. P.; Fayer, M. D. Direct Observation of Dynamic Crossover in Fragile Molecular Glass Formers with 2D IR Vibrational Echo Spectroscopy. *The Journal of Chemical Physics* **2017**, *146* (12), 124505. https://doi.org/10.1063/1.4978852.

(131) Thämer, M.; Marco, L. D.; Ramasesha, K.; Mandal, A.; Tokmakoff, A. Ultrafast 2D IR Spectroscopy of the Excess Proton in Liquid Water. *Science* **2015**, *350* (6256), 78–82. https://doi.org/10.1126/science.aab3908.

(132) King, J. T.; Ross, M. R.; Kubarych, K. J. Ultrafast $\ensuremath{\alpha}$-Like Relaxation of a Fragile Glass-Forming Liquid Measured Using Two-Dimensional Infrared Spectroscopy. *Phys. Rev. Lett.* **2012**, *108* (15), 157401. https://doi.org/10.1103/PhysRevLett.108.157401.

(133) Terranova, Z. L.; Corcelli, S. A. On the Mechanism of Solvation Dynamics in Imidazolium-Based Ionic Liquids. *The Journal of Physical Chemistry B* **2013**, *117* (49), 15659–15666. https://doi.org/10.1021/jp406419y.

(134) Daly, C. A.; Berquist, E. J.; Brinzer, T.; Garrett-Roe, S.; Lambrecht, D. S.; Corcelli, S. A. Modeling Carbon Dioxide Vibrational Frequencies in Ionic Liquids: II. Spectroscopic Map. *The Journal of Physical Chemistry B* **2016**, *120* (49), 12633–12642. https://doi.org/10.1021/acs.jpcb.6b09509.

(135) Berquist, E. J.; Daly, C. A.; Brinzer, T.; Bullard, K. K.; Campbell, Z. M.; Corcelli, S. A.; Garrett-Roe, S.; Lambrecht, D. S. Modeling Carbon Dioxide Vibrational Frequencies in Ionic Liquids: I. Ab Initio Calculations. *J. Phys. Chem. B* **2017**, *121* (1), 208–220. https://doi.org/10.1021/acs.jpcb.6b09489.

(136) Azov, V. A.; Egorova, K. S.; Seitkalieva, M. M.; Kashin, A. S.; Ananikov, V. P. "Solvent-in-Salt" Systems for Design of New Materials in Chemistry, Biology and Energy Research. *Chemical Society Reviews* **2018**, *47* (4), 1250–1284. https://doi.org/10.1039/C7CS00547D.

(137) Greaves, T. L.; Drummond, C. J. Protic Ionic Liquids: Evolving Structure–Property Relationships and Expanding Applications. *Chemical Reviews* **2015**, *115* (20), 11379–11448. https://doi.org/10.1021/acs.chemrev.5b00158.

(138) Hallett, J. P.; Welton, T. Room-Temperature Ionic Liquids: Solvents for Synthesis and Catalysis. 2. *Chemical Reviews* **2011**, *111* (5), 3508–3576. https://doi.org/10.1021/cr1003248.

(139) Batista, M. L. S.; Passos, H.; Henriques, B. J. M.; Maginn, E. J.; Pinho, S. P.; Freire, M. G.; Gomes, J. R. B.; Coutinho, J. A. P. Why Are Some Cyano-Based Ionic Liquids Better Glucose Solvents than Water? *Physical Chemistry Chemical Physics* **2016**, *18* (28), 18958–18970. https://doi.org/10.1039/C6CP02538B.

(140) Hayes, R.; Warr, G. G.; Atkin, R. Structure and Nanostructure in Ionic Liquids. *Chemical Reviews* **2015**, *115* (13), 6357–6426. https://doi.org/10.1021/cr500411q.

(141) Canongia Lopes, J. N. A.; Pádua, A. A. H. Nanostructural Organization in Ionic Liquids. *J. Phys. Chem. B* **2006**, *110* (7), 3330–3335. https://doi.org/10.1021/jp056006y.

(142) Samanta, A. Dynamic Stokes Shift and Excitation Wavelength Dependent Fluorescence of Dipolar Molecules in Room Temperature Ionic Liquids. *J. Phys. Chem. B* **2006**, *110* (28), 13704–13716. https://doi.org/10.1021/jp060441q.

(143) Jr, E. W. C.; Margulis, C. J.; Maroncelli, M.; Wishart, J. F. Ionic Liquids: Structure and Photochemical Reactions. *Annual Review of Physical Chemistry* **2011**, *62* (1), 85–105. https://doi.org/10.1146/annurev-physchem-032210-103421.

(144) Egorova, K. S.; Gordeev, E. G.; Ananikov, V. P. Biological Activity of Ionic Liquids and Their Application in Pharmaceutics and Medicine. *Chem. Rev.* **2017**, *117* (10), 7132–7189. https://doi.org/10.1021/acs.chemrev.6b00562.

(145) Tadesse, H.; Luque, R. Advances on Biomass Pretreatment Using Ionic Liquids: An Overview. *Energy Environ. Sci.* **2011**, *4* (10), 3913–3929. https://doi.org/10.1039/C0EE00667J.

(146) Watanabe, M.; Thomas, M. L.; Zhang, S.; Ueno, K.; Yasuda, T.; Dokko, K. Application of Ionic Liquids to Energy Storage and Conversion Materials and Devices. *Chem. Rev.* **2017**, *117* (10), 7190–7239. https://doi.org/10.1021/acs.chemrev.6b00504.

(147) Lin, R.; Taberna, P.-L.; Fantini, S.; Presser, V.; Pérez, C. R.; Malbosc, F.; Rupesinghe, N. L.; Teo, K. B. K.; Gogotsi, Y.; Simon, P. Capacitive Energy Storage from −50 to 100 °C Using an Ionic Liquid Electrolyte. *J. Phys. Chem. Lett.* **2011**, *2* (19), 2396–2401. https://doi.org/10.1021/jz201065t.

(148) Plechkova, N. V.; Seddon, K. R. Applications of Ionic Liquids in the Chemical Industry. *Chem. Soc. Rev.* **2007**, *37* (1), 123–150. https://doi.org/10.1039/B006677J.

(149) Smiglak, M.; Metlen, A.; Rogers, R. D. The Second Evolution of Ionic Liquids: From Solvents and Separations to Advanced Materials—Energetic Examples from the Ionic Liquid Cookbook. *Acc. Chem. Res.* **2007**, *40* (11), 1182–1192. https://doi.org/10.1021/ar7001304.

(150) Tamimi, A.; Bailey, H. E.; Fayer, M. D. Alkyl Chain Length Dependence of the Dynamics and Structure in the Ionic Regions of Room-Temperature Ionic Liquids. *J. Phys. Chem. B* **2016**, *120* (30), 7488–7501. https://doi.org/10.1021/acs.jpcb.6b05397.

(151) Ren, Z.; Ivanova, A. S.; Couchot-Vore, D.; Garrett-Roe, S. Ultrafast Structure and Dynamics in Ionic Liquids: 2D-IR Spectroscopy Probes the Molecular Origin of Viscosity. *J. Phys. Chem. Lett.* **2014**, *5* (9), 1541–1546. https://doi.org/10.1021/jz500372f.

(152) Khatun, S.; Castner, E. W. Ionic Liquid–Solute Interactions Studied by 2D NOE NMR Spectroscopy. *The Journal of Physical Chemistry B* **2015**, *119* (29), 9225–9235. https://doi.org/10.1021/jp509861g.

(153) Amith, W. D.; Hettige, J. J.; Castner, E. W.; Margulis, C. J. Structures of Ionic Liquids Having Both Anionic and Cationic Octyl Tails: Lamellar Vacuum Interface vs Sponge-Like Bulk Order. *The Journal of Physical Chemistry Letters* **2016**, *7* (19), 3785–3790. https://doi.org/10.1021/acs.jpclett.6b01763.

(154) Brooks, N. J.; Castiglione, F.; Doherty, C. M.; Dolan, A.; Hill, A. J.; Hunt, P. A.; Matthews, R. P.; Mauri, M.; Mele, A.; Simonutti, R.; Villar-Garcia, I. J.; Weber, C. C.; Welton, T. Linking the Structures, Free Volumes, and Properties of Ionic Liquid Mixtures. *Chemical Science* **2017**, *8* (9), 6359–6374. https://doi.org/10.1039/C7SC01407D.

(155) Gehrke, S.; von Domaros, M.; Clark, R.; Hollóczki, O.; Brehm, M.; Welton, T.; Luzar, A.; Kirchner, B. Structure and Lifetimes in Ionic Liquids and Their Mixtures. *Faraday Discussions* **2018**, *206*, 219–245. https://doi.org/10.1039/C7FD00166E.

(156) Zhang, X.-X.; Breffke, J.; Ernsting, N. P.; Maroncelli, M. Observations of Probe Dependence of the Solvation Dynamics in Ionic Liquids. *Physical Chemistry Chemical Physics* **2015**, *17* (19), 12949–12956. https://doi.org/10.1039/C5CP00814J.

(157) Prince, B. D.; Tiruppathi, P.; Bemish, R. J.; Chiu, Y.-H.; Maginn, E. J. Molecular Dynamics Simulations of 1-Ethyl-3-Methylimidazolium Bis[(Trifluoromethyl)Sulfonyl]Imide Clusters and Nanodrops. *The Journal of Physical Chemistry A* **2015**, *119* (2), 352–368. https://doi.org/10.1021/jp507073e.

(158) Baldelli, S. Interfacial Structure of Room-Temperature Ionic Liquids at the Solid–Liquid Interface as Probed by Sum Frequency Generation Spectroscopy. *J. Phys. Chem. Lett.* **2013**, *4* (2), 244–252. https://doi.org/10.1021/jz301835j.

(159) Tamimi, A.; Fayer, M. D. Ionic Liquid Dynamics Measured with 2D IR and IR Pump–Probe Experiments on a Linear Anion and the Influence of Potassium Cations. *J. Phys. Chem. B* **2016**, *120* (26), 5842–5854. https://doi.org/10.1021/acs.jpcb.6b00409.

(160) Shin, J. Y.; Yamada, S. A.; Fayer, M. D. Dynamics of a Room Temperature Ionic Liquid in Supported Ionic Liquid Membranes vs the Bulk Liquid: 2D IR and Polarized IR Pump–Probe Experiments. *J. Am. Chem. Soc.* **2017**, *139* (1), 311–323. https://doi.org/10.1021/jacs.6b10695.

(161) Ren, Z.; Brinzer, T.; Dutta, S.; Garrett-Roe, S. Thiocyanate as a Local Probe of Ultrafast Structure and Dynamics in Imidazolium-Based Ionic Liquids: Water-Induced Heterogeneity and Cation-Induced Ion Pairing. *J. Phys. Chem. B* **2015**, *119* (13), 4699–4712. https://doi.org/10.1021/jp512851v.

(162) Dutta, S.; Ren, Z.; Brinzer, T.; Garrett-Roe, S. Two-Dimensional Ultrafast Vibrational Spectroscopy of Azides in Ionic Liquids Reveals Solute-Specific Solvation. *Phys. Chem. Chem. Phys.* **2015**, *17* (40), 26575–26579. https://doi.org/10.1039/C5CP02119G.

(163) K. Kashyap, H.; J. Hettige, J.; R. Annapureddy, H. V.; J. Margulis, C. SAXS Anti-Peaks Reveal the Length-Scales of Dual Positive–Negative and Polar–Apolar Ordering in Room-Temperature

Ionic Liquids. *Chemical Communications* **2012**, *48* (42), 5103–5105. https://doi.org/10.1039/C2CC30609C.

(164) Amith, W. D.; Hettige, J. J.; Castner, E. W.; Margulis, C. J. Structures of Ionic Liquids Having Both Anionic and Cationic Octyl Tails: Lamellar Vacuum Interface vs Sponge-Like Bulk Order. *J. Phys. Chem. Lett.* **2016**, *7* (19), 3785–3790. https://doi.org/10.1021/acs.jpclett.6b01763.

(165) Paredes, X.; Fernández, J.; Pádua, A. A. H.; Malfreyt, P.; Malberg, F.; Kirchner, B.; Pensado, A. S. Using Molecular Simulation to Understand the Structure of [C2C1im]+–Alkylsulfate Ionic Liquids: Bulk and Liquid–Vapor Interfaces. *J. Phys. Chem. B* **2012**, *116* (48), 14159–14170. https://doi.org/10.1021/jp309532t.

(166) Anaredy, R. S.; Shaw, S. K. Long-Range Ordering of Ionic Liquid Fluid Films. *Langmuir* **2016**, *32* (20), 5147–5154. https://doi.org/10.1021/acs.langmuir.6b00304.

(167) Jurado, L. A.; Kim, H.; Arcifa, A.; Rossi, A.; Leal, C.; Spencer, N. D.; Espinosa-Marzal, R. M. Irreversible Structural Change of a Dry Ionic Liquid under Nanoconfinement. *Phys. Chem. Chem. Phys.* **2015**, *17* (20), 13613–13624. https://doi.org/10.1039/C4CP05592F.

(168) Shim, S.-H.; Zanni, M. T. How to Turn Your Pump–Probe Instrument into a Multidimensional Spectrometer: 2D IR and Vis Spectroscopies via Pulse Shaping. *Phys. Chem. Chem. Phys.* **2009**, *11* (5), 748–761. https://doi.org/10.1039/B813817F.

(169) Nishida, J.; Tamimi, A.; Fei, H.; Pullen, S.; Ott, S.; Cohen, S. M.; Fayer, M. D. Structural Dynamics inside a Functionalized Metal–Organic Framework Probed by Ultrafast 2D IR Spectroscopy. *PNAS* **2014**, *111* (52), 18442–18447. https://doi.org/10.1073/pnas.1422194112.

(170) Kanal, F.; Keiber, S.; Eck, R.; Brixner, T. 100-KHz Shot-to-Shot Broadband Data Acquisition for High-Repetition-Rate Pump–Probe Spectroscopy. *Opt. Express, OE* **2014**, *22* (14), 16965–16975. https://doi.org/10.1364/OE.22.016965.

(171) Luther, B. M.; Tracy, K. M.; Gerrity, M.; Brown, S.; Krummel, A. T. 2D IR Spectroscopy at 100 KHz Utilizing a Mid-IR OPCPA Laser Source. *Opt. Express, OE* **2016**, *24* (4), 4117–4127. https://doi.org/10.1364/OE.24.004117.

(172) Donaldson, P. M.; Greetham, G. M.; Shaw, D. J.; Parker, A. W.; Towrie, M. A 100 KHz Pulse Shaping 2D-IR Spectrometer Based on Dual Yb:KGW Amplifiers. *The Journal of Physical Chemistry A* **2018**, *122* (3), 780–787. https://doi.org/10.1021/acs.jpca.7b10259.

(173) Kearns, N. M.; Mehlenbacher, R. D.; Jones, A. C.; Zanni, M. T. Broadband 2D Electronic Spectrometer Using White Light and Pulse Shaping: Noise and Signal Evaluation at 1 and 100 KHz. *Opt. Express, OE* **2017**, *25* (7), 7869–7883. https://doi.org/10.1364/OE.25.007869.

(174) Tracy, K. M.; Barich, M. V.; Carver, C. L.; Luther, B. M.; Krummel, A. T. High-Throughput Two-Dimensional Infrared (2D IR) Spectroscopy Achieved by Interfacing Microfluidic Technology with a High Repetition Rate 2D IR Spectrometer. *J. Phys. Chem. Lett.* **2016**, *7* (23), 4865–4870. https://doi.org/10.1021/acs.jpclett.6b01941.

(175) Weiner, A. M. Femtosecond Pulse Shaping Using Spatial Light Modulators. *Review of Scientific Instruments* **2000**, *71* (5), 1929–1960. https://doi.org/10.1063/1.1150614.

(176) Cervetto, V.; Helbing, J.; Bredenbeck, J.; Hamm, P. Double-Resonance versus Pulsed Fourier Transform Two-Dimensional Infrared Spectroscopy: An Experimental and Theoretical Comparison. *The Journal of Chemical Physics* **2004**, *121* (12), 5935–5942. https://doi.org/10.1063/1.1778163.

(177) Kwak, K.; Park, S.; Finkelstein, I. J.; Fayer, M. D. Frequency-Frequency Correlation Functions and Apodization in Two-Dimensional Infrared Vibrational Echo Spectroscopy: A New Approach. *The Journal of Chemical Physics* **2007**, *127* (12), 124503. https://doi.org/10.1063/1.2772269.

(178) Johnson, C. A.; Parker, A. W.; Donaldson, P. M.; Garrett-Roe, S. An Ultrafast Vibrational Study of Dynamical Heterogeneity in the Protic Ionic Liquid Ethyl-Ammonium Nitrate. I. Room Temperature Dynamics. *J. Chem. Phys.* **2021**, *154* (13), 134502. https://doi.org/10.1063/5.0044822.

(179) Feng, Y.; Vinogradov, I.; Ge, N.-H. General Noise Suppression Scheme with Reference Detection in Heterodyne Nonlinear Spectroscopy. *Opt. Express, OE* **2017**, *25* (21), 26262–26279. https://doi.org/10.1364/OE.25.026262.

(180) Feng, Y.; Vinogradov, I.; Ge, N.-H. Optimized Noise Reduction Scheme for Heterodyne Spectroscopy Using Array Detectors. *Opt. Express, OE* **2019**, *27* (15), 20323–20346. https://doi.org/10.1364/OE.27.020323.

(181) Robben, K. C.; Cheatum, C. M. Edge-Pixel Referencing Suppresses Correlated Baseline Noise in Heterodyned Spectroscopies. *J. Chem. Phys.* **2020**, *152* (9), 094201. https://doi.org/10.1063/1.5134987.

(182) Ostrander, J. S.; Serrano, A. L.; Ghosh, A.; Zanni, M. T. Spatially Resolved Two-Dimensional Infrared Spectroscopy via Wide-Field Microscopy. *ACS Photonics* **2016**, *3* (7), 1315–1323. https://doi.org/10.1021/acsphotonics.6b00297.

(183) Aliaga, C.; Baldelli, S. A Sum Frequency Generation Study of the Room-Temperature Ionic Liquid−Titanium Dioxide Interface. *J. Phys. Chem. C* **2008**, *112* (8), 3064–3072. https://doi.org/10.1021/jp709753r.

(184) Erik Kvaleberg. *Custom colormap*. Custom colormap. https://www.mathworks.com/matlabcentral/fileexchange/42450-custom-colormap (accessed 2021-05-27).

(185) Torriero, A. A. J. Characterization of Decamethylferrocene and Ferrocene in Ionic Liquids: Argon and Vacuum Effect on Their Electrochemical Properties. *Electrochimica Acta* **2014**, *137*, 235–244. https://doi.org/10.1016/j.electacta.2014.06.005.

(186) Torriero, A. A. J.; Howlett, P. C. Ionic Liquid Effects on the Redox Potential of Ferrocene. *Electrochemistry Communications* **2012**, *16* (1), 84–87. https://doi.org/10.1016/j.elecom.2011.12.006.

(187) Frenzel, N.; Hartley, J.; Frisch, G. Voltammetric and Spectroscopic Study of Ferrocene and Hexacyanoferrate and the Suitability of Their Redox Couples as Internal Standards in Ionic Liquids. *Phys. Chem. Chem. Phys.* **2017**, *19* (42), 28841–28852. https://doi.org/10.1039/C7CP05483A.

(188) Thakurathi, M.; Gurung, E.; Cetin, M. M.; Thalangamaarachchige, V. D.; Mayer, M. F.; Korzeniewski, C.; Quitevis, E. L. The Stokes-Einstein Equation and the Diffusion of Ferrocene in Imidazolium-Based Ionic Liquids Studied by Cyclic Voltammetry: Effects of Cation Ion Symmetry and Alkyl Chain Length. *Electrochimica Acta* **2018**, *259*, 245–252. https://doi.org/10.1016/j.electacta.2017.10.149.

(189) Endres, F.; Freyland, W. Electrochemical Scanning Tunneling Microscopy Investigation of HOPG and Silver Electrodeposition on HOPG from the Acid Room-Temperature Molten Salt Aluminum Chloride−1-Methyl-3-Butyl-Imidazolium Chloride. *J. Phys. Chem. B* **1998**, *102* (50), 10229–10233. https://doi.org/10.1021/jp9824048.

(190) Zhang, J.; Bond, A. M. Practical Considerations Associated with Voltammetric Studies in Room Temperature Ionic Liquids. *Analyst* **2005**, *130* (8), 1132. https://doi.org/10.1039/b504721h.

(191) Zhang, J.; Bond, A. M.; Schumann, H.; Sühring, K. Voltammetric Studies on Decaphenylferrocene, Substituted Decaphenylferrocenes, and Their Oxidized Forms in Dichloromethane and Ionic Liquids. *Organometallics* **2005**, *24* (9), 2188–2196. https://doi.org/10.1021/om049117c.

(192) Hultgren, V. M.; Mariotti, A. W. A.; Bond, A. M.; Wedd, A. G. Reference Potential Calibration and Voltammetry at Macrodisk Electrodes of Metallocene Derivatives in the Ionic Liquid [Bmim][PF_6]. *Anal. Chem.* **2002**, *74* (13), 3151–3156. https://doi.org/10.1021/ac015729k.

(193) Brown, R. J. C.; Welton, T.; Dyson, P. J.; Ellis, D. J. 1-Butyl-3-Methylimidazolium Cobalt Tetracarbonyl [Bmim][Co(CO)4]: A Catalytically Active Organometallic Ionic Liquid. *Chem. Commun.* **2001**, No. 18, 1862–1863. https://doi.org/10.1039/b104601m.

(194) Ryan, D. M.; Riechel, T. L.; Welton, T. Electrochemistry of Vanadium Oxides and Oxyhalides in Chloroaluminate Room Temperature Ionic Liquids: Formation of a New Ionic Liquid. *J. Electrochem. Soc.* **2002**, *149* (4), A371. https://doi.org/10.1149/1.1454137.

(195) Snook, G. A.; Best, A. S.; Pandolfo, A. G.; Hollenkamp, A. F. Evaluation of a Ag|Ag+ Reference Electrode for Use in Room Temperature Ionic Liquids. *Electrochemistry Communications* **2006**, *8* (9), 1405–1411. https://doi.org/10.1016/j.elecom.2006.07.004.

(196) Mosby, J. M.; Prieto, A. L. Direct Electrodeposition of Cu $_2$ Sb for Lithium-Ion Battery Anodes. *J. Am. Chem. Soc.* **2008**, *130* (32), 10656–10661. https://doi.org/10.1021/ja801745n.

(197) Schneider, J. D.; Agocs, D. B.; Prieto, A. L. Design of a Sample Transfer Holder to Enable Air-Free X-Ray Photoelectron Spectroscopy. *Chem. Mater.* **2020**, *32* (19), 8091–8096. https://doi.org/10.1021/acs.chemmater.0c01895.

(198) Zheng, J.; Kwak, K.; Fayer, M. D. Ultrafasf 2D IR Vibrational Echo Spectroscopy. *Accounts of Chemical Research* **2007**, *40* (1), 75–83. https://doi.org/10.1021/ar068010d.

(199) Park, S.; Kwak, K.; Fayer, M. D. Ultrafast 2D-IR Vibrational Echo Spectroscopy: A Probe of Molecular Dynamics. *Laser Physics Letters* **2007**, *4* (10), 704–718. https://doi.org/10.1002/lapl.200710046.

(200) Ponder, J. W.; Wu, C.; Ren, P.; Pande, V. S.; Chodera, J. D.; Schnieders, M. J.; Haque, I.; Mobley, D. L.; Lambrecht, D. S.; Distasio, R. A.; Head-Gordon, M.; Clark, G. N. I.; Johnson, M. E.; Head-Gordon, T. Current Status of the AMOEBA Polarizable Force Field. *Journal of Physical Chemistry B* **2010**, *114* (8), 2549–2564. https://doi.org/10.1021/jp910674d.

(201) Wu, J. C.; Chattree, G.; Ren, P. Automation of AMOEBA Polarizable Force Field Parameterization for Small Molecules. *Theoretical Chemistry Accounts* **2012**, *131* (3), 1138. https://doi.org/10.1007/s00214-012-1138-6.

(202) Møller, C.; Plesset, M. S. Note on an Approximation Treatment for Many-Electron Systems. *Physical Review* **1934**, *46* (7), 618–622. https://doi.org/10.1103/PhysRev.46.618.

(203) Dunning, T. H. Gaussian Basis Sets for Use in Correlated Molecular Calculations. I. The Atoms Boron through Neon and Hydrogen. *The Journal of Chemical Physics* **1989**, *90* (2), 1007–1023. https://doi.org/10.1063/1.456153.

(204) Lagardère, L.; Jolly, L. H.; Lipparini, F.; Aviat, F.; Stamm, B.; Jing, Z. F.; Harger, M.; Torabifard, H.; Cisneros, G. A.; Schnieders, M. J.; Gresh, N.; Maday, Y.; Ren, P. Y.; Ponder, J. W.; Piquemal, J. P. Tinker-HP: A Massively Parallel Molecular Dynamics Package for Multiscale Simulations of Large Complex Systems with Advanced Point Dipole Polarizable Force Fields. *Chemical Science* **2018**, *9* (4), 956–972. https://doi.org/10.1039/c7sc04531j.

(205) Harger, M.; Li, D.; Wang, Z.; Dalby, K.; Lagardère, L.; Piquemal, J.-P.; Ponder, J.; Ren, P. Tinker-OpenMM: Absolute and Relative Alchemical Free Energies Using AMOEBA on GPUs. *Journal of Computational Chemistry* **2017**, *38* (23), 2047–2055. https://doi.org/10.1002/jcc.24853.

(206) Zhou, D.; Hao, H.; Ma, Y.; Zhong, H.; Dai, Y.; Cai, K.; Mukherjee, S.; Liu, J.; Bian, H. Specific Host–Guest Interactions in the Crown Ether Complexes with K^+ and NH_4^+ Revealed from the Vibrational Relaxation Dynamics of the Counteranion. *J. Phys. Chem. B* **2020**, *124* (41), 9154–9162. https://doi.org/10.1021/acs.jpcb.0c07032.

(207) Wei, Q.; Zhou, D.; Li, X.; Chen, Y.; Bian, H. Structural Dynamics of Dimethyl Sulfoxide Aqueous Solutions Investigated by Ultrafast Infrared Spectroscopy: Using Thiocyanate Anion as a Local Vibrational Probe. *J. Phys. Chem. B* **2018**, *122* (50), 12131–12138. https://doi.org/10.1021/acs.jpcb.8b10058.

Appendix A

Supplemental Information for Chapter 3

Section 1: Sample Preparation of Organic Carbonate Mixtures

A solution of a 1:1:1 ratio, by mass, of dimethyl carbonate (DMC, Sigma Aldrich, ≥ 99% anhydrous) with diethylene carbonate (DEC, Sigma Aldrich, ≥ 99% anhydrous) and ethylene carbonate (EC) was made. This mixture was used to make a 300 mM methyl thiocyanate (MeSCN) solution and was sonicated for 10 minutes. The cyanate stretch of MeSCN is used as a vibrational probe. Solutions with varied amounts of FEC were made by adding 5, 25, and 50% fluoroethylene carbonate (FEC) (Sigma Aldrich, ≥ 99% anhydrous) by volume and sonicating for 10 minutes. For spectroscopic measurements 25 µL of solution was sandwiched between two 1 mm CaF_2 plates (Crystran) with a 150 µm Teflon spacer (Harricks). For the measurements of the carbonyl region with and without the MeSCN probe, 5 µL of solution was sandwiched between two 1 mm CaF_2 plates with no spacer.

Table A1: *Each experimental sample in terms of the ratio of each carbonate to the probe molecule*

Component	0% FEC by Volume	5% FEC by Volume	25% FEC by Volume	50% FEC by Volume	100% FEC by Volume
	# molecules / MeSCN molecule				
DMC	14	13	10	7	0
DEC	11	10	8	5	0
EC	14	13	11	7	0
FEC	0	2	11	23	45

Section 2: FTIR Measurements

All FTIR measurements were made on a Bruker Optics Vertex 70, with a mid-IR source. The spectral resolution used was 2.0 cm^{-1} and 128 scans were averaged. The cyanate stretch of MeSCN is used as a molecular, vibrational probe for these experiments. Initial FTIR measurements were made to probe the response of the cyanate stretch in each solution of carbonates. It is seen that the vibrational mode has a slight shift to higher frequencies, broadening with increasing amounts of FEC (Figure A2). The FWHM of the peaks as a function of FEC is shown in Figure A3. This shift is minimal and within the spectral

resolution of the measurement (2.0 cm^{-1}). FTIR were fit with a single gaussian function using the Trust Region algorithm via the Matlab curve fitting toolbox.

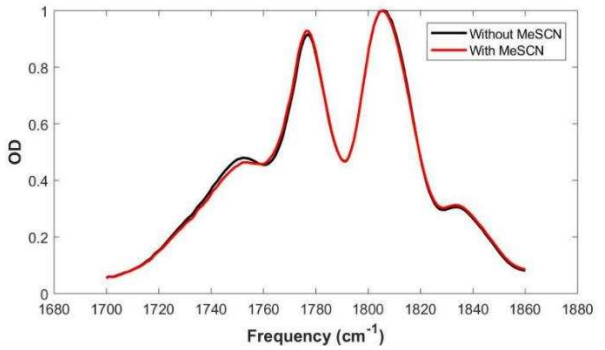

Figure A1: *Self-normalized FTIR spectra for carbonyl region of the 1:1:1 mixture of DMC:DEC:EC in black. In red is the 1:1:1 mixture of DMC:DEC:EC with 300 mM MeSCN*

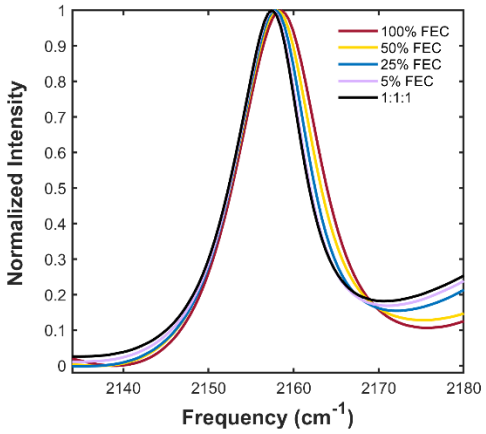

Figure A2: *Linear FTIR spectra for FEC in red, 50% FEC in gold, 25% FEC in blue, 5% FEC in purple and the 1:1:1 mixture of DMC:DEC:EC in black.*

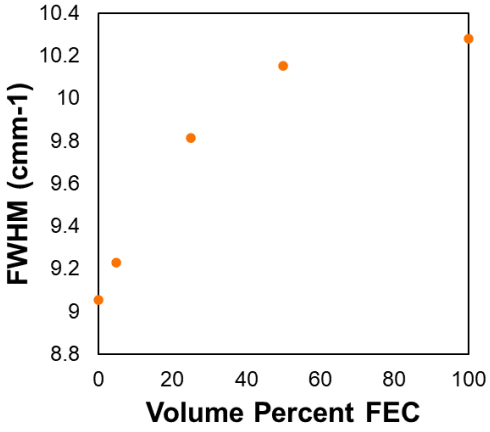

Figure A3: *The fit FWHM as a function of the volume percentage of FEC in the carbonate mixture.*

Section 3: Battery Control Experiment with MeSCN Probe

The working electrode is electrodeposited Cu_2Sb and the counter pseudo reference electrode is sodium metal.[196] A rendition of this half-cell is presented in Figure A4. The electrolyte solution is made up of the four carbonates listed Section S1A (with 5% by volume FEC) and 1M sodium perchlorate (Sigma Aldrich, ACS Reagent, ≥ 99 %) as the supporting electrolyte. The electrolyte solution was doped to be 300 mM MeSCN. The battery was cycled five times at a rate of C/5 between 0.01 and 1.5V vs. Na/Na^+ using Arbin BT2000 battery cycler. During discharge, the chemical reaction at the anode is the oxidation of sodium (Equation A1). Conversely the chemical reaction at the cathode during discharge is sodiation of antimony (Equation A2). During charge, the reverse reactions take place.

$$Na^0 \rightarrow Na^+ + e^- \quad \text{(A1)}$$

$$Sb^0 + 3Na^+ + 3e^- \rightarrow Na_3Sb \quad \text{(A2)}$$

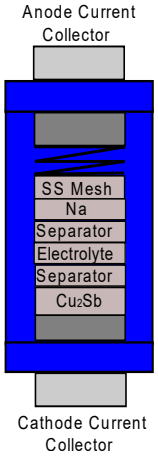

Figure A4: *Diagram of the battery setup. SS Mesh is stainless steel mesh. The separator is polyethylene plastic. The electrolyte is added to glass fiber, in between the separators.*

Section 4: Anode Characterization via X-ray photoelectron spectroscopy (XPS)

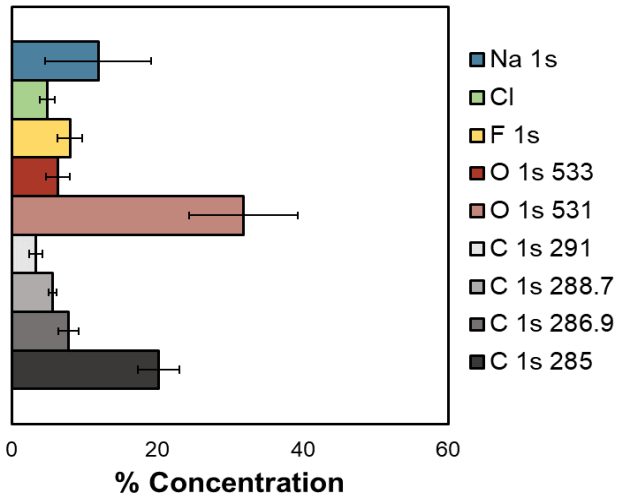

Figure A5: *Diagram of the battery setup. SS Mesh is stainless steel mesh. The separator is polyethylene plastic. The electrolyte is added to glass fiber, in between the separators.*

XPS analysis began with battery disassembly in argon glovebox (O_2 ppm <1) before transfer to the XPS intro chamber via an inhouse air free transfer holder.[197] The PE 5800 series Multi-Technique ESCA system utilized a Al K(α) monochromatic source operating 350.0 W to collect 30 minute High resolution scans of each element present in the survey scan (carbon, oxygen, antimony, chlorine, fluorine, sodium, and copper). It should be noted no sulfur was detected from possible incorporation of the MeSCN probe. This indicates that the probe was a passive participant in the bulk solution. XPS fitting followed a similar procedure to Gimble *et al*.[2]

Section 5: 2D IR Measurements

The 2D IR measurements were made using a 100 kHz, mid-IR source that drives a 2D IR spectrometer described previously.[112] In brief, generation of ultrafast mid-IR light is achieved with optical parametric chirped-pulse amplification (OPCPA) and difference frequency generation (DFG) in magnesium doped periodically poled lithium niobate (MgO:PPLN) and zinc germanium diphosphide (ZGP), respectively. Resulting mid-IR pulses are centered at 4.65 μm and are 220 fs in duration. All measurements discussed here were performed using the pump-probe geometry. The power measured before the sample focus for the probe line was ~ 4 mW giving a pulse energy of 40 nJ at 100 kHz.

The 2D IR spectra were collected using a series of 601 pump pulse pairs from 0 to 6 ps in 10 fs steps. Data along the pump axis was then zero-padded to 1202, giving a spectral resolution of 2.78 cm^{-1}. The power of the pump was ~ 17 mW then giving a 75 nJ pulse energy. Spectra were acquired with a four-frame phase cycling scheme and 1900 cm^{-1} rotating frame to remove background and scatter.[113] Each 2D IR spectrum was averaged fully between 500 and then replicated 3 times to generate error bars from the standard deviation of each replicate. A two-pixel noise reduction scheme described in previous work and based on work by Feng *et al*. and Robben *et al*. was used to generate clean data.[29,95,114]

A half wave plate followed by a wire grid polarizer along the probe line are used to rotate the polarization prior to the sample from polarization parallel to the pump (XXXX) or perpendicular (XXYY). Spectra from T_W equal to 0 to 30 ps were collected in XXYY and XXXX polarization schemes for the three solutions. For the first 0.9 ps 100 fs steps were taken, for the next 15 ps, 0.25 ps steps, and for the final 14 ps, 2 ps steps were taken. Another wire grid polarizer after the sample was used to collect the data either parallel or perpendicular to the pump.

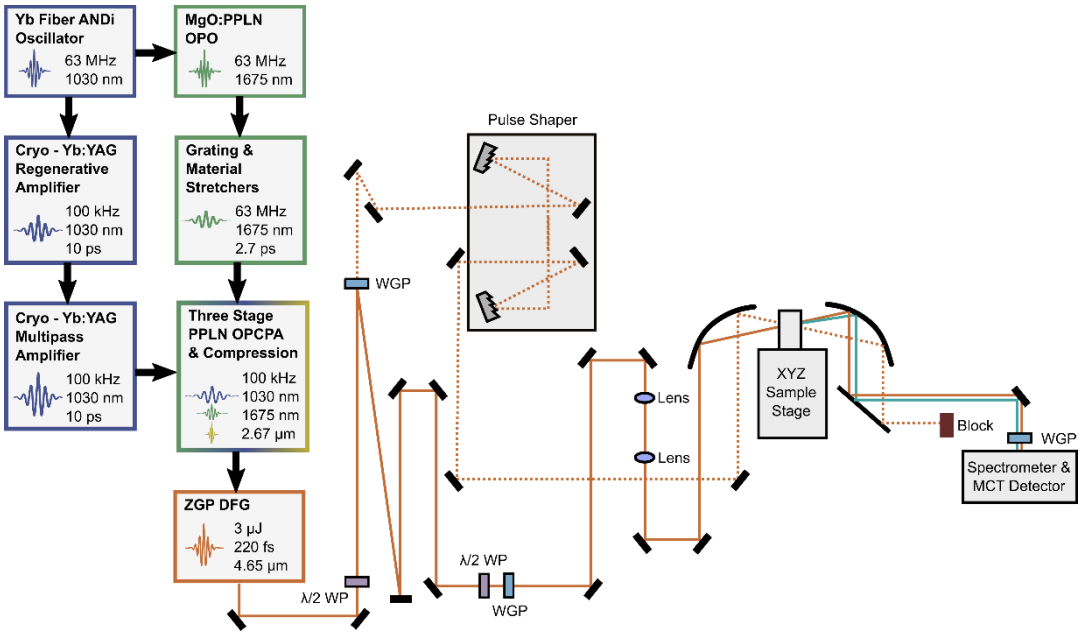

Figure A6: *Layout of the 2DIR spectrometer used in these measurements. Yb-Fiber meaning ytterbium fiber. ANDi meaning all normal dispersion. Cryo Yb:YAG meaning cryogenically cooled yttrium aluminum garnet doped gain medium. PPLN meaning periodically poled lithium niobite. OPO defined as optical parametric oscillator. OPCPA defined as optical parametrically chirped pulse amplification. ZPG meaning zinc germanium diphosphide. DFG defined as difference frequency generation. WP short for waveplate and WGP for wire grid polarizer. MCT stands for mercury cadmium telluride.*

Section 6: Center Line Slope Analysis

We performed inverse center line slope analysis (CLS)[198,199] of the collected 2DIR spectra to characterize the spectral diffusion dynamics of MeSCN in each solution. Inverse center line slope, as opposed to nodal line slope analysis was chosen due to the large red-shift between ESA and GSB with a peak-to-peak difference of 28 cm^{-1} for the MeSCN in FEC. This difference was determined by fitting gaussian functions to a slice through parallel to the ω_{probe} axis at ω_{pump} equal to 2157 cm^{-1}. To calculate the inverse CLS, six cuts parallel to the probe axis were taken and for each cut, the minima along the probe axis was found (black dots in Figure A7).

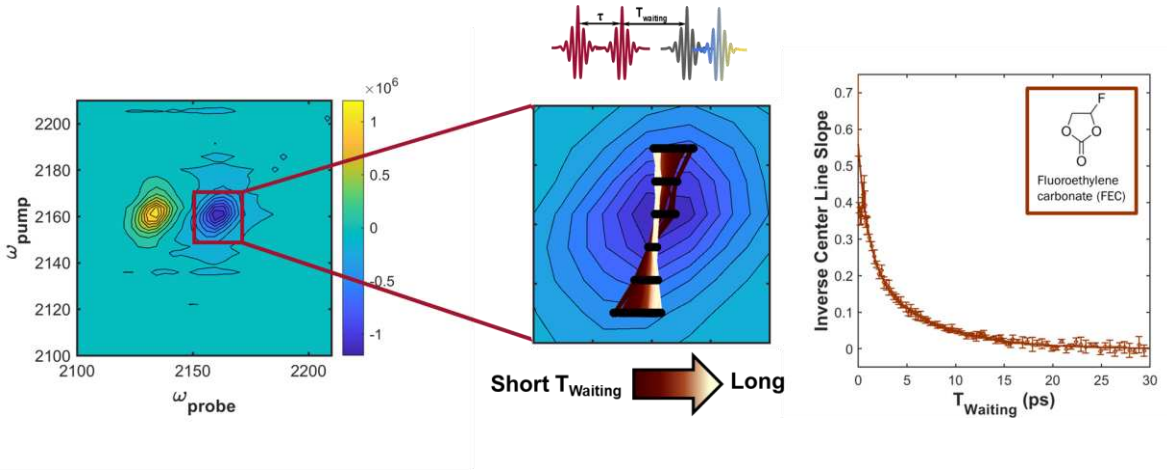

Figure A7: *(Left) 2D IR spectra at $T_{Waiting}$ equal to 900 fs for the 300 mM MeSCN in FEC. (Middle) The zoomed in portion shows the CLS from dark red to light red connecting filled black circles as a function of $T_{Waiting}$. The dots represent the minima for each pump cut analyzed. (Right) The resulting CLS decay with a biexponential fit overlaid. The error bars represent averages from triplicate measurements.*

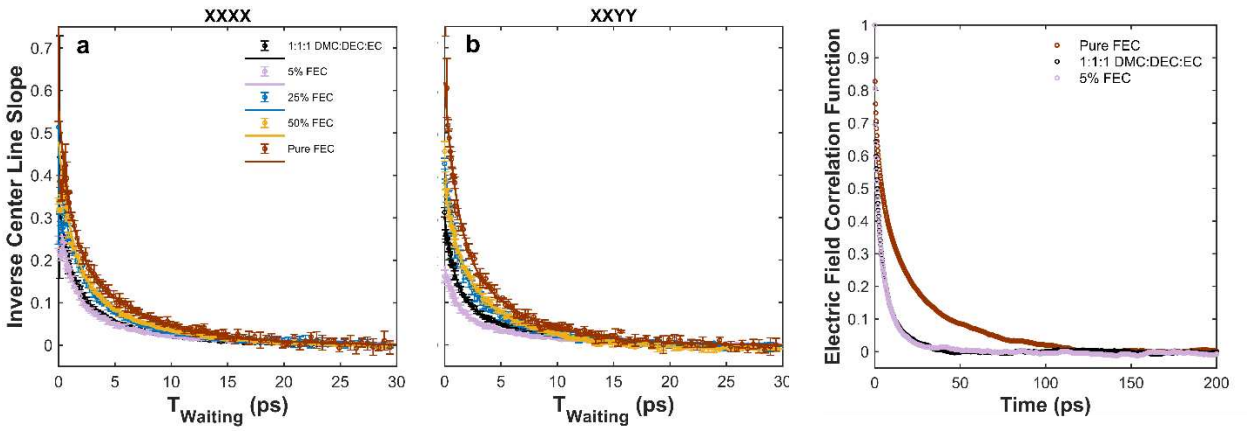

Figure A8: *Each decay is resulting from the averaging the center line slopes of triplicate measurements representing the approximate frequency fluctuation correlation function with error bars at each waiting time step from. Red representing MeSCN in FEC, gold represent MeSCN in 50% FEC in the 1:1:1 DEC:DMC:EC, blue as 25% FEC, purple as 5% FEC and black as the 1:1:1 mixture. Solid lines represent biexponential fits to the data (a) XXXX (b) XXYY (c) The calculated electric field correlation functions for the nitrogen (N) of MeSCN as a function of waiting time.*

Equation 1 was used to fit to the CLS decays (Figure A8). Fitting was done using the Levenberg Marquardt algorithm to minimize the least absolute residuals (LAR) via the Matlab curve fitting toolbox. Equation 3-1 shows C, the FFCF, as a function of T_W is then approximated by multiexponential equation defined by a short and long time constant, τ_{short} and τ_{long} with amplitudes a_1 and a_2 respectively. These data are representative of averages of triplicate measurements and the error presented is the error from fitting those averages and the resulting 95% confidence interval.

As a point of comparison with simulated electric field correlation functions the experimental CLS decays were integrated to generate a single weighted time constant and the ratios between each weighted time constant for the three comparable mixtures were taken (Figure A9).

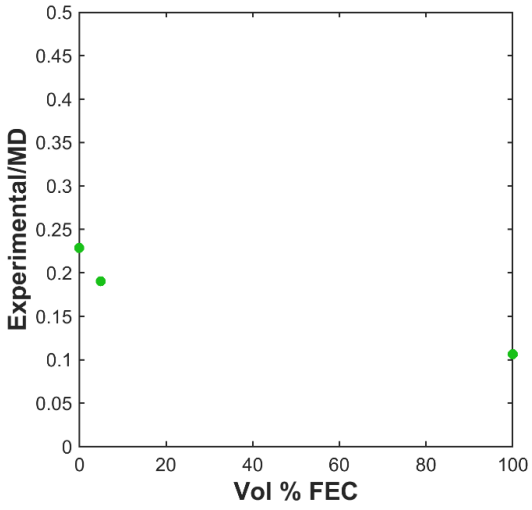

Figure A9: *The ratio of the integrated experimental CLS and the integrated simulated electric field correlation function*

Section 7: Molecular Dynamics Simulations Methods

Molecular dynamics (MD) simulations are performed on pure FEC, 1:1:1 DMC:DEC:EC, and 1:1:1 DMC:DEC:EC with 5% FEC by volume solutions using the TINKER modeling package and the AMOEBA force field. The systems are built using Packmol with each system containing four MeSCN molecules whose CN stretches serve as vibrational probes. Table A2 contains system details for each electrolyte component.

Table A2: *Each simulated sample in terms of the ratio of each carbonate to the probe molecule FEC.*

	0% FEC by Volume	**5% FEC by Volume**	**100% FEC by Volume**
Component	**# molecules/ MeSCN**		
DMC	13	13	0
DEC	13	13	0
EC	13	13	0
FEC	0	3	48

The AMOEBA force field is currently only parameterized for a select number of organic compounds, none of which are utilized in the electrolyte solutions of interest.[200] To parameterize DMC, DEC, EC, FEC, and MeSCN, an automated parameterization method, called Poltype, developed by Wu, Chattree, and Ren is

employed.[201] The automated process uses a series of quantum mechanical calculations utilizing Møller-Plesset perturbation theory[202] (MP2) with the aug-cc-pTVZ basis set[203] to determine the electrostatic multipoles, equilibrium bond lengths, and equilibrium angles. Next, a database is used to designate the valence parameters, van der Waals parameters, and polarizability based on similar atom types. Torsional parameters are then fit using additional MP2 calculations.

Prior to MD simulations, a geometry minimization is performed for 2500 steps of steepest-decent followed by 2500 steps of conjugant gradient. Next, the systems are heated in 100 ps increments to 100, 200, and 300 K in the canonical, or NVT, ensemble. To ensure the proper density is reached, a 500 ps simulation is performed in the isothermal-isobaric, or NPT, ensemble at 300 K and 1.0 bar. Next, to ensure the MeSCN environment is not influenced by the initial packing, the system is heated in 100 ps increments to 400, 500, and 600 K and then cooled in the same manner back to 300 K. After, another 500 ps NPT simulation is performed and the box is scaled to the appropriate density again. The extreme heating allows molecules to move more quickly to a more energetically favorable configuration and removes any hinderance due to viscosity. To finish equilibrating the system, a 1 ns NVT ensemble simulation is performed at 300 K to settle the system at the proper density. Production simulations are run for 100 ns in the NVT ensemble and data is collected every 0.2 ps. Monte Carlo barostat and Bussi-Donadio-Parrinello thermostat are used in these simulations per recommendations to maximize efficiency on the Tinker-OpenMM. The equilibration process and production is run on the Tinker-OpenMM platform.[204,205]

Section 8: Radial Distribution Functions

A general concern when working with probe molecules is to ensure aggregation of a specific component is not occurring near the reporter. Radial distribution functions (RDFs) provide insights into which molecules are in the first solvation shell of the probe. The N on the MeSCN is the reference atom and the densities are calculated for the carbonyl carbon of DMC, DEC, and EC, as it is the most electropositive carbon of the molecule. When evaluating FEC, the addition of fluorine makes the carbon it is bound to the most electropositive of the molecule. To determine whether the carbonyl carbon or fluorinated carbon should be

used to appropriately capture interactions with the probe in the solvation shell, radial distribution functions for both carbons of the FEC from the pure FEC and 1:1:1 DMC:DEC:EC with 5% FEC by volume solutions are compared, seen in Figure A10. Based on the distributions from both solutions, it is evident that FEC is oriented so that the fluorinated carbon is more directly interacting with MeSCN. Due to this, the fluorinated carbon is used for radial distribution functions. To evaluate potential aggregation, the radial distribution functions for each component are calculated and these distributions can be seen in Figure A11. The distribution functions show an even distribution of DMC and EC, with DEC commonly residing second solvation shell of MeSCN for both solutions. FEC appears to be residing in the first solvation shell at a higher ratio than DMC and EC; however, radial distribution functions are normalized, meaning they do not quantify aggregation.

Quantifying aggregation can be done by determining the percentage of the trajectory each component is the closest to MeSCN and comparing to the statistically expected value based on the number of molecules present. Calculated values are obtained by identifying the nearest molecule for each frame, summing up the number of times the specified molecule is closest, and dividing by the total number of frames. Distances are calculated from the N of and the minimum value is used to identify the nearest molecule. The statistically expected value is the number of specified molecules (DMC, DEC, EC, or FEC) divided by the total number of molecules in the solution. The resulting percentages can be seen in Table A3. Based on the percentages, the solutions have an appropriate distribution of nearest molecules, and no aggregation is evident.

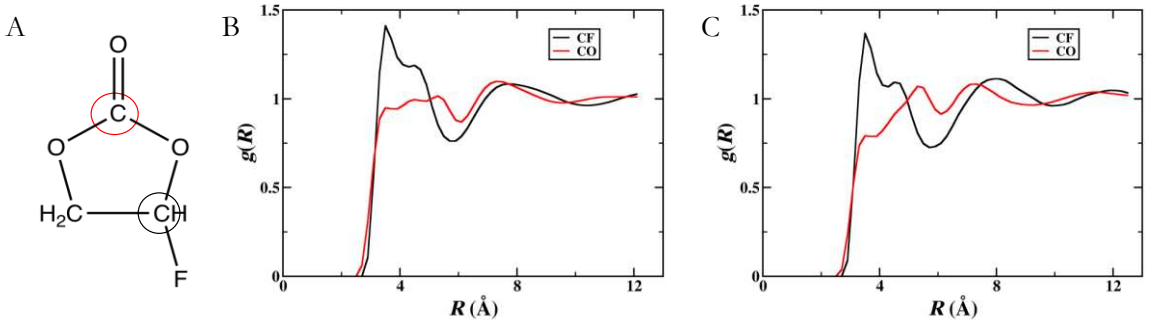

Figure A10: (A) A two-dimensional representation of FEC with the fluorinated C (circled in black) and carbonyl C (circled in red) highlighted. The radial distribution functions for the (B) pure FEC and (C) 1:1:1 DMC:DEC:EC with 5% FEC by volume solutions show that the fluorinated carbon resides most closely to the MeSCN probe.

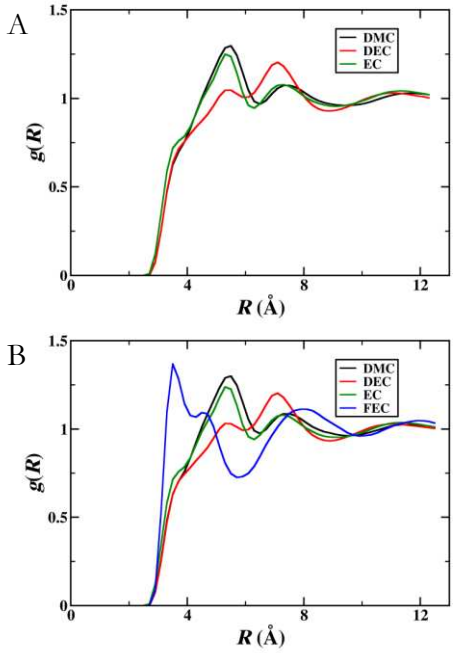

Figure A11: *The radial distribution functions between the N of MeSCN and the carbonyl C of DMC, DEC, and EC, and the fluorinated C in FEC for the (A) 1:1:1 DMC:DEC:EC and (B) 1:1:1 DMC:DEC:EC with 5% FEC by volume solutions.*

Table A3: *Percentage of the Trajectory the Specified Solvent is the Nearest Molecule to MeSCN*

	1:1:1 DMC:DEC:EC w/ 5% FEC				**1:1:1 DMC:DEC:EC**		
Solvent	**DMC**	**DEC**	**EC**	**FEC**	**DMC**	**DEC**	**EC**
Calculated	32.9	30.2	30.7	6.23	34.4	32.4	33.1
Expected	31.3	31.3	31.3	6.25	33.3	33.3	33.3

Section 9: Cylindrical Distribution Functions

CDFs are calculated to evaluate the solvent environment surrounding the probe. These distributions provide a look at the different solvation shells for the individual solvent molecules, which provide information about where the molecule is interacting with the probe. CDFs are calculated in a similar manner to the RDFs, where the N of MeSCN is the reference atom and the carbonyl carbon is the used for the density of DMC, DEC, and EC. The fluorinated carbon is used for the density of FEC. Resulting CDFs can be seen for 1:1:1 DMC:DEC:EC and 1:1:1 DMC:DEC:EC with 5% FEC by volume in Figures S12 and S13, respectively.

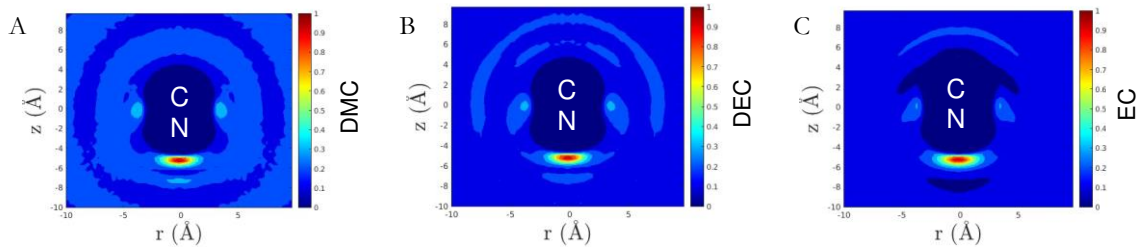

Figure A12: *The cylindrical distribution functions for (A) DMC, (B) DEC, and (C) EC in the 1:1:1 DMC:DEC:EC mixture . All frequencies are normalized.*

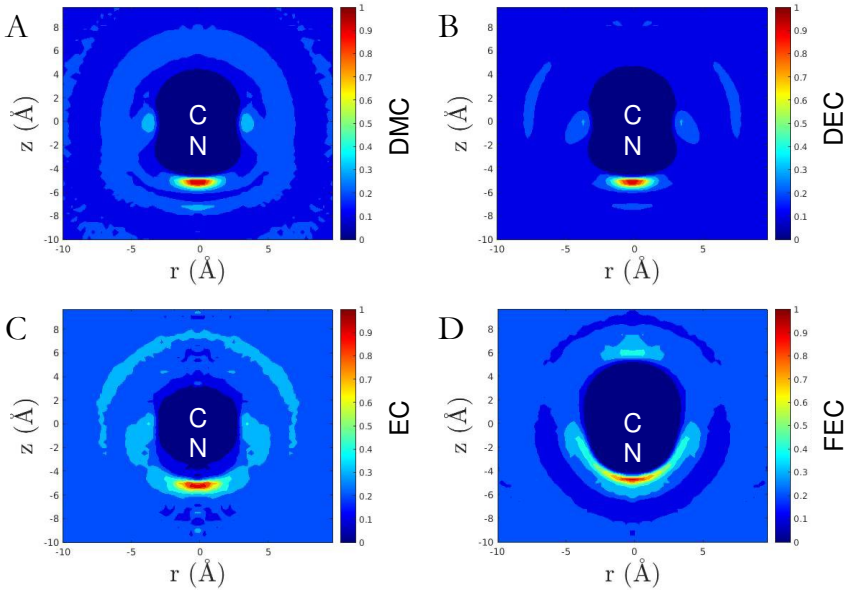

Figure A13: *The cylindrical distribution functions for (A) DMC, (B) DEC, (C) EC, and (D) FEC for the 1:1:1 DMC:DEC:EC with 5% FEC by volume mixture. All frequencies are normalized.*

Section 10: Anisotropy Analysis

Signal intensity as a function of T_W for parallel, $I_{\parallel}(T_W)$, and perpendicular $I_{\perp}(T_W)$ were extracted by integrating over a 10 cm^{-1} box centered on the peak of on-diagonal 2D IR peak. The signal intensity was then corrected for long term fluctuations in laser power by normalizing the 2D data with the probe power squared results in a stable 2D intensity. This analysis process is shown in more detail in prior work.[29] To then account for any error in shifts between XXXX and XXYY data collection schemes prior to averaging and fitting the signal intensities for the XXXX decay were self-normalized. The XXYY signal intensities were then self-normalized to 1/3. Then the anisotropy from the adjusted signal intensities was calculated using Equation 3-2. This adjustment is done with the approximation that no inertial reorientation occurred

before 200 fs [206,207]. Anisotropy results were then fit using the biexponential with and offset Equation 3-5.[106] The following series of equations were used to extract the cone diffusion time (D_c), the cone angle, and the global diffusion time (D_g).

$$\frac{1}{\tau_{fast}} = \frac{1}{\tau_{slow}} + \frac{1}{\tau_{cone}} \tag{A3}$$

$$\theta = \cos^{-1}\left\{\left(1/2\right)\left[\sqrt{1+8|S|}-1\right]\right\} \tag{A4}$$

From order parameter S in Equation 3-5 the angle of restriction can be calculated (Equation A4). This angle is the cone semi-angle. In addition, the wobbling-in-a-cone diffusion constant D_c can be calculated using S, τ_{cone}, and the cone semi angle (Equation A5).

$$D_c = \frac{x_c^2(1+x_c)^2\left\{\ln\left[\left(1+x_c\right)/2\right]+\left(1-x_c\right)/2\right\}}{\tau_c(1-S^2)[2(x_c-1)]} + \frac{(1-x_c)(6+8x_c-x_c^2-12x_c^3-7x_c^4)}{24\tau_c(1-S^2)} \tag{A5}$$

The long-time component contributing to the orientational relaxation can then be attributed to the global reorientation of the probe. This increase can be correlated with increases in the inverse global diffusion time D_g^{-1} (Equation A6) (Table A4).

$$D_g = \frac{1}{6\tau_{slow}} \tag{A6}$$

Table A4: *Fit parameters from the wobble-in-a-cone model to the experimental anisotropy curves*

vol % FEC	Excluded from Fit	τ_{Fast}	95% CI	τ_{Slow}	95% CI	S	D_g^{-1}	τ_{Cone}	θ (°)
100	first 4	0.61	0.06	6.93	0.30	0.80	41.58	0.67	30.58
50	first 3	0.49	0.12	5.09	0.34	0.85	30.56	0.54	26.13
25	first 5	0.69	0.19	5.66	0.80	0.78	33.97	0.79	32.56
5	first 4	0.60	0.08	4.27	0.34	0.75	25.62	0.69	34.46
0	first 4	0.52	0.08	4.57	0.32	0.77	27.42	0.59	33.34

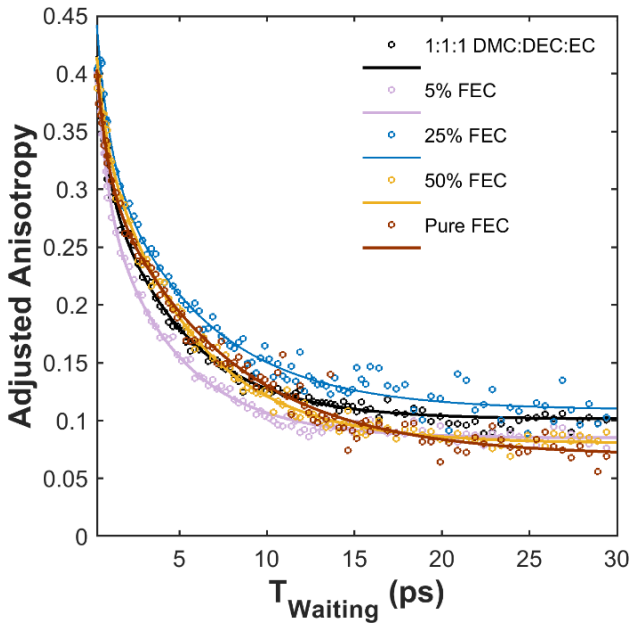

Figure A14: *The adjusted experimental anisotropy decays for each electrolyte mixture. Circles represent the data, and solid lines are fits using the wobble-in-a-cone model (Equation 3-5).*

Section 11: Viscosity Measurements

Using the TA Instruments (Discovery HR-2) Hybrid Rheometer. A 40 mm plate geometry was used with a 500 µm geometry gap. The measurements were made with 10 steps per decade. The experiment was a sweep over shear rates of 12-25 Hz for. Figure A15 shows the resulting viscosity (Pa.S) versus shear (Hz) and Figure A16 shows stress (Pa) versus shear (Hz)

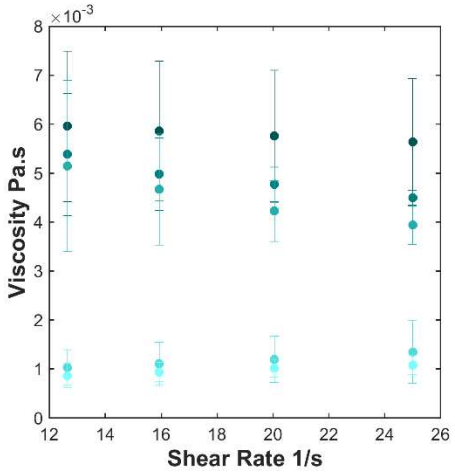

Figure A15: *Viscosity versus shear rate for each mixture. From dark to light; FEC, 50% FEC, 25% FEC, 5% FEC, and 0% FEC.*

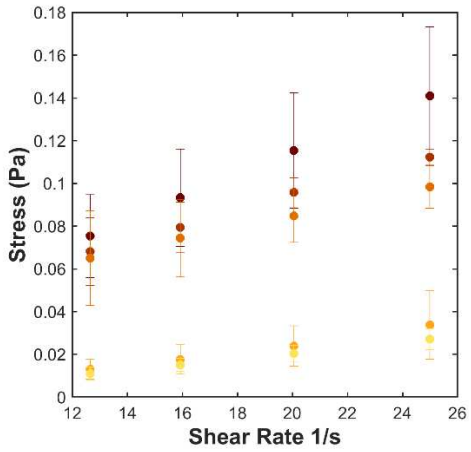

Figure A16: *Stress versus shear rate for each mixture. From dark to light; FEC, 50% FEC, 25% FEC, 5% FEC, and 0% FEC.*

Section 12: Simulated Rotational Correlation Functions

Rotational correlation functions provide information about which components have altered dynamics caused by the addition of FEC. The rotational correlation functions for the carbonyl bond of each electrolyte component can be seen in Figure A17. Visually, it is apparent that the only component with a significant dynamic change is FEC.

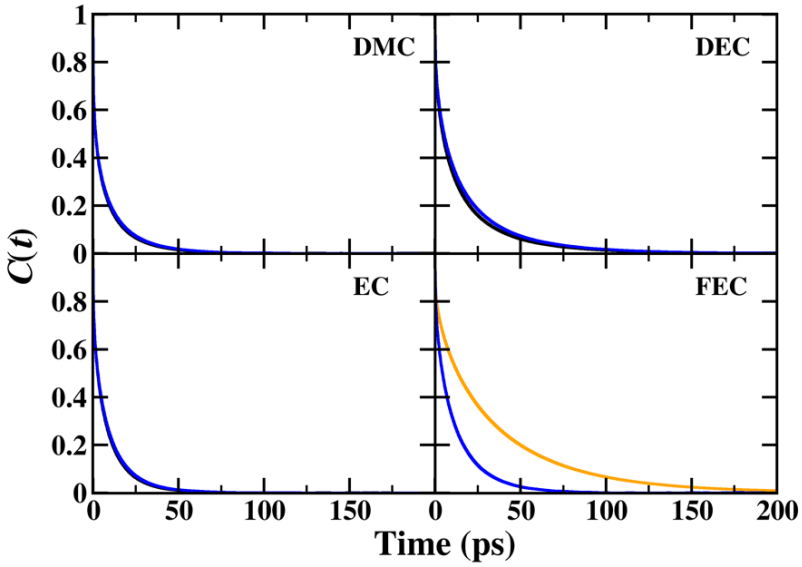

FIG A17: *The rotational correlation functions calculated for the specified components of the pure FEC (gold), 1:1:1 DMC:DEC:EC (black), and 1:1:1 DMC:DEC:EC with 5% FEC by volume (blue) electrolyte solutions*

Section 13: Example Matlab Code for 2D IR Analysis

The following code is an example of code that was used to extract raw data, Fourier Transform 2DIR spectra, normalize to probe power, extract CLS slopes, track signal intensities, and calculate normalized anisotropy. Fitting to CLS and anisotropy decays was done independently in the Matlab Curve Fitting Toolbox.

```
clear all, close all, clear hold

%Import Calibrated Wavelength Axis for Probe
WL= importdata('WL_axis');
WN=10000000./WL; %Converting axis to Wavenumbers

%% Importing Raw Data for XXXX dataset
for i = 1:98; % final # is the total # twaiting steps

%% 3 trials --> 3 segments per trial
%Total of 98 steps
name1 = ['CO_25FEC_trial2_10010_ ' num2str(i) '_10_ _0X_ _0Y_ 0'];
name2 = ['CO_25FEC_trial3_10010_ ' num2str(i) '_10_ _0X_ _0Y_ 0'];
name3 = ['CO_25FEC_trial5_10010_ ' num2str(i) '_10_ _0X_ _0Y_ 0'];
data1=importdata(name1); %make a variable with all the files
data2=importdata(name2);
data3=importdata(name3);
DT1(:,:,i)=data1(:,:,:); %Data stacked by file number
DT2(:,:,i)=data2(:,:,:);
DT3(:,:,i)=data3(:,:,:);
end

DT = cat(3,DT1,DT2,DT3); % concatonating trials together into 1 variable

for i=1:(98*3);
A(:,:,i)=DT(1:64,:,i); %PC data - with noise reduction applied
B(:,:,i)=DT(65:128,:,i); %0-0 phase to use for normalization
Tpc(:,:,i)=A(:,:,i)'; %transpose for plotting with pump on y and 64 probe array on x
zp(:,:,i)=padarray(Tpc(:,:,i),601,0,'post'); %zeropadding data (151 is the number of steps in tau)
FT(:,:,i)=fftshift(fft(zp(:,:,i)),1); %Fourier transformm zeropadded data
RFT(:,:,i)=real(FT(:,:,i))*-1; %real portion of the fourier transform
end

%% Importing Raw Data for XXYY dataset
for i = 1:98; % final # is the total # twaiting steps
name1X = ['CROSS_25FEC_trial1_10010_ ' num2str(i) '_10_ _0X_ _0Y_ 0'];
name2X = ['CROSS_25FEC_trial2_10010_ ' num2str(i) '_10_ _0X_ _0Y_ 0'];
name3X = ['CROSS_25FEC_trial3_10010_ ' num2str(i) '_10_ _0X_ _0Y_ 0'];
data1X=importdata(name1X); %make a variable with all the files
data2X=importdata(name2X);
data3X=importdata(name3X);
DT1X(:,:,i)=data1X(:,:,:); %Data stacked by file number
DT2X(:,:,i)=data2X(:,:,:);
```

```
DT3X(:,:,i)=data3X(:,:,:);
end
DTX = cat(3,DT1X,DT2X,DT3X); % concatonating trials together into 1 variable

for i=1:(98*3);
AX(:,:,i)=DTX(1:64,:,i); %PC data - with noise reduction applied
BX(:,:,i)=DTX(65:128,:,i); %0-0 phase to use for normalization
TpcX(:,:,i)=AX(:,:,i)'; %transpose for plotting with pump on y and 64 probe array on x
zpX(:,:,i)=padarray(TpcX(:,:,i),601,0,'post'); %zeropadding data (151 is the number of steps in tau)
FTX(:,:,i)=fftshift(fft(zpX(:,:,i)),1); %Fourier transformm zeropadded data
RFTX(:,:,i)=real(FTX(:,:,i))*-1; %real portion of the fourier transform
end

%% Make the Pump Frequency Axis
Dt=10e-15; %10fs step size in tau, delta t
Lt=1202; %Length in time, 1202 if there are 601 time steps (with zero padding to double # steps)
Dv=1/(Dt*Lt); %change in frequency space, delta v

 for k = 1:1202; %loop through length
    V(k)=Dv*((Lt/2)*(-1)+(k-1));
    V_axis(k)=(1/(299792458/V(k)))./100; %conversion to cm-1
 end
%% Account for Rotating Frame
 PumpAxis=V_axis+1900; %adding what value in wavenumbers you used for rotating frame

%% Tracking probe power overtime - to normalize 2DIR signal with
for j = 1:294;
MaxSig(:,j)=B(35,:,j); %Selecting most intense pixel in index 1
MaxSigX(:,j)=BX(35,:,j);
blank(j)=sum(MaxSig(:,j),1);
blankX(j)=sum(MaxSigX(:,j),1);
blankCombo=[blank blankX]; % combining cross & co-polarized data
square(j)=((blank(j).^2));%Squaring, using assuming signal scales linearly with pump and probe, and probe used as
similar to pump changes
squareX(j)=((blankX(j).^2));
end
squareCombo=[square squareX];
mx=max(squareCombo);
for j=1:294;
normsquare(j)=square(j)/mx; %normalizing the squared data after
normsquareX(j)=squareX(j)/mx;
end
%% Slices of data parallel to probe axis (choose 6 centered around peak)
RFT1=RFT(693:698,:,:);
RFT1X=RFTX(693:698,:,:);

%% Plotting Probe Shape XXXX over TW
figure()
hold on
for n=99:195; %last # is final tw
   shade=cool(294);%color for XXXX
   plot(WN,B(:,10,n),':','color',shade(n,:),'LineWidth',1); %co pol phase 00
end

%% Extracting Relevant Portion of the Spectrum/ Normalizing / Splining
for l=1:6
```

```
 for k=1:294;
   A1=RFT1(l,:,k); %relevant slice parallel to probe axis with most sig
   [Min,Imin]=min(A1,[],2); %finding minimum of data not splined
   IminS(l,k)=Imin; %% pixel of highest intensity
   MinS(l,k)=abs(Min); %% value at each minimum
   BlankCorrected(l,k)=MinS(l,k)./normsquare(k); %normalizing to probe power overtime
   BC_full1(l,:,k)=RFT1(l,:,k)./normsquare(k);
   BlankCorrectedNorm(l,k)=BlankCorrected(l,k)./(max(BlankCorrected(l)));
   NormMin(l,k)=MinS(l,k)/max(MinS(l));
    %splining normalized data & collecting data used for CLS
    dWN=linspace(WN(1,1),WN(1,64),10000); %x-axis to go with splined data
    spld1(l,:,k)= spline(WN,BC_full1(l,:,k),dWN); %splined along probe axis
    [sp_Min1(l,k),sp_Imin1(l,k)]=min(spld1(l,:,k),[],2); %searching for minima & index
    VMin(l,k)=dWN(sp_Imin1(l,k)); % frequency at found minima used for CLS
    spldNorm(l,:,k)=spld1(l,:,k)./sp_Min1(l,k); %self-normalizing each slice
 end
end

%% Plot Splined Cuts vs Twaiting
figure()
hold on
for g=196:294
    shade=autumn(98); %colormap - # should be equal to amount of Tw steps
    plot(dWN,spld1(6,:,g),'color',shade(g,:),'LineWidth',1); %
end
hold off

%% Integrating for Signal Intensity Tracking XXXX
 spld_int(:,:,:)=spld1(:,5021:5455,:); % select a range of pixels on the splined probe axis
 spld_trapz2(:,:)=trapz(spld_int(:,:,:),2); % integrate over the region on the probe axis
 spld_trapz1(:)=trapz(spld_trapz2(:,:),1); % integrate over pump axis (each slice)
 Int1=spld_trapz1(1:98); % trial 1
 Int2=spld_trapz1(99:196); % trial 2
 Int3=spld_trapz1(197:294); % trial 3
 avgInt=(Int1+Int2+Int3)./3; % average
 catInt=cat(1,Int1,Int2,Int3); % concatonate
 stdInt=std(catInt); % find standard deviation

 %% Minima for CLS XXXX
 VMin1(:,:)=VMin(:,1:98); % separate found minima for trial 1
 VMin2(:,:)=VMin(:,99:196);
 VMin3(:,:)=VMin(:,197:294);

%% Repeat for XXYY dataset
for l = 1:6;
  for m=1:294;
   A1X=RFT1X(l,:,m);
   [MinSX,IminSX]=min(A1X,[],2); %finding minimum of data not splined
   IminsX(l,m)=IminSX;
   MinsX(l,m)=abs(MinSX);
   BlankCorrectedX(l,m)=MinsX(l,m)./normsquareX(m);
   mxL(l)=max(BlankCorrectedX(l));
   BlankCorrectedNormX(l,m)=BlankCorrectedX(l,m)/mxL(l);
   NormMinX(l,m)=MinsX(l,m)/max(MinsX(l));
   %splining & cls data
   BC_full1X(l,:,m)=RFT1X(l,:,m)./normsquareX(m);
```

```
   BC_full1X_NoNorm(l,:,m)=RFT1X(l,:,m);
   spld1X(l,:,m)= spline(WN,BC_full1X(l,:,m),dWN);
   [sp_Min1X(l,m),sp_Imin1X(l,m)]=min(spld1X(l,:,m),[],2);
   VMinX(l,m)=dWN(sp_Imin1X(l,m));
  end
end
%% Integrating for Signal Intensity Tracking XXYY
 spld_intX(:,:,:)=spld1X(:,5021:5455,:);
 spld_trapz2X(:,:)=trapz(spld_intX(:,:,:),2);
 spld_trapz1X(:)=trapz(spld_trapz2X(:,:),1);
 Int1X=spld_trapz1X(1:98);
 Int2X=spld_trapz1X(99:196);
 Int3X=spld_trapz1X(197:294);
 avgIntX=(Int1X+Int2X+Int3X)./3;
 catIntX=cat(1,Int1X,Int2X,Int3X);
 stdIntX=std(catIntX);
%% Minima for CLS XXYY
 VMin1X(:,:)=VMinX(:,1:98);
 VMin2X(:,:)=VMinX(:,99:196);
 VMin3X(:,:)=VMinX(:,197:294);
%% CLS Slope values
TfitX_w_6=[2155.30696138295;2158.08203705015;2160.85711271736;2163.63218838456;2166.40726405177;21
69.18233971897];
%% Making Time Axes
time=0:.1:((10*.1)-.1); % segment 1
time2=0.9:0.25:(60*0.25)+0.9-0.25; % segment 2
time3=15.9:0.5:(28*0.5)+15.9-0.5; % segment 3
timeCombo=cat(2,time,time2,time3); %total
%% CLS for co-polarized data trial 1
for z=1:98;
Y_CLS_w6_CO_1(:,:,z)=VMin1(:,z);
Fit_w6_CO_1(:,z)=polyfit(TfitX_w_6,Y_CLS_w6_CO_1(:,:,z),1);
yvalsCLS6CO_1(z)=Fit_w6_CO_1(1,z);
interceptCO_1(z)=Fit_w6_CO_1(2,z);
%% error bars
[fitCLS1(:,z), errorstructure1(:,z)]=polyfit(TfitX_w_6,Y_CLS_w6_CO_1(:,:,z),1); % pulling out error mmatrix to
feed into polyparci fxn
CI1(:,:,z)=polyparci(fitCLS1(:,z),errorstructure1(:,z)); %generating a 2xN matrix of 90% CI corresponding to the
input of the polyfit coefficients, column 1 for slopes
error1(:,z)=CI1(2,1,z)-yvalsCLS6CO_1(z); %getting values to feed into errorbar fxn for plotting purposes
end
%% Trial 2
for v=1:98;
Y_CLS_w6_CO_2(:,:,v)=VMin2(:,v);
Fit_w6_CO_2(:,v)=polyfit(TfitX_w_6,Y_CLS_w6_CO_2(:,:,v),1);
yvalsCLS6CO_2(v)=Fit_w6_CO_2(1,v);
interceptCO_2(v)=Fit_w6_CO_2(2,v);
%% error bars
[fitCLS2(:,v), errorstructure2(:,v)]=polyfit(TfitX_w_6,Y_CLS_w6_CO_2(:,:,v),1); % pulling out error mmatrix to
feed into polyparci fxn
CI2(:,:,v)=polyparci(fitCLS2(:,v),errorstructure2(:,v)); %generating a 2xN matrix of 90% CI corresponding to the
input of the polyfit coefficients, column 1 for slopes
error2(:,v)=CI2(2,1,v)-yvalsCLS6CO_2(v); %getting values to feed into errorbar fxn for plotting purposes
end
%% Trial 3
for z=1:98;
```

```
Y_CLS_w6_CO_3(:,:,z)=VMin3(:,z);
Fit_w6_CO_3(:,z)=polyfit(TfitX_w_6,Y_CLS_w6_CO_3(:,:,z),1);
yvalsCLS6CO_3(z)=Fit_w6_CO_3(1,z);
interceptCO_3(z)=Fit_w6_CO_3(2,z);
%% error bars
[fitCLS3(:,z), errorstructure3(:,z)]=polyfit(TfitX_w_6,Y_CLS_w6_CO_3(:,:,z),1); % pulling out error mmatrix to feed into polyparci fxn
CI3(:,:,z)=polyparci(fitCLS3(:,z),errorstructure3(:,z)); %generating a 2xN matrix of 90% CI corresponding to the input of the polyfit coefficients, column 1 for slopes
error3(:,z)=CI3(2,1,z)-yvalsCLS6CO_3(z); %getting values to feed into errorbar fxn for plotting purposes
end
%% Averaging trials CLS results
avgclsCO=(yvalsCLS6CO_1+yvalsCLS6CO_2+yvalsCLS6CO_3)./3;
catCLS=cat(1,yvalsCLS6CO_1,yvalsCLS6CO_2,yvalsCLS6CO_3);
stdCLSCO=std(catCLS);
%% CLS for cross-polarized data trial 1
for z=1:98;
Y_CLS_w6_X_1(:,:,z)=VMin1X(:,z);
Fit_w6_X_1(:,z)=polyfit(TfitX_w_6,Y_CLS_w6_X_1(:,:,z),1);
yvalsCLS6X_1(z)=Fit_w6_X_1(1,z);
interceptX_1(z)=Fit_w6_X_1(2,z);
%% error bars
[fitCLS1X(:,z), errorstructure1X(:,z)]=polyfit(TfitX_w_6,Y_CLS_w6_X_1(:,:,z),1); % pulling out error mmatrix to feed into polyparci fxn
CI1X(:,:,z)=polyparci(fitCLS1(:,z),errorstructure1X(:,z)); %generating a 2xN matrix of 90% CI corresponding to the input of the polyfit coefficients, column 1 for slopes
error1X(:,z)=CI1X(2,1,z)-yvalsCLS6X_1(z); %getting values to feed into errorbar fxn for plotting purposes
end
%% Trial 2 CROSS
for z=1:98;
Y_CLS_w6_X_2(:,:,z)=VMin2X(:,z);
Fit_w6_X_2(:,z)=polyfit(TfitX_w_6,Y_CLS_w6_X_2(:,:,z),1);
yvalsCLS6X_2(z)=Fit_w6_X_2(1,z);
interceptX_2(z)=Fit_w6_X_2(2,z);
%% error bars
[fitCLS2X(:,z), errorstructure2X(:,z)]=polyfit(TfitX_w_6,Y_CLS_w6_X_2(:,:,z),1); % pulling out error mmatrix to feed into polyparci fxn
CI2X(:,:,z)=polyparci(fitCLS2(:,z),errorstructure2X(:,z)); %generating a 2xN matrix of 90% CI corresponding to the input of the polyfit coefficients, column 1 for slopes
error2X(:,z)=CI2X(2,1,z)-yvalsCLS6X_2(z); %getting values to feed into errorbar fxn for plotting purposes
end
%% Trial 3 CROSS
for z=1:98;
Y_CLS_w6_X_3(:,:,z)=VMin3X(:,z);
Fit_w6_X_3(:,z)=polyfit(TfitX_w_6,Y_CLS_w6_X_3(:,:,z),1);
yvalsCLS6X_3(z)=Fit_w6_X_3(1,z);
interceptX_3(z)=Fit_w6_X_3(2,z);
%% error bars
[fitCLS3X(:,z), errorstructure3X(:,z)]=polyfit(TfitX_w_6,Y_CLS_w6_X_3(:,:,z),1); % pulling out error mmatrix to feed into polyparci fxn
CI3X(:,:,z)=polyparci(fitCLS3(:,z),errorstructure3X(:,z)); %generating a 2xN matrix of 90% CI corresponding to the input of the polyfit coefficients, column 1 for slopes
error3X(:,z)=CI3X(2,1,z)-yvalsCLS6X_3(z); %getting values to feed into errorbar fxn for plotting purposes
end
%% Averaging trials
%% co
```

```
avgclsCO=(yvalsCLS6CO_1+yvalsCLS6CO_2+yvalsCLS6CO_3)./3;
catCLS=cat(1,yvalsCLS6CO_1,yvalsCLS6CO_2,yvalsCLS6CO_3);
stdCLSCO=std(catCLS);
%% cross
avgclsX=(yvalsCLS6X_1+yvalsCLS6X_2+yvalsCLS6X_3)./3;
catCLSX=cat(1,yvalsCLS6X_1,yvalsCLS6X_2,yvalsCLS6X_3);
stdCLSX=std(catCLSX);

%% Plot CLS with error bars
figure()
hold on
errorbar(timeCombo, yvalsCLS6CO_1, error1,'o','DisplayName','error CLS XXXX 1');
errorbar(timeCombo, yvalsCLS6CO_2, error2,'o','DisplayName','error CLS XXXX 2');
errorbar(timeCombo, yvalsCLS6CO_3, error3,'o','DisplayName','error CLS XXXX 3');
errorbar(timeCombo, yvalsCLS6X_1, error1,'o','DisplayName','error CLS XXYY 1');
errorbar(timeCombo, yvalsCLS6X_2, error2,'o','DisplayName','error CLS XXYY 2');
errorbar(timeCombo, yvalsCLS6X_3, error3,'o','DisplayName','error CLS XXYY 3');
errorbar(timeCombo, avgclsCO, stdCLSCO,'o','DisplayName','std dev CLS XXXX');
errorbar(timeCombo, avgclsX, stdCLSX,'o','DisplayName','std dev CLS XXYY');
ylim([-0.05 0.7]);
xlim([0 30]);
hold off

%% Combining splined data
sp_CO1=abs(Int1);
[MaxCO1,IMaxCO1]=max(abs(Int1));
sp_CO1norm=abs(Int1)./max(abs(Int1));
sp_CO1_unNorm=abs(Int1);
sp_CROSS1=abs(Int1X);
sp_CROSS1norm=abs(Int1X)./max(abs(Int1X));
sp_CROSS1normShift=sp_CROSS1norm;
[MaxCO2,IMaxCO2]=max(abs(Int2));
sp_CO2=abs(Int2);
sp_CO2norm=abs(Int2)./max(abs(Int2));
sp_CROSS2=abs(Int2X);
sp_CROSS2norm=abs(Int2X)./max(abs(Int2X));
sp_CO3=abs(Int3);
[MaxCO3,IMaxCO3]=max(abs(Int3));
sp_CO3norm=abs(Int3)./max(abs(Int3));
sp_CROSS3=abs(Int3X);
sp_CROSS3norm=abs(Int3X)./max(abs(Int3X));
sp_CO=abs(avgInt);
sp_CROSS=abs(avgIntX);

%% Adjusting signal intensity cross to make 1/3 co
% For trial 1
        Sadjustment1=(1/3)/sp_CROSS1norm(:,IMaxCO1) ;
        sp_CROSS1normAdjust=sp_CROSS1norm*Sadjustment1;
% For trial 2
     Sadjustment2=(1/3)/sp_CROSS2norm(:,IMaxCO2) ;
        sp_CROSS2normAdjust=sp_CROSS2norm*Sadjustment2;
% For trial 3
     Sadjustment3=(1/3)/sp_CROSS3norm(:,IMaxCO3) ;
        sp_CROSS3normAdjust=sp_CROSS3norm*Sadjustment3;

anisotropy1=(sp_CO1-sp_CROSS1)./((2*sp_CROSS1)+sp_CO1);
```

```
anisotropy2=(sp_CO2-sp_CROSS2)./((2*sp_CROSS2)+sp_CO2);
anisotropy3=(sp_CO3-sp_CROSS3)./((2*sp_CROSS3)+sp_CO3);
%% Adjusted signals then anisotropy
anisotropy1_S=(sp_CO1norm- sp_CROSS1normAdjust)./((2* sp_CROSS1normAdjust)+sp_CO1norm);
anisotropy2_S=(sp_CO2norm- sp_CROSS2normAdjust)./((2* sp_CROSS2normAdjust)+sp_CO2norm);
anisotropy3_S=(sp_CO3norm- sp_CROSS3normAdjust)./((2* sp_CROSS3normAdjust)+sp_CO3norm);
%% Averaging
anisotropy_avgbefore=(sp_CO-sp_CROSS)./((2*sp_CROSS)+sp_CO);
anisotropy_avgafter=(anisotropy1+anisotropy2+anisotropy3)./3;
anisotropy_avgafter_S=(anisotropy1_S+anisotropy2_S+anisotropy3_S)./3;

%% Plotting signal intensities
figure()
hold on
scatter(timeCombo, sp_CO1,'DisplayName','Norm 2DIR CO Intensity trial 1');
scatter(timeCombo, sp_CROSS1,'DisplayName','Norm 2DIR CROSS Intensity trial 1');
scatter(timeCombo, sp_CO2,'DisplayName','Norm 2DIR CO Intensity trial 2');
scatter(timeCombo, sp_CROSS2,'DisplayName','Norm 2DIR CROSS Intensity trial 2');
scatter(timeCombo, sp_CO3,'DisplayName','Norm 2DIR CO Intensity trial 3');
scatter(timeCombo, sp_CROSS3,'DisplayName','Norm 2DIR CROSS Intensity trial 3');
scatter(timeCombo, sp_CO,'DisplayName','Norm 2DIR CO Intensity');
scatter(timeCombo, sp_CROSS,'DisplayName','Norm 2DIR CROSS Intensity');
hold off

%% Plotting signal intensities ADJUSTED
figure()
hold on
scatter(timeCombo, sp_CO1norm,'DisplayName','Adj Norm 2DIR CO Intensity trial 1');
scatter(timeCombo, sp_CROSS1normAdjust,'DisplayName','Adj Norm 2DIR CROSS Intensity trial 1');
scatter(timeCombo, sp_CO2norm,'DisplayName','Adj Norm 2DIR CO Intensity trial 2');
scatter(timeCombo, sp_CROSS2normAdjust,'DisplayName','Adj Norm 2DIR CROSS Intensity trial 2');
scatter(timeCombo, sp_CO3norm,'DisplayName','Adj Norm 2DIR CO Intensity trial 3');
scatter(timeCombo, sp_CROSS3normAdjust,'DisplayName','Adj Norm 2DIR CROSS Intensity trial 3');
hold off

%% Plotting Anisotropy with Signal Intensities adjusted
figure()
hold on
scatter (timeCombo,anisotropy1_S, 'DisplayName','Anisotropy Trial 1');
scatter (timeCombo,anisotropy2_S, 'DisplayName','Anisotropy Trial 2');
scatter (timeCombo,anisotropy3_S, 'DisplayName','Anisotropy Trial 3');
scatter (timeCombo,anisotropy_avgafter_S, 'DisplayName','Anisotropy Trial 3');
hold off
```

Appendix B

Supplemental Information for Chapter 4

Section 1: Additional FTIR Fitting Results and Analysis

7.1 Linear IR Fitting Results and Analysis

Table B1: *Fit results for the three DCA modes of interest for each concentration of water. Error is the 95% confidence interval to the fit.*

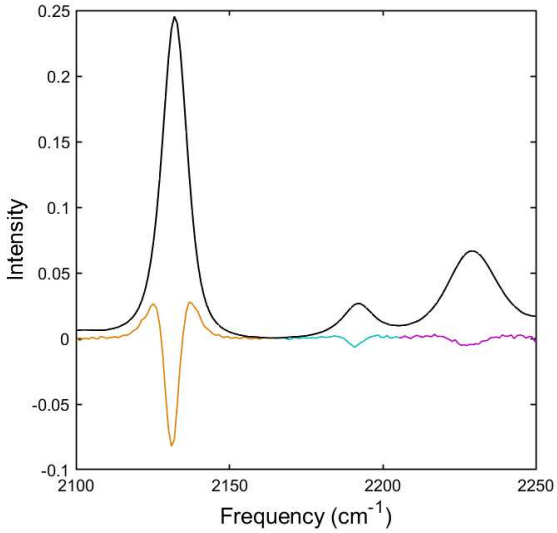

Figure B1: *Linear FTIR spectrum for the Environmental BmimDCA in BmimBF4 sample in black. The colored spectrum is the corresponding 2nd derivative spectrum.*

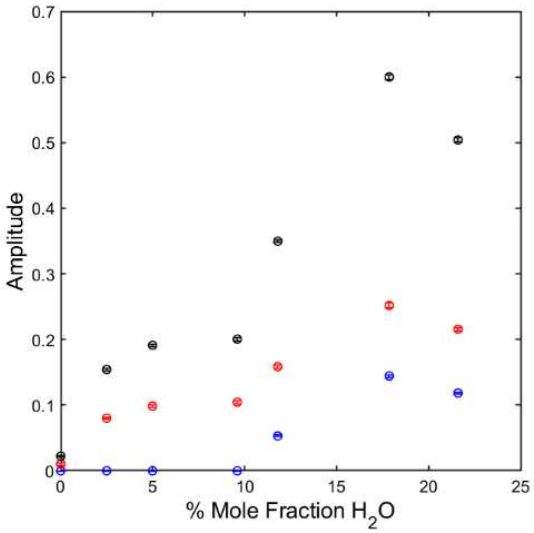

Figure B2: *Linear FTIR spectrum fitted amplitude to the three water peaks as a function of water. In black is the asymmetric stretch. Red is the symmetric stretch and blue is the bulk water peak.*

Table B1. *Fit results for the three DCA modes of interest for each concentration of water. Error is the 95% confidence interval to the fit.*

	Asymmetric Stretch			Symmetric Stretch			Combination Band		
Mole Fraction H_2O	**Center (cm^{-1})**	**FWHM (cm^{-1})**	**Amplitude**	**Center (cm^{-1})**	**FWHM (cm^{-1})**	**Amplitude**	**Center (cm^{-1})**	**FWHM (cm^{-1})**	**Amplitude**
Environmental (~1.32%)	2132 ± 1	10.6 ± 0.2	0.232 ± 0.004	2192 ± 1	8.5 ± 2.4	0.017 ± 0.004	2230 ± 1	18.24 ± 1.2	0.054 ± 0.003
2.5%	2133 ± 1	12.0 ± 0.3	0.136 ± 0.002	2193 ± 1	9.6 ± 2.8	0.011 ± 0.003	2232 ± 1	22.2 ± 1.5	0.034 ± 0.002
4.99%	2133 ± 1	12.3 ± 0.2	0.165 ± 0.002	2193 ± 1	11.1 ± 1.9	0.015 ± 0.002	2232 ± 1	21.9 ± 1.1	0.042 ± 0.002
9.6%	2133 ± 1	12.4 ± 0.3	0.114 ± 0.002	2193 ± 1	8.5 ± 3.3	0.008 ± 0.003	2232 ± 1	19.7 ± 1.6	0.028 ± 0.002
11.8%	2135 ± 0	13.4 ± 0.2	0.159 ± 0.002	2194 ± 1	12.1 ± 1.6	0.015 ± 0.002	2234 ± 0	23.4 ± 0.9	0.040 ± 0.001
17.86%	2137 ± 1	14.2 ± 0.1	0.184 ± 0.001	2197 ± 1	16.3 ± 1.2	0.021 ± 0.001	2237 ± 1	28.9 ± 0.7	0.048 ± 0.001
21.6%	2137 ± 1	14.2 ± 0.1	0.113 ± 0.001	2196 ± 1	14.6 ± 1.2	0.012 ± 0.001	2237 ± 0	25.6 ± 0.7	0.029 ± 0.001

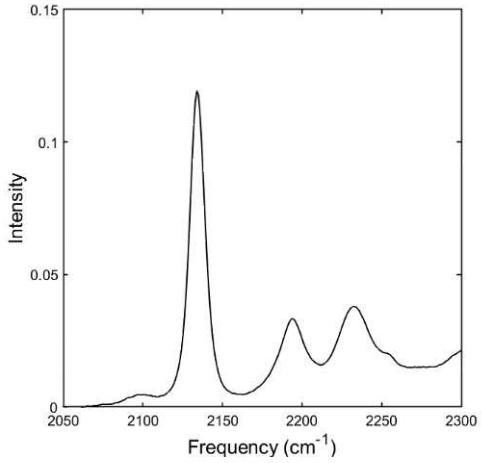

Figure B3: *Linear FTIR spectrum of the environmental BmimDCA in BmimTFSI.*

Section 2: Additional Rheology Results

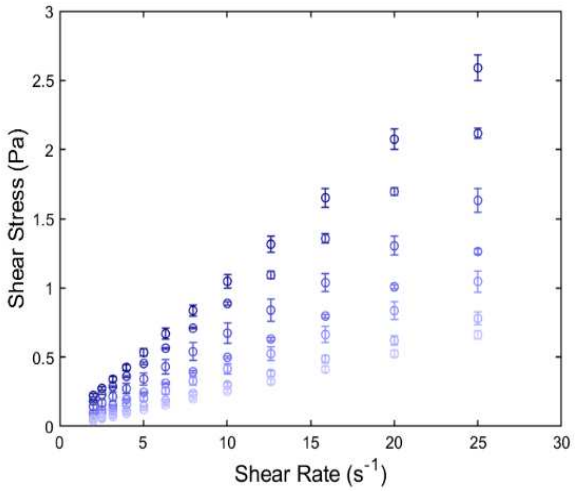

Figure B4: *Viscosity as a function of shear rate for each water sample, with dark to light being increasing amounts of water.*

Section 3: Additional 2D IR Data

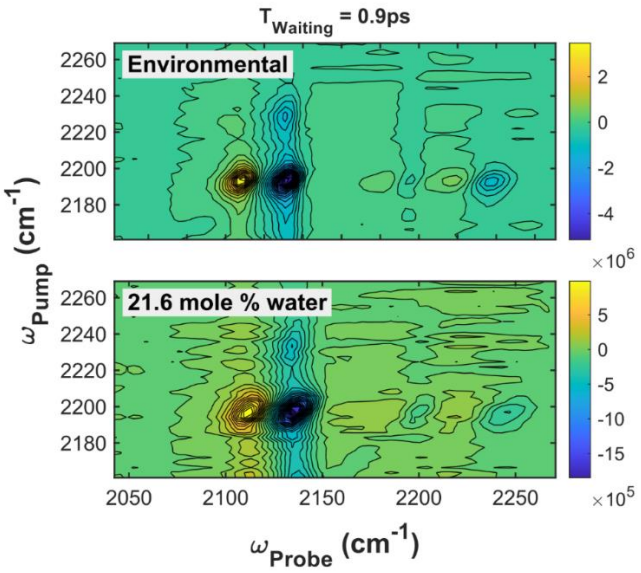

Figure B5: *Isotropic 2D IR spectra for two water concentrations; environmental (top) and 21.6 mole percent water (bottom) zoomed in on the symmetric and combination modes of DCA.*

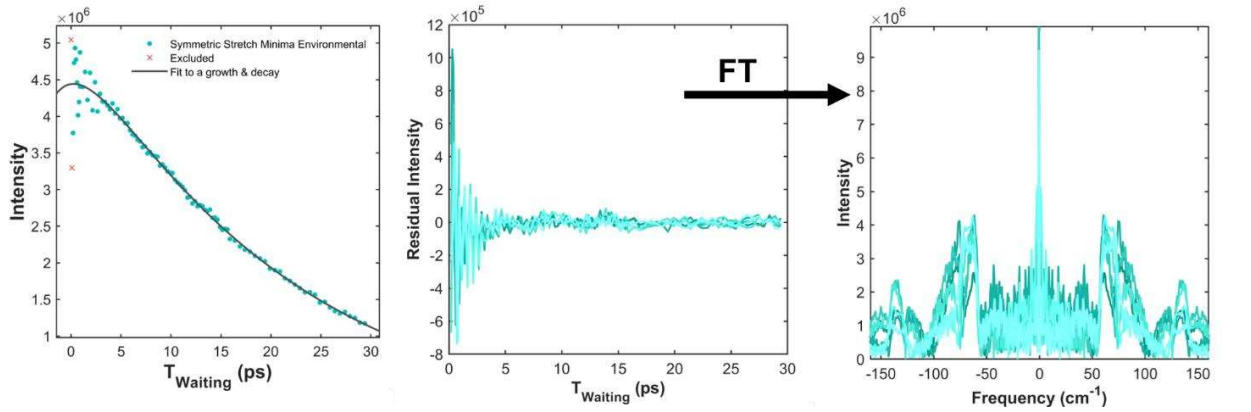

Figure B6: *Example fit, residuals and Fourier Transform used in the quantum beating analysis*

Table B2: *Short time amplitude from a biexponential fit to the signal decay at each concentration and each pump frequency across the asymmetric stretch peak*

		Short Time Amplitude Mole % Water						
		0	**2.5**	**5**	**9.6**	**11.8**	**17.9**	**21.6**
ω_{Pump} (cm^{-1})	**2127.6**	1.5E+07	5.9E+06	8.3E+06	5.9E+06	6.9E+06	5.6E+06	3.5E+06
	2130.3	2.8E+07	1.3E+07	1.8E+07	1.3E+07	1.5E+07	1.2E+07	7.2E+06
	2133.1	4.2E+07	2.3E+07	3.0E+07	2.4E+07	2.6E+07	2.1E+07	1.4E+07
	2135.9	4.5E+07	2.6E+07	3.5E+07	2.8E+07	3.4E+07	2.9E+07	2.2E+07
	2138.7	3.2E+07	2.1E+07	3.1E+07	2.3E+07	3.3E+07	3.1E+07	2.5E+07
	2141.4	1.5E+07	1.3E+07	2.1E+07	1.4E+07	2.6E+07	2.8E+07	2.4E+07
	2144.2	6.9E+06	6.5E+06	1.2E+07	7.1E+06	1.7E+07	2.1E+07	2.0E+07

Table B3: *Short time amplitude 95% confidence interval from a biexponential fit to the signal decay at each concentration and each pump frequency across the asymmetric stretch peak*

		Short Time Confidence Interval						
		Mole % Water						
		0	**2.5**	**5**	**9.6**	**11.8**	**17.9**	**21.6**
ω_{Pump} (cm^{-1})	**2127.6**	1.1E+06	5.0E+05	5.4E+05	4.7E+05	4.7E+05	4.1E+05	3.4E+05
	2130.3	1.5E+06	7.5E+05	8.4E+05	8.4E+05	7.7E+05	6.1E+05	4.6E+05
	2133.1	1.5E+06	9.0E+05	1.1E+06	1.1E+06	1.0E+06	8.9E+05	7.4E+05
	2135.9	1.5E+06	1.0E+06	1.3E+06	1.1E+06	1.3E+06	1.3E+06	1.1E+06
	2138.7	1.2E+06	9.0E+05	1.2E+06	9.9E+05	1.4E+06	1.4E+06	1.3E+06
	2141.4	6.5E+05	5.5E+05	7.9E+05	6.3E+05	1.0E+06	1.1E+06	1.2E+06
	2144.2	3.7E+05	2.8E+05	4.2E+05	3.5E+05	5.9E+05	7.1E+05	9.1E+05

Table B4: *Long time amplitude from a biexponential fit to the signal decay at each concentration and each pump frequency across the asymmetric stretch peak*

		Long Time Amplitude						
		Mole % Water						
		0	**2.5**	**5**	**9.6**	**11.8**	**17.9**	**21.6**
ω_{Pump} (cm^{-1})	**2127.6**	1.4E+07	6.4E+06	8.5E+06	6.6E+06	6.9E+06	5.4E+06	4.0E+06
	2130.3	3.0E+07	1.4E+07	1.8E+07	1.4E+07	1.4E+07	1.0E+07	6.9E+06
	2133.1	4.7E+07	2.4E+07	3.1E+07	2.5E+07	2.5E+07	1.9E+07	1.4E+07
	2135.9	5.2E+07	2.7E+07	3.7E+07	3.0E+07	3.3E+07	2.8E+07	2.2E+07
	2138.7	3.7E+07	2.2E+07	3.2E+07	2.4E+07	3.4E+07	3.1E+07	2.6E+07
	2141.4	1.9E+07	1.3E+07	2.2E+07	1.5E+07	2.8E+07	2.9E+07	2.6E+07
	2144.2	1.0E+07	7.2E+06	1.3E+07	8.3E+06	1.9E+07	2.2E+07	2.1E+07

Table B5: *Long time amplitude 95% confidence interval from a biexponential fit to the signal decay at each concentration and each pump frequency across the asymmetric stretch peak*

		Long Time Confidence Interval						
		Mole % Water						
		0	**2.5**	**5**	**9.6**	**11.8**	**17.9**	**21.6**
ω_{Pump} (cm^{-1})	**2127.6**	8.1E+05	4.3E+05	5.1E+05	4.2E+05	5.0E+05	3.7E+05	2.1E+05
	2130.3	1.2E+06	7.3E+05	8.7E+05	7.9E+05	8.5E+05	6.8E+05	5.2E+05
	2133.1	1.5E+06	9.7E+05	1.2E+06	1.1E+06	1.1E+06	1.0E+06	8.5E+05
	2135.9	1.7E+06	1.1E+06	1.5E+06	1.2E+06	1.5E+06	1.5E+06	1.3E+06
	2138.7	1.4E+06	1.0E+06	1.4E+06	1.1E+06	1.6E+06	1.6E+06	1.4E+06
	2141.4	7.3E+05	6.4E+05	9.3E+05	7.3E+05	1.2E+06	1.2E+06	1.2E+06
	2144.2	4.2E+05	3.3E+05	4.9E+05	4.0E+05	6.7E+05	7.8E+05	9.2E+05

Table B6: *Short time constant from a biexponential fit to the signal decay at each concentration and each pump frequency across the asymmetric stretch peak*

		Short Time Constant (ps) Mole % Water						
		0	**2.5**	**5**	**9.6**	**11.8**	**17.9**	**21.6**
ω_{Pump} (cm^{-1})	**2127.6**	1.55	1.66	1.74	1.66	1.82	1.47	1.09
	2130.3	1.66	1.76	1.87	1.70	1.94	1.81	1.76
	2133.1	1.91	1.96	1.99	1.88	1.92	1.82	1.72
	2135.9	2.05	2.11	2.04	2.00	1.91	1.77	1.56
	2138.7	2.11	2.11	2.00	1.94	1.75	1.56	1.34
	2141.4	2.13	2.07	1.89	1.88	1.58	1.42	1.23
	2144.2	2.30	2.02	1.73	1.79	1.50	1.35	1.20

Table B7: *Short time constant 95% confidence interval from a biexponential fit to the signal decay at each concentration and each pump frequency across the asymmetric stretch peak*

		Short Time Constant Confidence Interval (ps) Mole % Water						
		0	**2.5**	**5**	**9.6**	**11.8**	**17.9**	**21.6**
ω_{Pump} (cm^{-1})	**2127.6**	0.25	0.32	0.26	0.31	0.29	0.25	0.21
	2130.3	0.20	0.23	0.21	0.25	0.22	0.21	0.25
	2133.1	0.16	0.18	0.16	0.20	0.16	0.17	0.20
	2135.9	0.16	0.18	0.16	0.17	0.16	0.17	0.19
	2138.7	0.18	0.18	0.17	0.18	0.16	0.15	0.16
	2141.4	0.20	0.18	0.15	0.18	0.14	0.13	0.13
	2144.2	0.26	0.18	0.14	0.19	0.11	0.11	0.12

Table B8: *Long time constant from a biexponential fit to the signal decay at each concentration and each pump frequency across the asymmetric stretch peak*

		Long Time Constant (ps) Mole % Water						
		0	**2.5**	**5**	**9.6**	**11.8**	**17.9**	**21.6**
ω_{Pump} (cm^{-1})	**2127.6**	16.24	15.21	14.99	14.80	13.33	11.50	9.72
	2130.3	15.46	14.59	14.50	14.20	13.16	11.92	10.86
	2133.1	15.64	14.59	14.25	14.15	12.67	11.50	10.33
	2135.9	15.59	14.07	13.43	13.61	11.64	10.39	9.17
	2138.7	15.06	12.83	12.06	12.16	10.22	9.21	8.26
	2141.4	15.13	11.92	10.93	11.16	9.31	8.61	7.77
	2144.2	15.79	11.82	10.23	10.93	8.78	8.08	7.29

Table B9: *Long time constant 95% confidence interval from a biexponential fit to the signal decay at each concentration and each pump frequency across the asymmetric stretch peak*

		Long Time Constant Confidence Interval (ps)						
		Mole % Water						
		0	**2.5**	**5**	**9.6**	**11.8**	**17.9**	**21.6**
ω_{Pump} (cm^{-1})	**2127.6**	1.15	1.18	1.01	1.07	0.97	0.78	0.50
	2130.3	0.77	0.83	0.76	0.85	0.76	0.71	0.71
	2133.1	0.57	0.63	0.57	0.67	0.53	0.53	0.54
	2135.9	0.54	0.58	0.51	0.54	0.47	0.48	0.45
	2138.7	0.58	0.56	0.48	0.51	0.40	0.38	0.35
	2141.4	0.60	0.49	0.39	0.46	0.31	0.29	0.28
	2144.2	0.69	0.47	0.32	0.46	0.25	0.23	0.25

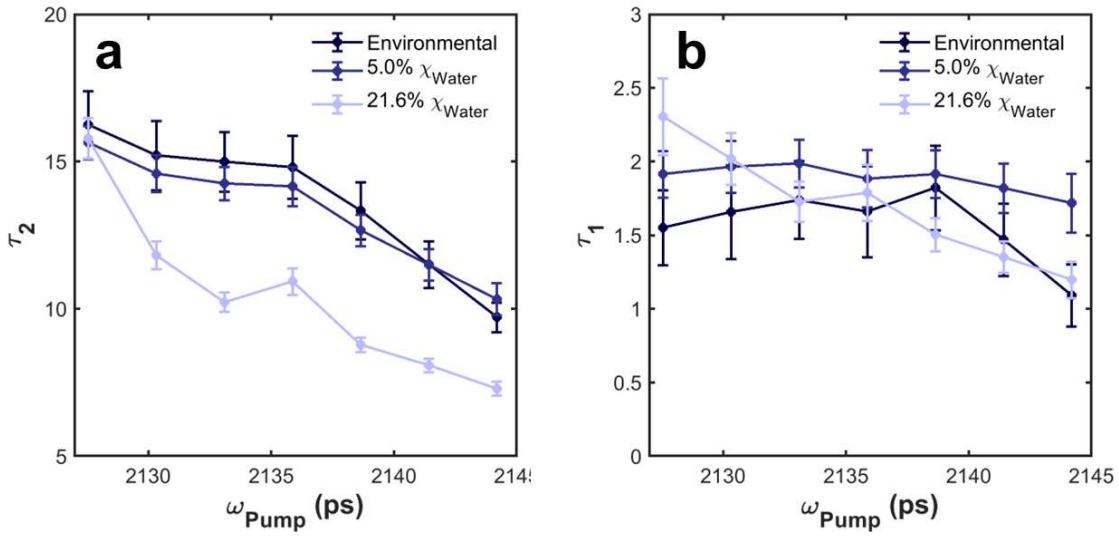

Figure B7: *Visualization of the (a) fast time component of the population relaxation for a water sample in the low, mid, and high water concentration regime and (b) slow time component. The error bars are from the 95% confidence interval of the fit. The data fit is an average of the data collected in triplicate.*

Appendix C

Turning on the Laser

Part 1: Chillers, Compressors, Air, OPO

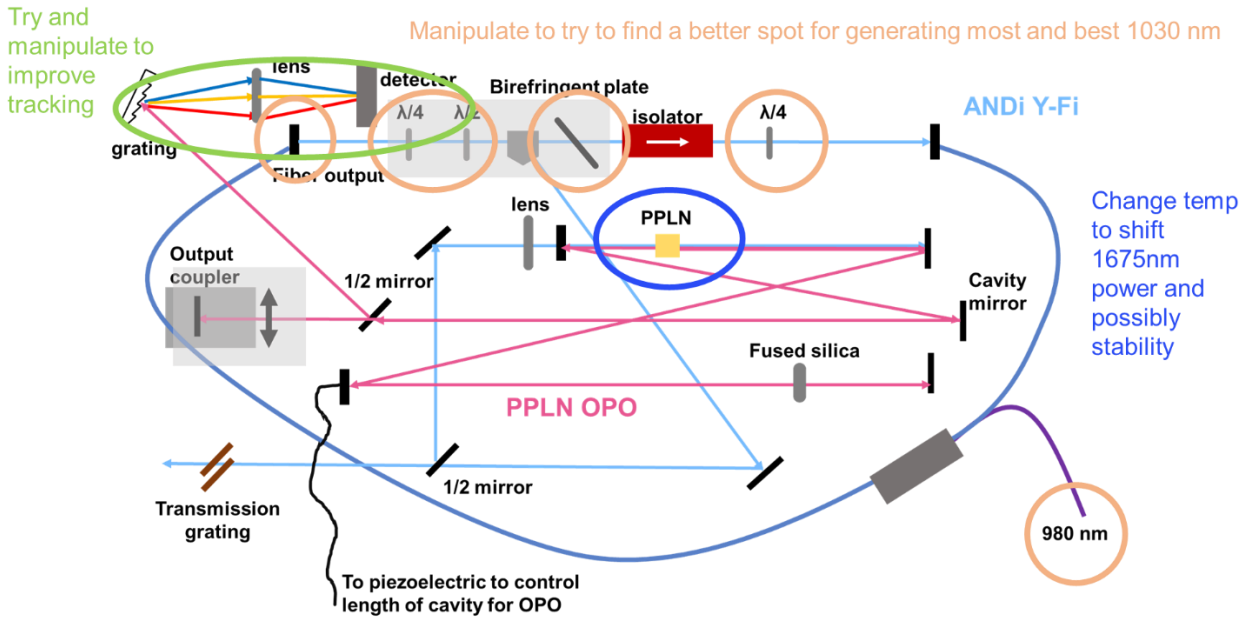

Figure C1: *Figure of the silver box interior including the ANDi Y-Fi (all normal dispersion ytterbium fiber oscillator) and the OPO (optical parametric oscillator). Notes corresponding to circled components, in green, salmon, and blue are suggestions for troubleshooting different issues that may arise.*

- Check that the pressure is less than # x 10^{-6} on the ion pump
- Turn on the water for the chiller (toggle switch & button on first box in closet)
- ONLY if ion pump pressure is okay then turn on the compressors with the 2 green buttons on the regen and multipass compressors
- Switch on the air to dry the table with toggle switch under box on the wall, in the closet
- Turn the air to the table on by making the switch parallel to the box (off is ~ 45 degrees)
- Check that the OPO is tracking, first try and recover with micrometer in the OPO (noted by the black double-sided arrow in the above Figure C1). You can use the spectrum of the 1675 nm light on the spectrometer (using 2nd flip mirror on the 1675nm line) in the LabView program named monochromator_calibrateV4.vi by clicking “continuous scan” under the spectrometer tab as a guide to find the light.

- To reset the voltage to keep the 1675nm tracking if it has stopped do the following:
    - Turn the PID controller to manual
    - Make note of the micrometer starting position
    - Then make small motions to try and center the light at 1675nm on the spectrometer
    - Note: If you can't find it, turn off the lights and use the Newport infrared sensor card placed on the 1675nm line coming out of the OPO (or look for red light in the box) to get some light – then you should be able to use the spectrometer again
- Check 1675 nm stability with the oscilloscope- using flip mirror # 1, bouncing off the next mirror onto the DET10N photodiode – connected to the oscilloscope, then maximize the intensity. Use an OD 2 filter in front of the photodiode. Measure the stability by hitting "measure" then "more" then "reset statistics" then "menu off" divide the standard deviation/mean should be less than 2% ideally (at most 3%).

- Check the temperature of the water on the Arryo Instruments Laser Diode Controller 6340
    - Should be ~ 14 – 17 °C after cooling for about 5-15 minutes
        - This temperature will probably oscillate, which is fine but will impact your power outputs (especially when it is cold or hot weather)
        - If higher than 17°C check the temperature setting on the chiller box in the closet and turn down if that's an option
        - If that's not an option measure the temperature of the incoming water to see if that's the issue – if the incoming temperature is too hot, the interlocks for the shaper, and Pockels cells will automatically trigger and shut down. In this scenario immediately turn everything off.

Part 2: Turning on the Pockels Cells, PhaseTech, and Regenerative Amplifier

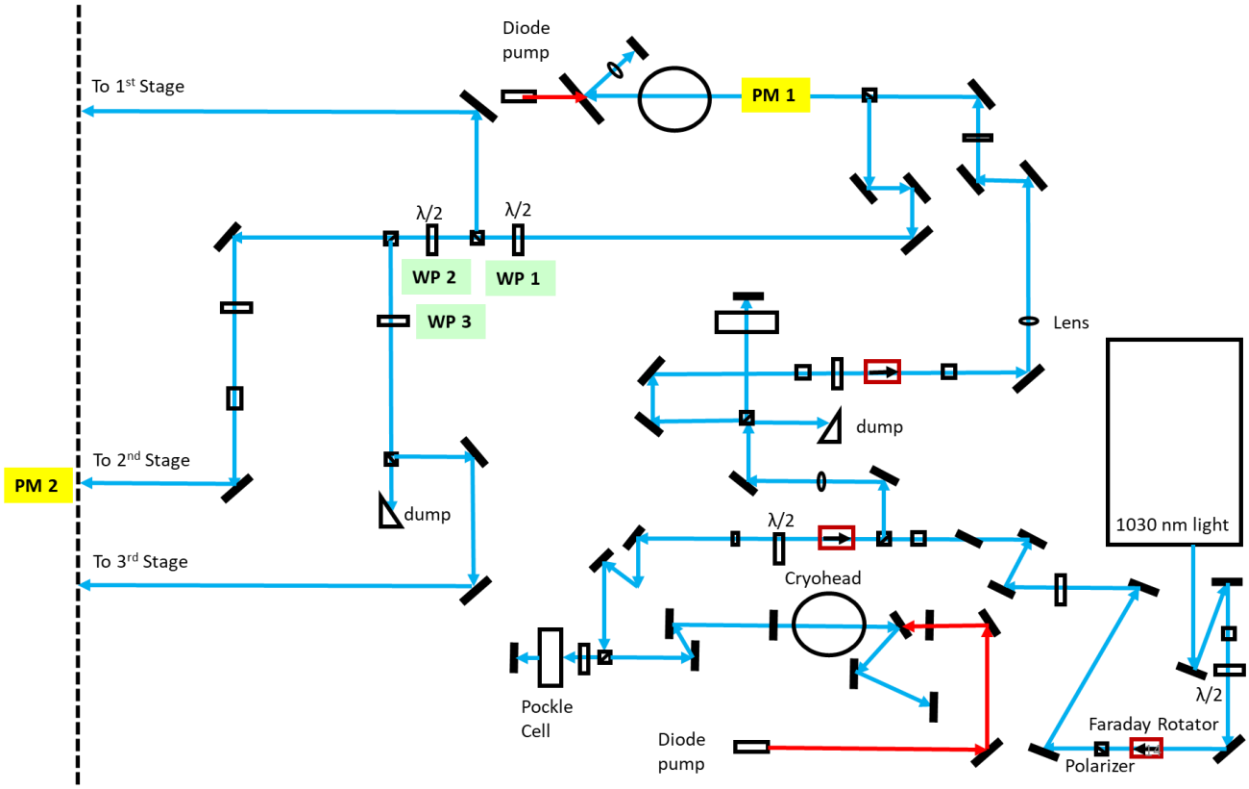

Figure C2: *1030 nm beam path through the regenerative and multipass amplifiers. WP stands for waveplate and PM for power meter.*

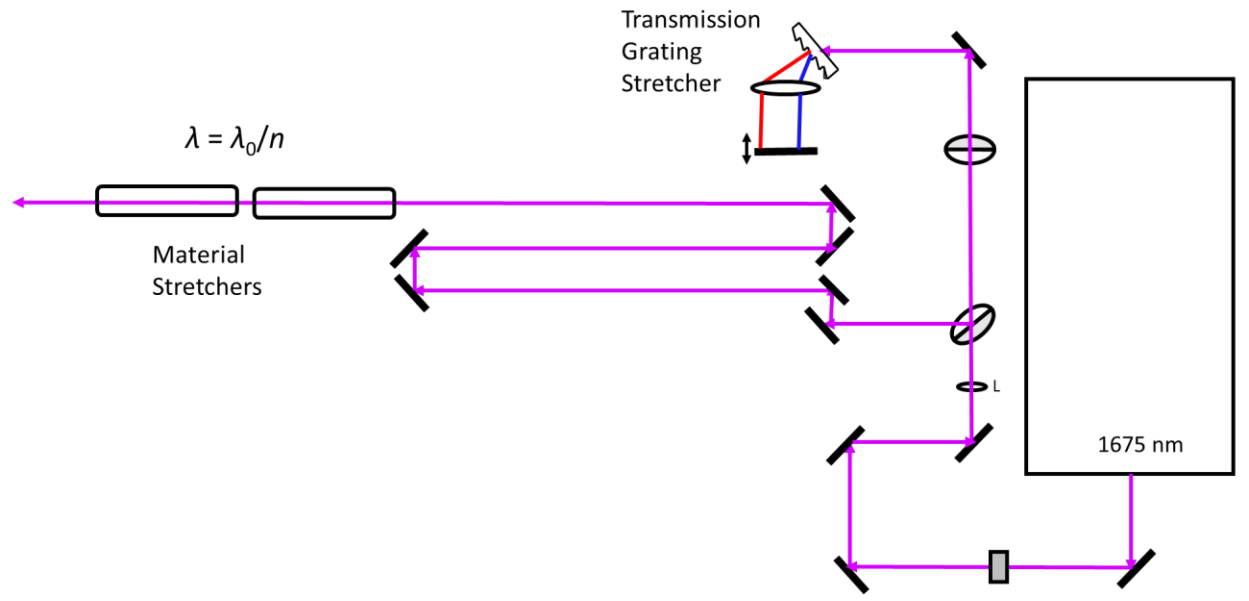

Figure C3: *1675 nm beam path out of the optical parametric oscillator through the grating and material stretchers before the PPLN stages.*

- ONLY if chiller temperature is in the acceptable range turn on the two Pockels cells (silver boxes – PCD8f2)
- Check the temperature of the Cryohead. The temperature should be -240C or lower before you turn on the regen or multipass.
- Place the power meter in front of the multipass cryohead, this is where you will record the power out of the Regen (shown in Figure C2 as the yellow box labelled PM 1 (power meter spot 1)) (any position after the clean-up Pockels cell is fine).
- Turn on Pulse Shaper – PhaseTech (You can do this at the start of the day or closer to when you are collecting data – sometimes the PT being on will cause the temperature of the water cycling through the Pockels cells/diodes etc. to increase so depending on if things are running too hot or too cold be turning it on at different times might be helpful).
    - The red light must turn on!
    - Turn on corresponding computer and hit update masks and update AWG (this can be done any time before aligning the pump light).
    - Note: There are two PT software options. The most recent version is found in folder QC_423 on the desktop. Open PT_QC (stands for PhaseTech Quick Control). An error will pop-up (Error 516) ignore this and hit continue.
    - PT settings to use:
        - Under the MAIN tab set the amplitude to 30% for alignment and typically between 6-15% for data collection (dependent on power output).
        - Mask Length: 8000 S
        - For alignment use BASIC mask.
- Turn on Regen, if S/D light is red – push little black button for interlock on top of box over the OPO

- Adjust the fiber controlling the regen pump to 21.8 Amps and get out ~ 5.0 W on the power meter (record the pump current and output power in the lab notebook daily). As turning up make sure that the power begins increasing (on the power meter) at 10 amps – this is when the cavity should start lasing. If not turn the knob to zero before shutting off. One potential issue: check the power meter and confirm it is not in averaging mode. Another issue: the timing is wrong – check the Stanford to see if there is an error light, if so, go to the Texas instrument program on the oscillator laptop and make sure the correct file is loaded. The correct file should be named 1134and6.3and63a.
- Wait ~ 30-45 min for fiber that is pumping the laser to warm up

Part 3: Turning on the Multipass Amplifier

- Take power meter to 2nd stage (PM2), outside of the black box
    - Keep beam block in until the meter is in place, then scoot closer to the hole
    - Check that the 3rd waveplate (Figure C2 WP 3) is at 146 degrees (this minimizes power going to 3rd stage)
    - Use 2nd waveplate to maximize power (WP 2)
    - Use 2nd waveplate to check minimized power to the 3rd stage look at green dot on a lollipop until it disappears
    - Use the 1st waveplate (WP 1) to check minimized power to the 1st stage look at green dot on a lollipop until it disappears
- Turn up the current to the multipass pump controller so that the output power is 10W on the power meter then use 2nd waveplate to turn down to 1W then turn current up to ~ 41.1 amps (check the lab notebook or yellow tape for exact value to use)
    - Record the daily multipass output after waiting ~ 30-45 min for the fiber to warm-up

Part 4: OPCPA and ZGP Alignment

General tip: *For aligning, use the mirror closest to the first iris to align the farthest iris, then use the mirror one step away to align on to the closest iris*

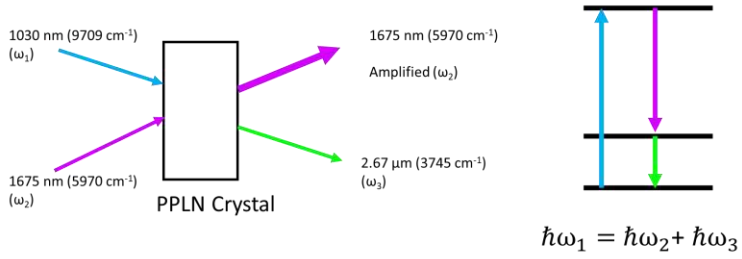

Figure C4: *Energy level diagram showing difference frequency generation and cartoon representation of the optical parametric amplification process occurring in the PPLN crystals with the 1030 nm pump, and the 1675 nm seed.*

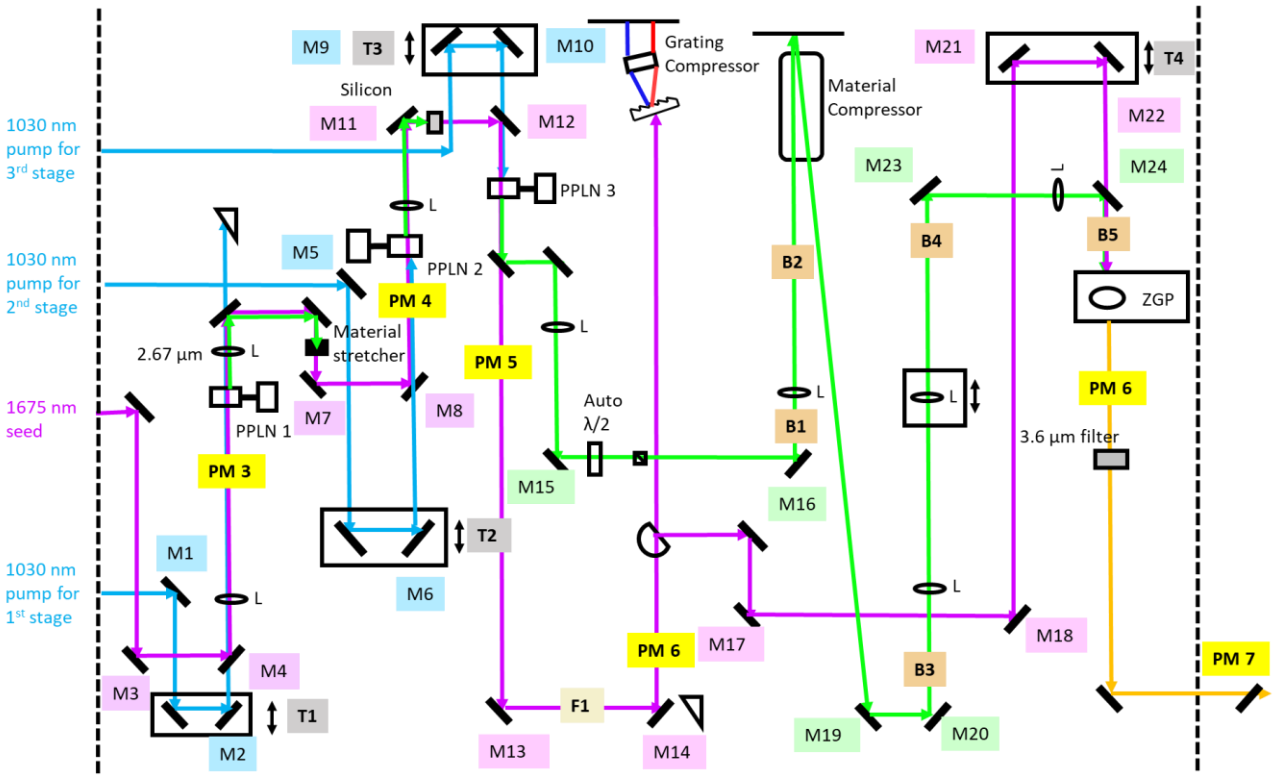

Figure C5: *Beam path in blue for the 1030 nm pump lines to each PPLN. 1675 nm beam paths shown in magenta. The lime green line is the generated 2.67 µm light and the gold is the generated mid-IR light. Codes starting with M are mirrors used in the alignment procedures. Codes beginning with PM are representative of locations to place the power meter. Codes beginning with B are spots to place the copper IR alignment block. L represents lenses. Codes starting with T are timing stages.*

Abridged Daily Alignment Procedure:

1. Make sure the 2nd waveplate (Figure C2 WP 3) is at 146
2. Place the power meter in front of PPLN 1 (PM 3 in Figure C3)
3. Adjust the 1030 nm pump power to ~ 650 mW using the 1st waveplate (WP 1 Figure C2)
4. Block everything
5. Zero power meter and check the power of the 1675 nm light after PPLN 1 (PM 4).
    a. Put power meter in front of PPLN 2 on the 1675 nm line (next to the hole in the black box)
        i. Open 1675 nm seed light
        ii. Open 1030 nm light to first stage
        iii. Use timing to maximize (labelled in Figure C3 with the grey box T1)
        iv. Use M4 in Figure C4 to maximize power
        v. Iterate between steps iii and iv directly above until power is maximized
        vi. Record pump power and output 1675 nm power in the current lab notebook (Hopefully over 5 mW, ideally 8-15 mW)
6. Block all and open 2nd stage
7. Use 2nd waveplate to turn the 1030 nm pump power to 3.75 W
8. Block everything
9. Put power meter after PPLN 3 (next to hole in box on the opposite from when measuring 1st stage power: PM 5)
10. Unblock power to the first stage (1675 nm first) (at this point you should be getting around 80% of the 1st stage power).
11. Then unblock 2nd stage (Make sure to block 1030 nm to the 3rd stage or you will measure more power than reality).
    a. Using T2 to change timing and maximize power

b. Tweak M8 to maximize power

c. Iterate between steps a and b directly above to maximize power

d. Record power meter reading in lab notebook

12. Place the power meter after the 2nd turning mirror after PPLN 3 (PM 6)
13. Use IR scope to align the 1675 nm (using M11 and M12) (alternating until both centered)
14. Block pump to 2nd stage
15. Open 1030 nm to the 3rd stage
16. Align with M9 and M10
17. Turn 2nd waveplate from 146 to 100
18. Record power at PM6 in lab notebook (Should be between 3.5 to 5.5 W typically)
19. Power meter after ZGP outside of the black box.
20. Close boxes
21. Let purge for at least 1 hour (1.5 to 2 is better)
22. Adjust the timing (T4) and position with micrometer and Allen wrenches outside of the box

Full Alignment of the OPCPA Stages and the ZGP

- Place a long-pass filter to remove light less than 1 micron (place in front of the 1st stage hole in the black box) this is to remove the "halo" around the 1030 nm light when aligning. You can also close preceding iris if the halo is too big
- Using IR viewer, align to two irises, one right after PPLN 1 with right mirror on T1 & iris before PPLN 1 and mirror right after the box hole (M1 and M2)
- Remove long-pass filter and open iris if you closed it
- Look at back reflection onto the iris in front of PPLN #1, make sure it is centered and slightly high
- Make sure PPLN #1 is on the 3rd period
    - Turn the 1030 nm power to between ~50-100 mW (the low power is to avoid burning)

- Place a flashcard behind PPLN 1- you should see a dot
- Scan through each period. Do this by twisting the silver knob to the far edge and then adjusting to the center (there are 5 periods total) only ever twist the side and top knobs, not the front knob
- Once in the correct period move to be approximately centered on the 3rd period – however you should try and avoid any burns or defects (You can do this by avoiding bright spots/ halos/ stripes)
- Scan the top knob to center the PPLN vertically, again avoiding burns

- Place the power meter in front of the PPLN #1 and adjust power to ~ 650 mW with WP1
- Block everything
- Put power meter in front of PPLN 2 and zero the power meter
  - Open 1675 nm light (anticipated ~ 8mW)
  - Open 1030 nm light (anticipated ~ 45mW)
  - If power, use T1 stage to maximize timing & M4 to maximize overlap with 1675 nm
  - If no power, align 1675nm light by place the power meter at PM4, and then iterating between partially closing the irises used for 1030 nm alignment and maximizing the 1675nm power with M4 and M3 for the far and close irises respectively
  - If still no power, use the camera to image the beams at PPLN1 (note: In this following process, be very careful not to send too much power to the camera and burn it)
    - First block everything
    - Unscrew the PPLN 1 oven and crystal and remove and set aside
    - Place the camera (hooked up to the 1675nm spectrometer computer via a USB cord) in place of the PPLN
    - In the Mightex Camera folder open the Mightex Camera e.vi program and start the camera, make sure you are viewing the full screen
    - Turn the room lights off

    - Place the power meter at PM3 and measure the 1030 nm power.
    - Turn the power down to under 30-70 mW
    - Add OD filters somewhere on the 1030 nm line before PPLN 1 (typically starting with more than needed) (say 2 OD1 and 1 OD2)
    - Remove the power meter carefully watching the LabView program. If you see a huge dot immediately block the light and then turn the power down or add a filter
    - Once you have a small dot mark the location with cursors
    - Block the 1030 nm light and move filters to the 1675nm line (you will probably need less filters for this line)
    - Unblock the 1675 nm light and tweak M4 to overlap the dot with the 1030 nm cursor position – now you are confident there is spatial overlap
    - Remove the camera and place PPLN 1 back (check the back reflection of the green light from the PPLN is centered and slightly high on the iris before the PPLN
    - Check the period of the PPLN as described above
    - Turn 1030 nm pump back to 650 mW and measure output 1675nm power
    - Tweak T1 to maximize power
- Record stage 1 power in the lab notebook
- Turn the second stage 1030 nm pump to 100 mW using WP2
- Using IR viewer align the 1030 nm onto PPLN2 (using M5 and M6 and the irises before and after PPLN 2)
- Put power meter back in front of PPLN #2 and turn power of pump to 3.75 W on 1030 nm using 2nd waveplate
- Unblock the 1675 nm
- If no power, check overlap with the camera

- Unblock power to 1st stage
- Unblock power to 2nd stage
- Use the T2 to maximize timing overlap
- Record power meter reading
- Align onto the 3rd stage as described in the abridged alignment above
- Unblock the 1030 nm to the 1st & 2nd stages
- Unblock the 1675 nm light
- Adjust WP3 to 100 from 146
- Adjust the T3 timing, using the timing rod on the side of the stage
- Turn WP3 back towards toward 146 for the following alignment (typically adjusting between 140 and 130 as needed)
- Place long-pass filter (F1) & check the back reflection
- Align 1675 nm onto grating compressor with irises M13 and M14 and the irises on the line before the grating compressor
- Align 1675 nm light onto timing stage with mirrors M17 and M18 and the two irises on the line following M18
- Aligning 2.67 µm light
    - Turn up power to 3rd stage ~136 degrees on WP3
    - Using the IR card on the copper block (Note: careful to keep safe eye position as the goggles don't block this light and keep your wrists up to avoid burns) start aligning far then near with mirrors M16 and M15 at spots B2 and B1 (locations to place the copper block)
    - Next align to B4 and B3 with M20 and M19 respectively. Note that this is a tricky place to align given how little distance there is between the mirror and first alignment location.

- Place power meter after the ZGP in front of the 3.6 µm long pass filter (allows light > 3.6 µm through) (PM 6)
- Block 1675 nm & 2.67 µm with foam blocks before the ZGP
- Place mount on stage with the ZGP to slide pinhole into beam path
- Use M22 to maximize 1675 nm light through the pinhole (checking by looking at the power meter for the maximized value) and then use M21 and the iris preceding the pinhole for the close alignment
- Use M24 to align the 2.67 µm through the pinhole (checking by looking at the power meter for the maximized value). If you don't see power check where the beam is going using an IR sensitive card and adjust pointing. For the close alignment place the copper block at B5, elevated. Close the preceding iris as far as you can and still see light on the card, then use M23 to maximize light through the iris, close tighter if possible and repeat until the 2.67 µm is centered through the iris on the card.
- Once both 1675 nm and 2.67 µm are aligned through the pinhole remove the mount in the ZGP stage micrometer. Remove the power meter. Check that the filter, F1, is removed and all irises used for alignment are open again.
- Turn WP3 to 100
- Close the boxes
- Adjust timing with T4 and pointing with M22 using the allen wrenches outside the box
- Shut box and dry at least an hour, preferrable 1.5-2 hours.
- Adjust timing with T4 and pointing with M22 using the allen wrenches outside the box
- Record ZGP output power in lab notebook

Part 5: Collecting a 2D IR Spectrum

Alignment For the Pump-Probe Geometry

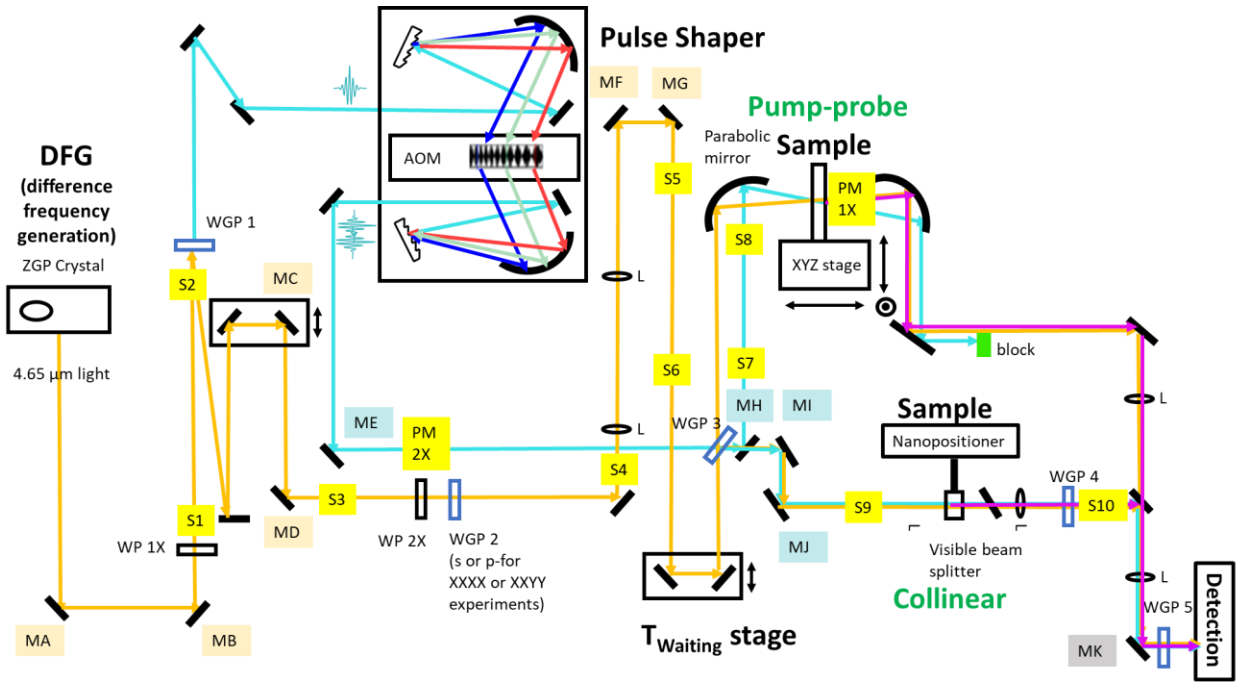

Figure C6: *Beam path in gold for the probe line. The pump line is shown in turquoise. The 2D IR signal is shown in magenta. Codes starting with M are mirrors used in the alignment procedures. Codes beginning with PM are representative of locations to place the power meter. Codes beginning with S are spots to place the copper IR alignment block. L represents lenses. Codes starting with T are timing stages. WP represents waveplate. WGP stands for wire grid polarizer.*

Probe Line:

- After dry: repeat timing and pointing adjustment with T4 and M22
- Use MA and MB (Figure C5) to align the mid IR light to S1 and S2 with the IR card on the copper block
- Use MC and MD to align the probe light to S3 and S4
- Then use MF and MG to align to S5 and S6. To see the card at S5 use a flashlight and look at the reflection of the block in the black box

Pump Line

- If not already, turn on the pulse shaper using the following settings for alignment
    - Basic
        - Amplitude : 0.30 V (30%)

        - Masklength : 8000 s
        - Hit update masks and update AWG
- Turn the WP 1X so maximum power is in the pump line
- Align pump to S7 and S8 using ME and removable mirror MH

Alignment through Pinhole at Sample Spot

- Fill the detector with liquid nitrogen (funnel into gold hole on top of red cylinder)
- Maximize probe light with WP 1X
- Turn on the FPAS

In the Labview Program Single Pixel 2D SpectrometerAA.vi

- Main →
    - Initialize FPAS – load the startup.txt configuration file in the folder named 'FPASN175_6416COLORADO_100kHz'
    - Initialize iHR320
    - Grating 1 (100 ln/mm grating)
    - Spectrometer →
        - Stage at zero
        - Entrance: front
        - Entrance slit: 0.15 mm
        - Exit: front
        - Exit Slit: 0.00
        - Desired wavelength: 4650 nm
        - Wavelength step: 1.000
        - Hit send command (do this twice)
    - Scan Controls →

        - Hit start scan
    - Maximize light on detector using both the vertical and horizontal adjustments of ML (the last pointing mirror before the detector)
    - Place the pinhole into the sample position in the pump probe geometry
    - Block the pump line
    - Adjust the Z position of the sample stage to 12.00 mm (or the relevant focus)
    - If there is still probe light on the detector maximize by using the X and Y controls of the sample stage
    - If there is no light scan the X and Y iteratively, starting at the most recent positions (from the lab notebook)
    - After maximizing on the detector place the power meter at PM 1X and maximize power with X and Y
    - Minimize probe power with WP 1X
    - Block probe power and unblock pump power
    - Maximize pump power through the pinhole with MH

Finding Time Zero

- Using WP 1X and WP 2X and ML get the pump and probe signal on the detector approximately equal
- Make sure that you are in the co-polarized set-up by checking the position of WGP 2
- Initialize $T_{Waiting}$ stage (labelled AGLS25-27P in LabView)
- Set the absolute stage position in LabView close to the T0 from the previous day (lab notebook)
- You should see fringes if you are close to T0. Maximizes these fringes with ML, WP 1X and WP 2X

- Move the stage far from T0 and take a background switching the Scan Type from Sample to background and back (Note: this background is taken with the probe and pump unblocked to make the fringes clearer)
- Click on the spec inter tab of the LabView program
- Set the scan time (typically 7-10 ps is good)
- Set the step size to 0.1
- Set the Start Stage position to something like 0.5 before the anticipated T0
- Hit start spec inter
- Select the center of the fringes in the interferogram by look at specific vertical lines
    - Visually approximate the center (shown in the left in Figure C6)
    - Set the cursor to that position
    - Click plot single pixel
    - Repeat until you find the least fringy shape.
- Another way to check T0 is with a homogenous sample like MeSCN in DMSO and check the 2D IR spectra as shown in Figure C7 on the right

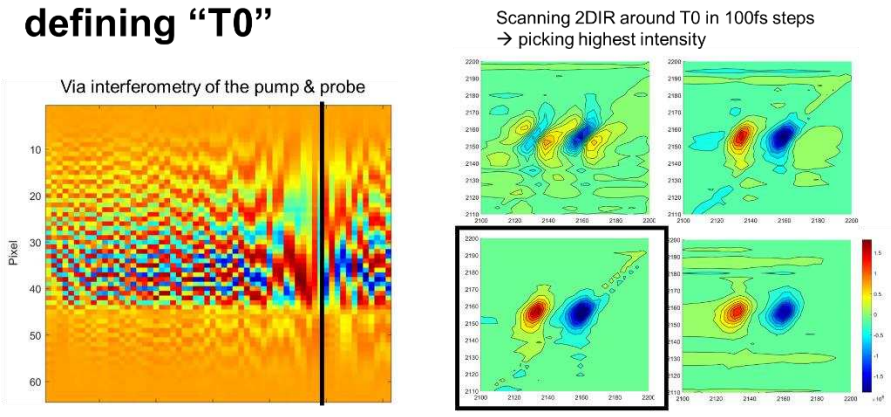

Figure C7: (Left) *Example interferogram between pump and probe pulses, the black line showing a visually estimated T0. (Right) MeSCN in DMSO samples 2D IR spectra taken around the T0. The Black box represents the sprectrum with the highest signal and thus closest to the T0.*

Collecting a 2D IR Spectrum

- Use WP 1X to send maximum power to the pump line
- Insert Sample
- Return to the PhaseTech Quick Control software and switch from the BASIC tab to the TIME tab. Use the following settings:
    - Type: Scan Delays
    - Form: Double Pulse
    - Direction: Backward
    - Step Size: 10 fs
    - Final Delay: 6000 fs
    - Rotating Frame Scanned: 1900 cm-1
    - Chop: off
    - Phase Cycling: on
    - Frames

Frame	Scanned Pulse	Fixed Pulse
1	**0** π	**0** π
2	**0** π	**1** π
3	**1** π	**1** π
4	**1** π	**0** π

    - Set amplitude to between 7-12% whatever gives you between 15 and 20 mW of pump power (measured at PM 2X)
    - Click Update Masks and Update AWG – this will take a minute to load
    - Insert notecard block at the green block spot in Figure C5 to block pump light getting to the detector (there is a sharpie line on the tale marking approximately where the card edge should go)
- Insert WGP 5 set to the co-polarized setting as noted by the notecard in the cupboard on the wall
- Use WP 2X to adjust the probe signal on the detector to below (if possible) or close to 2V

- Make sure the number of shots per scan under Scan Controls matches the number of pump time delays you set in the PT QC
- Click the 2D Scan tab
- Calculate B array used for the noise reduction procedure
    - Set # of shots for B to 10,000
    - Set Ref pix 1 for B to some pixel close to but lower than you anticipate having 2D IR signal
    - Set Ref pix 2 for B to some pixel close to but higher than you anticipate having 2D IR signal
    - Block the pump line with a card and click Run B (this only takes a very short time)
- Then click Alignment mode and set the # of scans to between 20 and 100 depending on anticipated signal strength
- Hit Start 2D IR
- Auto scale the display on the lower right and set the display element for TA value to be a pump pixel you anticipate being through your signal
- Then scan Z to higher values until you see your 2D IR signal. Then scan and maximize the signal using Z and MH (very small motions so you don't lose your signal)
- Now you are ready to collect 2D IR data!

For Microscope (Collinear geometry)

- Same alignment of probe line up to the recombination of the pump and probe lines at the removable wire grid polarizer, WGP 3.
- Make sure MH is removed and WGP 3 (blue box below) is in place on the magnetic mount

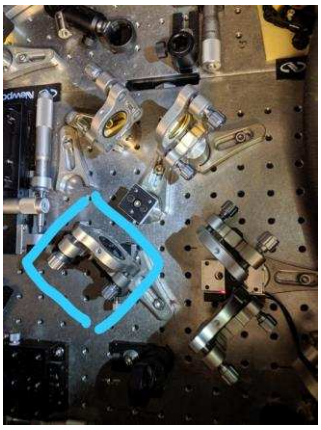

Figure C8: *Picture showing the location to insert the removable WGP for the collinear geometry highlighted in a blue box.*

- Add in MK and take everything out of the line after the WGP 3 and before MK

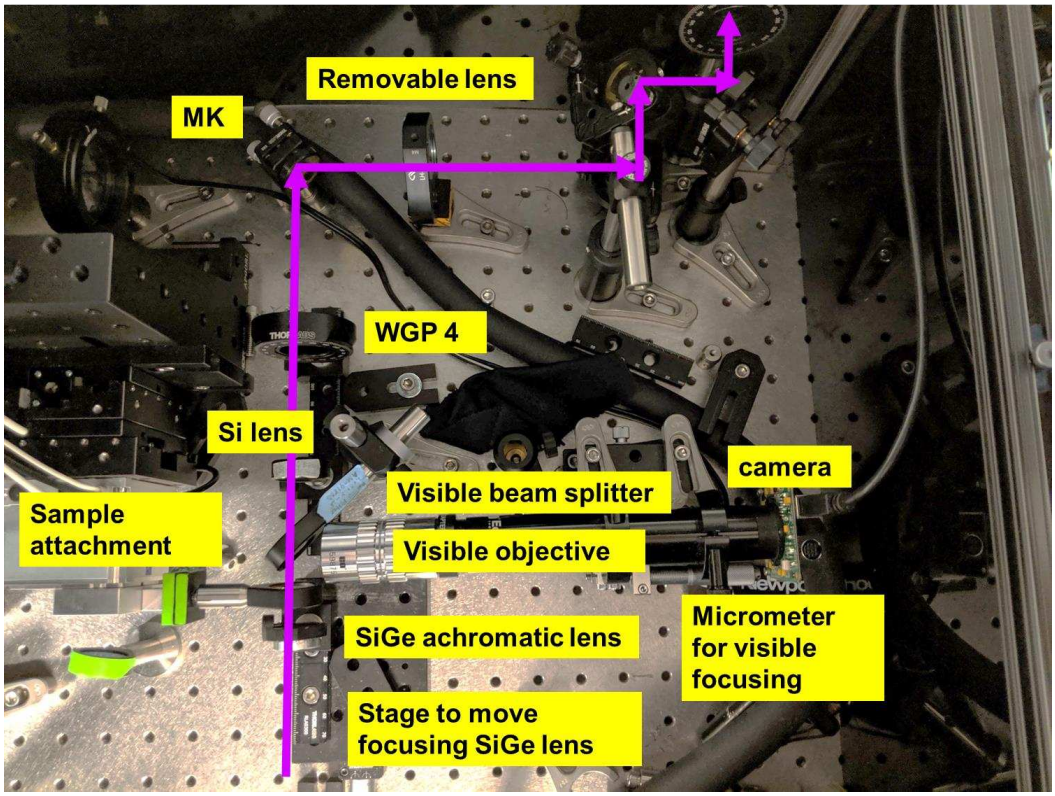

Figure C9: *Picture showing the important components of the collinear line after the WGP 3 in Figure C8. Si stands for silicon and Ge for germanium. MK is the removable mirror.*

- Use the copper block with the IR card and align the probe to S9 and S10 using the WGP 3 pointing and the stage on the base for control. For the near alignment use the base. Using the base you will only have horizontal movement so the preceding probe alignment must be excellent.
- Align the pump to S9 and S10 using MI and MJ
- Check overlap of pump and probe by imaging the heat sensitive paper
    - Place the SiGe achromatic lens (Figure C9)
    - Block the pump and probe
    - Click on the Microscope tab in the LabView program
    - Put the visible beam splitter in
    - Put the LMR1 with the heat sensitive paper in
    - Use a flashlight to illuminate the sample
    - Click Start Camera
    - Turn power to probe line with WP1X
    - Unblock the pump line – you should see an open ring on the Intensity Graph 2 – this is the pump light
    - Click Stop Camera and center cursors on the ring so you know the pump location
    - Block the pump and minimize the probe power with WP1X
    - Put the OD 1 Mid IR filter in somewhere in front of the heat sensitive paper (you may not need this filter depending on the probe power but use it to start with, so you don't accidentally burn the paper)
    - Illuminate the sample with the flashlight, start the camera, and unblock the probe – you should see a bright dot. If this dot is not overlapped with the cursors centered on the pump use the WGP 3 to adjust and center the probe on the pump
    - Remove the heat sensitive card
- Align through the pinhole
    - Replace the heat paper LMR1 with the LMR1 containing the 50 μm pinhole

- Click Start Camera
- Use a flashlight from the front of the pinhole to illuminate the pinhole (Note: there is a burn near the pinhole. To distinguish the two note that the burn is irregular and horizontal in shape and not circular). This burn is ~1048 μm from the pinhole. Record the pinhole and stage and cursor positions.
- You can check the focus of the visible camera by moving the objective in front of the camera until the burn is in focus (Figure C9)
- Place the power meter (on a shorter base) behind the pinhole
- Maximize power to the pump line by changing the New X Position and New Y Position boxes in LabView and then hitting Move ABS Pos.
- Check the focus of the SiGe lens by moving the micrometer on the stage it is on, maximize the power through the pinhole
- Maximize power to the probe line and then maximize probe power through the pinhole using WGP3
- You can reset the home stage position to this new pinhole center position, which now matches the beam centers

- Fill the detector with liquid nitrogen
- Maximize IR light to the pump line with WP1X
- Turn on FPAS
- Initialize Horiba and FPAS as described above
- Place the silicon lens after the pinhole

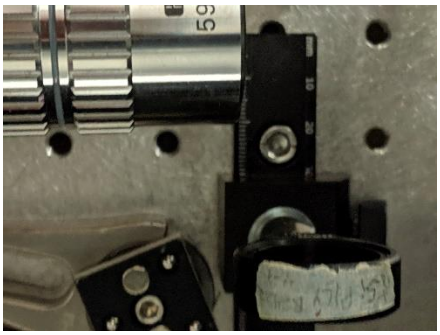

Figure C10: *Picture showing the location of the silicon lens after the sample in the collinear geometry.*

- Check probe signal on detector, check alignment through removable lens with MK
- Adjust pointing into detector
- Go through the Finding Time Zero section above
- Block probe and maximize pump
- Insert WGP before detector (WGP 5), set to cross polarized
- Insert and then minimize pump with WGP 4

Sample Positioning and Visible Imaging

- Remove the pinhole
- Block beams
- Insert your sample
- Insert visible beam splitter
- Use a flashlight to illuminate the sample
- Search around your sample to find the spot of interest and then move this spot to match the location of the pinhole/beam centers
- Check the focus of the visible camera again with the micrometer on the objective
- Take and save a visible image of the sample
- Remove the beam splitter and walk-through the section above to Collect a 2D IR Spectrum

Turning off the laser:

- Turn off the FPAS
- Switch off the air going into box
- Turn 2nd waveplate to 146
- Block the 2nd stage
- Block the 1st stage
- Block the 3rd stage
- Turn down the multipass pump current and then switch it off
- Turn down the Regen pump and then switch it off
- Turn off both Pockels cells
- Turn off the pulse shaper
- Turn off chiller
- Turn off compressors
- Turn off the air

Appendix D

Alignment Tutorial for Rotators

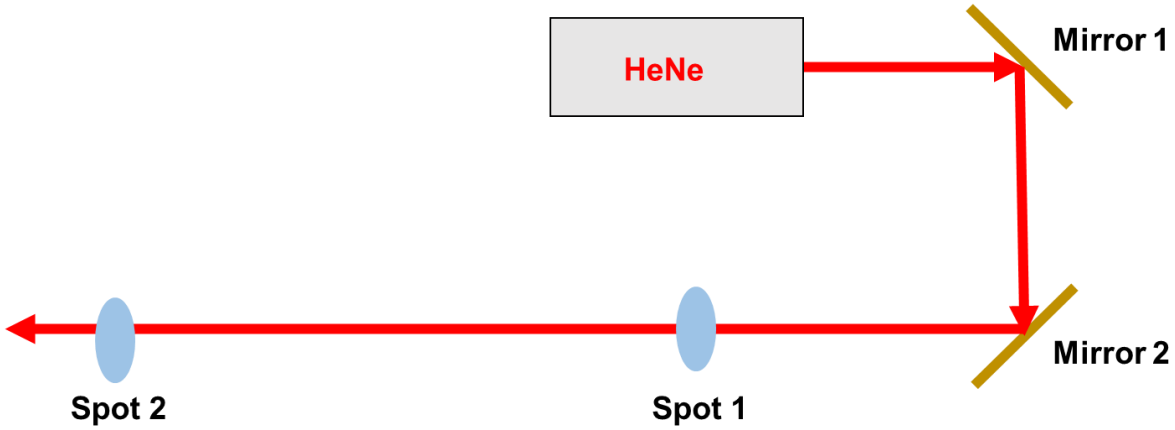

Figure D1: *Diagram showing example two mirror alignment mirrors and example alignment locations.*

Key initial design points:

- Set the laser as close to Mirror 1 as possible, to limit the amount the beam will have diverged before it hits Mirror 1.
- Maximize the distance between near and far alignment spots to be as far apart from each other as possible, to make the alignment easier and more precise.

General Procedure:

1) Mount the HeNe firmly to the table
2) Check optics and alignment card heights are all equal
3) Place a card where Mirror 2 will be (or further on the same line of holes)
4) Coarsely align Mirror 1:
    a. Do this by placing the mirror on the optical breadboard without screwing the mirror down.
    b. Make sure the beam hits the center of the mirror.
    c. Then, translate the mirror back and forth along the screw holes just a little bit, getting closer or further away from the laser (moving perpendicular to the card). This movement back and forth is one degree of freedom that you have to place the mirror. Notice that by moving the

mirror back and forth you change the position of the beam. Now rotate the mirror by loosening the post holder screw and rotating the post attached to the mirror. This is the second degree of freedom that you have to place the mirror (this movement changes the angle of the beam). Use these two degrees of freedom to center the beam on the card.

   d. Tighten the mount of M1 to the optical breadboard

5) Now choose two spots in the row next to the laser (if you want mark them with sharpie on the table), as indicated in the optical diagram for alignment. One will be close to M2 and the other as far as you have space for since the further way spot 1 and 2 are the easier and more precise your alignment will be.
6) Coarsely align Mirror 2 so that the beam hits the mirror dead on and so that the beam is roughly aligned to the two spots of your choosing.
7) Now do a fine alignment of the beam to the two spots. To do the fine alignment you are going to use the two knobs on each mirror holder. One knob moves the beam in the x direction (horizontally) and one knob moves the beam in the y direction (vertically). Use M1 to align to the near spot and M2 to the far spot. Repeat this procedure until the beam is aligned to both spots. You'll notice that the beam will slowly move into the right position. Essentially, what you are doing is setting the position of the beam with the first mirror and the angle of the beam with the second mirror.
   a. Note, if you run out of range on your knobs reset them to approximately center and reattempt your coarse alignment again.

NEXT… repeat this general procedure but with two mirrors on a translation stage to complete a full dogleg

Appendix E

How to use the FTIR Microscope and ATR

Instructions for Using the Focal Plane Array (FPA) FTIR Microscope

1. Cool with LN2 (~1 full thermos) to get temperature to 80 – 90 K
    a. Use the funnel and insert into correct detector (labeled FPA)
    b. Turn FPA on, with silver toggle switch on backside
    c. Check temperature
        i. Click the desktop icon – FPA Settings
        ii. Go to MicroEnable tab, dot next to temperature will be green if okay
2. Open OPUS
    a. Password: OPUS (all caps)
3. In Program (OPUS)
    a. Select wizard icon
    b. Make sure Hyperion 3000 – FPA is selected
    c. Click next and reset the stage – checking that the condenser is clear of the stage first (lower with large silver knobs under stage if not)
    d. Select parameters you want e.g. absorbance, the 15xIR headpiece, 64 scans
    e. Move the joystick and consequently stage such that the light is going through the sample
    f. Focus on the sample:
        i. With the large black knob on right side of stage for rough focusing
        ii. The smaller knob for fine adjustments
        iii. Joystick for side to side
        iv. You can track where you are approximately by looking at the light on the sample
            1. Adjust brightness with the sliding know next to image of lights
        v. Make sure to also focus the pinhole
            1. Do this by sliding the pinhole in or out with knob behind and under the stage

vi. Go back and forth between pinhole and sample to find the best focus

g. Once focused take ad image:

i. You can take a single image OR

ii. Image of a larger area

1. Select 3 border points to define your image by scanning with the joystick and clicking add new border point

h. Click next and then you will take a background:

i. Hit measure background once

1. If doing an air background: Hit current position

a. Remove your sample

b. Put in pinhole & refocus

c. Select IR icon

i. Right click on the FPA signal, click setup FPA image then click scale to min & max

ii. Focus pinhole

iii. Remove pinhole, right click on graph showing counts, click customize focal plane array, on pop up: Check temperature, and readjust the offset so your counts are in the light blue region

iv. Check IR light actually getting to sensor by sticking paper in between sample & sensor

v. Hit measure background

1. Don't touch bench during measurements

i. Put your sample back in

i. Refocus the stage (first in visible)

ii. Refocus pinhole (make sure not on a boundary between two parts of your sample

iii. Make sure pinhole is aligned with center yellow axis, use the small silver knobs

iv. Focus pinhole in the IR

v. Select purple box icon under the measurement positions title

1. Select grid size (typically 1 more than the visible)

vi. Make measurement

1. Name & save

2. Hit repeat

j. Examine your data:

i. Highlight peaks of interest

1. Drag cursor to select a region of interest

a. Right click and integrate

ii. You can extract spectra from particular points

1. Go to list

2. Right click and extract

iii. Once in other view save as

1. Make sure data point files (so they can be plotted in Matlab, Python etc.)

4. When finished:

a. TURN FPA OFF

b. Remove sample

c. Make sure funnel not inserted and gold lid is

How to Use the ATR

1. Bring your own sample surface
2. Lower the silver knobs underneath the stage to lower the condenser
3. Lower the stage with the black knob on the right side
4. Turn on the detector with the toggle switch on the right side

5. Retrieve the ATR objective in drawer #83 (ATR-20x A677-B10/FPA)
6. Take plastic distance ring off
7. DON'T apply any translational pressure
    a. Unscrew objective
8. Line up notches with neighboring visual objective, use the ball driver in the box to screw in the objective while you hold it in place, with the silver holes on the edge
9. Take small visual objective off if needed for space
10. Plug the grey cord into the side, the green light should flash
11. Place the coverslip
12. Hit video wizard in OPUS
    a. Select Hyperion 3000 – FPA ATR or MCT ATR
    b. Hit next
    c. Pick reflectance mode
    d. Select 20x ATR
    e. Raise stage until you see the surface, focus
    f. Take single image
    g. Measure the background
    h. Lower stage
    i. Use a kimwipe with methanol across the crystal very gently
    j. Engage pressure mode by pushing the silver switch on the side of the objective
        i. Starting with 1 is recommended
13. Measure background
    a. Always take a new background
    b. Select user defined position
    c. Hit set background
    d. Make sure in IR mode (interferogram is selected)

e. Slide the distance ring under objective for air background (the light turns green when engaged in pressure mode, the objective will retract after working)

f. Select # of points of interest

g. Next, measure sample, move slide to hit the spot you desire to measure

14. Hit end, examine spectra

15. Save file as, DPT mode, change path to what you want

16. Also save the experimental file, OPUS format

Appendix F

Using the Rheometer

1. INSTRUMENT SETUP

1.1. Turn on air

1.1.1. The air supply is to the left of the fume hood where the rheometer sits.

1.1.1.1. Turn the ball valve so the lever is in the same direction as the pipe.

1.2. Remove Spindle Cap

1.2.1. Underneath the monitor on the rheometer is a cap on the spindle should be removed. Do this by holding the cap with one hand and twisting the metal piece to the left which is located above the monitor on the top of the rheometer.

1.3. Place the plastic clear cup over the silver knob to reduce error due to the air current.

1.4. Turn on power

1.4.1. Inside the fume hood on the left a box with an orange front which has the TA logo on it. On the back of this box, left bottom side, is a power switch. Turn it on. Once on the lights on the orange box and rheometer itself should turn on.

1.5. Turn on the computer

1.5.1. Password to unlock the computer is same code as to get into the laser labs.

1.6. Open Trios software

1.6.1. It is a application with the TA logo names TRIOS on the desktop.A page should pop up and the left portion of the screen where it says Connect to instrument 5332-1971 @CSU should be selected. Click Connect.

1.7. Turn on chiller

1.7.1. Located to the left of the fume hood

1.7.2. First, take off the lid of the chiller by lifting up the green handle to insure there is enough chiller fluid.

1.7.2.1. If the chiller fluid does not fully cover the coils, add enough water or ethanol to fully cover them.

1.7.3. There is an on/off switch on the right, flip the switch to on.

1.7.3.1. The chiller will turn on and the green snowflake should be lit.

1.7.3.2. If the snowflake is not lit up, press and hold the arrow button on the right of the circle in the front until it says “ON”

2. CALIBRATION

2.1. Once a month calibration

2.1.1.1. On the bottom left of the screen is a “Calibration” tab.

2.1.1.1.1. Left click once.

2.1.1.2. On the left of the screen under “File Manager” is an “Instrument” button.

2.1.1.2.1. Left click twice.

2.1.1.3. There should be an “Inertia” section to this screen displaying the current inertia value being used and the date of the last calibration.

2.1.1.4. Left click  next to “Calibration”

2.1.1.5. Left click the “Calibrate” button at the bottom of this section.

2.1.1.6. Once calibration is done, if the new inertia is within +/-0.02 uN*m*s^2 of the old inertia, click “Accept”.

2.1.1.6.1. If the inertia is not within the acceptable limit, click cancel and, check that the instrument is level and restart the instrument. Then run the calibration again. Other things to try include cleaning the plates and reattaching the geometry again.

2.2. Daily Calibration

2.2.1. Put 40 mm flat plat on

2.2.1.1. Make sure the rheometer is raised sufficiently by pressing the ^ button until there is enough room to put plate on

2.2.1.2. Press the lock button on the front of the machine.

2.2.1.3. In the place where the cap was removed, slide the plate on with the line on the spindle matching the line on the top metal piece when placing on.

2.2.1.4. Tighten the spindle in place by turning the metal nut on the top of the machine

2.2.1.5. Replace plastic cup on top of the spindle

2.2.2. Inertia Calibration

2.2.2.1. Click on the "Geometries" tab on the lower left side of the screen

2.2.2.2. On the left of the screen under "File Manager" is a category for the 40 mm plate, select that

2.2.2.3. There should be an "Inertia" section to this screen displaying the current inertia value being used and the date of the last calibration.

2.2.2.4. Left click  next to "Calibration"

2.2.2.5. Left click the "Calibrate" button at the bottom of this section.

2.2.2.6. Once calibration is done, if the new inertia is within +/-0.02 of the old inertia, then click "Accept".

2.2.3. Friction Calibration

2.2.3.1. Under inertia section is a "Friction" section

2.2.3.2. Left click  next to "Calibration" in the fiction section

2.2.3.3. Left click the "Calibrate" button at the bottom of this section.

2.2.3.4. Once calibration is done, if the new friction is within a certain limit of the old friction, click "Accept"

3. TEMPERATURE

3.1. On the right side of the screen is an “Environmental” button

3.1.1. Left click once

3.2. Type “25” into the box and press “Apply”

4. ZERO GAP

4.1. Lower the machine with the down arrow button the actual rheometer (not to touch the bottom plate but close). This is just to speed up the instrument from doing the lowering itself.

4.2. Click on the “Gap” button on the right side of the screen

4.3. There is a picture  on the top of this selection with a “0” on it.

4.4. If you hover over the picture with the mouse it says “zero gap” click it.

4.4.1. The machine will lower until the zero gap is found.

4.5. Once done, the computer will ask if you want to raise to the loading gap.

4.5.1. Click “Yes”

5. EXPERIMENTAL PARAMETERS

5.1. You likely want to do a flow sweep procedure. Example files can be found in the folder “_Tibbetts”

5.1.1. A good geometry gap is 500µm (less if less sample)

5.1.2. 50 µm trim

5.1.3. 45000µm loading gap

6. SAMPLE

6.1. You will probably need ~700 -2000L of solution for 40 mm plate geometry

6.2. Micropippette your sample on the bottom plate centered under the top plate.

6.3. Lower the top plate to trim gap, add more solution until it fills to the edges of the top plate but isn’t seeping out.

6.4. Go to geometry gap and at this point remove any solution that is seeping out.

7. RUN EXPERIMENT

7.1. Hit the green play button

7.2. You can see the results in the results window

7.3. Once it is finished you can right click and hit export, plain text, and save in relevant folder

8. CLEAN UP & TURN OFF

8.1. Press the ^ arrow on the instrument and hold until the rotor is at a high enough height to remove the rotor.

8.2. Press the lock button on the instrument so the red light is above the lock.

8.3. Using a Kimwipe and some acetone to wipe the plate off

8.4. Hold the nut and remove your plate with the silver knob on top of the instrument. Place plate inside the container for storage

8.5. Close out Trios on the computer.

8.6. Turn the instrument off using the switch on the back of the box.

8.7. Turn the chiller off using the switch on the front.

8.8. Attach the spindle cover by screwing it on with the silver knob on top of the instrument.

8.9. Turn the air off so that the ball valve handle is perpendicular to the pipe.

List of Abbreviations

SEI- solid electrolyte interphase

FTIR- Fourier Transformed infrared spectroscopy

2D IR- two-dimensional infrared spectroscopy

LIB- lithium-ion battery

SIB- sodium-ion battery

V_{OC}- open circuit potential

FEC- fluoroethylene carbonate

VC- vinylene carbonate

IL- ionic liquid

RTIL- room temperature ionic liquid

NaCl- sodium chloride

FWHM- full-width half-max

DCA- dicyanamide

GSB- ground state bleach

SE- stimulated emission

ESA- excited state absorption

$T_{Waiting}$- Waiting time

FFCF- frequency-frequency correlation function

CLS- center line slope

NLS- nodal line slope

DMC- dimethyl carbonate

DEC- diethyl carbonate

EC- ethylene carbonate

XXXX- co-polarized

XXYY- cross-polarized

QB- quantum beating

PT- population transfer

Y-Fi- Ytterbium fiber

MCT- mercury cadmium telluride

ANDi- All normal dispersion

Yb-YAG- yttrium aluminum garnet doped ytterbium

PPLN- periodically poled lithium niobate

OPO- optical parametric oscillator

OPCPA- optical parametric chirped pulse amplification

ZGP- zinc germanium diphosphide

DFG- difference frequency generation

WP- waveplate

WGP- wire grid polarizer

Regen- regenerative amplifier

SHG- second harmonic generation

OPA- optical parametric amplification

AOM- acousto-optic modulator

MeSCN – methyl thiocyanate

MD – molecular dynamics

CDF- cylindrical distribution function

Bmim-1-butyl-3-methylimidazolium

BF4 - tetrafluoroborate

DSSC – dye-sensitized solar cell

TFSI - bis(trifluoromethylsulfonyl)imide

MgO:PPLN - magnesium doped periodically poled lithium niobate

B3LYP- Becke, 3-parameter, Lee-Yang-Parr

CN- carbon – nitrogen

Emim- 1-ethyl-3-methylimidazolium

SCN- thiocyanate

HB – hydrogen bond

DFT- density functional theory

2D ES- two-dimensional electronic spectroscopy

2D VE- two-dimensional vibrational electronic spectroscopy

TIPS-pentacene-

Ln/mm – lines per millimeter

HWHM – half-width half-max

Ti:sapphire- titanium sapphire

LO- local oscillator

FPA- focal plane array

Cryo-Yb- cryogenically cooled ytterbium

NA- numerical aperture

ROI- region of interest

CE- counter electrode

WE- working electrode

DOE- Department of Energy

LMR2- lens mount with retaining ring, 2 inch

XPS- x-ray photoelectron spectroscopy

LAR- least absolute residuals

MP2- Møller-Plesset perturbation theory

NVT- canonical ensemble (Number, volume, temperature)

NPT- isothermal-isobaric ensemble (Number, pressure, temperature)

RDF- radial distribution function

CI- confidence interval